Thesis Title

Underpinning the Molecular Barriers to Emergence of Novel Viruses

A PhD Thesis in Biomedical and Life Sciences

Presented by

Asmaa Nasr Saad Nasr
PhD student at the Division of Biomedical and Life Sciences
Student ID: 36018414

Under the Supervision of

Prof. Muhammad Munir
Professor of Virology and Viral Zoonoses
Biomedical and Life Sciences,
Lancaster University, Lancaster,
United Kingdom

Dr. Nikki Copeland
Senior Lecturer
Biomedical and Life Sciences,
Lancaster University, Lancaster,
United Kingdom

2026

Declaration of Originality

I declare that the content of this thesis is my own work and has not been submitted by me in substantially the same form for the award of a higher degree elsewhere. Any sections of the thesis which have been published have been clearly identified.

Asmaa Nasr

Experimental Contributions

Dr. Mustafa Atasoy contributed to the generation of data presented in Figures 4.2–4.3 and 4.13C and D.

Acknowledgment

I want to express my deep gratitude to Professor Muhammad Munir, who was to me not only an academic supervisor but also a true leader, teaching and guiding me through every step of building my research and professional career development and supporting me in both good and difficult times.

Many thanks to Dr. Nikki Copeland for his supervision and support during my thesis journey. His valuable insights have helped me explore alternative methods for establishing the work, and his assistance has created a smooth environment to accomplish the work whenever obstacles arise.

I would also like to thank all my laboratory members, BLS technicians and postdocs from other groups who provided me with technical assistance whenever needed.

My appreciation also goes to my family, who were there in every single moment of my journey, allowing and encouraging me to travel and chase my PhD dream.

Finally, I would like to thank the Egyptian Ministry of Higher Education and the British Council for funding my PhD study.

Abstract

Over the last two decades, bats have been linked to the emergence of several human viral pandemics. Molecular barriers to virus replication govern the viral host range, interspecies transmission, and potential spillover. N6-methyladenosine (m6A) is a post-transcriptional modification regulated by a wide range of cellular proteins, collectively referred to as the m6A machinery, which add (writers), remove (erasers), and recognise (readers) the modification on the target RNA. Angiotensin-converting enzyme 2 (ACE2) is an essential component of the renin-angiotensin system (RAS), and it also serves as a gateway for the replication of several coronaviruses. This study hypothesised the potential role of ACE2 and m6A as key barriers to the emergence of viruses in bats. Thus, the study examined the roles of these two barriers in the replication of recombinant Cedar virus green fluorescent protein (rCedPV-GFP) and bat coronavirus HKU5 carrying a SARS-CoV-1 spike ectodomain (BtCoV HKU5-SE) using *Rousettus aegyptiacus* (*R. aegyptiacus*)-derived cell lines, accompanied by comparisons to human m6A (hm6A) machinery and human ACE2 (hACE2). The study also incorporated comparative bioinformatic analyses of m6A components of *R. aegyptiacus*, *Pteropus alecto* (*P. alecto*), and *Homo sapiens* (*H. sapiens*). Initial bioinformatics and in silico analyses revealed that the identity matrices of m6A machinery of *R. aegyptiacus*, *P. alecto*, and *H. sapiens* have a high degree of similarity in the amino acid sequences of the machinery across the three species. Additionally, several syntenic genes were similarly detected in the m6A loci of these mammals. At the structural level, the m6A writer group in *R. aegyptiacus* and *P. alecto* was identical to that of *H. sapiens*. In contrast, erasers and readers exhibited polymorphism between the two bat species and between bats and humans. Adaptation of rCedPV-GFP in *R. aegyptiacus* cell lines (R06E and R05T) was performed using VeroE6 cells, while the virus failed to adapt using BHK-21. Screening of the human m6A machinery against rCedPV-GFP in human A549 cells revealed antiviral activity of methyltransferase-like 3 (METTL3) and Wilms' tumour 1-associating protein (WTAP) writers, the eraser AlkB homolog 5 (ALKBH5), and all reader proteins, with YTH domain-containing 2 (YTHDC2) being the most potent inhibitor of the virus. Establishment of R06E cell lines that overexpressed *R. aegyptiacus* METTL3 (RE-

METTL3) and its associated domains was performed using the piggyBac (pB) transposon system. Infection of these cell lines with rCedPV-GFP revealed that the full-length protein and its domains exerted comparable antiviral activity. Moreover, the full-length protein was translocated from the nucleus to the cytoplasm upon rCedPV-GFP infection. Infection of R06E wild-type (R06E WT) with the BtCoV HKU5-SE virus resulted in abortive infection due to the low expression level of ACE2. Using the pB system, the roles of both *R. aegyptiacus* ACE2 (RE-ACE2) and hACE2 in viral replication were investigated. While overexpression of RE-ACE2 significantly increased infection in R06E, it did not reach the level achieved with hACE2. Nevertheless, both receptors induced virus syncytia under the fluorescence microscope; moreover, both receptors underwent degradation upon virus infection, although hACE2 showed more pronounced degradation than RE-ACE2. Using protease inhibitors, BtCoV HKU5-SE was detected to depend on the transmembrane protease serine 2 (TMPRSS2) for its entry in R06E rather than cathepsin L (CTSL). Whereas qPCR results indicated significant upregulation of *RE-ACE2* and *TMPRSS2* at the peak of viral infection in the cells, the heat map analysis showed co-expression of *RE-ACE2* with the interferon-stimulated genes (ISGs). These results collectively provide fundamental approaches for understanding the role of m6A and the ACE2 receptor as key barriers to the emergence of novel viruses in bats.

List of Contents

List of Figures

List of Tables

List of Abbreviations

Abbreviation	Meaning
– ssRNA	Negative-sense single-stranded RNA
+ssRNA	Positive-sense single-stranded RNA
3D	Three-dimensional
5mC	5-methylcytosine
ACE2	Angiotensin-converting enzyme 2
ag	Attogram
ALKBH5	alkB homolog 5
Ang	Angiotensin
AngV	Angavokely virus
APN	Aminopeptidase
APS	Ammonium persulfate
BIRC7	Baculoviral IAP repeat containing 7
BPIV3	Bovine parainfluenza virus type 3
BSA	Bovine serum albumin
BtCoV HKU5-SE	Bat coronavirus HKU5 with SARS-CoV-1 spike ectodomain
BtCoVs	Bat coronaviruses
CD	Connecting domain
cDNA	Complementary DNA
CedPV	Cedar virus
CHIKV	Chikungunya virus
CL2	Containment level 2
CL3	Containment level 3
CL4	Containment level 4
CLD	Collectrin-like domain
CMC	Carboxymethylcellulose
CMs	Convoluted membranes
CPE	Cytopathic effect
Cq	Quantification cycle
CT	Cytoplasmic tail
CTD	C-terminal domain
CTSL	Cathepsin L
dACE2	delta ACE2
DAPI	4′,6-diamidino-2-phenylindole
DMS	Double-membrane spherules
DMSO	Dimethyl sulfoxide
DMVs	Double membrane vesicles
DPP4	Dipeptidyl peptidase-4
E	Envelope
E. dupreanum	Eidolon dupreanum
E. helvum	Eidolon helvum
ECL	Enhanced chemiluminescence
EDTA	Ethylenediaminetetraacetic acid
ER	Endoplasmic reticulum

ERGIC	ER-Golgi intermediate compartment
ERK	Extracellular signal-regulated kinase
EV71	Enterovirus 71
F	Fusion
FACS	Fluorescence-activated cell sorting
FBS	Fetal bovine serum
fs	Frame shift
FTO	Fat mass and obesity-associated protein
G	Glycoprotein
GDV	Genome Data Viewer
GE	Gene end
GhV	Ghana virus
GMEB1	Glucocorticoid modulatory element-binding protein 1
GMQE	Global Model Quality Estimation
GS	Gene start
H	Hemagglutinin
h	Hour/ hours
H. sapiens	Homo sapiens
HA	Hemagglutinin-neuraminidase
hACE2	Human ACE2
HBV	Hepatitis B virus
HCMV	Human cytomegalovirus
HCoV-229E	Human coronavirus 229E
HCoV-HKU1	Human coronavirus HKU1
HCoV-NL63	Human coronavirus NL63
HCoV-OC43	Human coronavirus OC43
HCoVs	Human coronaviruses
HCV	Hepatitis C virus
HE	Hemagglutinin-esterase
HeV	Hendra virus
HKU5-CoV-1	HKU5 coronavirus lineage 1
HKU5-CoV-2	HKU5 coronavirus lineage 2
hm6A	Human m6A
hMPV	Human metapneumovirus
hpi	Hours post-infection
HSV-1	Herpes simplex virus type I
IAV	Influenza A virus
ICTV	International Committee on Taxonomy of Viruses
IFA	Immunofluorescence assay
IFI6	Interferon alpha-inducible protein 6
IFIT1	Interferon-induced protein with tetratricopeptide repeats 1
IFIT3	Interferon-induced protein with tetratricopeptide repeats 3
IFITM1	Interferon-induced transmembrane protein 1
IFITM3	Interferon-induced transmembrane protein 3
IFITs	Interferon-induced proteins with tetratricopeptide repeats
IFN	Interferon

IFNAR1	Interferon alpha and beta receptor subunit 1
IFNs	Interferons
IFN-α	Interferon alpha
IFN-β	Interferon beta
IFN-λ	Interferon-lambda
IR	Intergenic region
IRES	Internal ribosome entry site
IRES2	Internal ribosome entry site 2
IRF3	Interferon regulatory factor 3
IRF7	Interferon regulatory factor 7
IRX3	Iroquois homeobox 3
ISGs	Interferon-stimulated genes
ITR	inverted terminal repeats
IVT	In vitro transcription
Kbp	Kilobase pairs
L	Large
LayV	Langya virus
LB	Luria broth
LDS	Lithium dodecyl sulfate
LLGL1	LLGL Scribble cell polarity complex component 1
LOD	Limit of detection
M	Matrix
M	Membrane
m1A	N1-methyladenosine
m3C	3-methylcytidine
m5C	5-methylcytidine
m6A	N6-methyladenosine
m6Am	N6,2′-O-dimethyl adenosine
m7G	N7-methylguanosine
MAVS	Mitochondrial antiviral signalling
MERS-CoV	Middle East respiratory syndrome coronavirus
METTL14	Methyltransferase-like protein 14
METTL3	Methyltransferase-Like 3
MHC-I	Class I major histocompatibility complex molecules
MHV	Murine hepatitis virus
MIEF2	Mitochondrial elongation factor 2
min	Minutes
miRNA	MicroRNA
MOI	Multiplicity of infection
MojV	Mojang virus
MTD	Methyltransferase domain
Mx1	MX dynamin-like GTPase 1
N	Nucleocapsid
N. vison	Neogale vison
N/A	Not Applicable
NCBI	National Centre for Biotechnology Information

NFW	Nuclease-free water
NF-κB	Nuclear factor kappa-light-chain-enhancer of activated B cells
NiV	Nipah virus
NK4IN4	Sodium/potassium transporting ATPase interacting 4
NLRP3	Nucleotide-binding oligomerization domain, leucine-rich repeat and pyrin domain-containing protein 3
NLS	Nuclear localization signal
nm	Nanometres
NMD	Nonsense-mediated mRNA decay
NSPs	Non-structural proteins
nt	Nucleotide
NTD	N-terminal domain
NTP	Nucleoside triphosphate
OAS1	2'-5'-oligoadenylate synthetase 1
ORF	Open reading frame
ORFs	Open reading frames
P	Phosphoprotein
P. abramus	Pipistrellus abramus
P. alecto	Pteropus alecto
PaBr	Pteropus alecto brain cells
PAGE	Polyacrylamide gel electrophoresis
PaKi	Pteropus alecto primary kidney cells
PAMPs	Pathogen-associated molecular patterns
pB	PiggyBac
PBS	Phosphate-buffered saline
PBST	Phosphate-buffered saline with Tween-20
PCR	Polymerase chain reaction
PD	Peptidase domain
PDA	Pancreatic ductal adenocarcinoma
PDB	Protein Data Bank
PE1	Promoter element 1
PE2	Promoter element 2
PFU/mL	Plaque-forming units per millilitre
PRNTase	polyribonucleotidyl transferase
PRRs	Pattern recognition receptors
PRV	Pseudorabies virus
PSI	Percentage spliced-in
pSTAT1	phosphorylated STAT1
PTC	Premature termination stop codon
PTM	Post-translational modification
PVDF	Polyvinylidene difluoride
QMEANDisCo	Qualitative Model Energy ANalysis—Distance Constraints. (QMEANDisCo)
R. aegyptiacus	Rousettus aegyptiacus
R06E WT	R06E wild-type

RAS	Renin-angiotensin system
RBD	Receptor-binding domain
RBP	Receptor-binding protein
RBPs	Receptor-binding proteins
rCedPV-GFP	Recombinant Cedar virus green fluorescence protein
RdRP	RNA-dependent RNA polymerase
RE-ACE2	Rousettus aegyptiacus ACE2
RE-METTL3	Rousettus aegyptiacus METTL3
Rep	Replication
RIG-I	Retinoic acid-inducible gene I
RIPA	Radioimmunoprecipitation assay
RLRs	Retinoic acid-inducible gene I (RIG-I)-like receptors (RLRs)
RNA-seq	RNA sequencing
RNP	Ribonucleoprotein
RPGRIR1L	RPGR interacting protein 1-like
RPM	Rounds per minute
RSAD2	Radical S-adenosyl methionine domain-containing 2
RT	Reverse transcription
RTC-CCC	Replication-transcription complex co-transcriptional capping complex
RTCs	Replication-transcription complexes
RT-qPCR	Reverse transcriptase quantitative polymerase chain reaction
S	Spike
S1	Spike protein subunit 1
S2	Spike protein subunit 2
SALL2	Spalt-like transcription factor 2
SAM	S-adenosylmethionine
SARS-CoV	Severe acute respiratory syndrome coronavirus
SARS-CoV-2	Severe acute respiratory syndrome coronavirus 2
SDS	Sodium dodecyl sulphate
SDTv1.2	Sequence Demarcation Tool version 1.2
SE	Spike ectodomain
Sec	Seconds
sg-mRNA	Sub-genomic mRNA
sg-mRNAs	Sub-genomic mRNAs
sgRNAs	Sub-genomic RNAs
SH	Small hydrophobic
SOD2	Superoxide dismutase 2, mitochondrial
SP	Single peptide
STAT1	Signal transducer and activator of transcription 1
STING	Stimulator of interferon genes
STOML2	Stomatin-like protein 2
SYNPO2	Synaptopodin 2
TBK1	TANK-binding kinase 1

TGEV	Transmissible gastroenteritis virus
TLR3	Toll-like receptor 3
TLR7	Toll-like receptor 7
TLR9	Toll-like receptor 9
TM	Transmembrane
T_m	Melting temperature
TMPRSS2	Transmembrane serine protease 2
TOX4	TOX high mobility group box family member 4
Tr	Transcription
TRS-B	Transcription regulatory sequences body
TRS-L	Transcription regulatory sequences leader
TTPA	α-tocopherol transfer protein
USP18	Ubiquitin-specific peptidase 18
UTR	Untranslated region
VSV	Vesicular stomatitis virus
WB	Western blot
WT	Wild-type
WTAP	Wilms' tumour 1-associating protein
YTH	YT521-B homology
YTHDC1	YTH domain-containing protein 1
YTHDC2	YTH domain-containing protein 2
YTHDF1	YTH domain-containing family protein 1
YTHDF2	YTH domain-containing family protein 2
YTHDF3	YTH domain-containing family protein 3
ZFD	Zinc finger domain
ZFD1	Zinc finger domain 1
ZFD2	Zinc finger domain 2
ΔΔCt	Delta-delta Ct

Chapter 1. General Introduction

1.1. Paramyxoviruses

1.1.1. Brief History and Zoonotic Origin

Paramyxoviruses have a long evolutionary history of spillover between humans and animals; human measles, for example, is a highly transmissible disease which is hypothesised to have evolved from cattle rinderpest [1], although, in terms of the case fatality rate, the most dangerous zoonotic paramyxoviruses are those of the genus *Henipavirus* (Hendra and Nipah).

The first recorded outbreak of Hendra began in September 1994 in Queensland, Australia, when an infected pregnant thoroughbred mare was brought into a training stable and died 2 days later. Within the next 14 days, twelve horses in the same or adjacent stable died from respiratory and neurological manifestations. The disease was transmitted to a stable hand and trainer who were in contact with the infected mare. Both suffered from respiratory signs, but the trainer died after developing respiratory and renal failure. Soon after this, quarantine and containment measures were implemented, and within a day of the outbreak investigation, the virus was identified as a putative new paramyxovirus member, initially called equine morbillivirus and later named Hendra virus (HeV) [2].

In 1995, a second HeV outbreak arose near Mackay, Queensland, in two horses and resulted in the death of their caretaker, who suffered from relapsing encephalitis 13 months after the initial contact with the two animals [3]. Later, in 1999, another horse near Cairns, Queensland, died from the virus [4]. Since then, investigations have taken place to identify the potential reservoir of the virus, which was traced back to fruit bats of the genus Pteropus (flying foxes) [5]. In 2021, a novel HeV genotype was discovered in two flying foxes that is closely related to the original strain. The novel strain caused vasculitis in bats and infected horses, similar to the original strain, highlighting its zoonotic potential [6].

Nipah virus (NiV) was discovered in Malaysia between September 1998 and April 1999; the virus caused an encephalitis outbreak in pigs that resulted in the culling of more than a million animals and the death of 105 humans who had been in contact with infected pigs [2,7]. In 2001, at the beginning of the 21st century, an outbreak of NiV was detected in Siliguri, India. Unlike the Malaysian epidemic, which involved pigs, the Indian outbreak involved direct transmission among family members and healthcare workers who handled infected patients [8]. In Bangladesh, the virus was initially detected in 2001 among cases who were in close contact with infected patients [9]; then, between December 2004 and January 2005, NiV was detected in patients associated with the consumption of raw date palm sap [10]. In the Philippines, on the other hand, the virus was detected in 2014 among villagers who consumed meat from infected horses, and it was subsequently transmitted to close contacts of those patients [11]. Until recently, outbreaks of NiV have been identified in Southeast Asia, where the primary reservoir, Pteropus bats, are abundant [12].

Cedar virus (CedPV) is another henipavirus that was isolated from the urine of Australian flying foxes. While zoonotic transmission of this virus has not been confirmed, its close similarity to HeV and NiV, along with its ability to infect human cells, raises concerns about its zoonotic potential [13,14].

In 2012, a novel henipa-like virus, called Mojiang virus (MojV), was potentially associated with three miners presenting with pneumonia in Mojiang, Yunnan Province, China. The virus was identified in rodents associated with the mine where the cases were detected [15]. In 2022, a novel shrew-borne henipa-like virus, Langya virus (LayV), was identified in China and was potentially associated with febrile illnesses and liver and kidney dysfunction in infected individuals [16].

Collectively, these outbreaks underscore the significant public health threat posed by zoonotic spillover events involving paramyxoviruses.

1.1.2. Classification

For a long time, the taxonomic classification of the family *Paramyxoviridae* has been contentious; The recent revisions by the International Committee on Taxonomy of Viruses (ICTV), 2025 release, have standardised its taxonomy based on the amino acid sequence of the Large (L) protein, which encodes the viral RNA-dependent RNA polymerase (RdRp). The *Paramyxoviridae* are members of the order *Mononegavirales*. This family is divided into several subfamilies: *Avulavirinae*, *Feraresvirinae*, *Glossavirinae*, *Ichthysvirinae*, *Kamposvirinae*, *Skoliovirinae*, *Metaparamyxovirinae*, *Orthoparamyxovirinae*, and *Rubulavirinae*. Among these, the genera *Henipavirus* and *Parahenipavirus* are encompassed within the

Orthoparamyxovirinae subfamily. While the *Parahenipavirus* genus contains viruses that infect bats and rodents with uncertain zoonotic potential, only confirmed zoonotic viruses are included in the *Henipavirus* genus. The name of the *Henipavirus* genus is derived from the two prototype viruses HeV and NiV, i.e. He (Hendra)/nip (Nipah), which are considered the most zoonotic paramyxoviruses with significant pathogenic potential in humans and animals. The genus *Henipavirus* consists of five species: HeV, NiV, CedPV, Ghana virus (GhV), and Angavokely virus (AngV) [17]. The recent ICTV taxonomy of the *Paramyxoviridae* family, including subfamilies and genera, and the phylogeny of the genus *Henipavirus* in relation to the closed *Parahenipavirus* members are illustrated in (**Table 1.1** and **Figure 1.1**).

Table 1.1. Recent ICTV taxonomy of the Paramyxoviridae family. Classification adopted from [17].

Subfamily	**Genus**
Avulavirinae	*Metaavulavirus*
	Orthoavulavirus
	Paraavulavirus
Feraresvirinae	*Ferlavirus*
	Aquaparamyxovirus
	Respirovirus
Glossavirinae	*Cynoglossusvirus*
Ichthysvirinae	*Hoplichthysvirus*
Kamposvirinae	*Hippocavirus*
Metaparamyxovirinae	*Synodonvirus*
Rubulavirinae	*Orthorubulavirus*
	Pararubulavirus
Skoliovirinae	*Scoliodonvirus*
Orthoparamyxovirinae	*Bovinavirus*
	Henipavirus
	Jeilongvirus
	Morbillivirus
	Narmovirus
	Parahenipavirus
	Parajeilongvirus
	Paramorbillivirus
	Salemvirus
	Tupaivirus

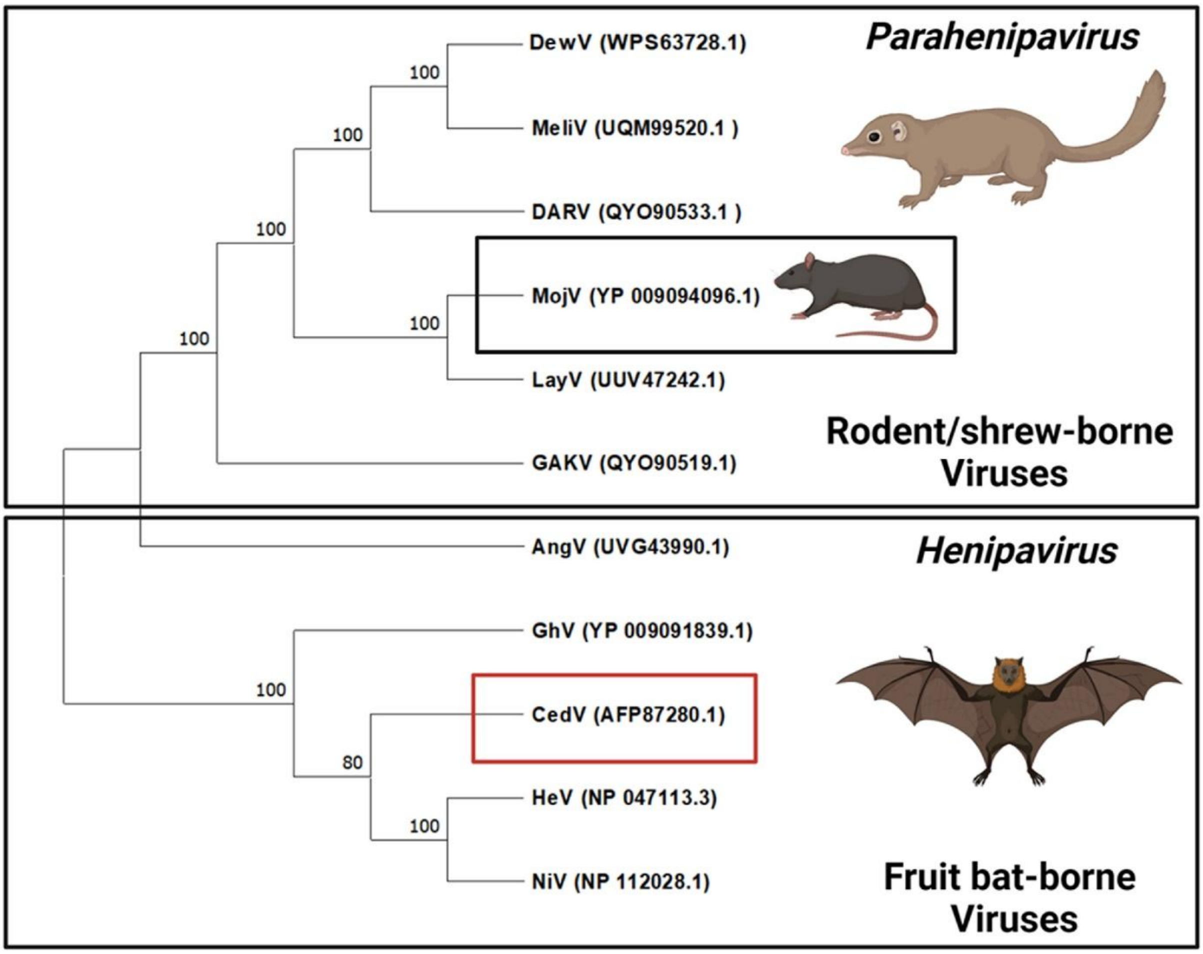

Figure 1.1. Phylogeny of genus Henipavirus. The genus includes HeV, NiV, CedPV, GhV, and AngV. CedPV is highlighted by a red rectangle. Figure imported from [13].

1.1.3. Morphology

Paramyxoviruses are enveloped, single-stranded RNA viruses that range in size from 150 to 500 nanometres (nm); they are pleomorphic and exhibit a range of morphologies, from filamentous to spherical. Structurally, a mature paramyxovirion consists of a ribonucleoprotein (RNP) surrounded by a bilipid envelope that carries two transmembrane glycoproteins, Fusion (F) and an attachment protein or receptor-binding proteins (RBPs) that include: Glycoprotein (G) (*Henipavirus* and Metapneumovirus), hemagglutinin (H) (*Morbillivirus*), and hemagglutinin-neuraminidase (HA) (*Avulavirus*, *Respirovirus*, and *Rubulavirus*). The viral RNP is a complex structure that consists of a herringbone-shaped helical nucleocapsid (N) associated with the phosphoprotein (P) and the L protein, which is embedded in the Matrix (M) protein that links the viral envelope and RNP. Additionally, a small hydrophobic (SH) transmembrane protein and a transmembrane (TM) protein have been associated with some paramyxoviruses [1,17] (**Figure 1.2**).

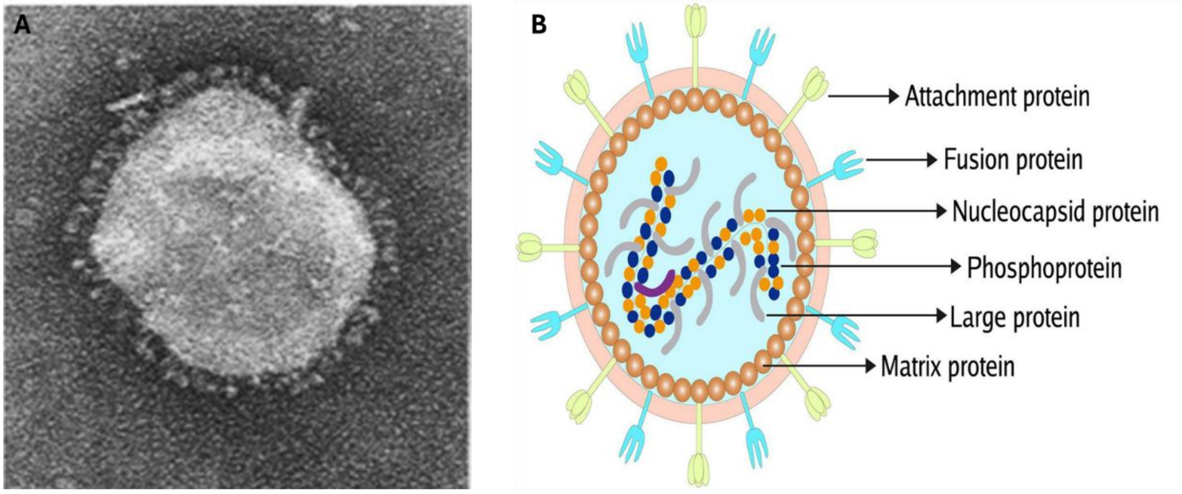

Figure 1.2. The overall structure of paramyxoviruses. (A) Negative contrast electron microscope of simian virus representing the spherical shape of the paramyxoviruses. (B) A cross-sectional schematic diagram of the paramyxovirus illustrating proteins involved in virus structure. Figures were adapted from [1,18] with modifications applied to the imported images.

1.1.4. Genome Organisation

Paramyxoviridae are non-segmented, negative-sense single-stranded RNA (–ssRNA) viruses with nucleotide (nt) lengths ranging from 13 to 19 kilobase pairs (kbp). Usually, the genomes of *Paramyxoviridae* follow the "rule of six" in their organisation, which means that the N protein must bind to six nucleotides for P gene editing, and the genome length must be a multiple of that number for effective viral replication [19]. The paramyxovirus genome is not capped or polyadenylated; instead, it is flanked by a short trailer sequence at the 5′ end and a leader sequence at the 3′ end. In proximity to these, there are two promoter elements, PE1 and PE2, which initiate the synthesis of the genome and antigenome. Members of *Paramyxoviridae* contain 6–10 coding genes, each separated by a short non-transcribed intergenic (IR) region, and contain flanking, approximately 10–13 nt, gene start (GS) and gene end (GE) signals, which regulate the initiation and termination of transcription, respectively. Generally, *Paramyxoviridae* encode 9–12 proteins, divided into structural (N, M, P, L, F, and G/H/HA) and non-structural proteins (NSPs) or accessory proteins. The latter are encoded by RNA editing of the P gene and vary according to the virus [20–22]. The paramyxovirus genome organisation and details of proteins encoded by the genome are illustrated, respectively, in (**Figure 1.3** and **Table 1.2**).

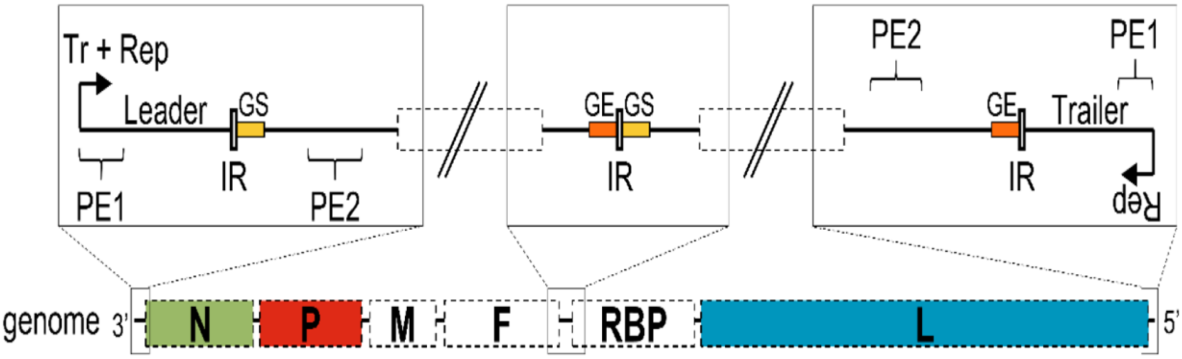

Figure 1.3. A schematic figure represents the genome structure and organisation of Paramyxoviridae. The viral genome contains leader and trailer sequences at the 3' and 5' ends, respectively, two promoter elements, PE1 and PE2, and coding genes separated by an intergenic (IR) region. Gene start (GS) and Gene end (GE) are present at each gene. The coding genes of paramyxoviruses include the nucleoprotein (N), phosphoprotein (P), matrix (M), fusion (F), receptor-binding protein (RBP), and large (L).Tr. Transcription and Rep. Replication. Diagram was adapted from[20] with modifications applied to the imported image.

Table 1.2. Proteins encoded by the paramyxovirus genome and their associated types and functions.

Protein	**Function**	**References**
G/H/HA	Attaching to the cell receptor	[18]
F	Fusion to the host cell membrane	[23]
L	Encoding RdRp/ viral RNA synthesis and capping of the newly synthesised RNAs	[24,25]
N	Binding to viral nucleic acid	[18]
M	Viral assembly/stabilises the viral envelope/ links the nucleocapsid with the virus membrane	[26]
P	Promoting RNA synthesis/ co-factor for L protein	[27]
D	Unknown, might be involved in virus replication	[28]
W	Immune evasion/ inhibition of TLR3	[29]
V	Immune evasion/ inhibition of IFN-α induction	[30]
C	Immune evasion/ inhibition of IRF7 phosphorylation	[31]
C′	Immune evasion/ degradation of STAT1	[32]
Y1	Immune evasion/ inhibition of TLR7/9 signalling	[31]
Y2	Immune evasion/ inhibition of TLR7/9 signalling	[31]

TLR3, toll-like receptor 3; IFN-α, interferon alpha; IRF7, interferon regulatory factor 7; STAT1, signal transducer and activator of transcription 1; TLR7, toll-like receptor 7; TLR9, toll-like receptor 9.

1.1.5. Replication

1.1.5.1. Attachment and Entry

The infection cycle of paramyxoviruses begins when the virus's attachment protein binds to its host cell receptor **(Table 1.3)**. Following receptor binding, host proteases, including furin, cleave the F protein at its basic sites, triggering conformational changes that result in fusion of the viral envelope with the cell membrane. In NiV and HeV, fusion occurs within the endosomal compartment using Cathepsin L (CTSL). Notably, in many species of paramyxoviruses, the fusion activity of the F protein is linked to the attachment protein; for example, the fusion capability of NiV and HeV is greatly enhanced in the presence of the G protein and reduced when the G protein is absent. In these contexts, once fusion occurs, the viral N protein is detached from the M protein and released into the cytoplasm to initiate the replication/transcription process [26].

Table 1.3. Cell receptors associated with the members of henipavirus. Data imported from [33].

Virus	**Receptor**
HeV	Ephrin-B2 / ephrin-B3
NiV	Ephrin-B2/ ephrin-B3
CedPV	Ephrin-B1/ ephrin-B2/ ephrin-A2/ ephrin-A5

1.1.5.2. Viral RNA, Structural and Accessory Proteins Synthesis

Although the precise mechanism of paramyxoviruses' replication is poorly understood, it generally follows the same steps as other –ssRNA viruses. Transcription of the template RNA initiates when the viral RNA polymerase complex (L and its cofactor P) binds to the promoter elements near the leader sequences at the 3′ end of the genome. The polymerase scans the region and begins adding nucleotides to the newly generated templates. As the polymerase proceeds, it moves to the GS, where it initiates synthesis of the sub-genomic mRNA (sg-mRNA), which stops when the polymerase reaches the GE signal, resulting in the release of the newly synthesised mRNA. Subsequently, the polymerase passes the IR region to locate the GS of another gene. This process generates subsets of mRNAs (i.e. sub-genomic mRNAs; sg-mRNAs) that are readily capped and polyadenylated during synthesis by the L protein. Polyadenylation is assumed to occur due to the poly U stretch present at the GE site

[21]. The nascent sg-mRNAs are translated into viral structural and accessory proteins.

While the translation of the structural proteins occurs directly from the corresponding gene, translation of accessory proteins involves RNA editing and leaky scanning of the P gene. In the former, the polymerase slips over the P gene, allowing insertion of additional nucleotide/s (mostly G) on the newly transcribed mRNA. Whereas in the latter, the polymerase bypasses the initiation codon within the overlapping open reading frame (ORF) and initiates translation from the subsequent start codon [34].

Following translation of the viral proteins, the paramyxovirus genome replication initiates. Similar to transcription, paramyxoviral genome replication also starts at the leader sequence; in this regard, the viral polymerase ignores the intermingled gene regions and directly uses the template negative-sense genome to synthesise a positive-sense antigenome. The trailer sequence at the new nascent antigenome is further used for the synthesis of new negative-sense templates [35].

1.1.5.3. Assembly and Egress

Assembly and budding of paramyxoviruses typically occur at the host cell membrane. In this regard, all viral proteins assemble to form the new virion; the N protein binds the viral nucleic acid, followed by the P and L proteins, to form the viral RNP complex. The F and receptor attachment proteins are also assembled on the newly formed particle. Notably, the M protein, which lines the inner plasma membrane, serves as the central core for assembly and clusters the viral attachment proteins with the RNP complex. The assembled virion then buds from the cell membrane to be released [26,27]. The overall diagram of paramyxovirus replication is illustrated in **(Figure 1.4)**.

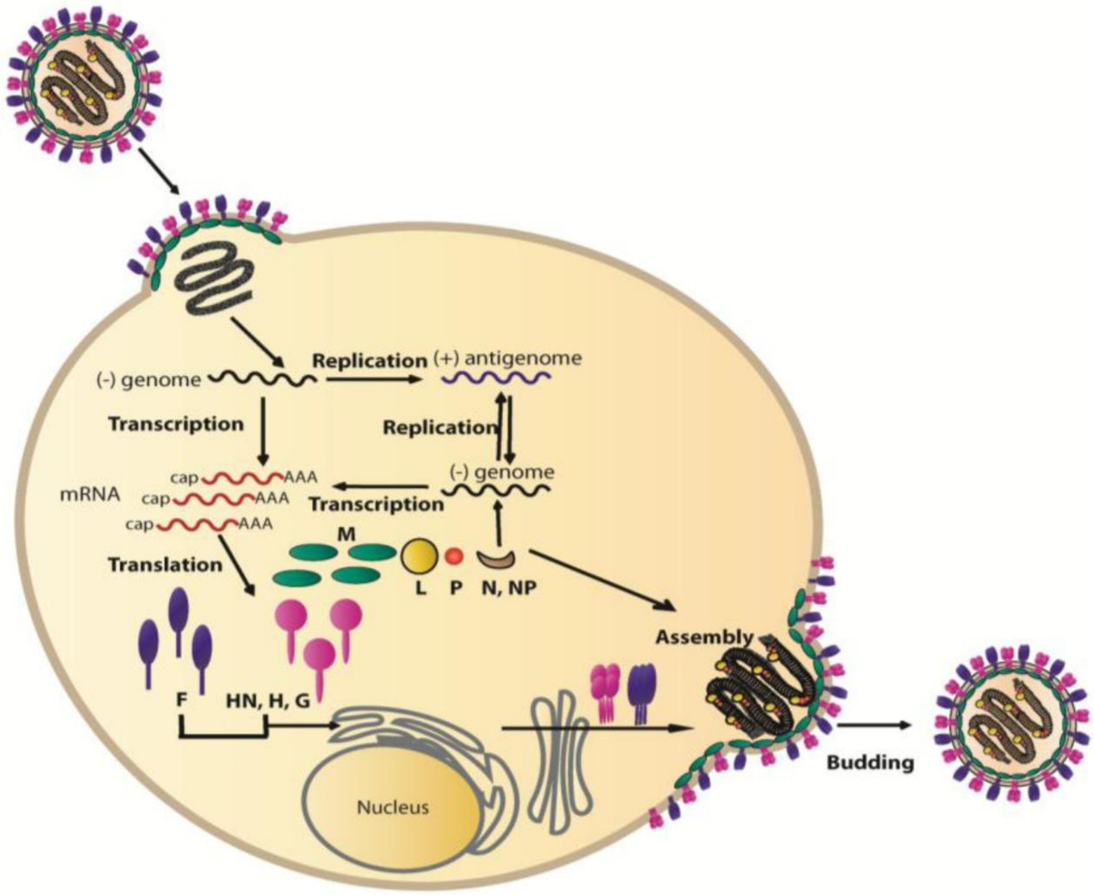

Figure 1.4. A schematic diagram of paramyxovirus replication. The virus attaches to and enters the cell via fusion, where the genome is released to initiate transcription, replication, and viral protein synthesis. The newly synthesised viral proteins are then assembled, and the nascent virion is released by budding. The figure is adapted from[26] with modifications applied to the imported figure.

1.1.6. Transmission and Clinical Signs

1.1.7. Prevention and Control

As discussed, zoonotic henipaviruses pose a significant threat to humanity; therefore, enhancing wildlife and animal surveillance is the most effective way to prevent spillover and henipavirus transmission to humans. Monitoring programs for bat populations, migration, and tracking diseases in pigs and horses are particularly crucial, as they are associated with HeV and NiV transmission to humans. Moreover, continuous genetic survey strategies for virus identification in bats residing in and around human niches can provide early signals for henipavirus outbreaks in humans. In this regard, the One Health approach should be conceptualised to impose the transdisciplinary efforts toward achieving optimal health for humans and animals and preventing zoonotic transmission of henipaviruses [40–42].

Avoiding direct and indirect contact with animals, washing hands subsequently after contact with infected animals, enhancing infection control measures in health-care facilities and avoiding consumption of raw date palm are effective measures to prevent henipavirus diseases in humans [43].

There is no specific treatment for henipaviruses in humans; however, monoclonal antibodies targeting the G or F proteins of henipaviruses have been developed to provide post-exposure protection against HeV and NiV outbreaks. Currently, no vaccines are approved for any of the henapiviruses in humans; however, several LayV, HeV, and NiV vaccines are under development. Equivac® is a subunit vaccine made using the soluble G protein of HeV, which is used in Australia for horse vaccinations, but it did not protect pigs against NiV. In pigs, various vector-based vaccine candidates are under development for NiV [36,40]

Generally, handling of HeV and NiV requires containment level 4 (CL4), which represents a challenge in research on these viruses. CedPV is a non-pathogenic henapivirus that is genetically close to HeV and NiV but lacks expression of V and M proteins, which protect HeV and NiV against immunity. Recently, the development of recombinant CedPV expressing GFP (rCedPV-GFP) has enabled broad study and the development of antiviral drugs against zoonotic henapiviruses in containment level 2 (CL2) facilities [13,44]

1.2. Coronaviruses

1.2.1. Brief History and Zoonotic Origin

Recent genomic analyses suggest that an ancient coronavirus-like epidemic may have affected East Asian populations more than 20,000 years ago. This inference is based on signatures of positive selection in human genes known to interact with coronaviruses, indicating long-term historical exposure to a coronavirus-related selective pressure in humans [45]. However, it was not until the 20th century that the first human coronavirus was characterised. In 1965, a coronavirus was isolated from the nasal discharge of a human patient with a common cold and named the 229E strain, B814. Notably, the virus had a similar shape to that of the infectious bronchitis virus of chickens.

Later in 1967, another coronavirus was isolated from medical students with the common cold and was termed OC43. Ongoing research and techniques in virology at that time identified that these two novel viruses had morphologies similar to those of other animal viruses, including the murine hepatitis virus (MHV) and the transmissible gastroenteritis virus (TGEV) of swine, with pleomorphic membranes and club-shaped projections. Therefore, it was accepted as a new group of viruses and officially termed as coronavirus [46]. Since then, infection with coronaviruses in humans has been widely associated with mild, self-limiting upper respiratory diseases. In the early 21st century, the severe acute respiratory syndrome coronavirus (SARS-CoV) emerged in Guangdong Province, China, ushering in a new era of coronavirus infections in humans [47]. Cases showed a typical pneumonia that rapidly spread throughout 29 countries, declaring the first human pandemic of coronaviruses, with more than 8000 infected cases and 900 mortalities [48]. In contrast to other human coronaviruses, the origin of SARS-CoV was linked to animals, the Himalayan palm civets and horseshoe bats [49], boosting research in coronaviruses and zoonotic transmission.

Following the discovery of SARS-CoV, NL63 and HKU1 were identified and traced back, along with 229E and OC43, to bats and rodents [50,51]. Ten years after the SARS pandemic, in 2012, a novel coronavirus named Middle East respiratory syndrome coronavirus (MERS-CoV) was isolated from the sputum of a Saudi man who suffered from acute pneumonia, progressive respiratory and renal failures. The virus belonged to a different lineage than the human coronaviruses and was phylogenetically related to the bat coronaviruses HKU4 and HKU5 [52]. Soon after that, the virus was isolated from dromedary camels, suggesting that MERS originated in bats and was then transmitted to humans via dromedary camels as an intermediate host [50,53]. As of September 2025, MERS has been reported globally, with more than 2600 cases and 957 deaths [54].

The emergence of severe acute respiratory syndrome coronavirus 2 (SARS-CoV-2) in 2019 in Wuhan, China, has drawn public attention. The virus spread around the globe, causing approximately 7 million deaths worldwide [55]. Until recently, the exact source of SARS-CoV-2 has remained obscure [56], although the detection of SARS-CoV-2-like viruses in bats has emphasised research on bats and their role in future spillover of coronaviruses to humans [57,58]. Recently, the discovery of a distinct HKU5 that can infect human cells has highlighted the possibility of zoonotic transmission of this virus [59], raising concerns about the emergence of another bat-borne coronavirus pandemic in humans.

1.2.2. Classification

Family *Coronaviridae is* classified in the Order Nidovirales, Suborder Cornidovirineae*,* within the *Coronaviridae,* into three subfamilies: *Orthocoronavirinae, Letovirinae,* and *Pitovirinae.* Coronaviruses are classified within the *Orthocoronavirinae*, which encompasses four genera: *Alphacoronavirus, Betacoronavirus, Deltacoronavirus, and Gammacoronavirus. Gamma* and *Delta* genera encompass viruses that infect birds, while *Alpha* and *Beta* genera include those that infect mammals, such as bats and humans (BtCoVs and HCoVs). Within these genera, HCoV 229E and HCoV NL63 belong respectively to the subgenera *Duvinacovirus* and *Setracovirus* of the *Alpha* genus, while SARS-CoV and SARS-CoV-2 are within the *Sarbecovirus* subgenera of the *Betacoronavirus.* HCoV-OC43 and HCoV-HKU1 are *Betacoronaviruses* associated with the subgenera *Embecovirus,* while MERS-CoV and HKU5 are *Merbecovirus* [17,60]. Recent ICTV classification of the family *Coronaviridae*, including the subfamilies, genera, and phylogenetic classification of the *Orthocoronavirinae,* including HKU5 and other HCoVs, is illustrated in (**Table 1.4** and **Figure 1.5**).

Table 1.4. Recent ICTV taxonomy of the Paramyxoviridae family. Classification adopted from [17].

Subfamily	Genus
Letovirinae	*Alphaletovirus*
Orthocoronavirinae	*Alphacoronavirus*
	Betacoronavirus
	Deltacoronavirus
	Gammacoronavirus
Pitovirinae	*Alphapironavirus*

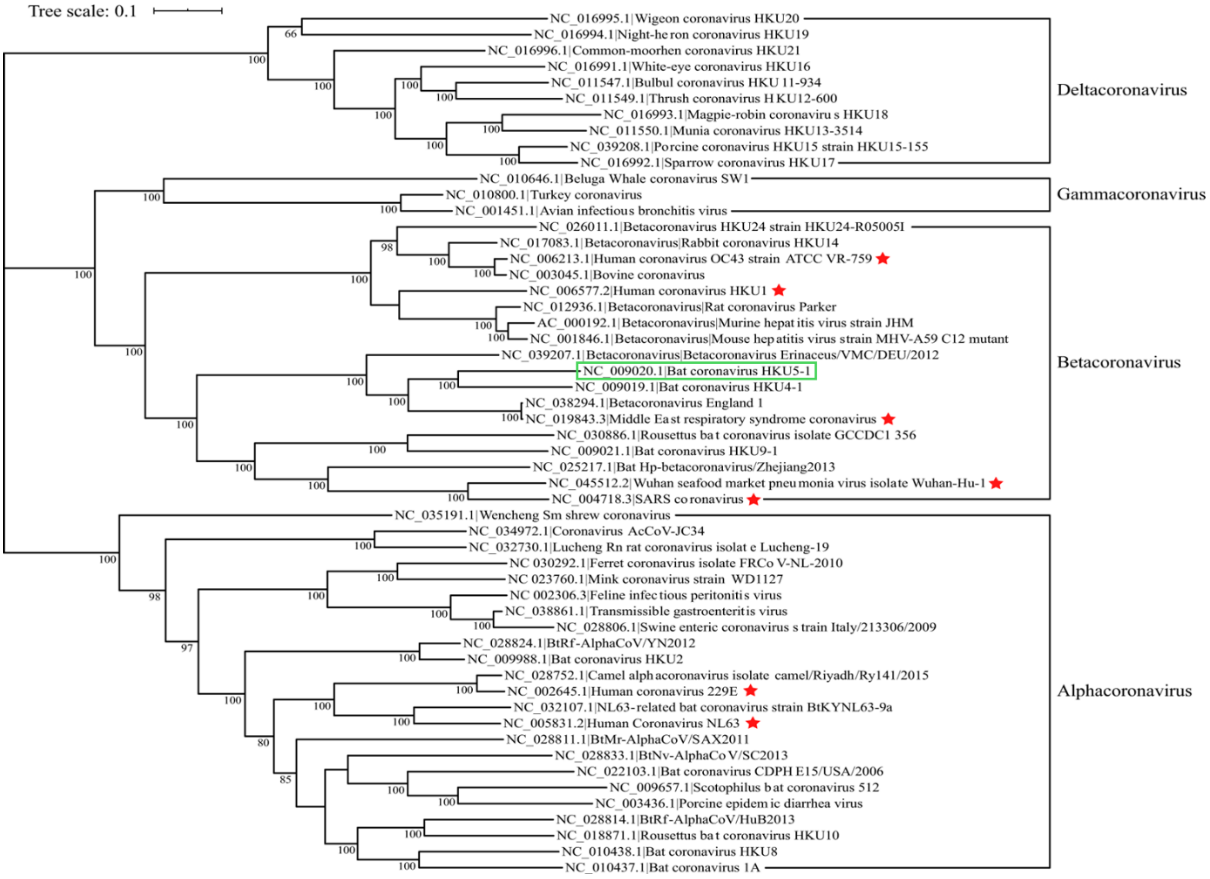

Figure 1.5. Phylogeny of Orthocoronavirinae. The genera include Alphacoronavirus, Betacoronavirus, Deltacoronavirus, and Gammacoronavirus. HKU5 is highlighted by a green rectangle while HCoVs are marked with red stars. Figure imported from [61].

1.2.3. Morphology

Coronaviruses are small viruses with a diameter of 50-200 nm. They are mostly spherical in shape, although viruses can be oval and pleomorphic [62]. Under the electron microscope, a single corona virion consists of a helical capsid and a bilipid envelope. The N protein encapsulates the viral nucleic acid, while the envelope is composed of three proteins: Spike (S), Membrane (M), and Envelope (E). The S forms club-like projections that give the characteristic crown shape morphology of the virus, and is responsible for virus attachment to the host cell, while the M and E are responsible for envelope rigidity and ring structure [62–64]. An additional structural protein, hemagglutinin esterase (HE), is present in some members of *Betacoronavirus,* assisting the virus in its attachment [65] (**Figure 1.6**).

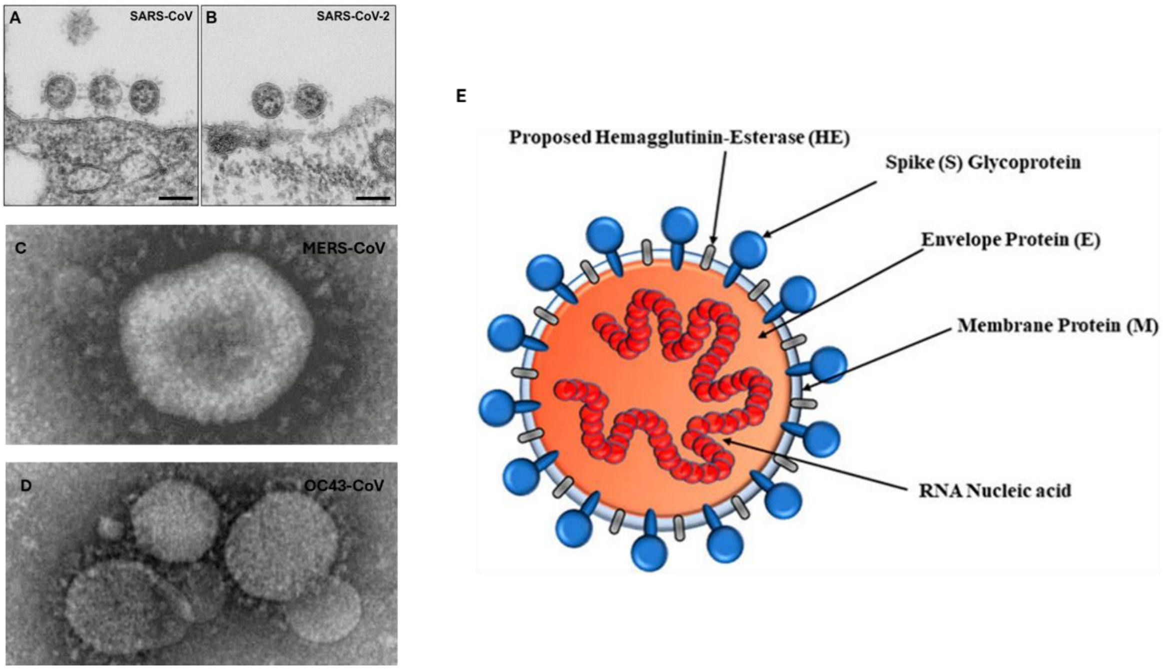

Figure 1.6. The overall morphology of the coronaviruses. (A) SARS-CoV-1 and (B) SARS-CoV-2 attached to the cell surface, showing substantial spherical morphology. (C) OC43 shows a spherical shape with club projections. (D) MERS-CoV demonstrates oval and polymorphic shapes. (E) A cross-sectional schematic diagram of the coronavirus illustrating proteins involved in virus structure. Diagram and Electron microscope images are adapted from [63,66–69] with modifications applied to the imported images.

1.2.4. Genomic Organisation and Structure

Coronaviruses are positive-sense single-stranded RNA (+ssRNA) viruses with genomic material ranging from 24.5 kbp to 31.8 kbp, with an average of approximately 30 kbp. It is the longest among the RNA viruses, although the actual size varies among the genera. Generally, the genomic organisation of coronaviruses follows the rule (5′-leader sequence - untranslated region (UTR) - replicase - S-E-M-N-3′-UTR-poly(A) tail), with accessory genes dispersed within the genome and at the 3′ end [60].

There are several open reading frames (ORFs) encoded within the corona genome; The ORF1a/b is the longest and constitutes two-thirds of the genome. It is located at the 5′ end and contains two overlapping ORFs (ORF1a and ORF1ab), which encode for the NSPs. Other ORFs are located at the 3′ end of the genome, and their translation leads to the production of both structural proteins and accessory proteins. Adjacent to the ORFs at the 3′ end of the viral genome and approximately 70 nucleotides away from the 5′ end, there are two respective regions of particular interest called transcription regulatory sequences body (TRS-B) and transcription regulatory sequences leader (TRS-L), both of which play an important role in virus replication (will be discussed later) [70,71].

Mainly, there are four structural proteins encoded by the viral genome: S, M, N, and E; nevertheless, the additional HE can be encoded in some members of the genus *Betacoronavirus*, for example, HCoV-OC43 and HCoV-HKU1 [65]. As a rule, coronaviruses encode 16 NSPs from ORF1a/b, and several accessory proteins vary across the virus group. NSPs are generally responsible for viral replication and transcription, while the accessory proteins are associated with pathogenesis and immune evasion [72]. Genomic structure and brief function of encoded proteins are illustrated in (**Figure 1.7**, **Figure 1.8**, and **Table 1.5**), respectively.

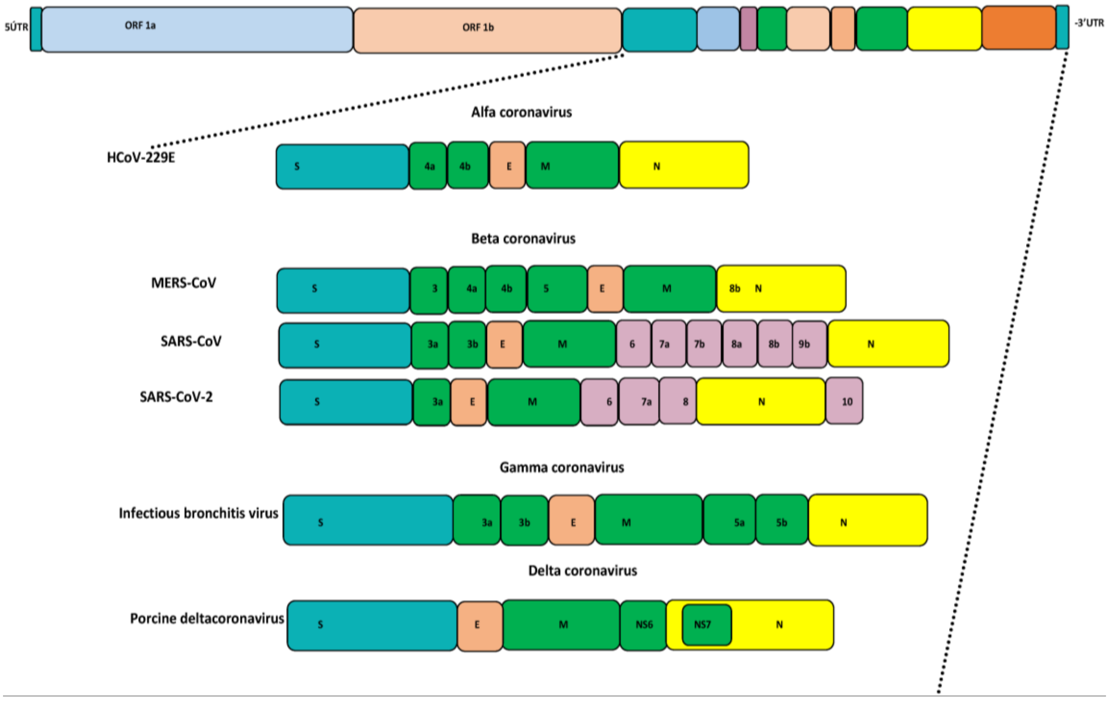

Figure 1.7. A schematic figure illustrates the genomic organisation of the coronavirus. The genome consists of ORF1a/b and the structural genes, which are conserved across all coronavirus species, whereas the accessory genes vary among viral species. Figure adapted from [73].

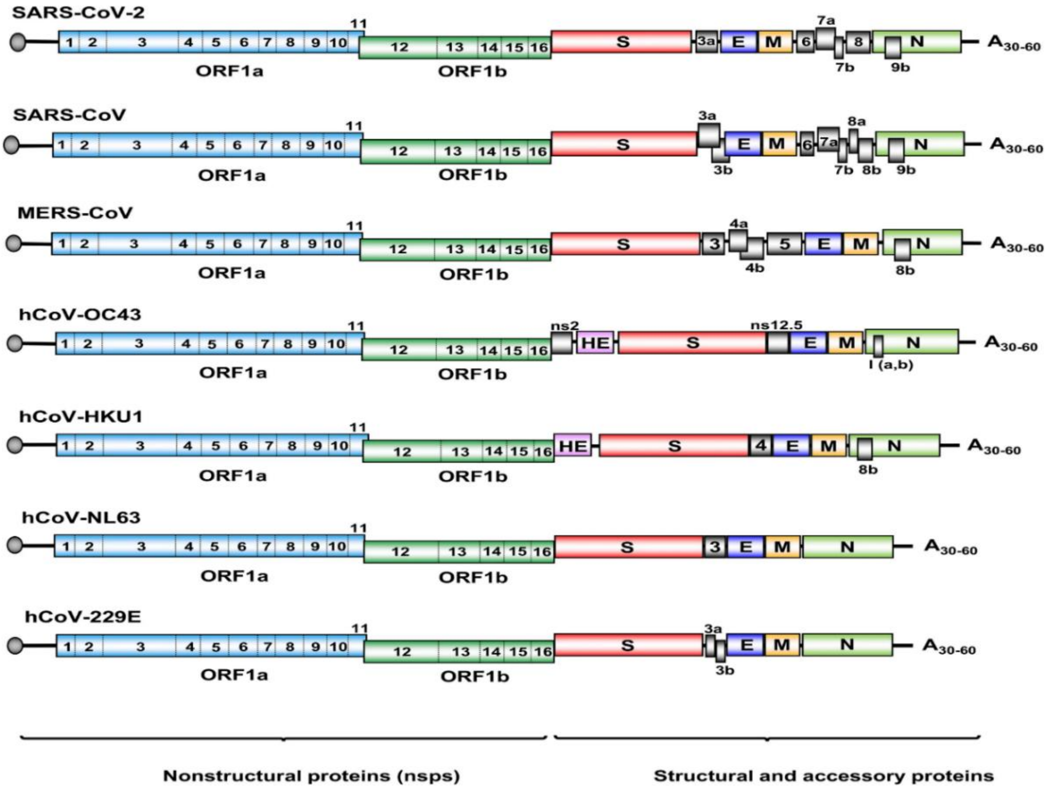

Figure 1.8. Genomic maps of the HCoVs illustrating proteins encoded by each virus. Figure adapted from [74].

Table 1.5. Proteins encoded by the coronavirus genome and their associated type and function. The table is based mainly on HCoVs proteins.

Protein	Function	Reference
NSP1	Hijacking the host translation mechanism	[75]
NSP2	Unknown function may contribute to viral pathogenicity and immune evasion	[76]
NSP3	Cleavage of ORF1a/b polyproteins/formation of DMVs of the viral RTCs	[77,78]
NPS4	Formation of DMVs of the viral RTCs	[78]
NSP5	Cleavage of ORF1a/b polyproteins	[77]
NSP6	Formation of DMVs of the viral RTCs	[75]
NSP7	Formation of the coronavirus polymerase complex	[79]
NSP8	Formation of the coronavirus polymerase complex	[79]
NSP9	Unknown function may contribute to viral pathogenicity and initiate viral RNA synthesis	[79,80]
NSP10	Promoting the methyl cap and viral RNA proofreading complex	[75,81]
NSP11	Unknown function may contribute to the viral frameshift translation	[80]
NSP12	Main RdRP/formation of the coronavirus polymerase complex	[79]
NSP13	Promoting viral replication and cap methylation	[74,81]
NSP14	Formation of the viral RNA proofreading complex	[74,81]
NSP15	Cleavage of viral RNA during replication	[72]
NSP16	Methyl cap formation	[82]
S	Attachment to the host cell receptor	[83]
M	Viral assembly/ binding to viral S and N, ensuring stability	[83]
N	Binding to viral RNA	[83]
E	Formation of the virus envelope / enhancing cell infectivity	[83]
HE	Attachment to the host cell receptor	[65]

ORF3a	Promoting viral assembly and release/ activating NF-kB signalling and apoptosis cascade	[84,85]
ORF3b	Immune evasion/ inhibition IRF3 translocation	[84,85]
ORF3c	Immune evasion/ cleavage of MAVS	[86]
ORF3d	Unknown, may interact with mitochondrial STOML2	[84]
ORF3	Apoptosis induction	[87]
ORF4a	Immune evasion/ inhibition of IFN-λ	[88]
ORF4b	Immune evasion/ inhibition of IFN-λ	[88]
ORF5	Immune evasion/ inhibition of NF-κB signalling	[89]
ORF6	Immune evasion/ suppressing STAT1 nuclear translocation	[90]
ORF7a	Immune evasion/ inhibition of STAT1 phosphorylation	[91]
ORF7b	Immune evasion/ inhibition of STAT1 phosphorylation	[91]
ORF8	Immune evasion/ downregulation of *MHC-I*	[92]
ORF8a	Unknown function constitutes an Ion channel protein	[93]
ORF8b	Immune evasion/ inhibition of *IFN-β* expression	[94]
ORF9b	Immune evasion/ inhibition of MAVS signalosome	[95]
ORF9c	Immune evasion/ inhibition of IFNs signalling components, including IFITs	[96]
ORF10	Immune evasion/ degradation of MAVS	[97]
ns12.9	Ion channel protein involved in viral morphology and pathogenesis	[98]
I protein	Unknown	[99]

DMVs, double membrane vesicles; RTCs, replication-transcription complexes; NF-κB, nuclear factor kappa-light-chain-enhancer of activated B cells; IRF3, interferon regulatory factor 3; MAVS, mitochondrial antiviral signalling; STOML2, stomatin-like protein 2; IFN-λ, interferon-lambda; *MHC-I*, class I major histocompatibility complex molecules; *IFN-β*, interferon beta; IFNs, interferons; IFITs, interferon-induced proteins with tetratricopeptide repeats

1.2.5. Replication

1.2.5.1. Attachment and Entry

The coronavirus S protein consists of 2 subunits (S1 and S2) and a polybasic furin cleavage site at the junction of S1 and S2 [100]. Virus replication begins when the receptor-binding domain (RBD) of S1 binds to the host cell receptor, which varies according to the virus (**Table 1.6**). The host protease furin cleaves the S protein into S1 and S2 at the furin cleavage site, activating the S2 subunit. Afterwards, the host serine protease, transmembrane protease, serine 2 (TMPRSS2), cleaves the S2 subunit, triggering several configurational cascades that culminate in the fusion of the virus to the cell membrane [101]. In addition to cell fusion, the virus can enter cells via endocytosis. In the latter case, the virus is engulfed within an endosome, inside which the cysteine protease CTSL activates the S2, resulting in fusion of the virus to the endosomal membrane and finally releasing the nucleocapsid to the cytoplasm [102,103].

Table 1.6. Receptors of known HCoVs and HKU5. Data imported from [104,105].

Virus	Receptor
HCoV-229E	APN
HCoV-NL63	ACE2
HCoV-HKU1	Sialic acids
HCoV-OC43	Sialic acids
SARS-CoV	ACE2
MERS-CoV	DPP4
SARS-CoV-2	ACE2
HKU5	ACE2

ACE2, angiotensin-converting enzyme 2; APN, aminopeptidase; DPP4, dipeptidyl peptidase-4.

1.2.5.2. Synthesis of Non-Structural Proteins

The genome of coronaviruses is + sense ssRNA, which means once the virus enters the cytoplasm, it is readily translated within the cell. Translation of the ORF1a/b at the 5′ end produces two polyproteins (pp1a and pp1ab). The latter is produced because of the -1 ribosomal frameshift of the region where ORF1a and ORF1b overlapped [106]. The pp1a corresponds to NSP1–11 while pp1ab corresponded to NSP12–16. Viral NSP3 and NSP5 are respectively responsible for the amino acid cleavage of pp1a and pp1ab, releasing each group of proteins accordingly. The pp1a corresponds to NSP1–11 while pp1ab corresponded to NSP12–16 [107].

NSp1 is the first protein released, responsible for shutting down the cell translation cycle and facilitating virus-cell hijacking [108]. The remaining NSPs (NSP 2–16) contribute to the formation of the viral RTCs, where genomic replication and sg-mRNAs synthesis occur. Each NSP plays a critical role in the RTCs function. NSP3, NSP4, and NSP6 are responsible for RTCs formation. NSP12, along with its two cofactors NSP7 and NSP8, are responsible for RNA replication [109]. NSP9, on the other hand, acts as an RdRp primer [110]. NSP13 initiates the formation of the Cap [111], while NSP14 jointly facilitates the replication-transcription complex co-transcriptional capping complex (RTC-CCC). Cap methylation of the synthesised mRNA is brought by the NSP16 [112]. The NSP14 serves as a SARS-CoV-2 proofreading enzyme, and NSP10 stimulates this activity by binding the exonuclease domain of the NSP14 [113]. Finally, NSP2 and NSP15 suppress host interferon (IFN) signalling, promoting viral replication [72,76].

1.2.5.3. Viral RNA, Structural and Accessory Proteins Synthesis

Viral + ssRNAs act as templates for the synthesis of − ssRNAs, which in turn produce more positive strands. These newly synthesised strands are further translated to produce more NSPs. For the production of the structure and accessory proteins, this process does not occur simultaneously; in fact, during negative-strands synthesis, the RTCs disrupt the transcription once reaching the TRS-B at the 3′ end, and then they re-initiate it again at the TRS-L at the 5′ end. This discontinuous step ensures the interaction between TRS-Bs of the negative strands and the TRS-Ls of the positive strands, whereupon the TRS-L re-initiation, a complementary strand copy of the leader sequence is added to the nascent RNAs (anti-leader sequence). As a result of this strategy, a subset of negative-strand RNAs known as sub-genomic RNAs (sgRNAs) is created, and those sgRNAs are used for the synthesis of positive-sense sg-mRNAs [107,114]. ORFs of those positive-sense sg-mRNAs, produced from the previous step, are further translated to generate the structural proteins (S, E, M and N). Interspersed between the ORFs of the structural genes are the ORFs of the accessory proteins. SARS-CoV-2 ORF9b is produced because of the leaky scanning of the N protein sgRNA, while ORF10 and ORF14 are postulated to be translated downstream of the N gene [114,115]. During the replication of the coronavirus, it induces convoluted membranes (CMs), small open double-membrane spherules (DMS), and DMVs, all of which are thought to be derived from the endoplasmic reticulum (ER). The CMs and DMS are major sites of NSPs accumulation, while DMVs are the sites for viral RNA synthesis [115–117].

1.2.5.4. Assembly and Budding

Assembly and budding of the coronavirus occur in the ER–Golgi intermediate compartment (ERGIC) [118]. After translation of the structural protein, viral assembly occurs. The M protein, along with the E protein, forms the virus envelope. The N-protein binds with the synthesised genome, forming the viral nucleocapsid protein [119]**.** The S protein enters the virions at this point to form a mature virion [120]. Those virion particles are then transported to the Golgi apparatus. After that, the virion particles are released outside the cell by exocytosis [118,121]. (**Figure 1.9**) illustrates an overall diagram of the coronavirus replication cycle.

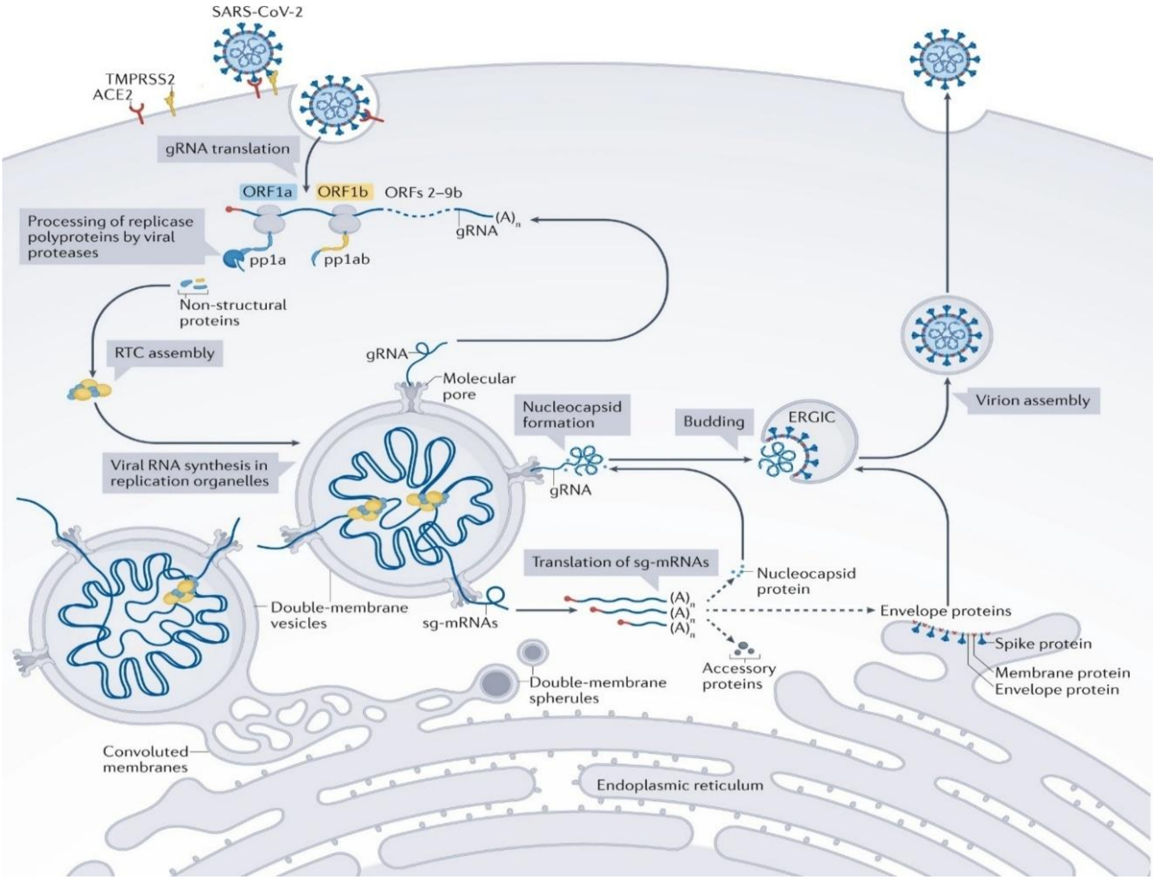

Figure 1.9. A schematic diagram illustrates the overall replication of the coronavirus. The virus enters via endocytosis or membrane fusion, then it is released into the cytoplasm, where the genomic RNA initiates replication and translation to produce structural and non-structural proteins. The virus assembly and budding take place in the ERGIC and are released via exocytosis. Figure adapted from [81].

1.2.6. Clinical Presentation and Transmission

The transmission of HCoVs is typically respiratory and involves human-to-human transmission via cough or sneezing. However, in SARS-CoV-2, the oro-faecal route is also a possible cause of infection [122]. In MERS, the zoonotic transmission is common through contact, either direct or indirect, with infected camels or their byproducts (meat, milk, urine [123].

The incubation period of all HCoVs ranges from a few days to 2 weeks, with an average of 2 to 5 days [124,125]. Clinical manifestations usually range from asymptomatic mild to severe respiratory manifestations (fever, headache, cyanosis, coryza, cough, dyspnoea, etc).

Patients with HCoV-HKU1 typically present with a runny nose, fever, and myalgia, while those with HCoV-229E often experience dyspnoea. Cyanosis and diarrhoea are more prominent in HCoV-OC43 and HCoV-NL63, respectively [126]. Notably, among HCOVs, OC43 is the most prevalent, followed by NL63, HKU1, and 229E [127]. SARS-CoV and SARS-CoV-2 cases primarily presented with fever, sore throat, myalgia, and non-productive cough, which developed into dyspnoea, hypoxia and death in some patients, although rhinorrhoea, pharyngalgia, olfactory defection, and gastrointestinal symptoms may also be included [72,128]. Infection with MERS-CoV resembles that of SARS-CoV and SARS-CoV-2, although pneumonia and renal failure are common findings [129]. Mortality rate varies among coronaviruses; MERS-CoV is associated with an approximately 34% death rate, while SARS-CoV is associated with 9%. SARS-CoV-2 has an approximately fatality rate of 2% at the beginning of its emergence (Wuhan-Hu-1), while this rate decreased later to less than 0.1% for some strains in certain vaccinated populations [130,131]. The fatality rate of other seasonal coronaviruses is low and usually occurs in hospitalised patients [132,133].

1.2.7. Prevention and Control

Vaccines are a useful approach to preventing human coronavirus diseases; however, they are only available against SARS-CoV-2 [134]. Thus, the simplest way to prevent and control coronaviruses is through supportive treatment for infected persons, good hygiene practices and social distancing. These include disinfecting contaminated surfaces with 70% alcohol, handwashing, properly disposing of contaminated materials, wearing face masks, avoiding touching the nose or mouth, quarantining infected persons, and avoiding contact with them. [135]. In MERS-CoV, avoiding contact with infected camels and heat treatment of animal milk and meat byproducts can be effective in preventing disease infection and spillover into humans [136].

1.3. ACE2 as a Pivotal Receptor for Coronaviruses, Determining the Viral Host Range

The discovery of the Renin-angiotensin system (RAS) pathway in 1889 by Tigerstedt and Bergman has led subsequently to the identification of a wide network of peptides, enzymes, and receptors that compose this pathway [137]. However, it was not until recently, in 2000, when the ACE2 receptor was discovered as a major part of the RAS pathway [138]. It regulates the cardiovascular system by converting angiotensin (Ang) I and II to Ang 1–9 and 1–7, respectively, leading to vasodilatation. Thus, ACE2 acts as a negative regulator of the RAS system [139]. Although recently it was identified as a major receptor for coronaviruses, including SARS-CoV-1, SARS-CoV-2, HCoV-NL63, and HKU5 [105,140–142].

Structurally, the canonical ACE2 is a homodimer protein that is composed of 805 amino acids, forming two main domains: an N-terminal peptidase domain (PD) and a C-terminal collectrin-like domain (CLD). The N-terminal PD domain cleaves Ang I and II and binds the coronavirus S1 spike, whereas the CLD regulates amino acid transport in the kidney and insulin exocytosis. Both domains are connected by a ferredoxin-like fold domain or neck domain, which is a part of CLD, while the hydrophobic transmembrane (TM) helix region, intracellular cytoplasmic tail (CT) and N-terminal signal peptide (SP) region are located distal to the CLD and PD, respectively [143–145] (**Figure 1.10**).

Figure 1.10. A schematic diagram of the ACE2 structure. The receptor is composed of a single peptide (SP) (red), a peptidase domain (PD) (green), a neck domain (ND) (sky blue), a collectrin-like domain (CLD) (orange), a transmembrane region (TM) (black), and a cytoplasmic tail (CT) (purple).

The interaction between the ACE2 receptor and the coronavirus spike is the first step in virus entry; accordingly, factors including receptor expression levels and polymorphisms will determine the virus's host range and govern cross-species transmission and zoonotic spillover.

As a type I transmembrane metalloprotease, ACE2 is ubiquitously expressed throughout the human body; however, its expression varies across different tissues. Organs such as the intestines, kidneys, testes, heart, and gallbladder exhibit high *ACE2* expression, whereas adipose tissue and thyroid glands exhibit lower expression. Basal expression levels can be detected in the liver, lung, and female genitalia, whereas a lack of expression is observed across the brain, skin, lymphoid tissue, and immune cells [146]. This inconsistent pattern of expression governs SARS-CoV-2 infection in humans, where COVID-19 severity increases with higher *ACE2* expression and vice versa [141,147].

Additionally, studies indicated that the ACE2 polymorphism restricts coronavirus infection both within and across species. Variants Ser19Pro, Ile21Val, Glu23Lys, Lys26Arg, Lys31Arg, His34Arg, and Thr92Ile are associated with high SARS-CoV-2 infection, while Asp38Val and Tyr83His are linked to the opposite, when all were expressed ectopically in HEK293 and infected with vesicular stomatitis virus (VSV) chimeric with SARS-CoV-2 spike [145,148]. Variants associated with high SARS-CoV-2 infection in HEK293 cells were found mainly in Africans and Europeans, while those associated with low HEK293 infection were detected in Asians, suggesting that genetic differences among human populations influence susceptibility and severity of COVID-19. Likewise, Gly352Val and Tyr515Cys ACE2 substitutions, which increased SARS-CoV infectivity in HEK 293, are present in minor amounts in the European population [148].

In animals, the ACE2s of primates, snakes, pigs, cats, ferrets, and orangutans show high similarity to the key determinants of human ACE2 (hACE2), facilitating interaction with SARS-CoV-2 and rendering these animals potential hosts for the virus. In contrast, the ACE2 of mice and rats are poorly susceptible to SARS-CoV-2, due to high polymorphisms in key binding sites of the receptor [149]. Likewise, that of *Rousettus aegyptiacus* (*R. aegyptiacus*) (Egyptian fruit bat or Egyptian rousette) [150].

Recently, the binding preferences of NeoCoV and PDF-2180 MERS-like coronavirus spikes were screened against ACE2 of several mammalian orthologues. While most of the tested species could be infected by both viruses, genetic determinants of ACE2 in those mammals restricted susceptibility to the two viruses, leading to classification of the tested species as potential, intermediate hosts, or less susceptible to NeoCoV and PDF-2180 infection [151]. Therefore, for a coronavirus to cross the species barrier, it must acquire the adaptability to utilise the ACE2 receptor in these species.

1.4. Role of Bats in Transmission of Coronaviruses and Paramyxoviruses

Next to rodents, bats (Order Chiroptera) are the most diverse mammalian species on Earth, roosting in a wide range of ecological niches. They are distinct mammals, comprising more than 1,400 species, contributing to pollination, seed dispersal, soil fertility, and the control of both vertebrate and invertebrate populations, helping to maintain environmental balance and biodiversity [152,153].

Compared to many other mammals, bats harbour more viruses, making them confirmed or potential reservoirs for many emerging diseases, including rabies, Ebola, and Marburg. Among bat-borne viruses, members of the *Coronaviridae* and *Paramyxoviridae* families constitute the majority of sequences isolated from bats, with many species posing significant or potential public health concerns [154]. (**Figure 1.11**). Indeed, pandemic coronaviruses (SARS-CoV, MERS-CoV, and SARS-CoV-2) and the prototype henipaviruses (HeV and NiV) are proven/hypothesised to have originated in bats and to have spilt over to humans, either directly or indirectly via an intermediate host, as previously discussed. However, none of these viruses is lethal in bats as they are in humans, making bats excellent hosts for the maintenance, survival, and spread of viruses [155]. The factors associated with bats as potential virus reservoirs are listed below.

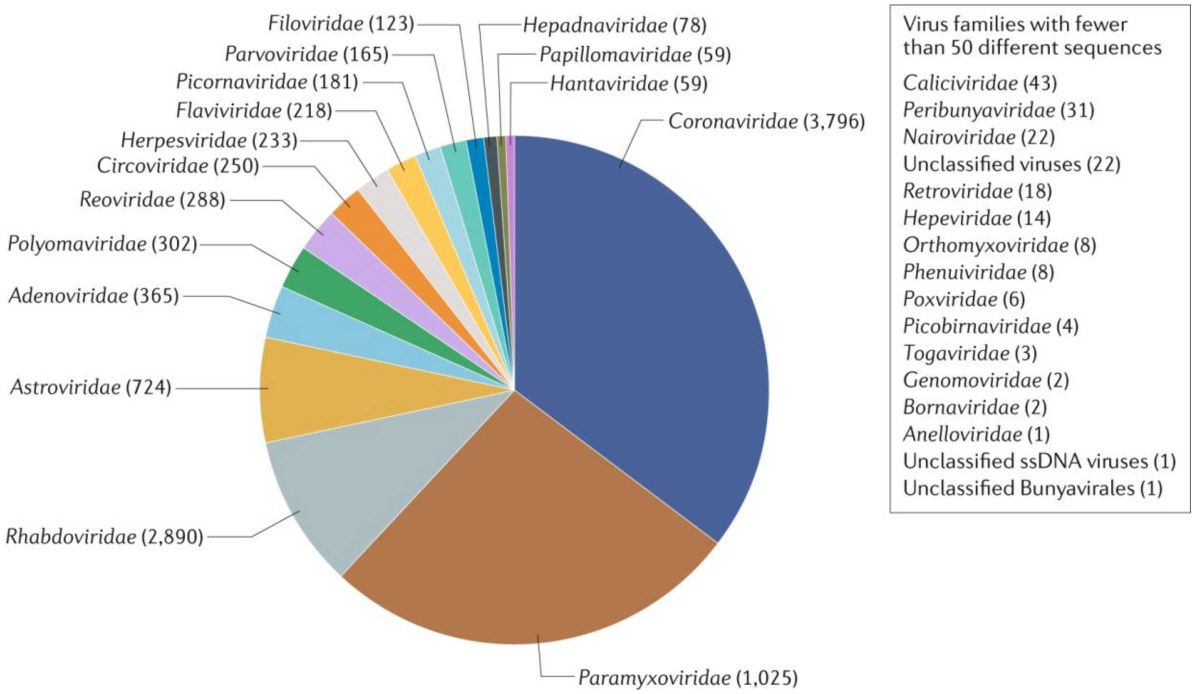

Figure 1.11. Viral sequences isolated from bats and their associated families. Notably, Coronaviridae and Paramyxoviridae represent the highest number of bat-borne virus isolates. Figure adapted from [154].

1.4.1. Species Diversity

While the divergence of the superorder Laurasiatheria occurred about 81 million years ago [156]. Fossil-calibrated molecular dating places the crown-group origin of bats at approximately 52–54 million years ago [157]. In contrast, molecular-clock analyses with limited fossil constraints estimate the basal divergence of Chiroptera at roughly

62 million years ago [158]. This extensive evolutionary history has led to significant divergence in habitat use, diet, and taxonomic richness at the species level. With more than 1,400 species, bats are dispersed across most continents, inhabiting a wide range of ecologies, including temperate and boreal zones. They exhibit highly diverse diets, including insectivory, frugivory, carnivory, piscivory, hematophagy, nectarivory, and scavenging. Accordingly, this ecological and dietary diversity contributes to tremendous diversity in the viruses they harbour, making bats important reservoirs [149,159]

1.4.2. Adaptation to Fly

Bats are the only mammalian species capable of flight. This results in a higher metabolic rate in bats compared to birds and other small mammals. Therefore, when a virus infects a bat, its body responds less effectively to the metabolic products stimulated during the immune response. Additionally, flight increases body temperature in bats, mimicking mammalian fever (38 ºC–41 ºC), thereby boosting innate and adaptive immunity and counteracting viral replication. As a result, a bat might harbour the virus without showing signs of infection [160].

1.4.3. Prolonged Life Span

Compared to similarly sized mammalian species, bats have an unexpectedly long-life span that can extend to 30 years in some species [161]. Considering that virus replication is reduced in bats and bats can carry viruses without clinical manifestations, the long age feature of Chiroptera enables them to harbour and transmit many pathogens to other hosts for a long time [155]. For example, NiV seroconversion waning in *Pteropus vampyrus* bats over one year suggested that the virus may persist for a long period in certain tissues, allowing later horizontal transmission among the bats [162]. Similarly, *Myotis lucifugus* was found to harbour *Alphacoronavirus* in their intestines and lungs during the hibernation period, which suggested transmission among bats that share the same hibernation sites [163].

1.4.4. Colonisation and Roosting Behaviour

Bats colonise and roost in a wide range of ecological habitats, including trees, caves, rock crevices or even those created by humans. This behaviour allows social interaction within a bat population, whether of the same or different species, to mate, eat, labour, and provide maternal care [164]. Nevertheless, this crowded condition would provide a zone where bats transmit diseases among themselves or to animals and humans exploring the roosting areas [165].

1.4.5. Transmission Dynamics in the Bat Population

A mix of ecological and behavioural factors influences the transmission dynamics of viruses in bat populations. Virus transmission often follows complex seasonal and population-driven patterns. As explained previously, the roosts are foci of virus transmission; therefore, the more bats colonise the roost, the more virus dissemination is anticipated [166]. A second factor that determines the viral dynamics is seasonality. In NiV, for example, the infection peak is associated with the birthing and maternity season of bats [167]. Likewise, the seasonal migration of bats from one region to another influences the geographical distribution of the virus [168].

1.4.6. Bat Immunity

In addition to the above, bat immunity is considered a substantial factor influencing the virus carrier status of bats. Over the course of evolution, bats have developed species-specific immunity distinct from that of mammals, which confers viral persistence. The highly conserved serine residue (Ser358) mutation in the bat Stimulator of interferon genes (*STING*) has conferred a dampened IFN response, which permits the virus to exist in bats for a long period [169]. In some species, like the black flying fox (*P. alecto*), the bat has evolved constitutive expression of IRF7 in wide varieties of tissue that would result in a rabidly enhanced IFN response against RNA viruses [170]. Similarly, many bat species have developed a distinct IRF3 rather than that of mammals, which boosts antiviral immune response [171]. Additionally, bats have developed anti-inflammatory mechanisms to counteract damage resulting from viral infection or flight, including reduced nucleotide-binding oligomerization domain, leucine-rich repeat and pyrin domain-containing protein 3 (NLRP3) inflammasome activation compared to other mammals [172].

1.5. Virus Spillover Events in the 21st Century and Bats

1.5.1. Key Spillover Events in the 21st Century

Throughout human history, several spillover events have arisen from different animals. The Justinian Plague, caused by the bacterium *Yersinia pestis,* was likely one of the first recorded pandemics that originated from rodents [173]. Nonetheless, spillover events caused by bat-borne viruses were of no less public health importance.

The first relation between the bats and virus spill over was dated back to the 1930s of the last century when Joseph Pawan described the rabies virus as an outbreak of encephalitis in both humans and animals and linked this spillover to the vampire bats [174] Since then, zoonotic spillover viruses from bats slowly accumulated in the following years, leading to the discovery of several viruses, including NiV, HeV, and Marburg [2,175].

Over the past two decades, a massive surge in virus spillover from bats has emerged among the human populations. As previously mentioned, SARS-CoV, SARS-CoV-2, and MERS, which caused the 21st century coronavirus pandemics, have been hypothesised to have originated in bats [176–178]. In this regard, the ongoing discovery of numerous novel coronaviruses in a wide variety of bat species in diverse geographical areas has highlighted the potential of virus recombination events, particularly those associated with the S protein, predisposing cross-species transmission and future pandemics. This suggests bats as a major reservoir for coronavirus ancestors and those which can switch their host tropism [58].

While NiV and HeV are prototype henipaviruses that were discovered in the 20th century, recent increases in their spillover events in humans and the discovery of novel HeV genotypes have raised an alarm about novel henipaviruses and their future pandemics [179,180]. Such instances are GhV and AngV, which are novel henipaviruses that were discovered in 2012 and 2022, respectively, since viral genomes were detected in the spleen and urine of *Eidolon helvum* (*E. helvum*) and *Eidolon dupreanum* (*E. dupreanum*) (non-*Pteropus* bats) in Africa, which represents a new geographical zone beyond what is known for henipaviruses (i.e., Southeast Asia) [181,182], raising the threats of henipaviruses worldwide.

Filoviruses, including Ebola and Marburg, are highly lethal viruses in humans. Although they have been discovered in the last century, the massive outbreaks in West Africa between 2000 and 2015 have reinforced the research community to focus on these viruses and their [175,183,184]. Although the natural host of the Marburg has been confirmed epidemiologically to be *R. aegyptiacus*, the exact role of bats as a reservoir of Ebola has not been confirmed, yet it cannot be excluded [185,186]. Indeed, the current evidence of filovirus-reactive sera in several bat species and bat hunters in India in 2019 has highlighted the implications of zoonotic spillover of filoviruses worldwide outside Africa [187].

For a long time, zoonotic influenza in humans has remained a disease associated with avian origin [188,189]. Although the identification of novel influenza subtypes in bats, H17N10 and H18N11 in early 2010, H18N12 in 2023, and several H5 influenza-related spillover events to vampire bats between 2011 and 2024 [190–192]. This has immediately raised the question about the genetic diversity of influenza in bats and their possible role in genetic reassortment of influenza, spillover and pandemic potentiality.

1.5.2. Factor Associated with Increasing Spillover Events

1.5.2.1. Increased Human-Bat Contact

The growing human population over the last two decades has led to expansion into wildlife habitats, which has not only increased contact between humans and animals but also disrupted wildlife habitats, including those of bats, raising the opportunity for the emergence of novel viruses [193]. Such an example is the HeV and Ebola virus spillovers, which emerged in the human population [194,195].

1.5.2.2. Intensive Farming and Agriculture

The increased demand of the human population over the last few years has increased the demand for animal byproducts, which has favoured the concentration of farming and animal livestock facilities that encompass a high density of animals. This creates an environment where viruses can spread easily among animals and their handlers. In Italy, intensive pig farming has attracted insects, which in turn are associated with higher bat activity and hence BCoVs-pig spillovers [196].

1.5.2.3. Climatic Changes

Over the past few years, drastic changes in climatic conditions, including high temperatures, prolonged droughts or heavy rainfall, have reflected the ecology and habitats of bats, leading to changes in their migration patterns, transmitting the viruses to new ecological and geographical territories. For example, low temperatures in the cold seasons could force *Desmodus rotundus,* the reservoir of the rabies virus, to change its range north or south of its current niches, leading to demographic change of the disease [197].

1.5.2.4. Global Trade and Travel

The current ease of international human travel, along with the global trade of animals and animal by-products, has significantly increased the spread and transmission of bat-borne zoonoses across borders. A key example is the emergence of MERS-CoV outside the Arabian Peninsula, in South Korea in 2015, where human-to-human transmission was confirmed, leading to 185 infections, the quarantine of 16,752 individuals, and 35 deaths. Likewise, the spread of SARS-CoV in China has been linked to illegal international wildlife trade, particularly involving small carnivores such as viverrids, mustelids, and canids [198,199].

1.5.2.5. Lack of Rabid Diagnostic Tests and Appropriate Surveillance

One of the major advantages of the diagnostic tests and surveillance strategies is the early detection of diseases prior to their emergence. In this regard, the continuous surveillance of viruses in bats and the development of reliable diagnostic tests in both human and animal populations allow the timely spotting of zoonotic spillover events prior to their occurrence, while a lack of them renders the spillover events unnoticed. For example, lack of diagnostic and inadequate surveillance during the 2014 Ebola outbreak has led to exaggeration of cases, hindering appropriate actions, preparedness and early responses as the initial cases remained undetected for a long time [200].

1.5.2.6. Lack of Healthcare System Infrastructure and Social Awareness

An effective healthcare system represents a critical line of defence against the spread of spillover outbreaks. While this is widely implemented in many countries, certain communities still struggle to maintain adequate healthcare systems; consequently, the lack of healthcare facilities in these settings renders them incapable of controlling the spread of infectious diseases once spillover from bats to humans occurs. Similarly, low social awareness in certain cultures plays a role in the spread of outbreaks; for example, the bushmeat of bats is customary as a source of food in some communities. Additionally, some witchcraft beliefs during the 2014 Ebola outbreak were spread, discouraging people from engaging in the vaccines and intervention strategies [201,202].

1.6. Virus-Host Interaction and Epi-transcriptomics in Brief

IFNs are the first arm of cellular defence against viruses [203]. They are activated by sensing the pathogen-associated molecular patterns (PAMPs) of the virus through pattern recognition receptors (PRRs). Several PRRs have been identified in the cell for that purpose [204]. On the other hand, viruses can exploit some cellular regulators to establish their replication or survival.

Over the past few years, the role of epigenetics in shaping the output of host-virus interactions has become an exciting area of research [205]. Epigenetics, in general, describes the reversible changes that control how cells regulate gene expression; these changes allow cells to read genetic information in different ways without altering the genetic material itself [206]. In recent times, several chemical modifications have been discovered, including methylation of DNA and RNA.

Methylation is the chemical process of adding a methyl group to the nucleic acids [207]. In the DNA, it involves the modification of the cytosine to 5-methylcytosine (5mC), while in the mRNA, several nucleotides have been identified, including N6-methyladenosine (m6A), 5-methylcytidine (m5C), 3-methylcytidine (m3C), N7-methylguanosine (m7G), N1-methyladenosine (m1A), and N6,2′-O-dimethyladenosine (m6Am) [207–209]. These nucleic acids modifications have roles in gene expression, host development, and disease progression [207,210–213].

DNA and RNA methylation can shape the host-pathogen interaction, where many viruses reprogramme the host methylation to facilitate their transmission within the host, while the host also fine-tunes its methylation to turn on antiviral programs and restrict pathways viruses need [214,215]. For example, hepatitis B virus (HBV) increases the methylation of certain DNA promoter regions, leading to the progression of liver cirrhosis and hepatocellular carcinoma [216]; meanwhile, host NSUN2 mediate m5C methylation of SARS-CoV-2 transcripts, facilitating their degradation [217]. Although among the DNA and RNA modifications, m6A has attracted significant interest in the scientific community, as it modulates cellular innate and IFN responses and is found in several viruses, including coronaviruses and paramyxoviruses [218–220].

1.6.1. N6-methyladenosine

m6A is an epi-transcriptomic modification that involves the addition of a methyl group to the sixth nitrogen atom of the adenosine nucleotide base. It was first identified in 1970 in the mRNAs of Novikoff Hepatoma Cells, with a rate of three modifications per single transcript [221]. Afterwards, it was discovered in the mRNA of bacteria, plants and viruses [222–224], making it the most prevalent post-transcriptional modification in mRNA. However, not all cellular transcriptomes undergo methylation. With the advances in sequencing technologies, it is now evident that the mRNAs of some housekeeping genes are not methylated [225]. Furthermore, the m6A is mainly clustered in the long internal exons, locations near stop codons, and 3′ and 5′-UTR of the mRNA [226–229] Consensus sequences of the RRACH motif (R = A or G, H = A, C, or U) were recognised as the target for the mRNA methylation process (**Figure 1.12**), although GAC in the RAC motif was modified three to twelve times more than the ACC [221,229].

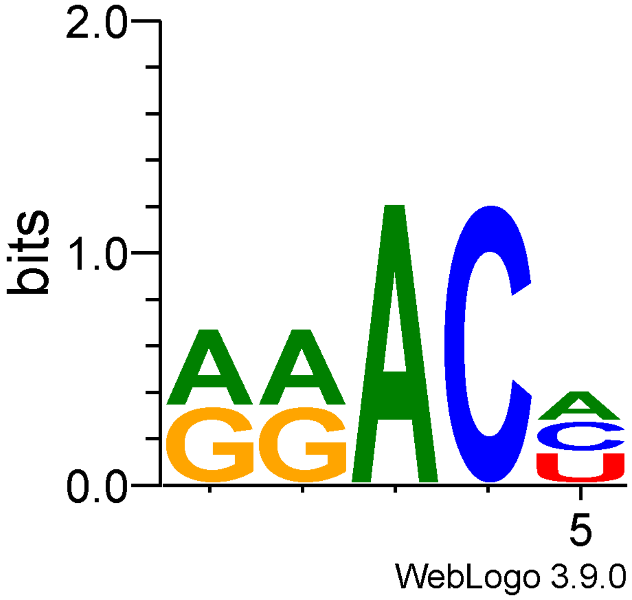

Figure 1.12. A schematic figure illustrating the RRACH motif of the m6A modification. R = A or G, H = A, C, or U. Figure made by WebLogo [230].

1.6.2. Structural and Functional Background of m6A Machinery

The m6A machinery is a group of cellular proteins that are involved in m6A metabolism. These are classified into “writers” (m6A methyltransferases), “erasers” (m6A de-methyltransferases), and “readers” (proteins recognising m6A) [231].

1.6.2.1. Background of m6A Writers

Writers of m6A are responsible for adding the methyl group to the target transcript. The main functional component of these proteins is the methyltransferase complex (Methyltransferase-Like 3, METTL3 and methyltransferase-like-14, METTL14). An additional accessory protein, called Wilms' tumour 1-associating protein (WTAP), is necessary for the completion of the process [232].

The process of m6A addition is a sequential process where the METTL3-METT14 complex binds the target RNA with the RRACH motif, then the methyl group is added to the RNA from the S-adenosylmethionine (SAM) molecule by METTL3 [229]. The attachment of the WTAP to the methyltransferase complex regulates the process, where it enhances the nuclear localisation of the complex and ensures its binding to the RNA [233].

METTL3 was identified in 1992 as the first and main catalytic subunit of the m6A writer complexes [234]. On the other hand, METTL14 was identified later in 2014. However, both proteins are located in the nuclear speckles [232,233].

The METTL3-METTL14 complex belongs to the methyltransferase family [235], which is characterised by the presence of the methyltransferase domain (MTD). This domain spans residues 369–570 in METTL3 and 117–402 in METTL14. However, the sequence identity between the two domains is only 22%. The MTD of METTL3 is composed of 8 β-sheets (β1–β8) flanked by 4 α-helices. Furthermore, three distinct loops were identified within the METTL3 that are important in the heterodimer: gate loop 1 (residues 396–410), gate loop 2 (residues 507–515) and interface loop (residues 462–479) (**Figure 1.13**). Gate loops 1 and 2 are responsible for adenosine recognition of the SAM molecule, while the interface loop mediating the interaction between METTL3 and METTL14 allows the two domains to bind to each other. Moreover, the SAM-binding site is localised within the METTL3, facing the DPPW (Asp, Pro, Pro, Trp) motif (residues 395–399) of gate loop 1 [236].

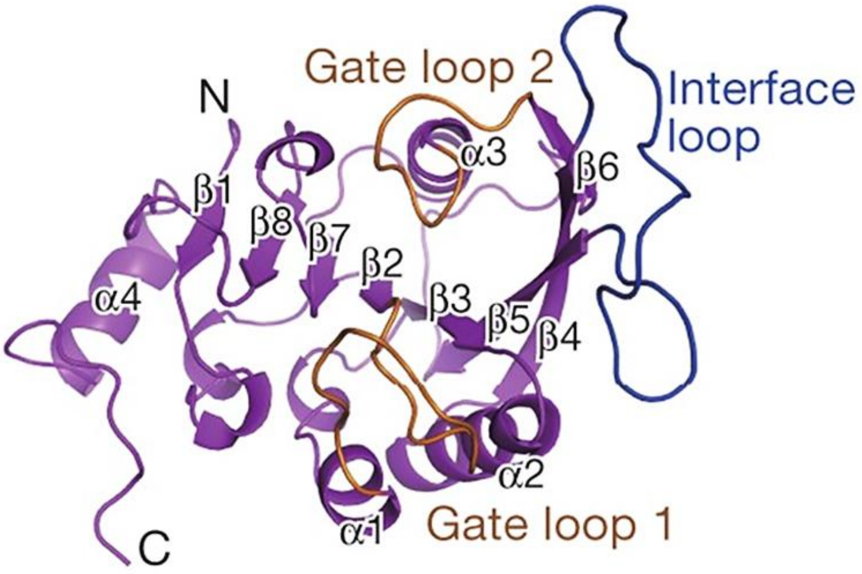

Figure 1.13. The overall structure of the METTL3 methyltransferase domain (MTD). The domain consists of gate loop 1 (residues 396–410), gate loop 2 (residues 507–515) and interface loop (residues 462–479). Gate loops 1 and 2 are coloured in orange, while the interface loop is coloured in blue. Figure adopted from [237] with modification applied to the imported figure.

Although METTL14 lacks catalytic activity due to the absence of the SAM-facing DPPW motif, it binds to METTL3, forming a scaffold for RNA binding. The N-terminal of the METTL14 MTD has unusual extensions of approximately 50 residues, forming a long helix, several loops, and shorter helices; the latter two mediate the binding of METTL14 to METTL3 [238]. RNA, on the other hand, is sandwiched within a positively charged groove between METTL3 and METTL14 (**Figure 1.14**). This groove contains many positively charged residues, including Arg 465, Arg 471, His 474 and His 478 from METTL3 and Arg 245, Arg 249, Arg 254, Arg 255, Lys 297 and Arg 298 from METTL14 [237].

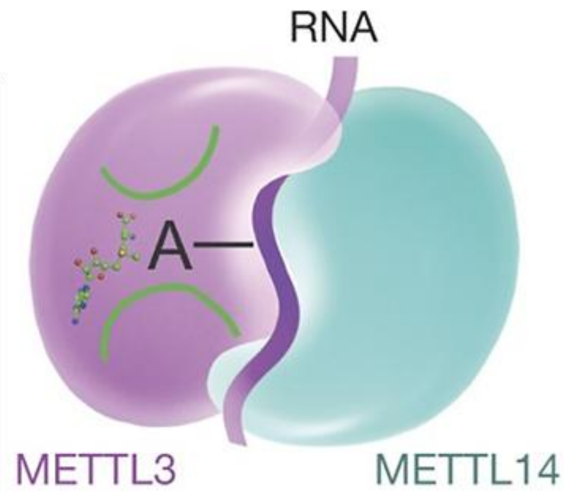

Figure 1.14. An RNA-binding model within the methyltransferase complex. RNA, coloured in magenta, is located within the positive groove between the METTL3-METTL14 complex. Green arcs represent gate loops 1 and 2, which pin the adenosine moiety of the RNA (marked in black). Figure imported from [237] with modification applied to the imported figure.

The methyltransferase activity of the METTL3-METTL4 complex cannot occur only with the MTD. A domain located in the N terminus of the METTL3, termed the zinc finger domain (ZFD), is found to be crucial for the methyltransferase activity, without which the MTD activity is lost. This domain binds only to the RNA with the RRACH motif. Thus, it is responsible for installing the methyl group onto the target RNA. Structurally, the ZFD domain contains two CCCH-type zinc fingers, ZFD1 (residues 259–298) and ZFD2 (residues 299–336), which are held together with two anti-parallel β chains. The methylated RNA is held within the hydrophobic pocket of ZFD2, consist of Ser 315, Phe 316, Cys 320, Phe 321, and His 322 [236].

In 2014, WTAP was first discovered as an m6A regulator. WTAP does not have a catalytic domain, but it plays a key role in the m6A methylation. This protein is required for activating and recruiting the METTL3-METTL14 complex to nuclear speckles, where RNA binding occurs. Meanwhile, neither METTL3 nor METTL14 affected WTAP localisation in the nuclear speckles [232,233]. The initial study by Ping et al., which identified WTAP as a cofactor for METTL3-METT14 localisation, did not reveal the structure of WTAP, although it indicated that the interaction between WTAP and the heterodimer is mediated by the N-terminal region of WTAP [233]. However, a recent cryo-EM study modelling residues 64–247 of the WTAP N-terminus described the region as a homodimer, with each monomer comprising four helices and three linkers. The binding of the WTAP to the METTL3-METTL14 heterodimer is mediated by α3 and α4 (residues 148-176) and (residues 177-249), respectively [239].

1.6.2.2. Background of m6A Erasers

The m6A erasers/demethylases remove the methyl group from the adenosine. Until recently, two m6A erasers have been identified, including fat mass and obesity-associated protein (FTO) and alkB homolog 5 (ALKBH5) [231]. Both belong to the AlkB family of non-heme Fe (II)/α-KG-dependent dioxygenases that remove the methyl group from nucleobases, and both are situated in the nuclear speckles [240–242].

The FTO was originally linked to obesity (165) and was later shown to be an m6A eraser. (247). Structural analysis of truncated FTO (Δ1-31) identified two domains: the N-terminal domain (NTD) (residues 32–326), and the C-terminal domain (CTD) (residues 327–498) (**Figure 1.15**). The CTD is mainly a helical structure consisting of several α-helixes chains (α7-α12). The end of the seventh helix interacts with the NTD to stabilise the protein configuration. On the other hand, the NTD consists of multiple distorted β-helices; β5- β12 forms the jelly-roll motif, or the catalytic core of the FTO and contains His 231, Asp 233, and His 307, which bind Fe^{2+}. Nevertheless, the NTD alone cannot initiate demethylation and must be combined with the CTD to be active, as the latter stabilises the former. Besides the distinct folding of the CTD, another important feature linked to the FTO-deselection against double- and unmethylated-nucleic acids is a long extra loop (L1 loop). This loop spans the outer walls of β6, β11, β8, and β9 of the NTD and comprises residues 213–224. L1 loop is unique to the FTO and not present in other members of the AlkB family (**Figure 1.16**). The interaction between this loop and the catalytic roll motif is mediated by a Trp 230 [243].

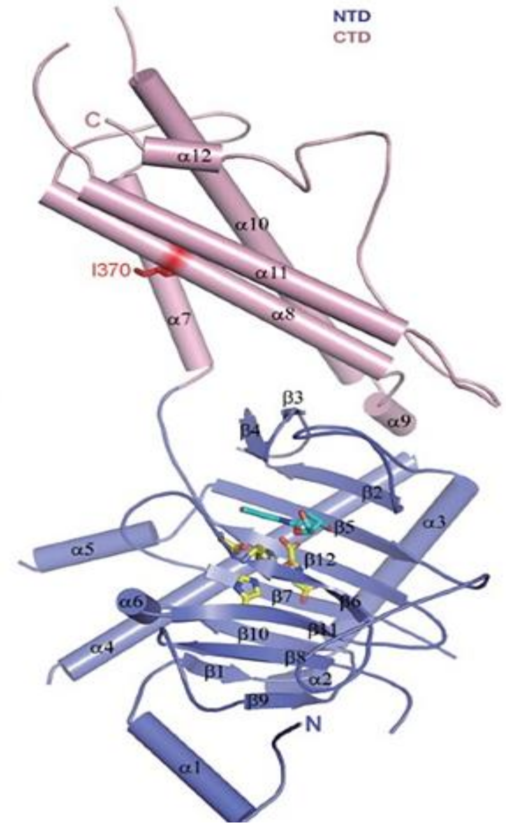

Figure 1.15. A Stereo view describing the overall structure of FTO. The protein consists of N-terminal domain (NTD) (residues 32–326) and C-terminal domain (CTD) (residues 327–498). NTD and CTD are marked in light purple and blue, respectively, whereas the iron binding coordinates are shown in yellow sticks. Figure adopted from [243] with modification applied to the imported figure.

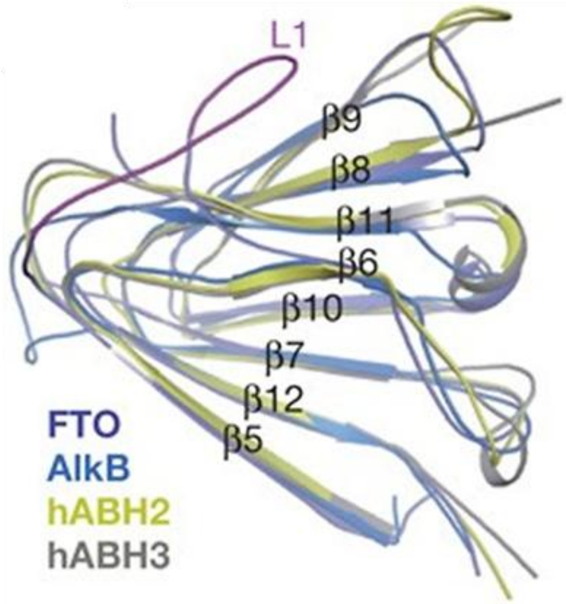

Figure 1.16. An alignment of the jelly-roll motif of FTO and AlkB family members, illustrating the distinguished L1 loop of FTO. Motif of the AlkB, hABH2, and hABH3 are shown in blue, olive green, and grey, respectively, whereas the distinguished L1 loop of FTO is shown in magenta. Figure adopted from [243] ***with modification applied to the imported figure.***

ALKBH5 is the second identified m6A demethylase, and it was found to play a role in the nuclear exportation of the mRNA transcripts [244]. Similar to the FTO, the ALKBH5 prefers single-stranded methylated RNA [244,245]. In the crystal, the ALKBH5 consists of 7 chains of α helices and nine chains of β sheets. The jelly-roll motif of ALKBH5 has a fold called the DSBH fold. This fold comprises 6 β chains (β4–β9) and has the conserved metal-ion-coordinating residues His 204, Asp 206, and His 266, forming the conserved HX(D/E) *XnH* motif. The outer side of the DSBH fold has the characteristic nucleotide recognition lid, which consists of 2 regions unique to the ALKBH5 Flip 1 (residues 117–129) and Flip 2 (residues 136–165), that are responsible for binding to the m6A. Furthermore, an additional region referred to as Flip 3 formed due to the disulfide bond between residues Cys 230 and Cys 267. This region gives the ALKBH5 selectivity toward the unmethylated double-stranded nucleic acids [245,246] (**Figure 1.17**).

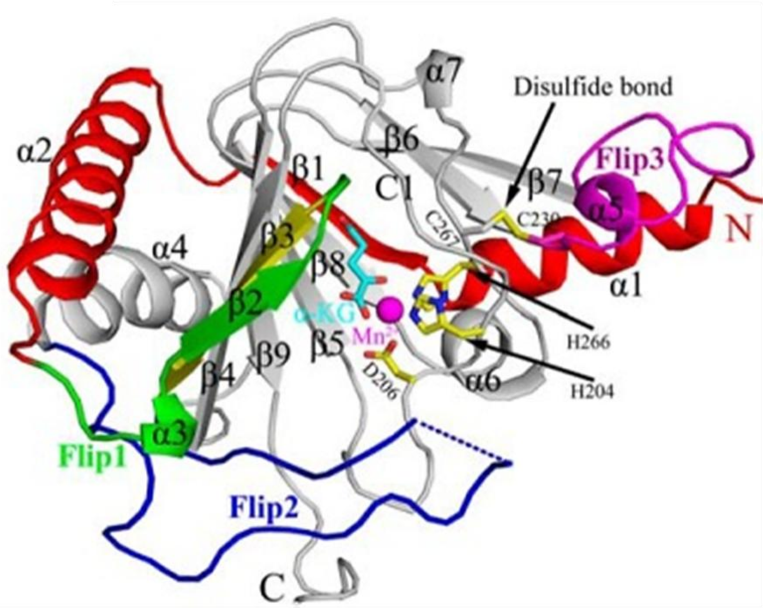

Figure 1.17. The overall structure of the ALKBH5 catalytic motif. The jelly roll motif consists of Flip 1(green), Flip 2 (blue), and Flip 3 (purple). The disulfide bond between Cys230 and Cys267 is highlighted in a black arrow. The key residues His-204 and His-266 are highlighted in black arrows. Figure adopted from [245] with modification applied to the imported figure.

1.6.2.3. Background of m6A Readers

Readers of m6A recognise the site of modification and direct the methylated transcripts towards distinct biological functions, including splicing, nuclear export, translation, and decay. The most famous group of this protein are a group of YT521-B homology (YTH) domain, including YTH domain-containing family protein 1

(YTHDF1), YTH domain-containing family protein 2 (YTHDF2), YTH domain-containing family protein 3 (YTHDF3), YTH domain-containing protein 1 (YTHDC1), and the RNA helicase YTH domain-containing protein 2 (YTHDC2) [247,248].

The YTHDC1 is localised in the nucleus, while YTHDF1, YTHDF2 and YTHDF3 have been found in the cytoplasm. The YTHDC2, on the other hand, exists both in the cytoplasm and in the nucleus [249]. The YTHDF1 increases the translation efficiency of mRNAs bearing m6A by enhancing the interaction between the translation initiation factors, mRNA and ribosomes, leading to the ribosomal upload of the methylated mRNA [250]. YTHDF2 mediates mRNA degradation [250,251]. Whereas YTHDF3 represents the connection between YTHDF1 and YTHDF2, where it binds to each protein, initiating its target process [252,253]. Splicing and nuclear exportation of the mRNA are mediated by YTHDC1[254], while YTHDC2 enhances mRNA translation efficacy [255].

The location of the YTH domain differs among the YTH family; it corresponds to residues 361–559, 380–579, 403–571, 345–509, 1277–1430 in YTHDF1/2/3 and YTHDC1/2, respectively. Furthermore, the domain sequence identity among the three YTHDFs is about 86%, and they have a nearly identical architecture. However, the sequence identity to the YTHDC1 domain was only 27% [256–259].

A distinguished feature of the YTH main family is the presence of an aromatic cage that situates the methylated adenine. This cage consists mostly of two or more aromatic residues that are conserved throughout the family [256]. In YTHDF1, the methylated adenosine is housed in a hydrophobic pocket formed by Trp 411, Trp 465, and Trp 470. The pocket is formed from Tyr 418, Trp 432, Trp 486 and Trp 491 in the YTHDF2, where Trp 432 and Trp 486 were found to be specifically bound to m6A. The m6A in YTHDF3 is found at Trp 492, Trp 438, and Trp 497. Notably, the cage consists of Trp 377, Trp 428, and Leu 439 in YTHDC1, and Trp 1310, Trp 1360, and Leu 1365 in YTHDC2 [257,260–262].

Crystallographic analysis of the YTH domain reveals nearly identical structure across the five readers. The YTH domain of YTHDF1, as an example, consists of five chains of α helices (α0–α4) and six β sheets (β1–β6) arranged in a typical barrel order of β6-

β1-β3-β4-β5-β2. The first three helices (α1–α3) are packed against the β barrel. A long loop is found at the end of the α0 helix, and a small additional 3_{10} helices are found at the end of the fifth β sheet. The methylated RNA binding pocket of the YTHDF1 consists of the C termini of β1, α1, β2, the N terminus of α2, and the loop between β4 and β5 [256] (**Figure 1.18**).

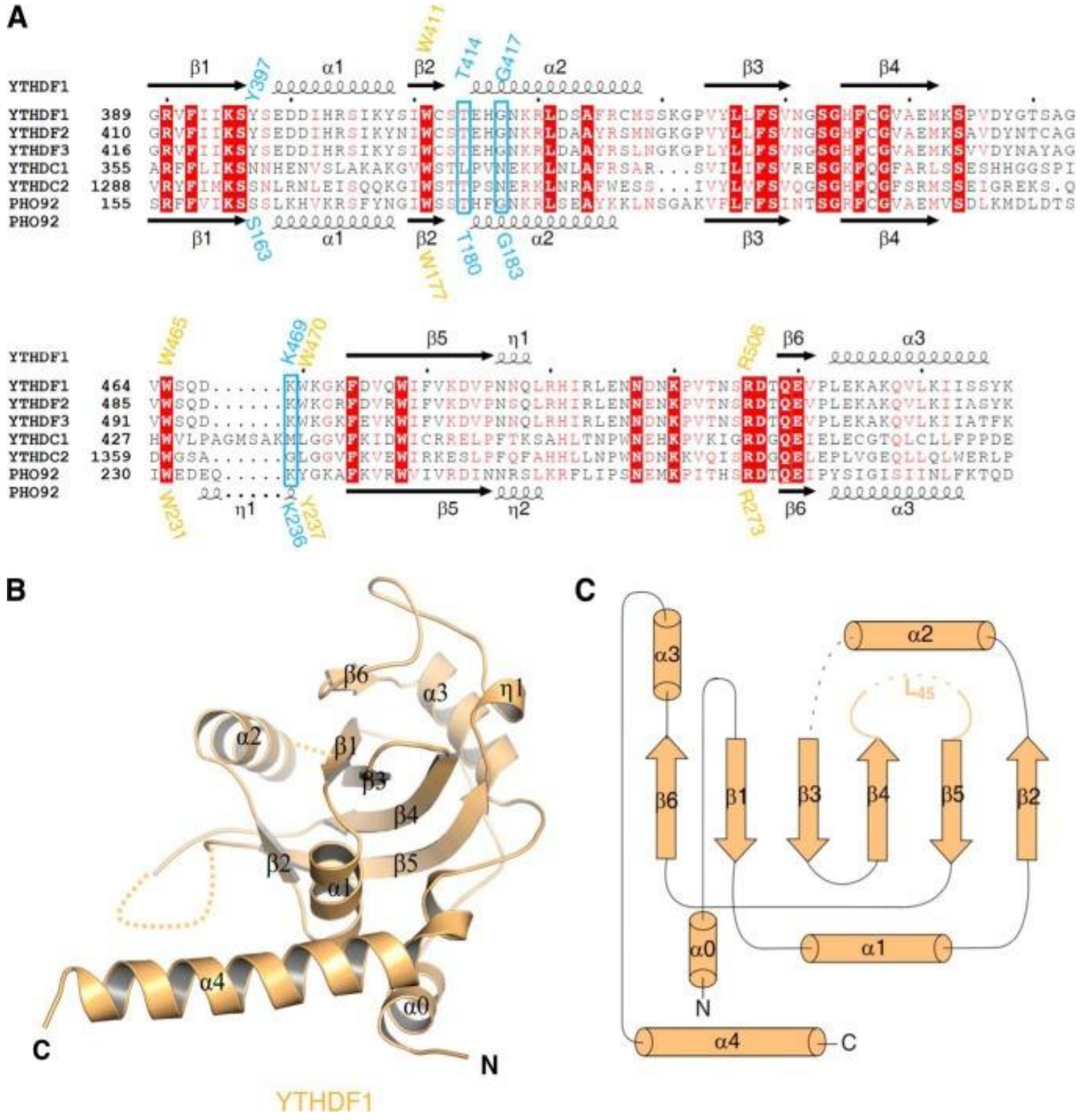

Figure 1.18. The overall structure of the YTHDF1 YTH domain, along with the sequence alignment of YTH domain proteins. (A) Alignment of the YTHDF1 domain sequence against the sequences of the YTH domain family proteins and Pho92 protein, which is the only YTH domain family protein in Saccharomyces cerevisiae. (B) The overall structure of the YTH domain of the YTHDF1. (C) Topological figure of the YTHDF1 domain secondary structure. Figure adopted from [256].

1.6.3. Role of m6A in Innate Immunity Regulation and Viral Infection

1.6.3.1. General Background of m6A Machinery as Viral and Immune Regulators

Viral sensing by host PRRs is considered a critical step in limiting the spread of infection within the host. Stimulation of PRRs triggers a strong antiviral response mediated by type I IFN. In this context, the cytoplasmic retinoic acid-inducible gene I (RIG-I)-like receptors (RLRs) are vital receptors that can strongly stimulate type I IFN [263]. Activation of RLRs leads to the stimulation of MAVS, which, in turn, triggers cascades of events culminating in the activation of IRF3 and IRF7. Activated IRF3 and IRF7 are translocated into the nucleus, leading to upregulation of type I IFN, which eventually inhibits viral replication [264,265].

In the battle between viruses and immunity, viruses can adopt regulators to establish their infection. The m6A and its machinery can regulate several cellular functions, including innate sensing of pathogens and IFN responses. Suggesting that m6A modification could enhance or block viral infection; however, only a few studies have addressed this topic. It has been reported that ALKBH5 acts as an IFN inhibitor in response to VSV stimulation by preventing the nuclear export of MAVS transcripts, leading to an overall decline in IFN expression [266]. Viral sensing by the retinoic acid-inducible gene I (RIG-I) receptor was indeed investigated in the presence and absence of the modified nucleotide on the RNA of the hepatitis C virus (HCV), and it was proven that the viral genomes modified with the m6A bond weakly to the receptor and elicited less IFN-β signal than the canonical one [267].

Aside from IFN modulation mechanisms, m6A has been shown to affect viral replication through unknown mechanisms, with a proviral or antiviral impact depending on the virus. Members of the flaviviruses (Zika virus and HCV) replicated more when YTHDF proteins were silenced, suggesting an antiviral effect of YTHDF proteins [268,269]. In contrast to the flaviviruses, the m6A readers YTHDF1 and YTHDF3 were shown to enhance Chikungunya virus (CHIKV) replication upon knockdown, whereas YTHDF2 had the opposite effect. The CHIKV genome is enriched with m6A at the first 2000 nucleotides near the 5′ end, and indeed the virus's RNA has been shown to bind to those proteins. YTHDF3 and YTHDF1 enhance cellular mRNA translation, while YTHDF2 promotes mRNA degradation; however, the implications of these mechanisms in CHIKV replication remain inconclusive [270].

In coronaviruses, studies have described 8 sites of m6A modification on the SARS-CoV-2 genome [218]. In fact, experiments showed that m6A does affect the SARS-CoV-2 replication. Depletion or inhibition of m6A writers (METTL3/14) or readers (YTHDF proteins) can significantly reduce SARS-CoV-2 replication by decreasing viral RNA synthesis and N protein production [271]. Additionally, FTO depletion increased viral m6A marks, boosting SARS-CoV-2 replication. This suggests that higher m6A levels can promote viral replication [272].

1.6.3.2. Role of METTL3 in Modulation of Virus Replication and Innate Immunity

METTL3 is the central player in the m6A methylation process, which adds a methyl group to the target adenine in RNA. While its role is inevitable for directing the biological processes in the cell [273], METTL3 can be targeted by or against viruses.

1.6.3.2.1. Proviral Role of METTL3

Recent studies have elucidated that viruses possess m6A within their genes. This strategy usually assists the virus in evading immunity, as m6A is typically recognised by the cell as a self-marker [274]. By methylation of viral RNA, METTL3 can further enhance virus replication, transcription, translation, and escape innate immunity. For example, the SARS-CoV-2 genome has been decorated with several m6A peaks at ORF1ab and the 3′ end, particularly at the N gene. During viral infection, METTL3 methylates the SARS-CoV-2 genome, decreasing RIG-I binding to the viral genome and thereby suppressing cytokine and chemokine responses [275]. Similarly, overexpression of METTL3 during human metapneumovirus (hMPV) infection enhanced viral replication by modulating viral m6A levels, whereas depletion of viral m6A led to greater induction of the type I IFN and NF-κB-RIG-I pathways [274], suggesting the RIG-I pathway as a major target for METTL3-viral enhancement regulation.

So how do viruses override METTL3? The answer lies in recruitment. While METTL3 is primarily a nuclear protein [235], when a virus replicates in the cytoplasm, the protein is exported to the cytoplasm to bind and add m6A to viral RNA. Evidence of this redistribution has been documented in multiple viruses, including VSV, SARS-CoV-2, NiV, Herpes simplex virus type I (HSV-1), and enterovirus 71 (EV71) [220,276–279]. Indeed, the role of METTL3 as a proviral factor is much more than an antiviral effect, and many of these studies propose that it suppresses the immune system and enhances viral infection by recruiting proteins.

Direct regulation of post-translational modification (PTM) processes represents another mechanism by which METTL3 can enhance virus replication. In EV71, METTL3 stabilises the viral RdRP (3D polymerase) through SUMOylation and ubiquitination, thereby enhancing viral replication [280]. However, this remains the only detailed study to describe the proviral mechanism of METTL3 beyond its role in suppressing innate immunity. Indeed, the current direct evidence regarding METTL3's impact on other PTMs of viral proteins beyond SUMOylation and ubiquitination is limited. Nevertheless, these studies underscore the multifaceted role of METTL3 in promoting viral replication.

1.6.3.2.2. Antiviral Role of METTL3

In contrast to the well-documented proviral effects of METTL3, the role of METTL3 as an antiviral protein is limited. As mentioned, m6A is typically recognised as an endogenous epi-transcriptomic modification, thus cannot be detected by the innate immune system, a feature that many viruses exploit through METTL3-mediated methylation. Although few studies reported that METTL3 can promote antiviral immunity rather than suppress it. In human cytomegalovirus (HCMV), METTL3 was found to regulate m6A on the mRNA of the interferon-stimulated genes (ISGs), interferon-induced transmembrane protein 1 (*IFITM1*) and MX dynamin-like GTPase 1 (*Mx1*), enhancing their translation. Notably, this effect was extended to VSV, which was also inhibited by overexpression of METTL3 [281]. During prototypical alpha-herpesvirus pseudorabies virus (PRV) infection, METTL3 is activated by extracellular signal-regulated kinase (ERK)-mediated phosphorylation, which significantly enhances *IFN-β* and *NF-κB* promoter activity [282]. Similarly, in VSV and HSV-1, the TANK-binding kinase 1 (TBK1)-METTL3 axis was required for the induction of type I IFN response, as well as stabilising the mRNA of IRF3 [283].

1.7. Research Aims

Given that bats are effective reservoirs for many viruses, and based on the above-mentioned literature, it was hypothesised in this thesis that ACE2 and m6A could shape the emergence of viruses in bats. Thus, this work aimed to test this hypothesis against coronaviruses and paramyxoviruses, using the bat-borne viruses Cedar and HKU5 in *R. aegyptiacus* cell lines as examples.

Research on bat-associated viruses and bat cell lines has remained a major challenge in biology. Compounded by high species diversity, limited published studies, and limited genomic information available in databases, bat cell lines are scarce, and the majority are not commercially available. Additionally, many bat-derived cell lines are not readily supportive for viral replication unless modified, which would constrain research on these interesting mammals. Likewise, the isolated bat-borne viruses are not readily grown or detected in available cell cultures unless genetically modified, due to limited reagents, further complicating matters since most bat-borne viruses are classified as high contaminant levels, including contaminant level 3 (CL3) or CL4.

Therefore, in my thesis work, I sought to establish a foundation for studying m6A and ACE2 entry barriers against Cedar and HKU5 viruses in *R. aegyptiacus* cell lines, leveraging each virus's chimaera structure, incorporating a wide range of bioinformatics and functional assays. The results of this work will greatly assist all researchers aiming to explore this challenging and under-investigated area by overcoming the significant barriers posed by scarce bat cell lines, limited viral susceptibility, and restricted experimental resources for studying bat-borne viruses.

Chapter 2. Materials and Methods

2.1. In Silico and Bioinformatics Analysis

2.1.1. Amino Acid Sequence Retrieval

Homo sapiens (*H. sapiens*), *Pteropus alecto* (*P. alecto*) *and R. aegyptiacus* m6A-related proteins were downloaded and retrieved from the National Centre for Biotechnology Information (NCBI) protein database [284]. Additionally, the same protein sequences were collected from different mammalian, avian, reptilian, amphibian, and osteichthyan orthologues. All sequences were downloaded in FASTA format and subsequently used for the comparative analysis. The accession numbers used in this study are shown (**Table 2.1**).

Table 2.1. Accession numbers for R. aegyptiacus, P. alecto, and H. sapiens m6A machinery used in this study.

Protein	*R. aegyptiacus*	*P.alecto*	*H. sapiens*
METTL3	XP_016021052.1	XP_006918390.1	NP_062826.2
METTL14	XP_016000318.1	XP_006917799.1	NP_066012.1
WTAP	XP_016008204.1	XP_006915095.1	NP_001257460.1
ALKBH5	XP_016000686.1	XP_006908504.1	NP_060228.3
FTO	XP_036087171.1	XP_024900335.1	NP_001073901.1
YTHDF1	XP_015991582.1	XP_006922028.1	NP_060268.2
YTHDF2	XP_015987496.1	XP_006924394.1	NP_057342.2
YTHDF3	XP_036088717.1	XP_024896891.1	NP_689971.4
YTHDC1	XP_006916569.1	XP_015978851.2	NP_001026902.1
YTHDC2	XP_036081156.1	XP_006913349.1	NP_073739.3

2.1.2. Identity Matrices Calculation and Visualisation

The MUSCLE alignment tool in the Sequence Demarcation Tool Version 1.2 (SDTv1.2) software [285] was used to calculate a pairwise identity matrix for the m6A orthologous protein sequences. The resulting identity plots were annotated and grouped accordingly.

2.1.3. Genomic Comparison and Synteny Analysis

H. sapiens, P. alecto, and R. aegypticus genomes were downloaded in FASTA and GFF formats from the NCBI. Genomic comparison was performed using the MCScanX algorithm in TBtools version 1.106 [286], and chromosomes and scaffolds of m6A were determined for both species. Moreover, m6A-related genes, along with 6 upstream and downstream flanking genes, were identified and compared in both species using the NCBI Genome Data Viewer (GDV) [287]. Synteny analysis and gene orientation mapping were then conducted based on these annotations. The genomes and RefSeq assembly used in the comparison are shown in (**Table 2.2**).

Table 2.2. Genome and Ref Seq assembly used in the study.

Organism	NCBI Genome and Ref Seq Assembly
H. sapiens	GRCh38.p14, GCF_000001405.40
P. alecto	ASM32557v1, GCF_000325575.1
R. aegyptiacus	mRouAeg1.p, GCF_014176215.1

2.1.4. Amino Acid Alignment and Tertiary Protein Structure Comparison

Amino acid alignment of human and bat's m6A machinery was performed and visualised using Clustal W alignment of the BioEdit 7.2 software [288]. To establish the protein's 3D structure comparison, the tertiary structures of the human m6A (hm6A) proteins were downloaded and retrieved from the Protein Data Bank (PDB) [289] (**Table 2.3**), while the 3D structure of the Egyptian fruit bat m6A machinery was predicted and downloaded using the SWISS-MODEL homology modelling server [290,291]. The same server was used to predict the ligand-domain interaction of YTHDC1 in both species. Identity, coverage, and Global Model Quality Estimation (GMQE) were parameters used to select the best template on the SWISS-Model, while GMQE and Qualitative Model Energy Analysis-Distance Constraints. (QMEANDisCo) were used to select the best predicted models. The tertiary structure of the proteins of the two species was visualised and edited using PyMOL 2.5 [292].

Table 2.3. PDB ID of the m6A proteins used in the study.

Protein Name	PDB Identification Code (ID)
METTL3 (MTD)	5IL0
METTL3 (ZFD)	5ZOT
METTL14 (MTD)	5k7u
WTAP (N-terminus)	7VF5
ALKBH5	4NJN
FTO	3LFM
YTHDF1	4RCI
YTHDF2	4WQN
YTHDF3	5ZOT
YTHDC1	4R3I
YTHDC2	6K6U

2.1.5. YTH Domain Sequence Alignment and Secondary Structure Information

To compare the YTH domain of the *H. sapiens, P. alecto, and R. aegypticus*, the YTH domain of the five m6A readers was aligned using ClustalW of BioEdit 7.2. The YTHDF2 PDB entry code 4WQN, along with the BioEdit alignment file, was submitted to the ESPript 3.0 server [293]. The domain, secondary structure and key amino acids were determined and annotated in the figures accordingly.

2.1.6. METTL3 Amino Acid Alignment and Determination of Nuclear Localization Signal in the Egyptian Fruit Bat and Human.

For the determination of the nuclear localization signal (NLS) of METTL3 in *R. aegyptiacus*, amino acid sequences of the protein were retrieved for the bat and the human from the NCBI protein database (Accession numbers NP_062826.2 and XP_016021052.1). Amino acid alignment of human and bat's METTL3 sequences was performed and visualised using Clustal W alignment of the BioEdit 7.2 software. The NLS of the protein was determined and annotated in each species accordingly.

2.2. Cell Lines and Virological Methods

2.2.1. Cell Maintenance and Splitting

Cells used in this study were maintained in DMEM low glucose, GlutaMAX™ Supplement, pyruvate (Gibco™, Thermo Fisher Scientific), supplied with 10% heat-inactivated fetal bovine Serum (FBS) (Gibco™, Thermo Fisher Scientific) and 1% penicillin-streptomycin (Gibco™, Thermo Fisher Scientific). Cells were incubated in a 37 ºC incubator supplied with 5% CO2. Splitting and subculturing of the cells were performed twice per week using a combination of 0.2X 2.5 % trypsin (Gibco™, Thermo Fisher Scientific) and 0.1X versene in phosphate-buffered saline (PBS) solution (pH 7.2). Cell lines used in the study are listed in (**Table 2.4**).

Table 2.4. Cell lines and resources used in the study.

Cell	Resource
VeroE6	UKHSA- 85020206
A549	ATCC-CCL-185
A549-hACE2-TMPRSS2	NIBSC-101004
A549-hACE2-EGFP	This study
BHK-21	ATCC-CCL-10
BHK-21-hACE2-EGFP	This study
BHK-2-RE-ACE2-mScarlet	This study
R05T	BEI Resources-ATCC-NR-49168
R06E	BEI Resources-ATCC-NR-49168
R06E-hACE2-EGFP	This study
R06E-RE-ACE2-mScarlet	This study
R06E-METTL3-WT-mScarlet	This study
R06E-METTL3-ZFD1-mScarlet	This study
R06E-METTL3-ZFD2-mScarlet	This study
R06E-METTL3-ZFD1 & 2-mScarlet	This study
R06E-METTL3-MTD-mScarlet	This study
R06E -METTL3-ZFD1, 2 & MTD-mScarlet	This study
R06E -METTL3-ZFD2 & MTD-mScarlet	This study
R06E -mScarlet	This study

2.2.2. Freezing and Thawing of Cells

After subculture, cells were examined for signs of contamination and viability before freezing. Generally, cells were healthy, with 80-90% confluency and free of contamination. The procedure involved trypsinisation of the cells, pelleting, and resuspension in ice-cold freezing media (5% to 10% Dimethyl sulfoxide (DMSO) in FBS). Afterwards, cells were dispensed into cryovials and slowly cooled to -80 ºC at a rate of 1 to 3 ºC per minute to reduce ice crystal formation. Once cells were frozen, they were transferred to liquid nitrogen for long-term preservation. Cell thawing was performed quickly at 37 ºC to minimise damage from ice crystals. The thawed vial was diluted slowly into a 10 mL tube containing fresh medium, and a gentle centrifugation step was performed at 1000 rounds per minute (RPM) for 5 minutes (min) to remove residual DMSO. Following supernatant discard, the cell pellet was suspended in new, fresh growth medium and allowed to recover and expand in a T25 flask.

2.3. Virus Propagation and Titrations

2.3.1. Virus Propagation

Recombinant Cedar virus green fluorescence protein (rCedPV-GFP) was kindly provided by Dr. Christopher C. Broder, Uniformed Services University, USA. Recombinant bat coronavirus HKU5 with SARS-CoV-1 spike ectodomain (BtCoV HKU5-SE) was purchased from the BEI Resources-ATCC. SARS-CoV-2 Omicron (B.1.1.529) variant was purchased from UKHSA, UK. The viruses were propagated in VeroE6 cells using 100 µL of the original virus stock, and the cells were daily observed for the development of viral cytopathic effect (CPE). After a total of 72 hours post-infection (hpi), the viruses were harvested, and the supernatant was clarified, distributed into aliquots and stored in -80 ºC for further use.

2.3.2. Virus Titration

2.3.2.1. rCedPV-GFP

rCedPV-GFP was titered using the VeroE6 cells. Briefly, VeroE6 cells were seeded in a 12-well plate, and 70 µL of the virus-containing supernatant was ten-fold serially diluted in 630 µL DMEM. Afterwards, 500 µL of diluted viruses were added to the cells and allowed for 2 hours (h) of adsorption in a 37 ºC incubator with intermittent shaking every 15 min. Viral inoculum was removed, and the plate was washed with PBS, followed by the addition of 2% carboxymethylcellulose (CMC) overlay medium. At the end, cells were incubated for an additional 5 days at 37 ºC until plaques developed. At the end of the incubation period, 1 mL of 4% paraformaldehyde in PBS (pH 7.2) (Sigma Aldrich) was added to the plates and left on the shaker for 1 hour (h) to fix the cells. 1 mL of 0.5% crystal violet (Sigma Aldrich) was used to stain the plaques for 20 min. Finally, the plates were washed with distilled water (DW) and allowed to dry at room temperature to count the plaques. The rCedPV-GFP plaques appeared as hollow, clear circles on the stained purple cell monolayer.

2.3.2.2. BtCoV HKU5-SE

To quantify BtCoV HKU5-SE, VeroE6 cells were seeded in a 6-well plate. BtCoV HKU5-SE virus titration and adsorption were carried out as described for rCedPV-GFP, except that 0.8% agarose was used as the overlay medium and 3 days were allowed for virus plaque 4% development. Fixation and staining of the plaques were performed using the same procedure previously described for rCedPV-GFP. The overall workflow and experimental setup used for the titration of rCedPV-GFP and BtCoV HKU5-SE are illustrated in (**Figure 2.1)** and (**Figure 2.2)**, respectively.

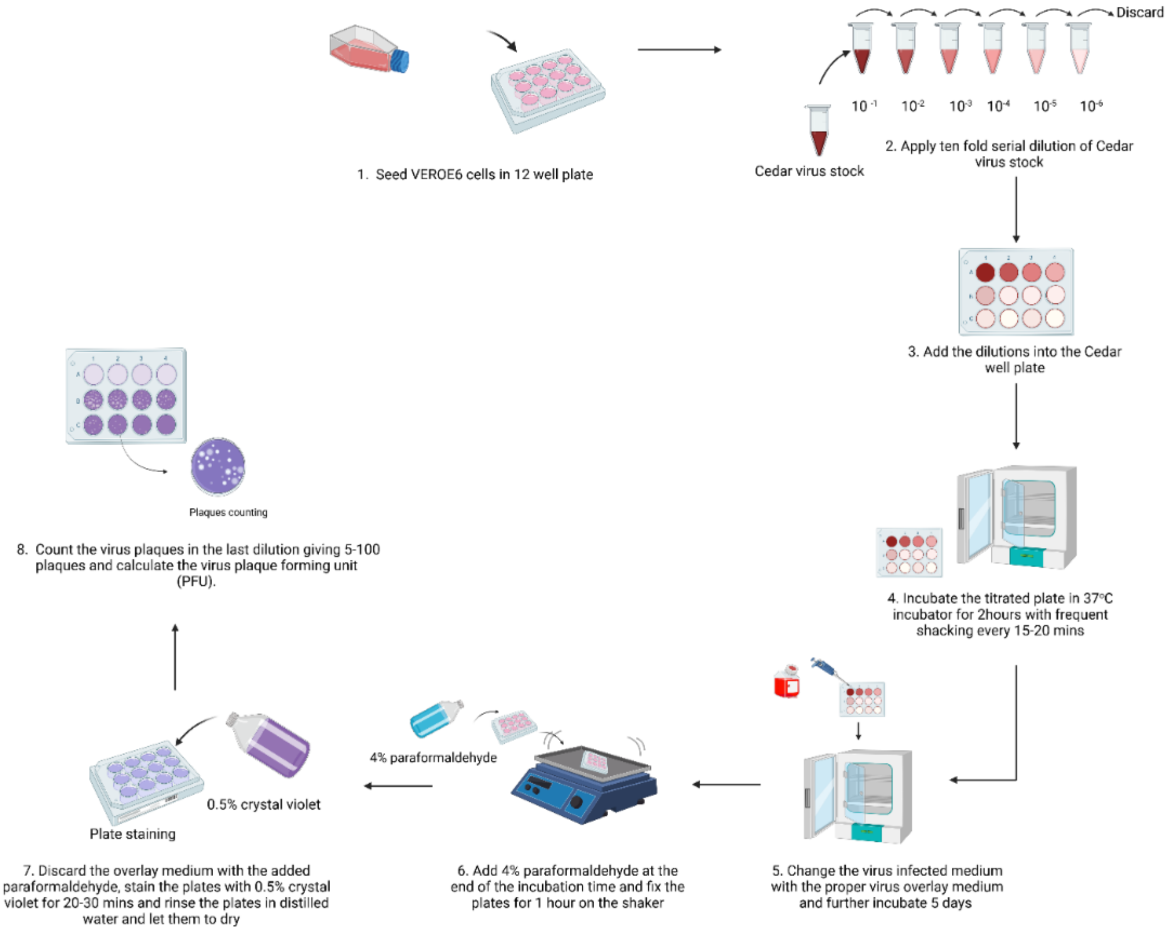

Figure 2.1. A schematic overview of rCedPV-GFP titration steps. Virus titration was performed in VeroE6 seeded in a 12-well plate, using tenfold serial dilutions. Cells were incubated for 5 days, fixed with 4% paraformaldehyde, and stained with 0.5% crystal violet. Plaques were counted, and plaque-forming units per millilitre (PFU/mL) was calculated. Figure made by BioRender.

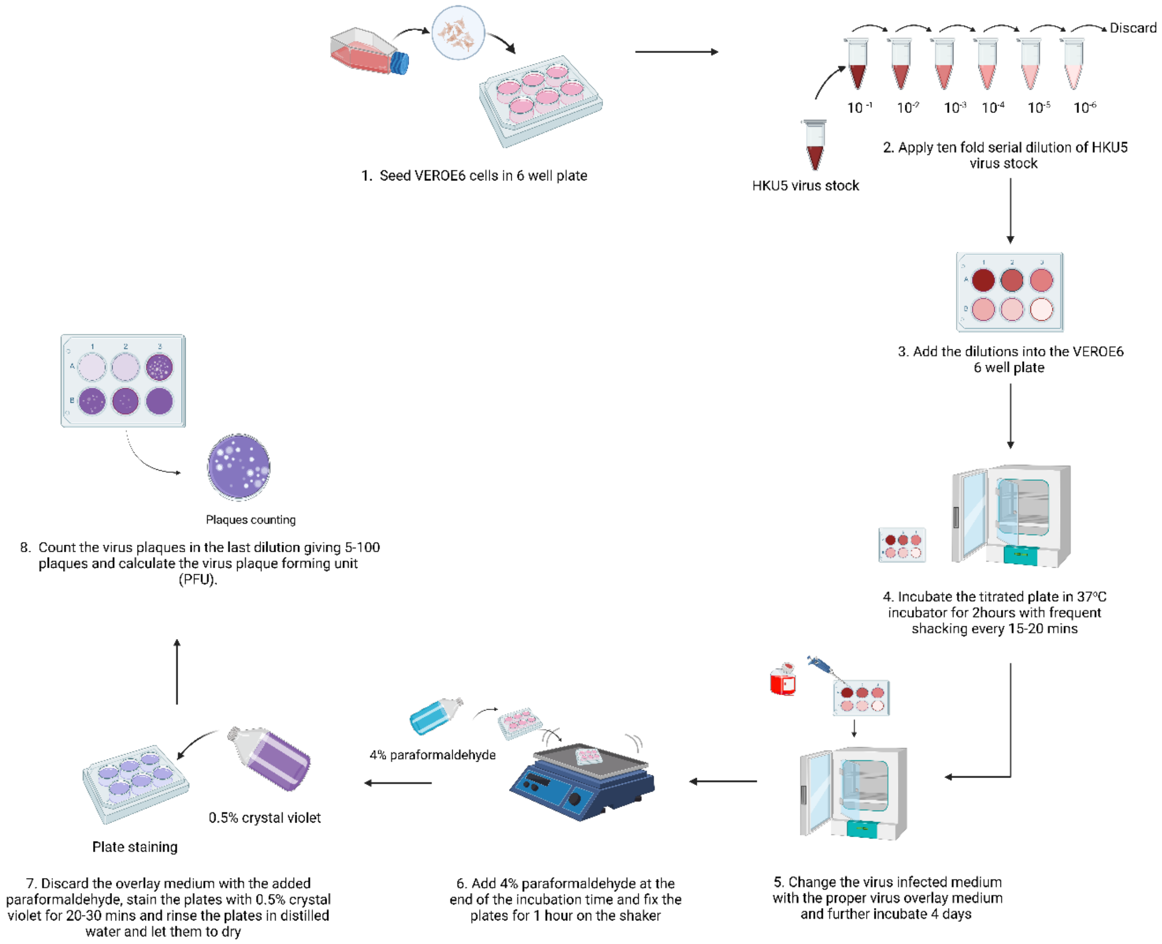

1. Seed VEROE6 cells in 6 well plate

2. Apply ten fold serial dilution of HKU5 virus stock

3. Add the dilutions into the VEROE6 6 well plate

4. Incubate the titrated plate in 37°C incubator for 2hours with frequent shacking every 15-20 mins

5. Change the virus infected medium with the proper virus overlay medium and further incubate 4 days

6. Add 4% paraformaldehyde at the end of the incubation time and fix the plates for 1 hour on the shaker

7. Discard the overlay medium with the added paraformaldehyde, stain the plates with 0.5% crystal violet for 20-30 mins and rinse the plates in distilled water and let them to dry

8. Count the virus plaques in the last dilution giving 5-100 plaques and calculate the virus plaque forming unit (PFU).

Figure 2.2. A schematic overview of BtCoV HKU5-SE titration steps. Virus titration was performed in VeroE6 seeded in a 12-well plate, using tenfold serial dilutions. Cells were incubated for 5 days, fixed with 4% paraformaldehyde, and stained with 0.5% crystal violet. Plaques were counted, and plaque-forming units per millilitre (PFU/mL) was calculated. Figure made by BioRender.

For the calculation of the virus titre, the well of the last viral dilution with a number of plaques ranging from 5 to 100 was identified in triplicate, and the average number of plaques was calculated. The dilution factor of the last dilution, along with the initially added viral inoculum (in mL), was added to the equation to calculate the plaque-forming units per millilitre (PFU/mL) (**Figure 2.3**).

$$\mathbf{PFU/mL} = \frac{\textbf{Average number of the plaques}}{\textbf{Dilution factor X Volume of added viral inoculum in mL}}$$

Figure 2.3. Calculation equation of the virus plaque-forming units per millilitre (PFU/mL).

2.4. rCedPV-GFP/BtCoV HKU5-SE Virus Infection

For each independent experiment, the desired viral multiplicity of infection (MOI) was calculated and inoculated into the target cells. Virus infection was made in DMEM medium that was serum-free. The virus was allowed to adsorb for 2 h, and the cells were mixed every 15 min. At the end of the adsorption period, the inoculum was aspirated, the cells were washed by PBS, and the medium was replaced with normal growth medium containing 5% FBS. Cells were further incubated according to the desired experiment.

2.5. Plasmid Propagation, Purification, and Cassette Design

2.5.1. Plasmid Propagation

For plasmid propagation, DH5α competent cells (NEB®) were used. The propagation steps involved mixing 1 µL of the plasmids into 40 µL competent cells, followed by gentle tapping of the tube mixture several times. Next, the bacteria/DNA mixture was incubated on ice for 30 min, subjected to heat shock for 45 seconds (sec) at 42 ºC and placed back on ice for 5 mins. 200 µL Luria broth (LB) medium without antibiotics was then added to the mixture, and the transformed bacteria were allowed to grow for 1 h in a 37 ºC shaking incubator set at 230 RPM. After the outgrowth period, 10-20 µL of the transformed cells was plated on LB agar containing 100 µg/mL Ampicillin. Following an overnight incubation at 37 °C, one bacterial colony was picked for further propagation in 5 mL LB broth containing 100 µg/mL Ampicillin. The broth propagation was also performed overnight in a 37 ºC shaking incubator set to 200 RPM. Plasmids used in the study are supplied in (**Table 2.5**).

Table 2.5. Plasmids and vectors used in the study.

Plasmid	Resource	Catalogue number
pcDNA3.1-ACE2-GFP	Addgene	Plasmid #154962
pcDNA3/Flag-METTL3	Addgene	Plasmid #53739
pcDNA3/Flag-METTL14	Addgene	Plasmid #53740
pcDNA3/Flag-WTAP	Addgene	Plasmid #53741
ALKBH5-dCas9	Addgene	Plasmid #134783
FTO-dCas9	Addgene	Plasmid #134781
pSNAPf-hYTHDF1	Addgene	Plasmid #155346
pcDNA3-flag-YTHDF2	Addgene	Plasmid #52300

pSNAPf-hYTHDF3	Addgene	Plasmid #155348
pcDNA3-FLAG-HA-hYTHDC1	Addgene	Plasmid #85167
pT7-MS2-HA-C1-HsYTHDC2_AD	Addgene	Plasmid #148490
pCAGGs-GFP	Dr. Luis Martinez-Sobrido, Texas Biomedical Research Institute, USA	N/A
pCAGGs-Empty	Dr. Luis Martinez-Sobrido, Texas Biomedical Research Institute, USA	N/A
pB-CAG-EGFP	Dr. Mike McGrew, The Roslin Institute, UK	N/A
Hybase-CAG	Dr. Mike McGrew, The Roslin Institute, UK	N/A
RE-ACE2-EGFP-pB	Dr. Darrell R. Kapczynski, The USDA, USA	N/A
hACE2-EGFP-Flag-C-pB	This study	N/A
RE-ACE2-Flag-N-mScarlet-pB	This study	N/A
RE-ACE2-Flag-C-mScarlet-pB	This study	N/A
RE-METTL3-WT-V5-N-mScarlet-pB	This study	N/A
RE-METTL3-ZFD1- V5-N -mScarlet-pB	This study	N/A

RE-METTL3-ZFD2-V5-N-mScarlet-pB	This study	N/A
RE-METTL3-ZFD1 and 2-V5-N-mScarlet-pB	This study	N/A
RE-METTL3-MTD-V5-N-mScarlet-pB	This study	N/A
RE-METTL3-ZFD1, 2 & MTD-V5-N-mScarlet-pB	This study	N/A
RE-METTL3-ZFD2 & MTD-V5-N-mScarlet-pB	This study	N/A
mScarlet-pB	This study	N/A

N/A, not applicable

2.5.2. Plasmid Purification

Purification of the plasmids was performed according to the instructions of the GeneJET Plasmid Miniprep Kit (Thermo Fisher Scientific). First, the bacterial culture was pelleted for 5 min at 6800 × *g* in a room-temperature microcentrifuge and resuspended in 250 µL resuspension buffer containing RNase. Then, two tube-inverting steps were performed; in between, 250 µL and 350 µL of lysis and neutralisation buffer were added to lyse the suspended bacteria and neutralise the released plasmid, respectively. Following that, the tube mixture was centrifuged at maximum speed for 10 min, and the supernatant was transferred to the Thermo Scientific GeneJET spin column, which was then centrifuged at 12000 × *g* for 1 min. The flow-through was discarded, and 500 µL of the two washing solutions was applied to the column to wash the silica-bound DNA. The silica membrane column was then dried by centrifugation at 12000 × *g* for 1 min. Finally, the dried column was transferred to a new clean tube to which 30 µL elution buffer was added to elute the plasmid.

2.5.3. RE-METTL3 PiggyBac Cassette Design.

To construct the RE-METTL3-WT-V5-N-mScarlet-pB plasmid cassette, the ORF of the *R. aegyptiacus METTL3* (*RE-METTL3*) gene (accession number XM_016165566.2) was utilised for the design. A V5 epitope tag was added upstream to the gene, and a stop codon was incorporated at the end of the sequence. To enable tracking of the transfected cells, the red mScarlet fluorescence protein was included downstream in the construct. Bicistronic expression of mScarlet and RE-METTL3 was achieved by an internal ribosome entry site 2 (IRES2) placed between the two proteins. The entire expression cassette was codon-optimised for mammalian expression, synthesised, and cloned into pB-CAG-EGFP by GeneArt (Thermo Fisher Scientific). Upon delivery, 5 µg of the plasmid was used for propagation as previously mentioned in step 2.5.1.

2.6. Cloning and Generation of Plasmid Constructs

2.6.1. RE-METTL3 PiggyBac Constructs

2.6.1.1. PCR Amplification of RE-METTL3 Domains

For the generation of V5-tagged RE-METTL3 domain vectors, ZFD1, ZFD2, and MTD were either individually or combined amplified from the RE-METTL3-WT-V5-N-mScarlet-pB vector. Moreover, mScarlet was co-amplified with the domains to generate mScarlet-pB as an expression vector control. PCR amplification was performed using Q5® High-Fidelity DNA Polymerase (NEB®) with primers containing the vector restriction sites, and the reaction conditions are provided in (**Table 2.6** and **Table 2.7**) respectively.

Table 2.6. Primer sequences used for cloning of RE-METTL3 pB plasmids.

Primer	Oligonucleotide sequence (5′ to 3′)	Vector generated
RE- METTL3-ZFD1- AgeI-V5- F	CACCTTACCGGTCGCCACCATGGGCAAGCCCATTCCTAATCCTCTGCTGGGCCTCGACAGCACCAGCATCGTGGAAAAGTTCAGA	RE-METTL3-ZFD1-V5-N -mScarlet-pB/ RE-METTL3-ZFD1 and 2-V5-N-mScarlet-pB/ RE-METTL3-ZFD1, 2 & MTD-V5-N-mScarlet-pB
RE- METTL3-ZFD1- MluI -V5-R	CACCTTACGCGTTCAGTGCAGCTTTCTGCAAGG	RE-METTL3-ZFD1-V5-N -mScarlet-pB
RE- METTL3-ZFD2- AgeI -V5 - F	CACCTTACCGGTCGCCACCATGGGCAAGCCCATTCCTAATCCTCTGCTGGGCCTCGACAGCACCTTCCGGCGGATCATCAACAAGCAC	RE-METTL3-ZFD2-V5-N-mScarlet-pB/ RE-METTL3-ZFD2 & MTD-V5-N-mScarlet-pB
RE- METTL3-ZFD2-MluI-V5-R	CACCTTACGCGTTCAGCAGGCGTCGATCTCGTAGTGC	RE-METTL3-ZFD2-V5-N-mScarlet-pB/ RE-METTL3-ZFD1 and 2-V5-N-

		mScarlet-pB
RE- METTL3-MTD- AgeI -V5- F	CACCTTACCGGTCGCCACCATGGGCAAGCCCATTCCTAATCCTCTGCTGGGCCTCGACAGCACCCAGAGCGTCGGCGGAGAT	RE-METTL3-MTD-V5-N-mScarlet-pB
RE- METTL3-MTD- MluI-V5-R	CACCTTACGCGTTCACAGGTTCTTGGGCTTGCTGATGATGC	RE-METTL3-MTD-V5-N-mScarlet-pB/ RE-METTL3-ZFD1, 2 & MTD-V5-N-mScarlet-pB/ RE-METTL3-ZFD2 & MTD-V5-N-mScarlet-pB
mScarlet BbsI-V5-F	CACCTTGCGGCCGCTCATTTGTACAGCTCG	mScarlet-V5-N--pB
mScarlet NOTI- R	CACCTTTTCGAAGCCACCATGGTTTCCAAG	mScarlet-V5-N--pB

Table 2.7. Q5® High-Fidelity DNA Polymerase PCR setup.

Step	Cycles	Temperature	Time
Initial denaturation	1	98 ºC	3 min
Denaturation	40	98 ºC	15 sec
Annealing/ extension	40	72 ºC	4 min
Final extension	1	72 ºC	10 min

2.6.1.2. Analysis and Agarose Gel Extraction of the Amplified PCR Product

Following the PCR amplification, products were visualised on a 1% agarose gel. The target bands were excised from the gel and purified using the GeneJET Gel Extraction Kit (Thermo Fisher Scientific). The procedures involved adding 1:1 volume of Binding Buffer to the gel slice, followed by incubation at 60 ºC until complete dissolution of the gel was observed. After that, 1 gel volume of 100% isopropanol was further added to the solubilised gel. The entire mixture was then loaded onto the GeneJET purification column, which was centrifuged at 12000 × g for 1 min to bind the DNA to the silica membrane. Consequently, 700 µL of washing buffer was added twice to the membrane and the column was dried at maximum centrifugation speed for 1 min. Finally, the column was transferred to a new, clean microcentrifuge tube, and the DNA was eluted in 30 µL of elution buffer.

2.6.1.3. Restriction Digestion of the PCR Product and the RE-METTL3 PiggyBac Vector

In this step, AgeI-HF®, MluI-HF®- HF® (NEB®) were used for the digestion of the RE-METTL3 domains and RE-METTL3-WT-V5-N-mScarlet-pB plasmid, whereas BbsI-HF® and NotI-HF® (NEB®) were used to digest the mScarlet along with the same vector. The respective enzymes were added simultaneously into two 0.3 mL PCR tubes containing the targeted DNA, and the restriction digestion was done overnight at 37 ºC under the conditions listed in (**Table 2.8**). Cleaved products were then analysed on a 1% agarose gel, excised, and purified using the GeneJET Gel Extraction Kit as described in the previous step.

Table 2.8. Restriction digestion mixture used in the study.

Reagent	Quantity tube 1	Quantity tube 2
AgeI-HF®/BbsI-HF®	1 µL	1 µL
MluI-HF® /NotI-HF®	1 µL	1 µL
rCutSmart™	5 µL	5 µL
pB vector	1 µg	
Resulted PCR product		1 µg
Nuclease-free water (NFW)	Up to 50 µL	Up to 50 µL

2.6.1.4. Ligation of the Digested Products and Transformation of the Ligated Constructs

The ligation of the linearised vector and PCR product was carried out using the T4 DNA Ligase (NEB®). The ligation reaction was performed at room temperature or in a fridge, with ratios ranging from 1:1 to 1:5, using the conditions listed in Table 2.9. After the ligation, the reaction was heat-inactivated at 65 ºC for 10 min, chilled on ice, and 3.5 µL of the ligation mixture was then transformed into DH5α cells using the same steps previously mentioned in 2.5.1.

Table 2.9. T4 ligation reaction components used in the study.

Reagent	**Quantity**
Digested pB vector (~ 8 kbp)	50 ng
Digested insert (~ 3.7 kbp)	Ratio variable
T4 DNA Ligase	1 μL
T4 DNA Ligase Buffer (10X)	2 μL
NFW	Up to 20 μL

2.6.1.5. Colony PCR and Sequencing of the Generated Plasmids

In order to perform the colony PCR of the generated constructs, colonies were picked from the ratio which showed the highest number of colonies. Colonies were propagated in LB broth and purified as previously described in steps 2.5.1 and 2.5.2. PCR of the purified colonies was performed with the Q5® High-Fidelity DNA Polymerase using primers pB-F (5′ GCCTCTGCTAACCATGTTCATG-3′) and mScarlet NOTI- R. Reaction conditions were mentioned previously in section 2.6.1.1, and analysis of the PCR products was performed using 1% agarose gel. Once the target bands were visualised on the gel, one positive colony was selected and sent for sequencing. Primer pB-F was used to confirm the target insertions in the RE-METTL3-WT-V5-N-mScarlet-pB backbone.

2.6.2. ACE2 PiggyBac Plasmid Constructs

2.6.2.1. hACE2

To generate the hACE2-EGFP-Flag-C-pB vector, hACE2-EGFP was amplified using pcDNA3.1-ACE2-GFP plasmid as a template and primers hACE2-AgeI-F (5′-CACCTTACCGGTCGCCACCATGTCAAGCTCTTCCTGGCTC-3′) and EGFP-Flag NotI-R (5′-CACCTTGCGGCCGCTTACTTGTCGTCATCGTCTTTGTAGTCCTTGTACAGCTCGTCCATG-3′). Notably, a flag tag sequence was included in the reverse primer for the detection of the receptor in the downstream applications. Restriction digestion was performed using AgeI and NotI enzymes on the purified PCR product and pB-CAG-EGFP plasmid. While ligation of the linearised insert and vector was executed using the T4 ligase. Colony PCR was performed using primers pB-F and EGFP-Flag

NotI-R, and positive clones were submitted for Sanger sequencing. Sequence verification of the constructs was carried out using primer IRES-R (5′-GGCCCTCACATTGCCAAAAG-3′). The PCR amplification, gel purification, restriction digestion, and ligation steps were performed as described previously in section 2.6.1.

2.6.2.2. RE-ACE2

Cloning of RE-ACE2-Flag-C-mScarlet pB and RE-ACE2-Flag-N-mScarlet pB was performed using the same steps described in 2.6.1. Briefly, the RE-ACE2 was amplified from the RE-ACE2-EGFP-pB plasmid using primers containing the AgeI and MluI restriction sites and a flag tag sequence positioned either in the 5′ or 3′ end of the gene, depending on the construct design. Restriction digestion and ligation were performed using the purified PCR product and the RE-METTL3-WT-V5-N-mScarlet-pB plasmid as the vector backbone, and the colony PCR was performed using primers pB-F and mScarlet-R. Sequence verification of the constructs was carried out using primer pB-F. Primers used for the cloning steps are listed in (**Table 2.10**).

Table 2.10. Primer sequences used for cloning of RE-ACE2-mScarlet-pB plasmids.

Primer	**Oligonucleotide sequence (5′ to 3′)**
RE-ACE2-AgeI-Flag-F	CACCTTACCGGTCGCCACCATGGACTACAAAGACGATGACGACAAGTCAGGCTCTTTCTGGCTCTTT
RE-ACE2-MluI-R	CACCTTACGCGTTCAAAATGAAGTCTGAACATCATCGTTATTT
RE-ACE2-AgeI-F	ACCTTACCGGTCGCCACCATGGACTACAAAGACGATGACGACAAGTCAGGCTCTTTCTGGCTCTTT
RE-ACE2-MluI-Flag-R	CACCTTACGCGTTCAAAATGAAGTCTGAACATCATCGTTATTT

2.7. Establishment of Stable Cell Lines Expressing the Cloned Constructs

2.7.1. Establishment of R06E Expressing the METTL3-Derived Constructs

R06E cells were seeded in 12-well plates and co-transfected with either mScarlet, full-length RE-METTL3, or its domain constructs together with the Hybase-CAG vector at a 1:1 ratio using FuGENE® 4K (Promega), following the transfection procedure described in (**Table 2.11**). The transfected cells were then selected with Puromycin Dihydrochloride (Gibco™) at 0.5 µg, and the cells were expanded thereafter in fresh medium containing 10% FBS.

Table 2.11. FuGENE ® 4K transfection method protocol.

Step	FuGENE ® 4K
Used cell density	50–90%
Transfection reagent: DNA mixture ratio	1:3
Incubation time	15 min

2.7.2. Development of Stable Cell Lines Expressing hACE2 Receptor

2.7.2.1. R06E

To incorporate the flagged hACE2-EGFP into the R06E genome, cells were seeded in 12-well plates and co-transfected with 1:1 hACE2-EGFP-Flag-C-pB and Hybase-CAG plasmid using FuGENE ® 4K as mentioned in the previous step. Following transfection, cells were subjected to puromycin selection; however, due to the low transfection efficiency rate of the bat cells and some death of hACE2-EGFP-expressing cells occurring during the selection, the R06E puromycin selection was prematurely terminated on the fourth day, and fluorescence-activated cell sorting (FACS) was performed to enrich for hACE2-EGFP-positive cells. The fluorescence-activated cell sorting (FACS) procedure was conducted according to a protocol provided by Dr Amanda Thomaz (Lancaster University).

The protocol involved cell trypsinisation, pelleting three times at 1500 RPM for 5 min, and subsequent PBS washing. At the final centrifugation, the cell pellet is suspended in sorting solution (1X PBS, 2% FBS and 1-5mM of ethylenediaminetetraacetic acid (EDTA)) and adjusted to the desired concentration of sorting (1-10 million cells/mL). The cell suspension was then filtered through a cell strainer to remove visible clumps, sorted using a cell sorter gate set to the highest level of EGFP expression, and allowed to expand in a T25 flask (**Figure 2.4**).

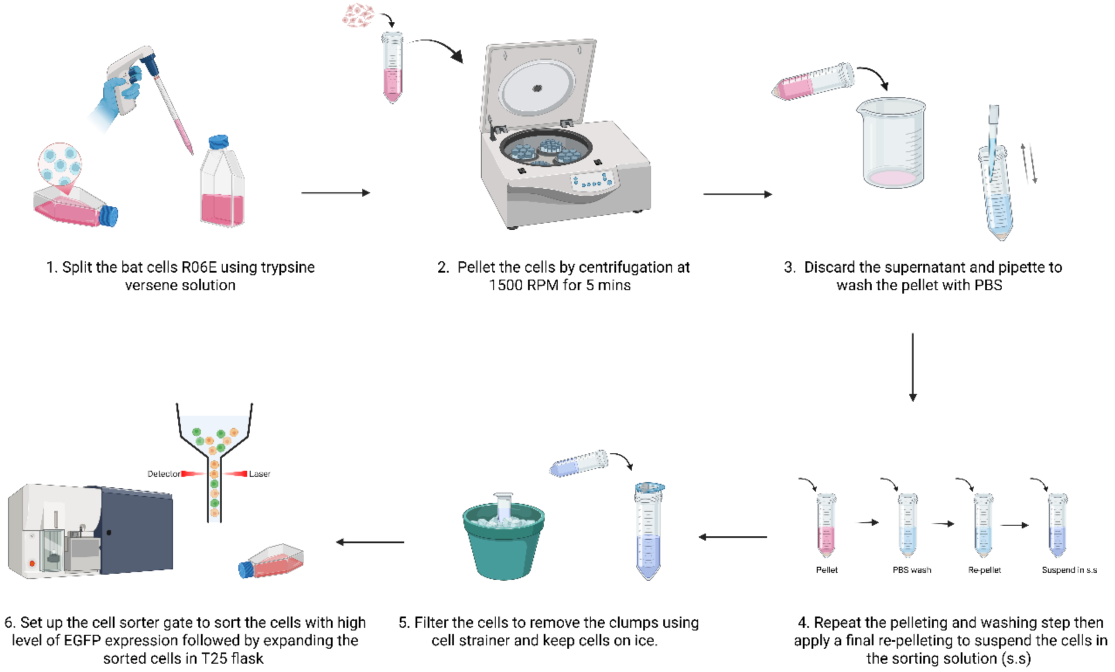

Figure 2.4. A schematic diagram showing the overall steps of R06E-hACE2-EGFP cell sorting. Cells were trypsinised, pelleted, washed with PBS, and resuspended in cell-sorting solution. Clumps were filtered and removed before the cells were transferred to the cell sorter. The cells were expanded in a T25 following the cell sorting process. Figure made by BioRender.

2.7.2.2. A549 and BHK-21

The establishment of A549 and BHK-21 hACE2-EGFP involved the same procedures as in the R06E, except for the transfection, which was performed using ViaFect™ (Promega), as illustrated in (**Table 2.12**). Puromycin selection was then applied at concentrations of 3 µg/mL for A549 cells and 5 µg/mL for BHK-21 cells.

Table 2.12. ViaFect™ transfection protocol.

Step	**ViaFect™**
Used cell density	75%
Transfection reagent: DNA mixture ratio	1:3
Incubation time	20 min

2.7.3. Development of Stable Cell Lines Expressing RE-ACE2 Receptor.

Except for the cell sorting, the generation of R06E and BHK-21 cell lines constantly expressing the RE-ACE2 receptor was carried out similarly to the establishment of the hACE2-GFP and METTL3 cell lines. R06E and BHK-21 were seeded in 12-well plates and co-transfected with either of the RE-ACE2 pB constructs along with Hybase-CAG vector at a ratio of 1:1. Transfection, antibiotic selection, and clonal expansion of each cell line were performed as previously described in step 2.7.1. for R06E and step 2.7.2.2. for BHK-21.

2.8. Molecular Methods

2.8.1. Detection of the PiggyBac Genomic Integration in R06E by Polymerase Chain Reaction

2.8.1.1. DNA Extraction

The targeted cells were grown in a 6-well plate. The genomic DNA was extracted using the Blood & Cell Culture DNA Mini Kit (Qiagen) protocol. Briefly, 1 volume ice-cold buffer C1 and 3 volumes of ice-cold distilled water were added to 500 µL sample. The sample was then centrifuged at 4 ºC for 15 min at 1300 × *g*. After that, 250 µL ice-cold buffer C1 and 750 µL ice-cold distilled water were added to the pellet and the mixture was centrifuged again under the same conditions. The resulting nuclei pellet was suspended in 1 mL of Buffer G2, and 25 µl proteinase K was used to inactivate the nucleases at 50 ºC for 30 min. Prior to isolation of genomic DNA, the QIAGEN Genomic-tip 20/G was equilibrated with 1 mL of Buffer QBT and allowed to drain by gravity. The sample was then applied to the genomic tip and left to enter the resin via the gravity flow. The column was washed three times with 1 mL Buffer QC. Subsequently, 1 mL Buffer QF was added twice to elute the sample. The DNA was precipitated by adding 1.4 mL of isopropanol. The sample was centrifuged at >5000 × *g* for at least 15 min at 4 ºC, then 1 mL of 70% ethanol was added to wash the DNA pellet. The DNA was mixed and further spun at >5000 × *g* for 10 min at 4 ºC. Finally, the DNA was resuspended in 50 µL TE buffer and dissolved overnight at 55 ºC for 1 h.

2.8.1.2. Polymerase Chain Reaction Amplification and Product Analysis

Polymerase Chain Reaction (PCR) on the R06E genomic DNA was performed using DreamTaq PCR Master Mix (2X) (Thermo Fisher Scientific). Primers used were RE-METTL3-ZFD 1- AgeI-V5- F, RE- METTL3-ZFD 1- MluI -V5-R, RE- METTL3-ZFD 2- AgeI-V5- F, and RE- METTL3-ZFD 2- MluI -V5-R. Reaction setup and conditions are mentioned in the (**Table 2.13** and **Table 2.14**). The resulting PCR products were visualised using a 1.5% agarose gel.

Table 2.13. Reaction components of genomic DNA amplification of R06E.

Reaction component	Quantity
DreamTaq PCR Master Mix (2X)	25 µL
Forward primer (10 µM)	1 µL
Reverse primer (10 µM)	1 µL
Template DNA (500 ng)	Variable
NFW	Up to 50 µL

Table 2.14. PCR steps of genomic DNA amplification of R06E.

Step	Cycles	Temperature	Time
Initial denaturation	1	95 ºC	3 min
Denaturation	40	95 ºC	30 sec
Annealing	40	63 ºC	30 sec
Extension	40	72 ºC	30 sec
Final extension	1	72 ºC	5 min

2.8.2. Establishment of TaqMan Reverse Transcriptase Quantitative Polymerase Chain Reaction Assay for the Quantitative Detection of BtCoV HKU5-SE

2.8.2.1. Primer and Probe Design

In this experiment, BtCoV HKU5-SE-F (5′-CCTGCCCCTAATACCACTGTCT-3′) and BtCoV HKU5-SE-R (5′-CTCCGCCAATACCCAGCATTC-3′) primers were designed to amplify 137 bp of the HKU5 N gene (accession number EF065512.1). The primers were synthesised and ordered from Thermo Fisher Scientific. The BtCoV HKU5-SE probe (5′- ACCCAGCACGGTAAGCAGCCTCT-3′) was synthesised by Eurofins. For TaqMan-based amplification of the virus, primer and probe design were conducted using Geneious Prime 2023 software [294]. The primers were carefully selected to have an average length of 22 nt and 40-60% GC content. Additionally, hairpins, self-complementary and secondary structures were avoided during the design. The probe was designed in proximity to the forward primers, using the same primer design parameters, with a melting temperature (T_m) 5–10 ºC higher than the primers.

2.8.2.2. Viral RNA Extraction

For the preparation of BtCoV HKU5-SE and SARS-CoV-2 Omicron RNA templates, VeroE6 cells were infected at an MOI of 1. Viral infection, adsorption, harvest, and clarification were performed as previously described in 2.4. The viral RNA extraction was performed according to the manufacturer's instructions for the QIAamp Viral RNA Mini Kit (Qiagen). Briefly, 560 µL of Buffer AVL-carrier RNA was used for lysis; 140 µL of the sample was used, and a 10 min incubation was performed to ensure efficient lysis. After that, 1:1 (v/v) 96−100% ethanol was added to the sample, and the whole mixture was loaded into the QIAamp Mini column for centrifugation at 8000 RPM for 1 min. Next, 500 µL of Buffer AW1 was added to the column, and the mixture was centrifuged at 8000 RPM for 1 min. The column was further washed by 500 µL Buffer AW2 and spun at 13000 RPM for 3 min. Any residual buffer was removed by centrifugation of the column at full speed for 1 min. A single elution step using 30 µL AVE buffer was then performed to elute the viral RNA. The eluted nucleic acid was stored in -80 ºC for further processing.

2.8.2.3. Specificity Evaluation of the BtCoV HKU5-SE TaqMan Assay

To assess the specificity of the designed primers and probe, the SARS-CoV-2 Omicron (B.1.1.529) strain was used. The Reverse Transcriptase Quantitative Polymerase Chain Reaction (RT-qPCR) was performed with 100 ng of total RNA extracted using the Luna® Universal Probe One-Step RT-qPCR Kit (NEB®). The specific reaction components and RT-qPCR setup are detailed in (**Table 2.15** and **Table 2.16**) respectively.

Table 2.15. Reaction components of the BtCoV HKU5-SE TaqMan assay.

Reaction component	**Quantity**
Universal Probe One-Step Reaction Mix (2X)	5 µL
Luna WarmStart® RT Enzyme Mix (20X)	0.5 µL
Forward primer (10 µM)	0.4 µL
Reverse primer (10 µM)	0.4 µL
Probe (10 µM)	0.2 µL
Template RNA (100 ng)	Variable
NFW	Up to 10 µL

Table 2.16. Thermal profile of BtCoV HKU5-SE TaqMan assay.

Step	Cycles	Temperature	Time
Reverse transcription	1	55 ºC	10 min
Initial denaturation	1	95 ºC	1 min
Denaturation	40	95 ºC	10 sec
Extension/data collection	40	60 ºC	30 sec

2.8.2.4. In Vitro Transcription of BtCoV HKU5-SE N gene

2.8.2.4.1. Preparation of cDNA Template

Following the specificity confirmation of the BtCoV HKU5-SE TaqMan RT-qPCR assay, the LunaScript® RT SuperMix (NEB®) kit was used to generate cDNA from BtCoV HKU5-SE. Reaction and reaction conditions were done according to the manufacturer's instructions (**Table 2.17** and **Table 2.18**). The generated cDNA was then stored in -20 ºC for further downstream processing.

Table 2.17. Reaction mixture of BtCoV HKU5-SE cDNA synthesis.

Reaction component	Quantity
LunaScript RT SuperMix (5X)	10 µL
RNA sample (1µg)	Variable
NFW	Up to 20 µL

Table 2.18. Steps of BtCoV HKU5 cDNA synthesis.

Step	Cycles	Temperature	Time
Annealing	1	25 ºC	2 min
cDNA synthesis	1	55 ºC	10 min
Heat inactivation	1	95 ºC	1 min

2.8.2.4.2. cDNA PCR Amplification

In this experiment, primers BtCoV HKU5-SE-F and BtCoV HKU5-SE-R were used to amplify the virus cDNA. However, to render the PCR product suitable for the in vitro transcription (IVT), the T7 promoter sequence (5′-TAATACGACTCACTATAG-3′), along with two Gs, was incorporated upstream of the forward primer. PCR amplification was performed using Thermo Scientific DreamTaq PCR Master Mix (2X) as described in 2.8.1.2.

2.8.2.4.3. PCR Product Analysis and Gel Extraction

Following the PCR amplification of the BtCoV HKU5-SE, a 1% agarose gel was used to visualise the PCR product. After visualisation, the band was excised from the gel and purified using the GeneJET Gel Extraction Kit as described in 2.6.1.2.

2.8.2.4.4. RNA Transcription Reaction

In vitro transcription of the BtCoV HKU5-SE was done using the PCR product generated in the previous step as a template. The transcription reaction was carried out using T7 RiboMAX™ Express Large Scale RNA Production System (Promega) according to the manufacturer's instructions, with overnight incubation at 37 ºC. The reaction setup is listed in (**Table 2.19**).

Table 2.19. Reaction mixtures of BtCoV HKU5-SE IVT.

Reaction component	Quantity
RiboMAX™ Express T7 2X Buffer	10 µL
DNA template (1µg)	Variable
Enzyme Mix, T7 Express	2 µL
NFW	Up to 20 µL

2.8.2.5. RNA Purification, Analysis, and Quantification

Following the IVT, a typical NEB® DNase I reaction was applied at 37 ºC for 1 h to break down the DNA template (**Table 2.20**). Plasmid pGEM® Express Positive Control Template (Promega) was used as a positive control for the reaction. Subsequently, the RNA was subjected to clean up using the Monarch® Total RNA Miniprep Kit (NEB®) protocol. Briefly, 100 µL RNA lysis buffer was added to each 50 µL IVT reaction, followed by the addition of 1:1 (v/v) ethanol (≥ 95%). The whole mixture was then transferred to the RNA purification column supplied with the kit. A spin step at 16000 × *g* for 30 sec was then applied to allow the RNA to bind the column membrane. Next, in two separate steps, 500 µL of RNA Wash Buffer (WZ) was applied to wash the silica membrane at 16000 × *g* for 30 sec and 2 min, respectively. Finally, the column was then transferred into a new collecting tube to be dried at full speed for 1 min. Elution of the RNA was done in 50 µL NFW and further kept on ice for determining the quality and quantity by NanoDrop One Spectrophotometer (Thermo Fisher Scientific). 5 µL of the measured RNA was later analysed on 2% agarose gel to check for any residual DNA. Once the analysis was checked, the RNA was kept on ice until use.

Table 2.20. DNase I reaction components.

Reaction component	**Quantity**
DNase I Reaction Buffer (10X)	10 µL
DNAse I (RNase-free)	1 µL
RNA	~ 10 µg RNA
NFW	Up to 100 µL

2.8.2.6. Establishment of the Standard Curve of BtCoV HKU5-SE

In this step, DNase/RNase-free water was used to perform a 10-fold dilution of the viral RNA. PCR reaction was performed using primers, reaction, and conditions mentioned in 2.8.2.1 and 2.8.2.3. To ensure the reliability of the generated results, each dilution was tested in two technical and two biological replicates. Additionally, no RT reaction was included in parallel to confirm the absence of residual DNA contamination. The BtCoV HKU5-SE standard curve was made using Microsoft Excel, and the limit of detection (LOD) is determined based on the last dilution displayed intra-variability more than 0.5 quantification cycle (Cq). All steps involved in the BtCoV HKU5-SE TaqMan RT-qPCR assay development are illustrated in (**Figure 2.5**).

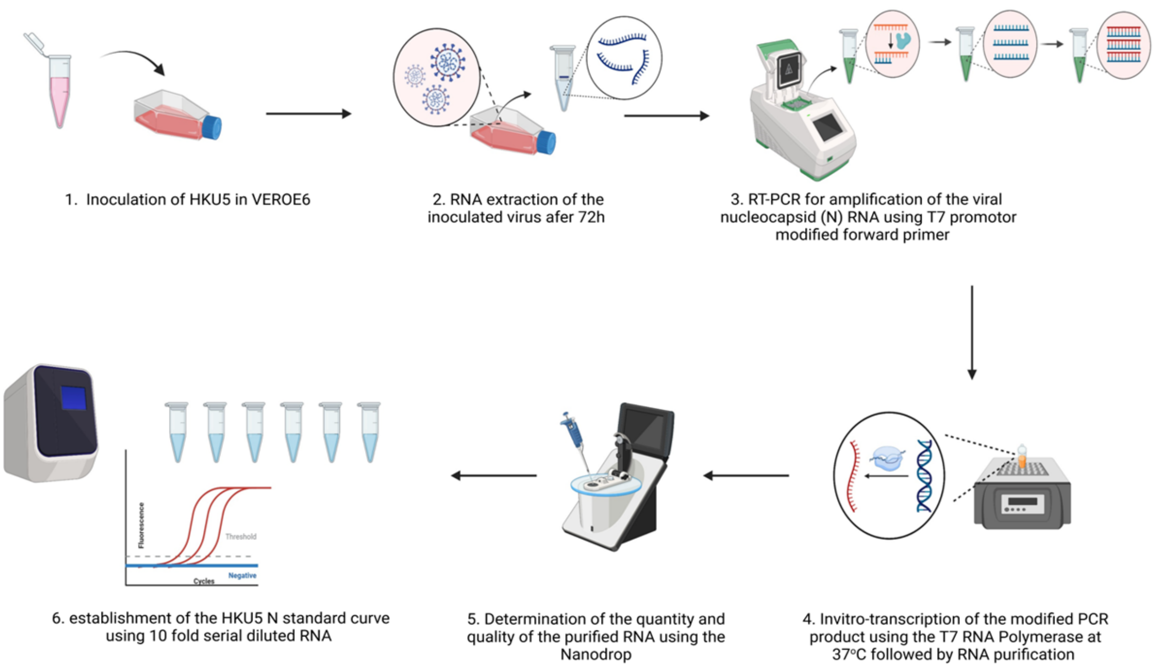

Figure 2.5. A schematic diagram illustrating the overall steps of the BtCoV HKU5-SE IVT reaction and the standard curve establishment. BtCoV HKU5-SE was inoculated in VeroE6 cells, subjected to RNA extraction and RT-PCR using the specific primers. In vitro transcription (IVT) on the purified PCR product was performed using the T7 RNA polymerase. The generated RNA was purified and assessed for quality before the establishment of the standard curve. Figure made by BioRender.

2.8.3. Development of RT-qPCR for the Quantification of mRNA Expression Level of R06E

2.8.3.1. Primer Design

Primers utilised in this study were designed based on the *R. aegyptiacus* sequences available in the NCBI. The *R. aegyptiacus* genome assembly, GCF_014176215.1, was used as the reference to retrieve the nucleotide sequences. Geneious Prime 2023 software was employed to design the primers. The primers were designed as previously described in 2.8.2.1. The custom oligonucleotides were synthesised and delivered by Thermo Fisher Scientific. (**Table 2.21**) lists all targets and primer sequences used in the study.

Table 2.21. Primers used for RT-qPCR for the quantification of the mRNA expression level of R06E.

Target gene	Primer	Oligonucleotide sequence (5′ to 3′)
RE-ACE2	RE-ACE2-F	CGCACAGAGAAAGATGTCAGGCT
	RE-ACE2-R	CAGGAGTGGATTGAGCAGCAGTT
RE-TMPRSS2	RE-TMPRSS2-F	CCCAGAAAGCCATTTGAGCAAGC
	RE-TMPRSS2-R	AGTTTGGAGCAGAGCAAGGTGAG
RE-CTSL	RE-CTSL-F	GACATCCATCAGCAGGAGAGG
	RE-CTSL-R	GGGTCTTTGCTGCTGTACTCT
hACE2	hACE2-F	CCTGCTCATTTGCTTGGTGATA
	hACE2-R	GTCCACCATTGCATCAGTAACA

2.8.3.2. Establishment of the RT-qPCR

The RT-qPCR of the study was carried out using GoTaq® One step RT-qPCR (Promega). Using the relative quantification method, the gene expression changes of the R06E upon the virus infection were analysed. The delta-delta Ct **(**ΔΔCt) was employed to calculate the fold changes in mRNA expression between the infected and mock-infected control groups using *RE-EEFA1* as a reference gene (**Table 2.22–2.24**). show the PCR setup, kit protocol and the reference gene primers.

Table 2.22 . Reaction components of the RT-qPCR used in the study.

Reaction component	Quantity
GoTaq® qPCR Master Mix (2X)	10 µL
Forward primer (10 µM)	1 µL
Reverse primer (10 µM)	1 µL
RNA template (200 ng)	Variable
GoScript™ RT Mix	0.4 µL
NFW	Up to 20 µL

Table 2.23. Thermal profile of the RT-qPCR used in the study.

Step	Cycles	Temperature	Time
Reverse transcription	1	50 ºC	15 min
Initial denaturation	1	95 ºC	10 min
Denaturation	40	95 ºC	10 sec
Annealing	40	60 ºC	30 sec
Extension/ data collection	40	72 ºC	30 sec
Melting curve	1	65-95 ºC	20 min

Table 2.24. R. aegyptiacus reference gene primer sequences used in the study.

Target gene	Primer	Oligonucleotide sequence (5′ to 3′)	Reference
RE-EEFA1	RE-EEFA1-F	GTATGCCTGGGTCTTGGATAAA	[295]
	RE-EEFA1-R	GCCTGTGATGTGCCTGTAA	

2.8.4. Total RNA Extraction from Cells.

The total RNA was extracted from the infected cells according to the user guide of PureLink® RNA Mini Kit (Thermo Fisher Scientific). Cells were pelleted at 2000 × *g* for 5 min at 4 ºC, and the appropriate volume of 2-mercaptoethanol-lysis buffer was added to the sample. Next, 1:1 (v/v) 70% ethanol was added to the lysate, and the mixture was transferred to the spin cartilage for centrifugation at 12000 × *g* for 15 sec at room temperature. Afterwards, the column was washed twice by Wash Buffer I and once by Wash Buffer II and further dried at 12000 × *g* for 1-2 min. Finally, the RNA was eluted in 30 µL RNase–Free Water and kept at -80 ºC for further processing.

2.8.5. RT-qPCR for Viral and Gene Expression Level Quantification

For each of the independent experiments, the target cells were either uninfected or infected with the virus and subjected to the total RNA extraction using PureLink® RNA Mini Kit as described in the previous step. For TaqMan quantification of HKU5-SE using Luna® Universal Probe One-Step RT-qPCR Kit, 100 ng of purified RNA was used, and the resulting Cq value was compared against the established standard curve to determine intracellular viral load. For the relative gene expression analysis in R06E cells using GoTaq® One-Step RT-qPCR, 200 ng of purified RNA was used, and expression levels were normalised to the reference gene to calculate fold change using the ΔΔCt method. Reaction conditions for each of the Luna® Universal Probe One-Step RT-qPCR Kit and GoTaq® One-Step RT-qPCR were described in step 2.8.2.3 and 2.8.3.2. respectively.

2.9. Immunological Assays

2.9.1. Detection of the Overexpressed Proteins in the Established Cell Lines Using Western Blot.

2.9.1.1. Sample Preparation, Loading and Electrophoresis.

To detect the expression of the overexpressed proteins using Western blot (WB), wild-type (WT) R06E, A549, BHK-21 and their genetically modified derivatives were cultured in T25. 24 h post-seeding, the cells were washed with 3 mL of ice-cold PBS and trypsinised using 3 mL of the trypsin-versene solution mentioned in 2.2.1. The cells were then centrifuged at 1000 RPM for 5 min, and the supernatant was discarded. Afterwards, 200 µL of Radioimmunoprecipitation Assay (RIPA) buffer (Thermo Fisher Scientific) and cOmplete™ Protease Inhibitor Cocktail (Roche) mixture was added to the pellet and left on ice for 1 h on the shaker. The cell lysate was next spun at 13000 RPM for 10 min at 4 ºC. The supernatant was transferred into a clean new tube, and 10% of β-mercaptoethanol l- 2x-Lithium dodecyl sulfate (LDS) sample buffer mix was added to the lysate. Accordingly, the lysate was boiled at 95 ºC for 5 min to denature the proteins. 25 µL of protein ladder (Abcam) as well as the samples were loaded onto 5% stacking gel and allowed to run at 70 volts (V) for 30 min before running at 100V in the resolving gel. The percentage and running time of the resolving gel were determined according to the protein size. Details of the Sodium dodecyl sulphate (SDS) polyacrylamide gels are listed in (**Table 2.25** and **Table 2.26**).

Table 2.25. WB stacking gel recipe.

Reagent	Stacking gel (5%)
30% Acrylamide/bis	670 µL
0.5M Tris-HCl, pH 6.8	500 µL
10% SDS	40 µL
10% ammonium persulfate (APS)	40 µL
TEMED	4 µL
Distilled water (dH2O)	2.7 ml
Total volume	4 mL

Table 2.26. WB resolving gel recipe.

	Resolving gel		
	8%	**12%**	**20%**
Reagent/ Target protein size			
Target protein size	100-120 KD	80-25 KD	>10 KD
30% Acrylamide/bis	4 mL	6 mL	10 mL
1.5M Tris-HCl, pH 8.8	3.8 mL	3.8 mL	3.53 mL
10% SDS	150 µL	150 µL	150 µL
10% APS	150 µL	150 µL	75 µL
TEMED	12 µL	6 µL	7.5 µL
dH2O	6.9 mL	4.9 mL	1.03 mL
Total volume	15 mL	15 mL	15 mL

2.9.1.2. Protein Transfer and Blotting

Following the electrophoresis, the gels were transferred to a pre-activated polyvinylidene difluoride (PVDF) membrane (Thermo Fisher Scientific). The PVDF activation was done by immersing the membrane in 5 mL methanol (Sigma) for a few seconds, followed by rinsing with dH2O and soaking in 5 mL transfer buffer for 5 min. For blotting, the gel as well as the membrane were cast into the Trans-Blot Turbo Transfer System (Bio-Rad) using 2 pieces of filter paper wetted with the transfer buffer. The semi-dry method was then applied to transfer the protein bands. The transfer was done using the semi-dry method, running at 1.3A, 25V for 10 to 30 min.

2.9.1.3. Membrane Blocking and Antibody Binding.

Blocking the membrane was carried out at room temperature for 1 h using 5 ml of blocking solution (5% skimmed milk powder in Phosphate-Buffered Saline with Tween-20 (PBST)). After that, the membrane was washed three times with PBST and incubated overnight at 4 ºC with 1: 3000 primary antibodies in blocking solution. At the end of the incubation, the membrane was rinsed three times with PBST, and 1: 3000 secondary antibodies in blocking solution were added for 2 h at room temperature away from the light. Finally, the membrane was washed three times with PBST prior to the detection. The primary and secondary antibodies used in the study are listed in (**Table 2.27**).

Table 2.27 . Antibodies used in the study for the WB technique.

Antibody/ Catalogue #	Type	Species raised	Supplier
ANTI-FLAG® M2 / F3165-.2MG	Primary	Rabbit	Merck
Anti-V5 tag antibody [SV5-Pk1] / ab27671	Primary	Mouse	Abcam
Anti-alpha Tubulin antibody [DM1A] - Loading Control / ab7291	Primary	Mouse	
Goat Anti-Mouse IgG H&L (HRP) / ab205719	Secondary	Mouse	Abcam
Goat Anti-Rabbit IgG H&L (HRP) / ab6721	Secondary	Rabbit	Abcam

2.9.1.4. Chemiluminescent and Band Detection

Immediately after washing the membrane, 1 mL of detection reagent 1 and 1 mL of detection reagent 2 from Pierce™ ECL Western Blotting Substrate (Thermo Fisher Scientific) were mixed to prepare the enhanced chemiluminescence (ECL) substrate. The membrane was then subjected to imaging using the ChemiDoc Imaging System (Bio-Rad).

2.9.2. Development of an Immunofluorescence Assay for the Detection of Viral Antigens and Overexpressed Proteins.

For the immunofluorescence assay (IFA), cells were seeded into a 24-well plate containing 16 mm glass coverslips and infected with the desired viral MOI. At the end of the experiment, cells were washed with 500 µL of PBS and fixed for 1 h with 500 µL of 4% paraformaldehyde in PBS (pH 7.2). To permeabilize the cells, 500 µL of 0.1% Triton X-100 (Sigma) was added and incubated for 10 min. Cells were then washed three times with PBS prior to blocking. Blocking was performed by incubating the cells with 500 µL of 1% bovine serum albumin (BSA) in PBS (Sigma) for 1 h. After blocking, cells were rinsed with 500 µL of PBS, followed by the addition of 500 µL of primary antibody diluted 1:1000 in 0.5% BSA. The primary antibody was incubated overnight at 4 ºC. After that, the cells were washed with PBS three times to remove the non-specific binding of the antibody. Accordingly, 500 µL of 1: 2000 fluorescence-conjugated secondary antibody in 0.5% BSA was added to the cells. The secondary antibody was incubated at room temperature for 2 h in the dark, and the unbound antibodies were rinsed three times with 500 µL of PBS. The nuclear staining of the cells was performed using 300 µL of 1:10.000 4′,6-diamidino-2-phenylindole (DAPI) (Thermo-Fisher Scientific), and the stain was incubated for a further 15 min. At the end of the incubation time, the cells were washed once with 500 µL of PBS. Finally, the coverslips were mounted on glass slides using VECTASHIELD® (2BScientific) for visualisation on the fluorescence microscope. Antibodies used in the study are listed in (**Table 2.28**).

Table 2.28. Antibodies used in the study for the IFA.

Antibody/ Catalogue #	**Type**	**Species against**	**Supplier**
ANTI-FLAG® M2/ F3165-.2MG	Primary	Rabbit	Merck
Anti-V5 tag antibody [SV5-Pk1] / ab27671	Primary	Mouse	Abcam
SARS-CoV/SARS-CoV-2 Spike Protein S1 Chimeric Recombinant Mouse Monoclonal Antibody / MA551599	Primary	Mouse	Invitrogen
Goat anti-Rabbit IgG (H+L) Cross-Adsorbed Secondary Antibody, Alexa Fluor™ 488 / # A-11008	Secondary	Rabbit	Invitrogen
Goat anti-Mouse IgG (H+L) Cross-Adsorbed Secondary Antibody, Alexa Fluor™ 700 / # A-21036	Secondary	Mouse	Invitrogen

2.10. Live Cell Imaging

Unless specified for the immunofluorescence, all cell images produced in this study were obtained under live conditions. Live cell imaging was performed using a ZOE Fluorescent Cell Imager (Bio-Rad), an inverted digital imaging system equipped with a brightfield channel and three integrated fluorescence channels (blue, green, and red). Cells were imaged directly in standard tissue culture plates placed on the motorised stage, using the built-in 20× objective to visualise overall morphology, transfection efficiency, and signs of viral infection. Samples were observed, according to the experiment, in brightfield, blue, green, and red fluorescence channels. Once representative fields of view were identified, images were acquired in live mode and saved using the instrument’s onboard software as high-resolution digital files.

2.11. Cell-Based Viability Assay

In a 96-well plate, R06E-hACE2-EGFP, hACE2-TMPRSS2 and hACE2-EGFP-A549 were seeded. Cells were treated with different concentrations of DMSO, 10 µM Camostat mesylate (Abcam), and EST (Sigma-Aldrich). 24 h post-treatment, 10 µL of PrestoBlue™ cell viability reagent (Thermo Fisher Scientific) was added to the wells and incubated for 1 h at 37 ºC. Reading and assessment of the cell viability was performed using the Tecan Infinite M200 plate reader model according to the manufacturer's instructions, and cell viability was expressed as a percentage relative to untreated controls.

2.12. Statistical Analysis

For each experiment, three or four independent replicas were performed. Student's *t*-test, multiple *t*-test were used when two groups were involved for the comparison, while one-way or two-way ANOVA was used when comparing more than two groups with one or more variables involved. All tests were performed using the Graphpad Prism 10.5.0 Software, which was used to generate the resulting graphs and calculate the P values. The P values were computed and determined for each experiment as follows: ns ($P > 0.05$), * ($P \leq 0.05$), ** ($P \leq 0.01$), *** ($P \leq 0.001$), and **** ($P \leq 0.0001$).

Chapter 3. In-silico and Bioinformatic Analysis of m6A Machinery in the Egyptian Fruit Bat (*Rousettus aegyptiacus*), the Black Flying Fox (*Pteropus alecto*), and *Homo sapiens*: a Bat–Human Comparative Insight

3.1. Introduction

The central dogma of life describes the fundamental process by which genetic information is transferred from DNA to a protein via RNA [296]. However, gene expression is a complex process that involves both canonical and non-canonical modifications in DNA and RNA. While epigenetics involves modifications to DNA, RNA modifications are called epi-transcriptomics [297]. m6A is the most abundant, most distributed epi-transcriptomics modification that is present widely across different classes of prokaryotic and eukaryotic RNAs, shaping their cellular metabolism [298,299]. Moreover, because it regulates the immune response, m6A is utilised by various RNA and DNA viruses to evade the host's innate immunity [214,300].

m6A machinery is a group of at least ten proteins that are responsible for processing every step of the modification. Writers (METTL3, METTL14, and WTAP) add the methyl group to the RNA, while erasers (ALKBH5 and FTO) remove it. The recognition of the modification on RNA is carried out by readers, which involve many proteins, among which those of the YTH family (YTHDF1–3 and YTHDC1–2) are the most important [301].

Over the past few years, the emergence of the bioinformatics field has propelled significant steps in protein research. Recently, tools and databases have been widely implicated to annotate, predict and identify protein structures and functions [302,303]. While this enabled researchers to explore the m6A machinery across different organisms [304–307], no similar approach has been applied in bats, despite their critical role as reservoirs of many viruses that infect humans.

R. aegyptiacus and *P. alecto* are important reservoirs of zoonotic members of paramyxoviruses, including Sosuga, NiV, and HeV, which are associated with severe febrile illnesses in humans [12,38,308,309]. In Australia, *P. alecto* was implicated in the transmission of henipaviruses, NiV, HeV and CedPV [14,310,311], while in Africa, several henipa-like viruses have been isolated from *R. aegyptiacus* [181,312], highlighting *R. aegyptiacus* as a potential reservoir for henipaviruses, including CedPV.

Genomic annotation is available for *R. aegyptiacus* and *P. alecto*; however, characterisation of their m6A machinery remains limited in relation to that of the well-characterised human counterpart.

In this study, a hypothesis was made that the sequence identity and structural similarity of m6A machinery in *R. aegyptiacus*, *P. alecto*, and *H. sapiens* could provide a comparative framework for understanding the biology of CedV replication among any of the three species. Thus, this work aimed to test this hypothesis via the establishment of a comprehensive comparative in silico and bioinformatics analysis of the m6A machinery in *R. aegyptiacus*, *P. alecto*, and *H. sapiens*.

3.2. Specific Objectives

3.2.1. Amino acid sequence retrieval of m6A writers, easers, and readers of different mammalian and non-mammalian orthologues, including bats, ungulates, canines, felines, primates, fishes, reptiles and amphibians.

3.2.2. Identification of the amino acid identity of the m6A proteins of *R. aegyptiacus, P. alecto,* and *H. sapiens* among different orthologues.

3.2.3. Genomic alignment and genetic synteny identification of the m6A machinery among *R. aegyptiacus, P. alecto,* and *H. sapiens.*

3.2.4. Three-dimensional (3D) structural prediction of the bat's m6A machinery and PDB recovery of the corresponding machinery in the *H. sapiens.*

3.2.5. m6A proteins alignment and 3D structural comparison among *R. aegyptiacus, P. alecto,* and *H. sapiens.*

3.3. Results

3.3.1. m6A-Associated Proteins of *Rousettus aegyptiacus* Exhibit Comparable Amino Acid Identity to those of the *Pteropus alecto*, *Mammals* and *Homo sapiens*.

To gain further insight into the degree of identity of the m6A machinery of *R. aegyptiacus* and those of *H. sapiens* and *P. alecto,* a comparative analysis of the amino acid sequences across species was conducted. To this end, the amino acid identities of the ten-core regulators were calculated and compared using the taxonomically diverse panel of mammalian and non-mammalian species. Species included in the comparative analyses were selected from various mammalian classes, including Mammalia (Carnivora: canids and felids; Perissodactyla: equids; Artiodactyla: ungulates; Rodentia: rodents; Primates: non-human primates; Chiroptera: bats), and various non-mammalian classes, including Aves, Reptilia, Amphibia, and Actinopterygii.

Amino acid identity percentages for *R. aegyptiacus* revealed a high degree of identity with those of *P. alecto* across the ten m6A machinery components (96.7%–100%), except for FTO, which showed 79.8% identity between the two chiropterans. Additionally, the identity of two bat m6A was higher and more related to those of mammals. In the METTL3 and YTHDF2, for example, the percentage identity was 100% in both bats when compared to certain mammalian orthologues (**Figure 3.1A** and **Figure 3.3B**). In contrast, the FTO demethylase showed the lowest identity matrix among ten regulators in both bats, with percentages of 72.8% and 74.1% in *R. aegyptiacus* and *P. alecto,* respectively (**Figure 3.2A**). Identity in the YTHDF1 was the second lowest among the m6A regulators, with values of 83.1% and 82.7% in *R. aegyptiacus* and *P. alecto,* respectively (**Figure 3.3A**). The remaining m6A regulators of both bats exhibited high conservation with their mammalian counterparts, where the amino acid identities ranged from 86.1% to 99.6% in *R. aegyptiacus* and from 94.4% to 100% in *P. alecto* (**Figure 3.1–3.4**).

With regards to *R. aegyptiacus*, *P. alecto* and *H. sapiens*, the identity matrices revealed a high degree of sequence conservation between the m6A-associated proteins of the two bat species and their human orthologues. Among the ten machinery, YTHDF2 stood out as the most conserved protein between bats and humans, with

99.3% identity across both bat species (**Figure 3.3B**). In contrast, FTO and YTHDF1 remained the least conserved in the comparison, demonstrating 76.1% and 83.6% in *R. aegyptiacus* and 83.4 % and 84 % in *P. alecto,* respectively (**Figure 3.2A** and **Figure 3.3A**). Other regulators exhibited identities ranging from 94.6% to 98.9% in *R. aegyptiacus* and 95.6% to 98.6% in *P. alecto* (**Figure 3.1–3.4**).

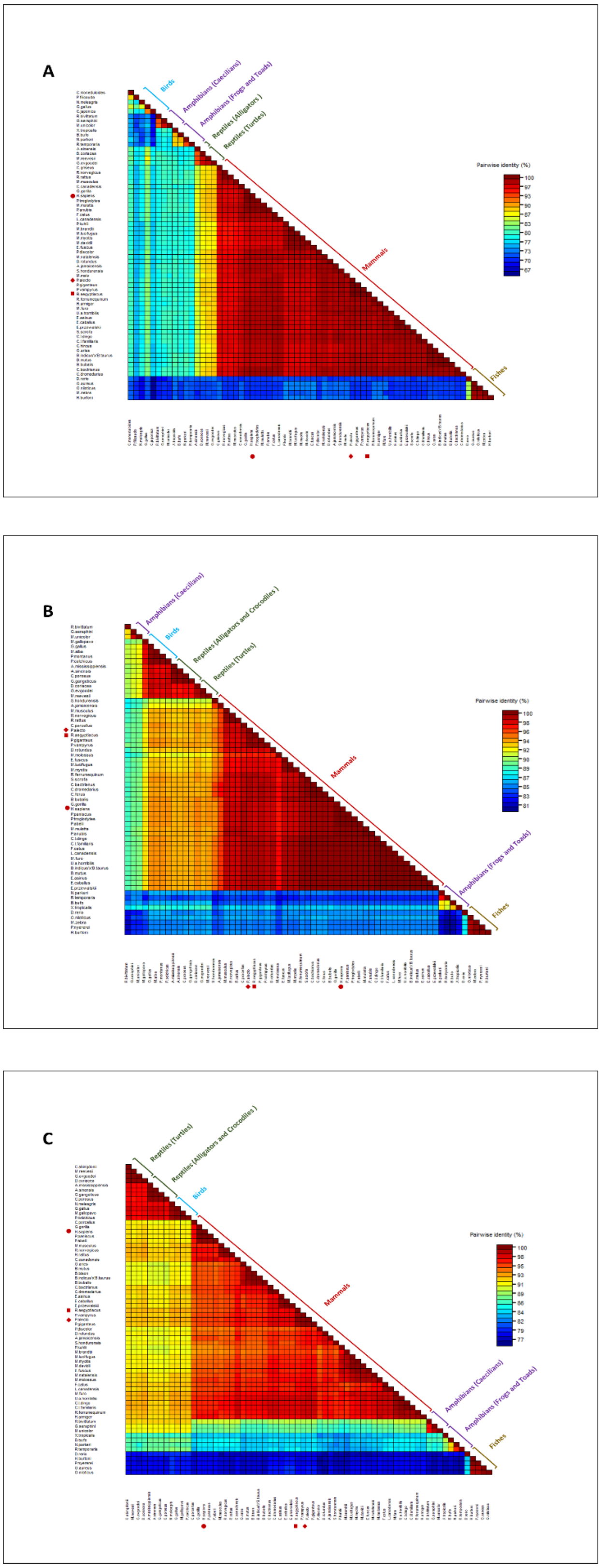

Figure 3.1. Identity matrices of m6A writer complex orthologues. (A) Matrix identity of the METTL3 orthologues showing the highest identity of R. aegyptiacus and P. alecto to those of other mammalian orthologues. (B) Matrix identity of the METTL14 orthologues. (C) Matrix identity of the WTAP orthologues. m6A-related proteins of R. aegyptiacus, P. alecto and H. sapiens are marked with solid red cube, diamond, and circle shapes, respectively. Figure adapted from [313] with modification applied to the imported figure.

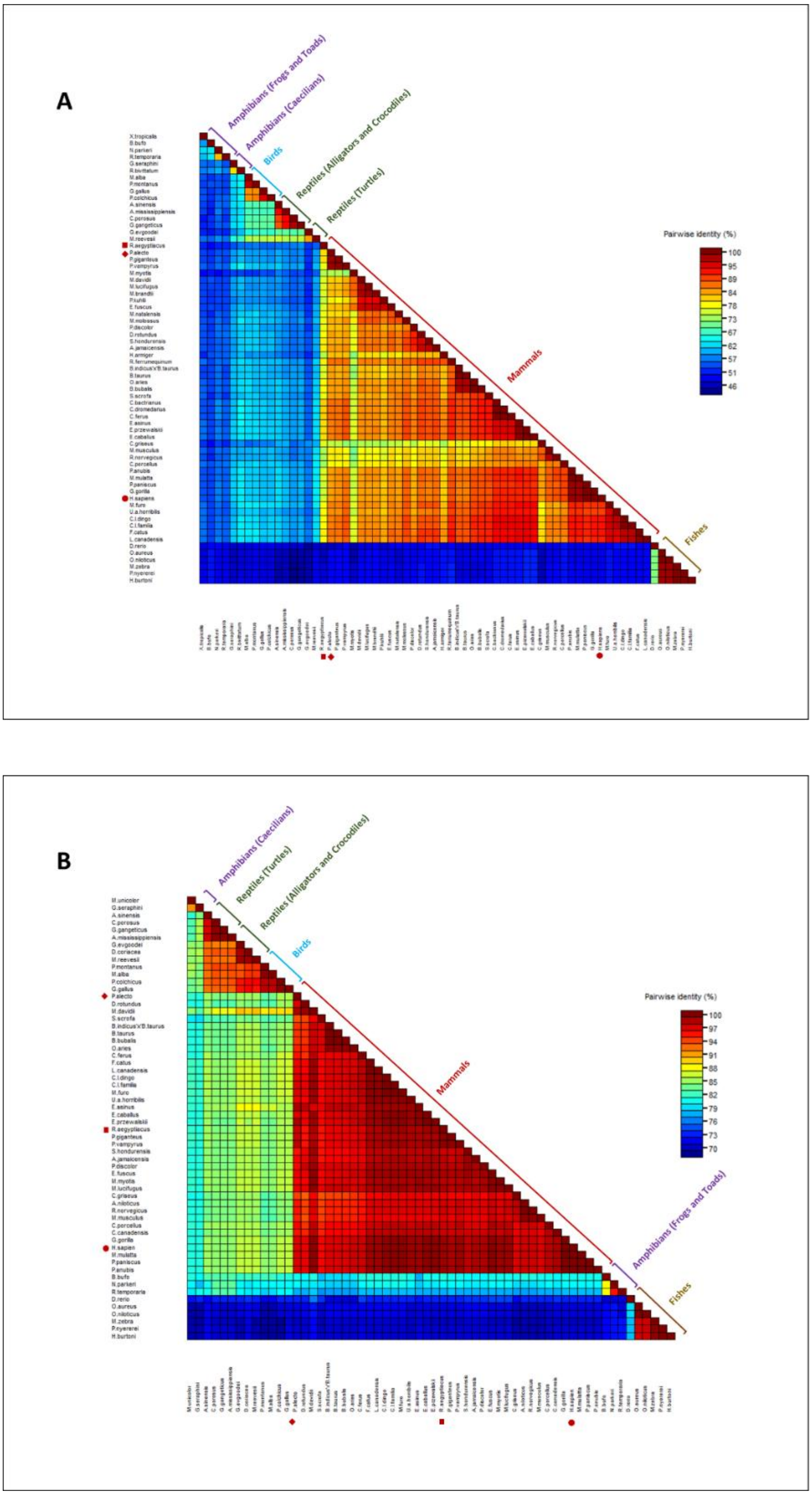

Figure 3.2. Identity matrices of m6A erasers orthologues. (A) Matrix identity of the FTO orthologues showing the lowest identity of R. aegyptiacus and P. alecto to those of H. sapiens and other mammalian orthologues. (B) Matrix identity of the ALKBH5 orthologues. m6A-related proteins of R. aegyptiacus, P. alecto and H. sapiens are marked with solid red cube, diamond, and circle shapes, respectively. Figure adapted from [313] with modification applied to the imported figure.

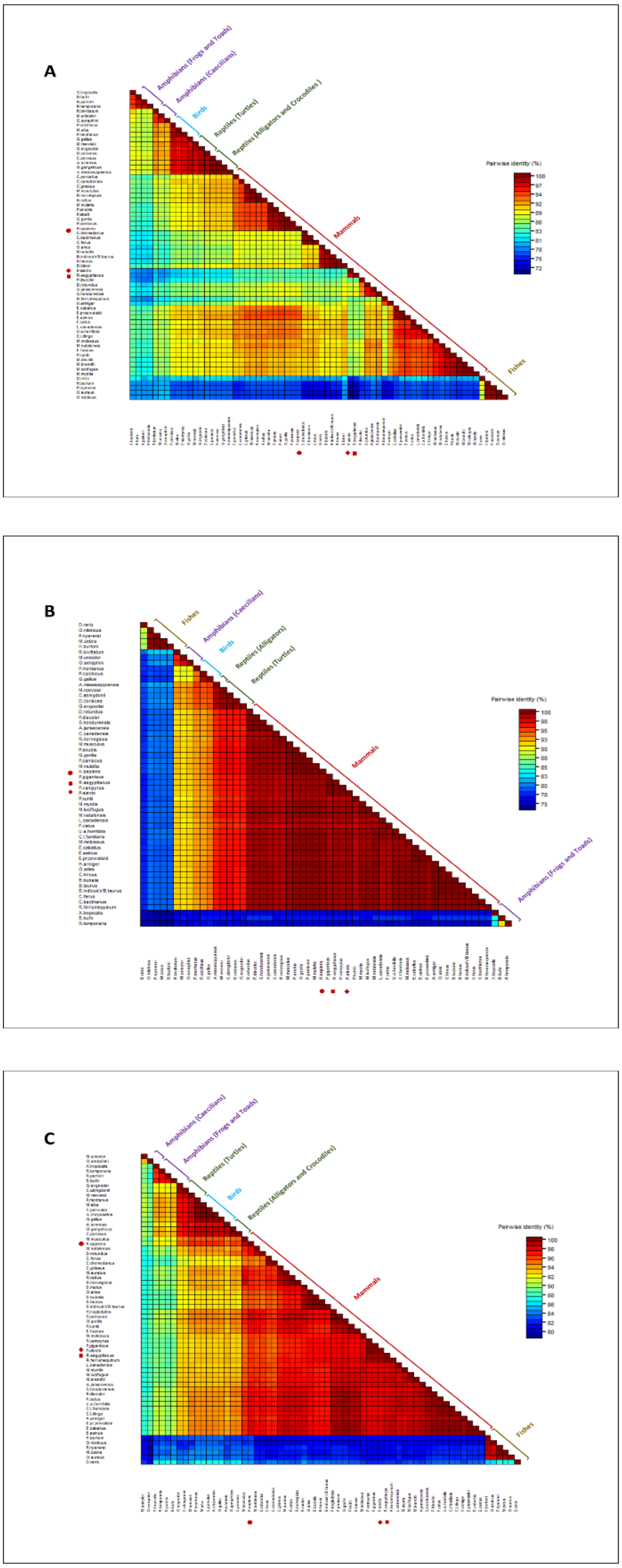

Figure 3.3. Identity matrices of m6A YTHDF readers orthologues. (A) Matrix identity of the YTHDF1 orthologues showing the second lowest identity of R. aegyptiacus and P. alecto to those of H. sapiens and other mammalian orthologues. (B) Matrix identity of the YTHDF2 orthologues shows the highest identity of R. aegyptiacus and P. alecto to those of H. sapiens and other mammalian orthologues. (C) Matrix identity of the WTAP orthologues. m6A-related proteins of R. aegyptiacus, P. alecto and H. sapiens are marked with solid red cube, diamond, and circle shapes, respectively. Figure adapted from [313] with modification applied to the imported figure.

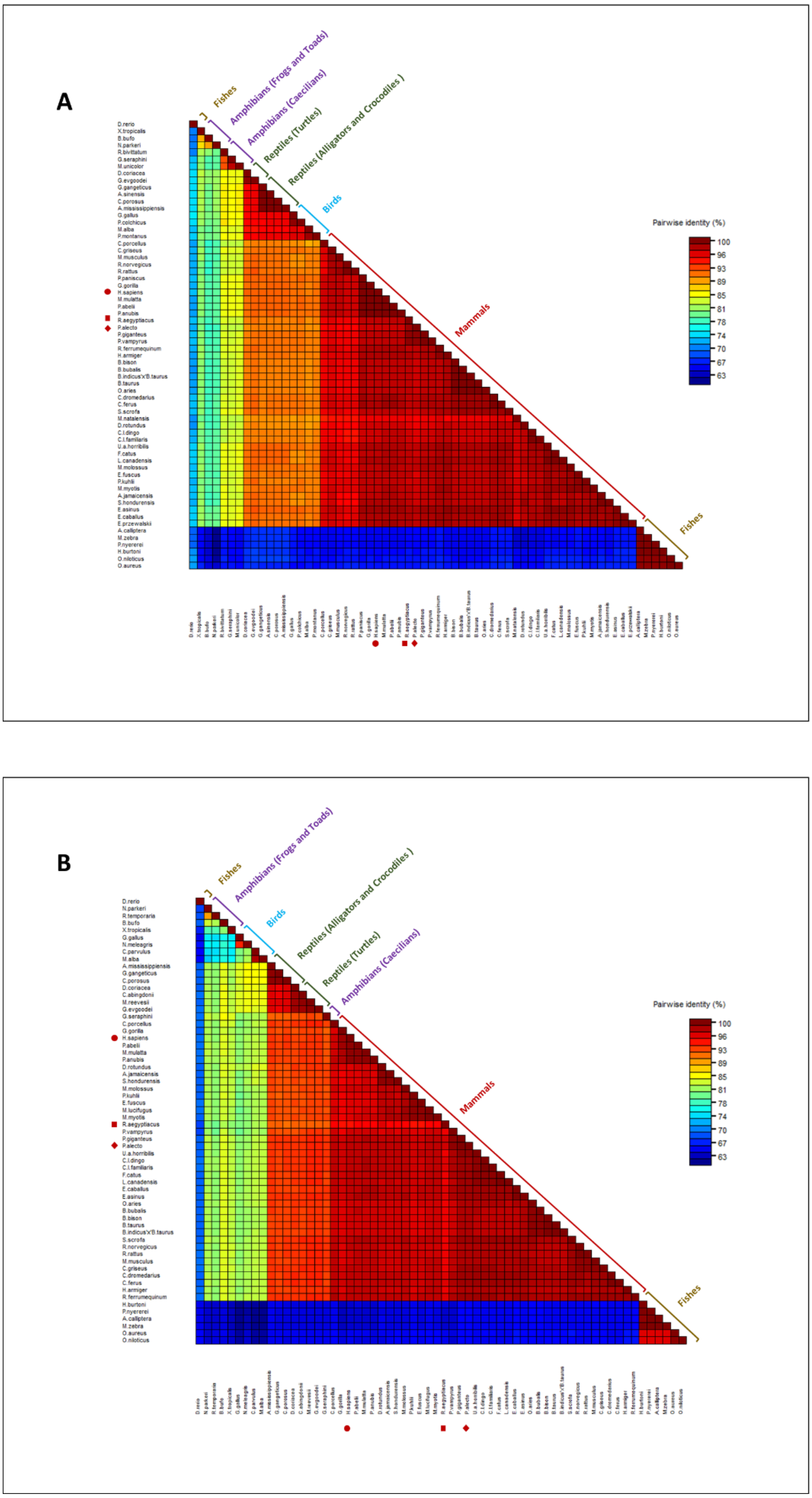

Figure 3.4. Identity matrices of m6A YTHDC readers orthologues. (A) Matrix identity of the YTHDC1 orthologues. (B) Matrix identity of the YTHDC2 orthologues. m6A-related proteins of R. aegyptiacus, P. alecto and H. sapiens are marked with solid red cube, diamond, and circle shapes, respectively. Figure adapted from [313] with modification applied to the imported figure.

3.3.3. Genomic Complexity Versus Syntenic Conservation of m6A Genes in *Rousettus aegyptiacus*, *Pteropus alecto*, and *Homo sapiens*

To gain preliminary insights into the functionality and genetic relationship of the m6A-associated proteins of *R. aegyptiacus* to those of *H. sapiens* and *P. alecto,* whole-genomic and genetic synteny comparisons were performed. For the genomic comparison, the genomes of the three mammalian species were downloaded from NCBI and aligned using the MCScanX algorithm in TBtools, while for genetic synteny, the m6A genes of the three species were identified, along with 6 flanking genes, using NCBI GDV. In humans, the m6A genes were located on a wide variety of somatic chromosomes, including chromosomes numbers 1, 4, 5, 6, 8, 14, 16, 17 and 20. Notably, the fourth chromosome carried two m6A-related genes, METT14 and YTHDC1. In bats, on the other hand, the m6A genes were distributed across various unplaced scaffolds, mainly due to partially annotated genomes (**Figure 3.5**). This method did not allow for predicting the functional roles of m6A regulatory genes in *R. aegyptiacus* with respect to *P. alecto* and *H. sapiens*. As an alternative approach, genetic synteny was assessed using three genes upstream and downstream of the m6A genes in the three species.

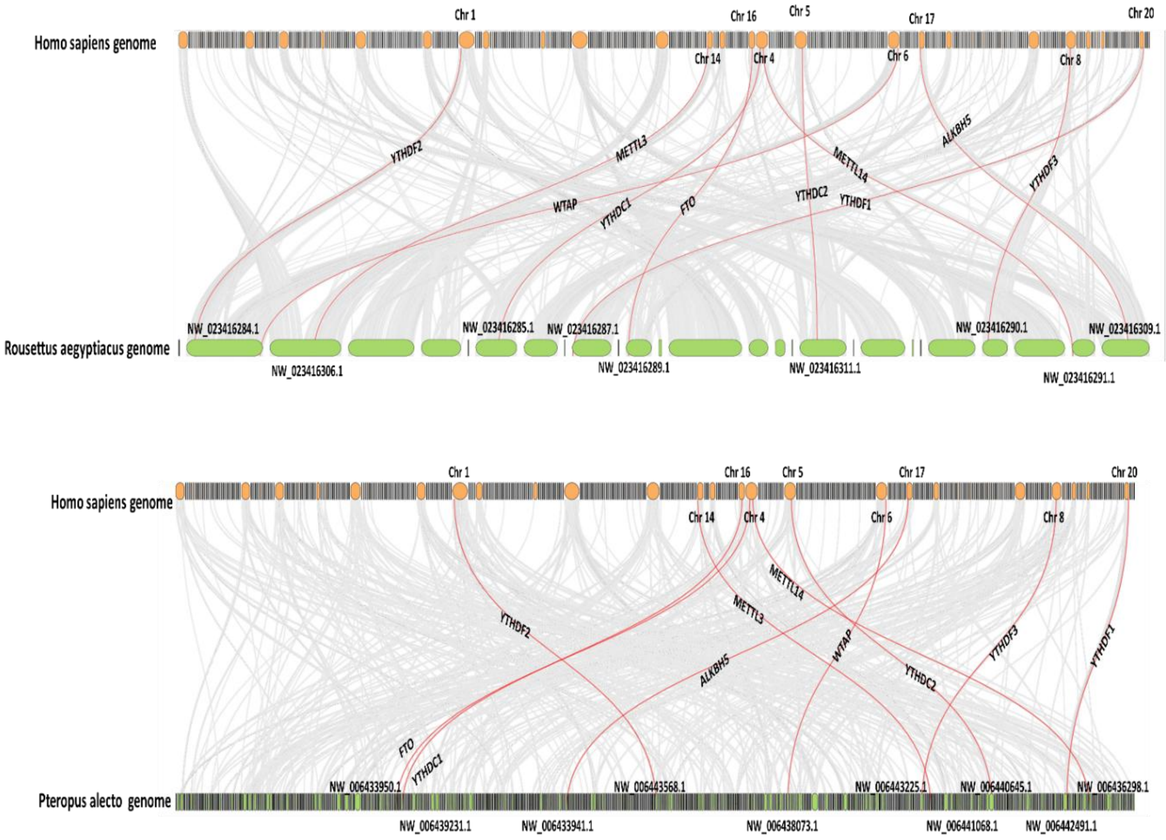

Figure 3.5. Comparative genomics of R. aegyptiacus, P. alecto and H. sapiens showing the location of m6A genes on each genome. (A) Genome alignment of H. sapiens and R. aegyptiacus. (B) Genome alignment of H. sapiens and P. alecto. The location of each m6A gene is shown on the corresponding genome of each of the three mammalian species and highlighted in red. Figure adapted from [313] with modification applied to the imported figure.

Overall, the gene synteny analysis across the ten m6A loci revealed a conservation of several genes shared among *R. aegyptiacus*, *P. alecto*, and *H. sapiens*. The loci of the bats' m6A writers had several encoding genes similar to those in human loci. The *METTL3* loci had TOX high mobility group box family member 4 (*TOX4*) and spalt-like transcription factor 2 (*SALL2*) genes (**Figure 3.6A**). Expressions of the three genes changed in human acute lymphocytic leukaemia [314], which suggests a link between *METTL3*, *TOX*, and *SALL2* in humans and, accordingly, the two bats.

The *METTL14* locus in *H. sapiens* was noted to carry synaptopodin 2 (*SYNPO2*), where a mutation forming a loop between the first intron of *SYNPO2* and the *METTL14* promoter has been associated with increased susceptibility to ovarian cancer in humans. These genes were also found in the *METTL4 R. aegyptiacus* and *P. alecto* loci [315] (**Figure 3.6B**).

On the *WTAP* loci, Superoxide dismutase 2, mitochondrial *(SOD2*) was shared among the three mammals (**Figure 3.6C**). In humans, a single mutation in *SOD2* was found to upregulate *WTAP* expression, a change that has been linked to the preservation of tissue integrity in bladder cancer patients [316].

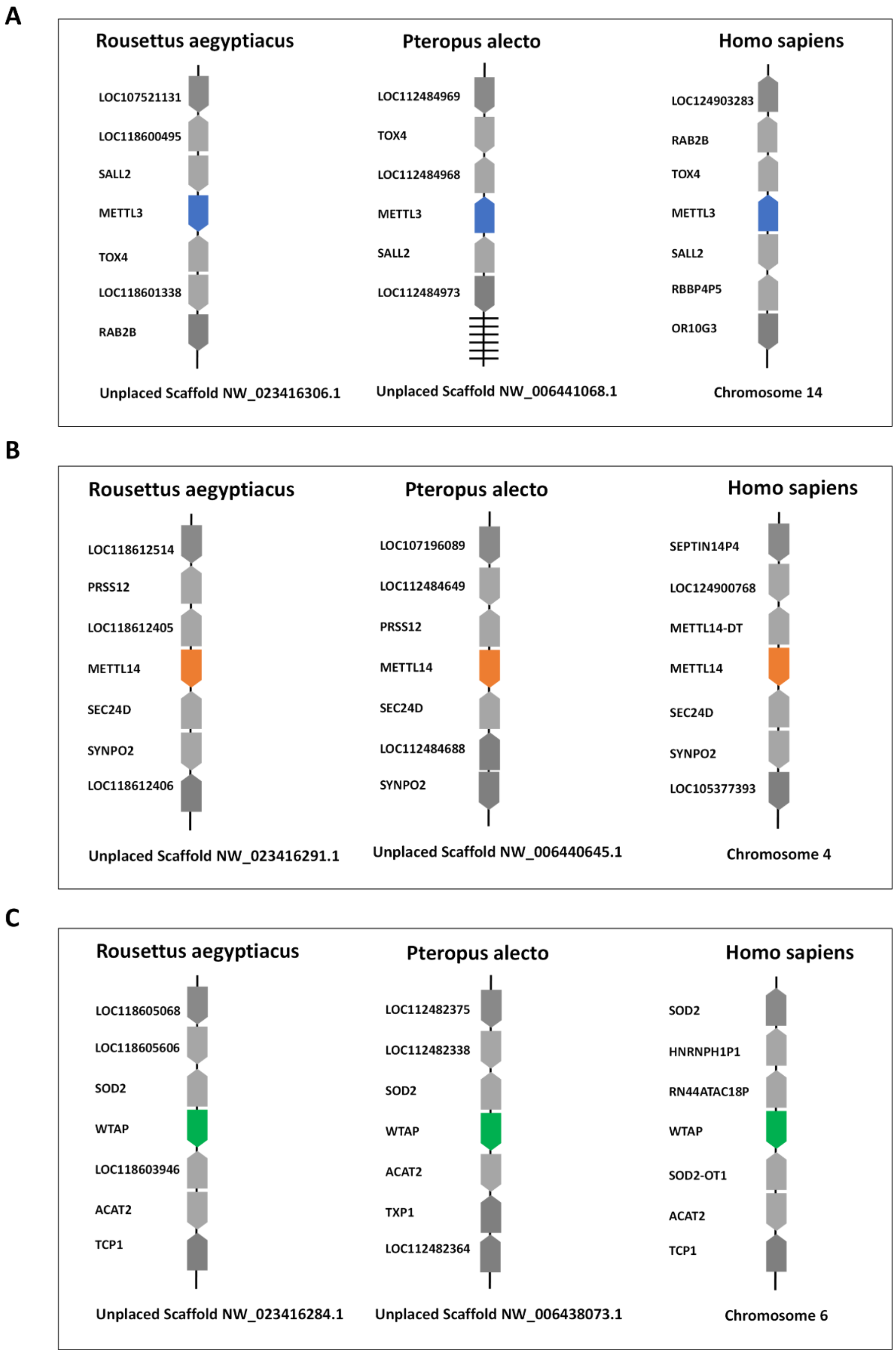

Figure 3.6. Genetic synteny of m6A writer complex loci in R. aegyptiacus, P. alecto, and H. sapiens, showing conserved genes among the three species. (A) Genetic synteny of METTL13 loci. (B) Genetic synteny of METTL14 loci. (C) Genetic synteny of WTAP loci. Figure adapted from [313] with modification applied to the imported figure.

Similarly, in the m6A eraser's loci, two genes were shared between the human and bat *FTO*s, RPGR interacting protein 1 like (*RPGRIR1L*) and iroquois homeobox 3 (*IRX3*). Although the human *IRX3* was found to be located further from *FTO* than it was in bats (data not shown), both *RPGRIR1L* and *IRX3* were upregulated in humans by *FTO* [317], which contributed to lean mass deposition (**Figure 3.7A**).

In the *ALKBH5* loci, *LLGL* Scribble cell polarity complex component 1 (*LLGL1*) and mitochondrial elongation factor 2 (*MIEF2*) were allocated among *R. aegyptiacus*, *P. alecto*, and *H. sapiens* loci, where the upregulation of the *LLGL1* gene in human xenograft tumours was linked to the *ALKBH5* [318]. Similarly, *ALKBH5* and *MIEF2* were upregulated together in the T regulatory cells of metastatic melanoma in humans [319] (**Figure 3.7B**).

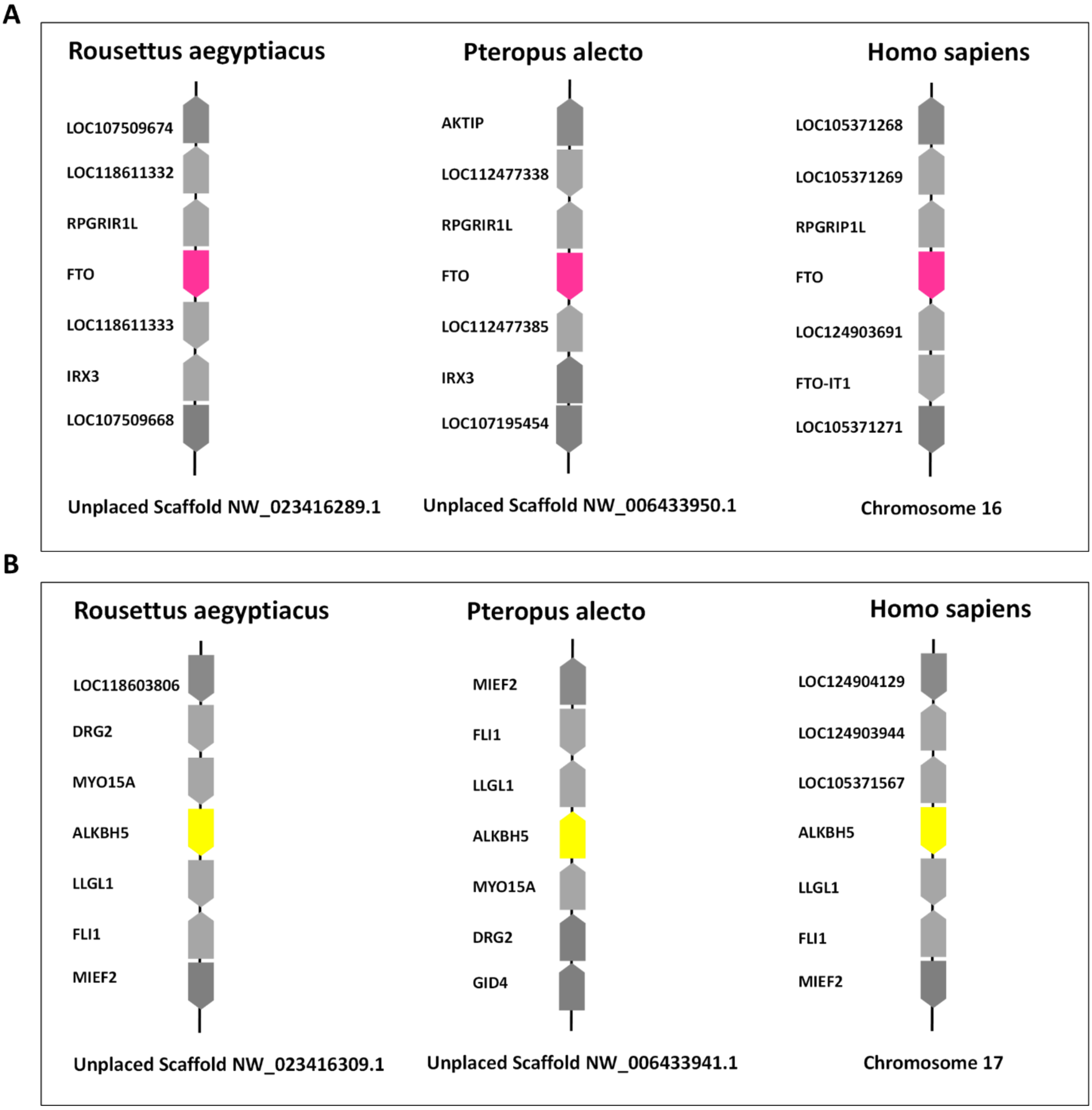

Figure 3.7. Genetic synteny of m6A eraser complex loci in R. aegyptiacus, P. alecto, and H. sapiens, showing conserved genes among the three species. (A) Genetic synteny of FTO loci. (B) Genetic synteny of ALKBH5 loci. Figure adapted from [313] with modification applied to the imported figure.

Genetic synteny of the *YTHDF* readers loci revealed several conserved genes between humans and the two Chiroptera species. In *H. sapiens*, the *YTHDF1* locus carried baculoviral IAP repeat containing 7 (*BIRC7*) and sodium/potassium transporting ATPase interacting 4 (*NK4IN4*); such genes were also found in *YTHDF1* loci of *R. aegyptiacus* and *P. alecto*. In humans, mutations in *YTHDF1* have been associated with reduced expression of *BIRC7* and *NK4IN4* in hepatoblastoma [320] (**Figure 3.8A**).

The *YTHDF2* loci in all three species carried glucocorticoid modulatory element binding protein 1 (*GMEB1*). A duplication event involving both *GMEB1* and *YTHDF2* has been reported in cases of human megalocephaly [321], suggesting their potential involvement in the aetiology of this condition (**Figure 3.8B**).

The *YTHDF3* loci in both humans and bats contained the α-tocopherol transfer protein (*TTPA*) gene (**Figure 3.8C**); however, no direct functional link between *YTHDF3* and *TTPA* has been identified in humans to date.

No syntenic overlap was observed between the human and bats at the *YTHDC1* and *YTHDC2* loci (**Figure 3.9**). Notably, the locations of syntenic genes at the m6A loci differed between *H. sapiens* and the two bat species (*R. aegyptiacus* and *P. alecto*), as well as between the two bats themselves.

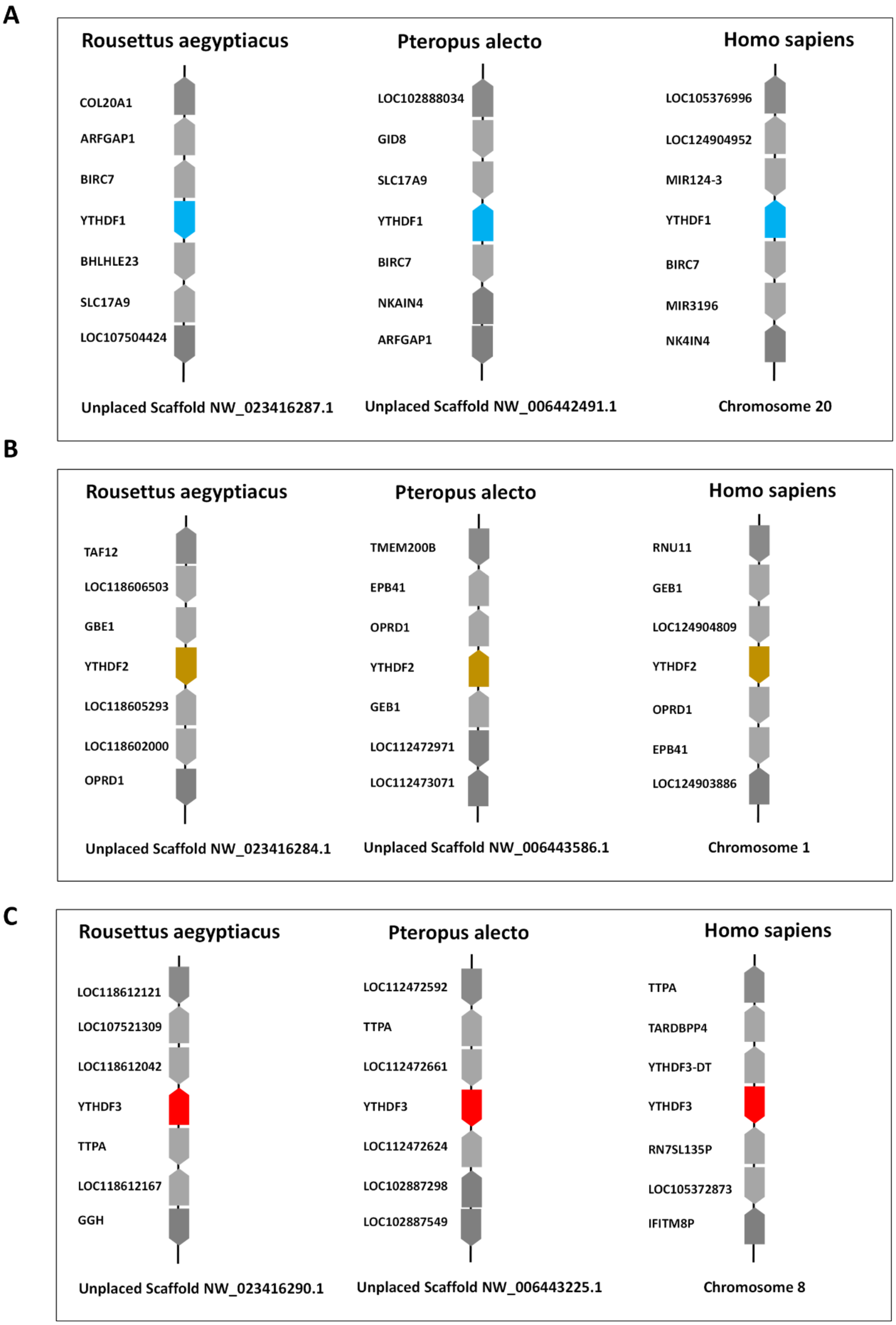

Figure 3.8. Genetic synteny of YTHDF readers in R. aegyptiacus, P. alecto, and H. sapiens, showing conserved genes among the three species. (A) Genetic synteny of YTHDF1 loci. (B) Genetic synteny of YTHDF2 loci. (C) Genetic synteny of YTHDF3 loci. Figure adapted from [313] with modification applied to the imported figure.

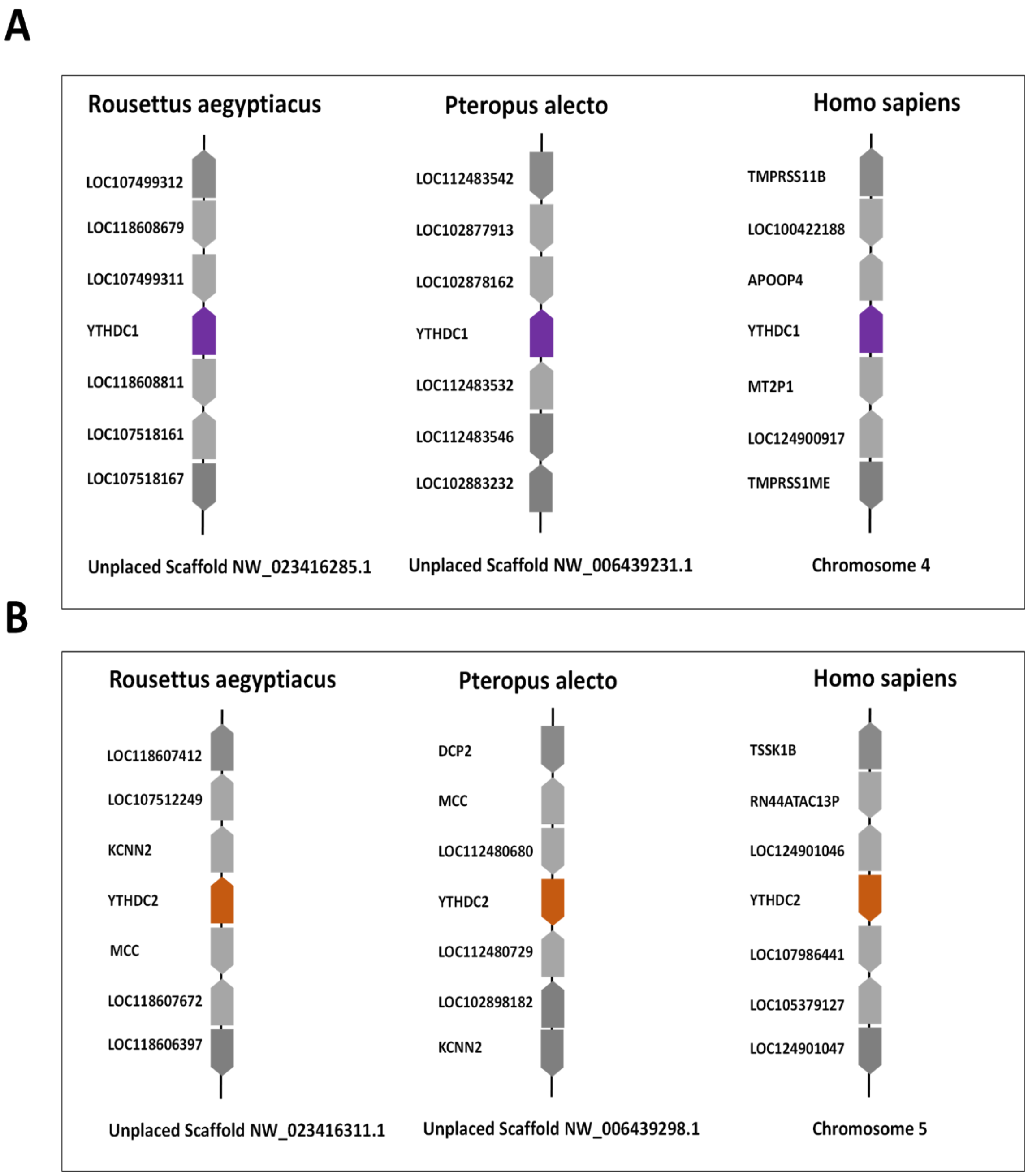

Figure 3.9. Genetic synteny of YTHDC readers in R. aegyptiacus, P. alecto, and H. sapiens, showing the absence of syntenic genes between humans and bats. (A) Genetic synteny of YTHDC1 loci. (B) Genetic synteny of YTHDC2 loci. Figure adapted from [313] with modification applied to the imported figure.

3.3.4. Structural Analysis of m6A Proteins in *Rousettus aegyptiacus*, *Pteropus alecto*, and *Homo sapiens* Reveals Conservation with their Writer orthologues, but not with Erasers or Readers

Next, the potential role of the *R. aegyptiacus* m6A machinery in m6A processing was predicted by comparing their 3D protein structures with those of *P. alecto* and the well-characterised human orthologues. With this objective in mind, the total of 10 m6A-related proteins in *H. sapiens* were retrieved from the PDB, their counterparts in *R. aegyptiacus* and *P. alecto* were predicted, and the structural similarity among the three species was examined. Additionally, the corresponding protein sequences were aligned using the ClustalW algorithm to identify functional domains and assess amino acid similarity across species.

METTL3 is the main catalytic unit responsible for adding a methyl group to the target RNA via its MTD [238,239]. Studies of the human METTL3 have revealed that the MTD (residues 369 and 570) contains three key functional loops involved in m6A methylation: gate loop 1 (residues 396–410), gate loop 2 (residues 507–515) and an interface loop (residues 462–479). Gate loops 1 and 2 recognise the adenosine of the SAM molecule, while the interface loop facilitates the interaction between METTL3 and METTL14 to form a heterodimer [239]. Another essential region of METTL3 is its ZFD, which recognises the m6A consensus RRACH motif on RNA. The domain consists mainly of two zinc fingers, ZFD1 (residues 259–298) and ZFD2 (residues 299–336); however, the RRACH motif recognition occurs via the hydrophobic residues Ser 315, Phe 316, Cys 320, Phe 321, and His 322 within the ZFD2 domain [237].

The METTL3 protein alignment showed identical amino acid sequences across *R. aegyptiacus*, *P. alecto* and *H. sapiens.* This identity was observed throughout the three functional loops and the entire MTD. Additionally, ZFDs *(*ZFD1 and ZFD2), including the critical restudies identifying the RRACH motif, were conserved among all three species (**Figure 3.10A**). Similarly, the aforementioned structures were conserved across the three species in the three-dimensional structural comparisons (**Figure 3.10B–G**).

METTL14 is the second component of the m6A writer complex that enhances the catalytic activity of METTL3 [238,239]. Structural studies of the METTL14 revealed that the MTD of the protein (residues 117–402) contained a long N-terminal extension (residues 116–165) to mediate the METTL14-METTL3 heterodimer interaction [239]. These structures did not change among *H. sapiens*, *P. alecto*, and *R. aegyptiacus*, neither in the alignment nor in the structural analysis (**Figure 3.11**).

WTAP is the third accessory component of the m6A writer complex, which is responsible for the recruitment of the METTL3-METTL14 heterodimer to the nucleus [233]. Protein structural analysis of the WTAP in *H. sapiens* demonstrated that the WTAP is a dimeric protein with two four-helices and three linkers in each monomer. The third and fourth helices of the protein (residues 148–176) and (residues 177–249), respectively, contain Lys 155, 160, 192, 230 and Gly 170, which mediate the binding of the WTAP to the METTL3-METTL14 heterodimer [239]. Protein alignment of the WATP has revealed conservation in these residues among *R. aegyptiacus*, *P. alecto* and *H. sapiens*. Additionally, the entire protein N-terminus, except for one mutation, was conserved across the three species (**Figure 3.12A**). Likewise, the same region did not exhibit any significant difference in structure across the three mammals (**Figure 3.12B–D**).

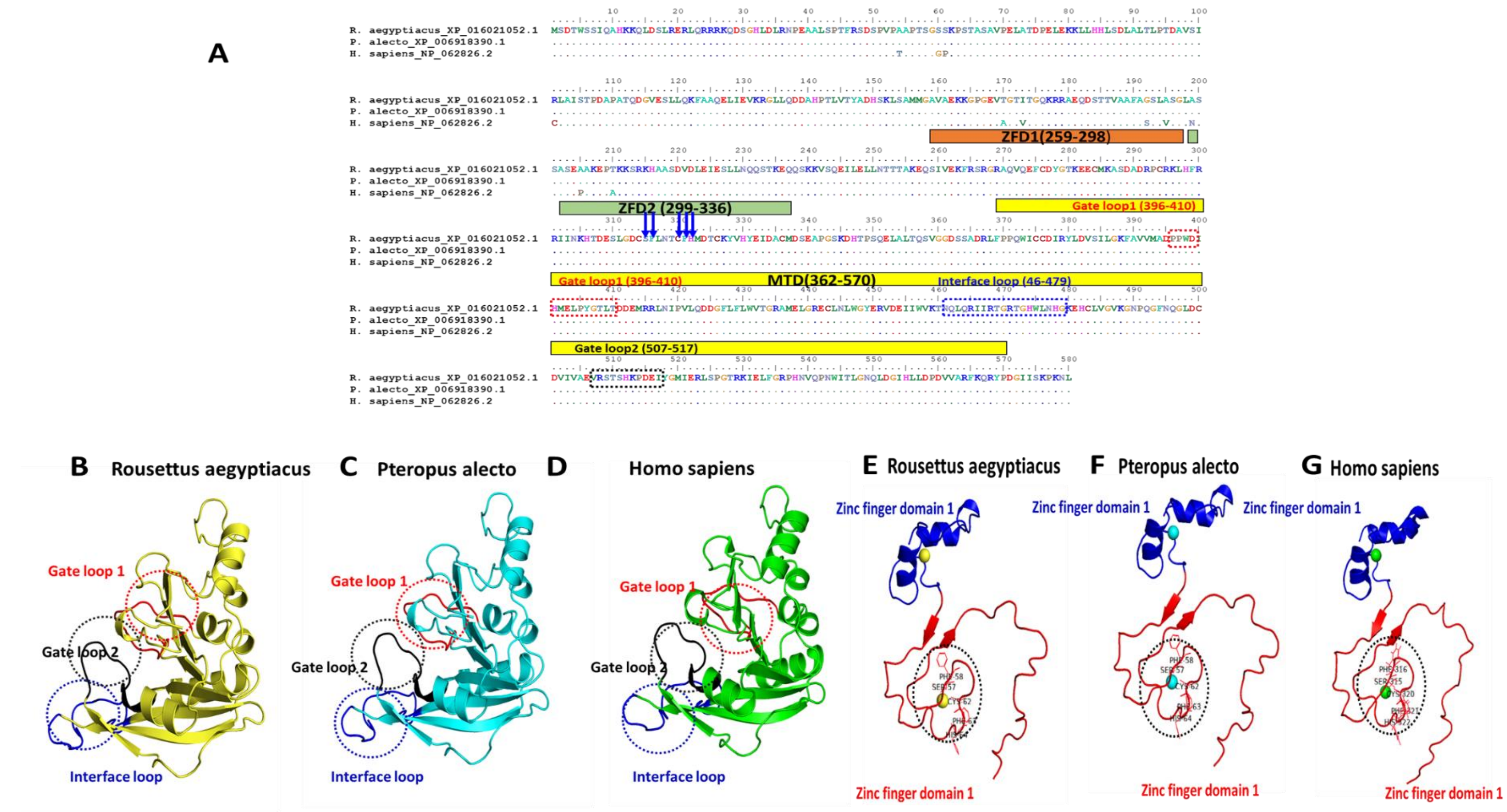

Figure 3.10. Amino acid alignment and protein structural analysis of R. aegyptiacus, P. alecto and H. sapiens METTL3. (A) Amino acid sequence alignment of METTL3 proteins of R. aegyptiacus, P. alecto and H. sapiens. Solid orange and olive-green rectangles, respectively, indicate the corresponding ZFD1 and ZFD2 sequences. Blue arrows indicate the conserved ZFD2 hydrophobic residues (Ser 315, Phe 316, Cys 320, Phe 321, and His 322). A solid yellow rectangle highlights the corresponding sequences of METTL3 MTD. Red, black, and blue dashed frames, respectively, highlight the amino acids of gate loop 1, gate loop 2, and interface loop. Three-dimensional structure comparison of METTL MTD among (B) R. aegyptiacus, (C) P. alecto, and (D) H. sapiens. The interface loop, gate loop 1, and gate loop 2 are indicated by dashed circles in red, black, and blue, respectively. Overall METTL3 ZFD structures among (E) R. aegyptiacus, (F) P. alecto, and (G) H. sapiens. The conserved hydrophobic residues are shown in line format and highlighted in black dashed circles. PDB IDs of MTD and ZFD of METTL3 are 5IL0 and 5ZOT, respectively. Figure adapted from [313] with modification applied to the imported figure.

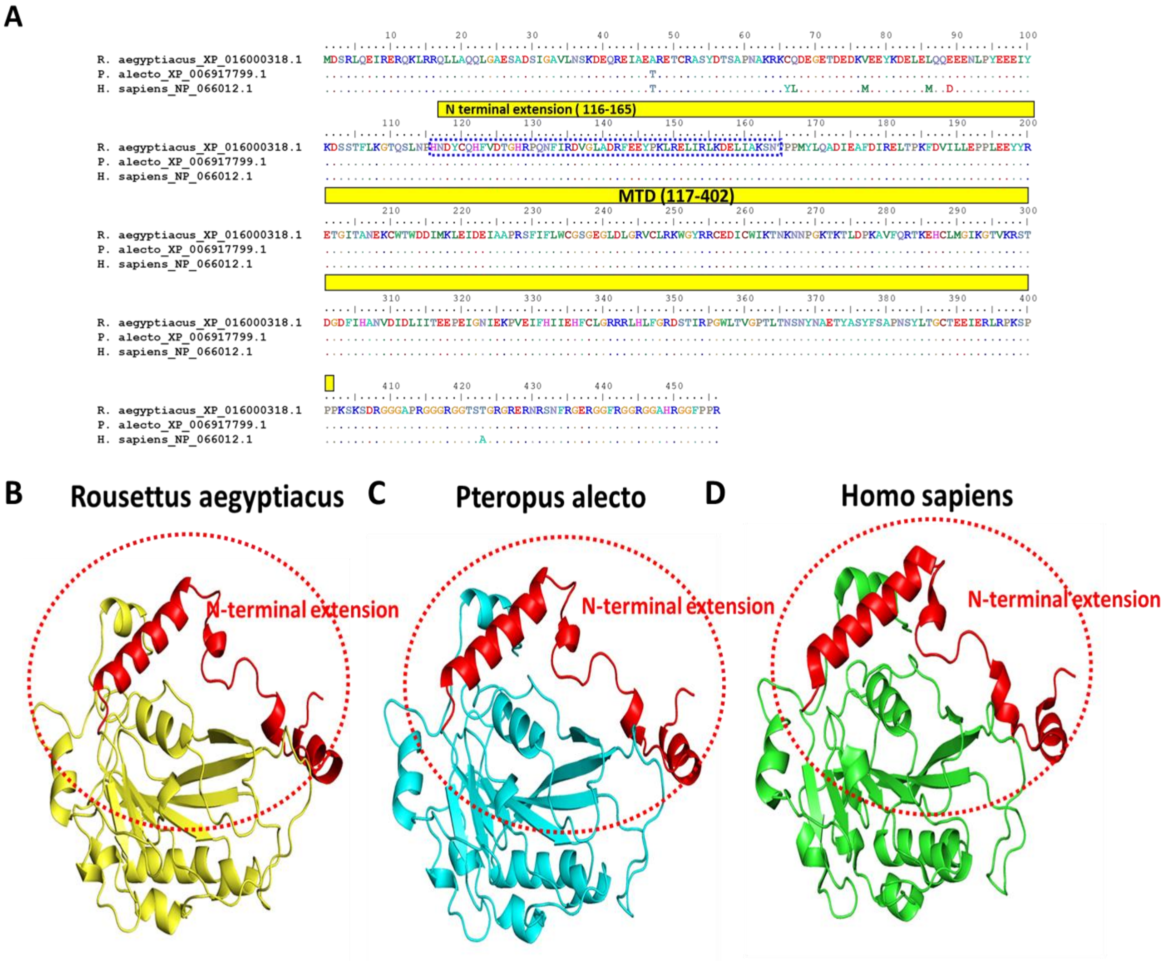

Figure 3.11. Amino acid alignment and protein structural analysis of R. aegyptiacus, P. alecto and H. sapiens METTL14. (A) Amino acid sequence alignment of METTL14 proteins of R. aegyptiacus, P. alecto and H. sapiens. A solid yellow rectangle highlights the corresponding sequences of METTL14, MTD, and the N-terminal extension. Three-dimensional structure comparison of METTL14 MTD among (B) R. aegyptiacus, (C) P. alecto, and (D) H. sapiens. Red dash circles highlight the N-terminal extension. PDB ID of the METTL14 MTD is 5k7u. Figure adapted from [313] with modification applied to the imported figure.

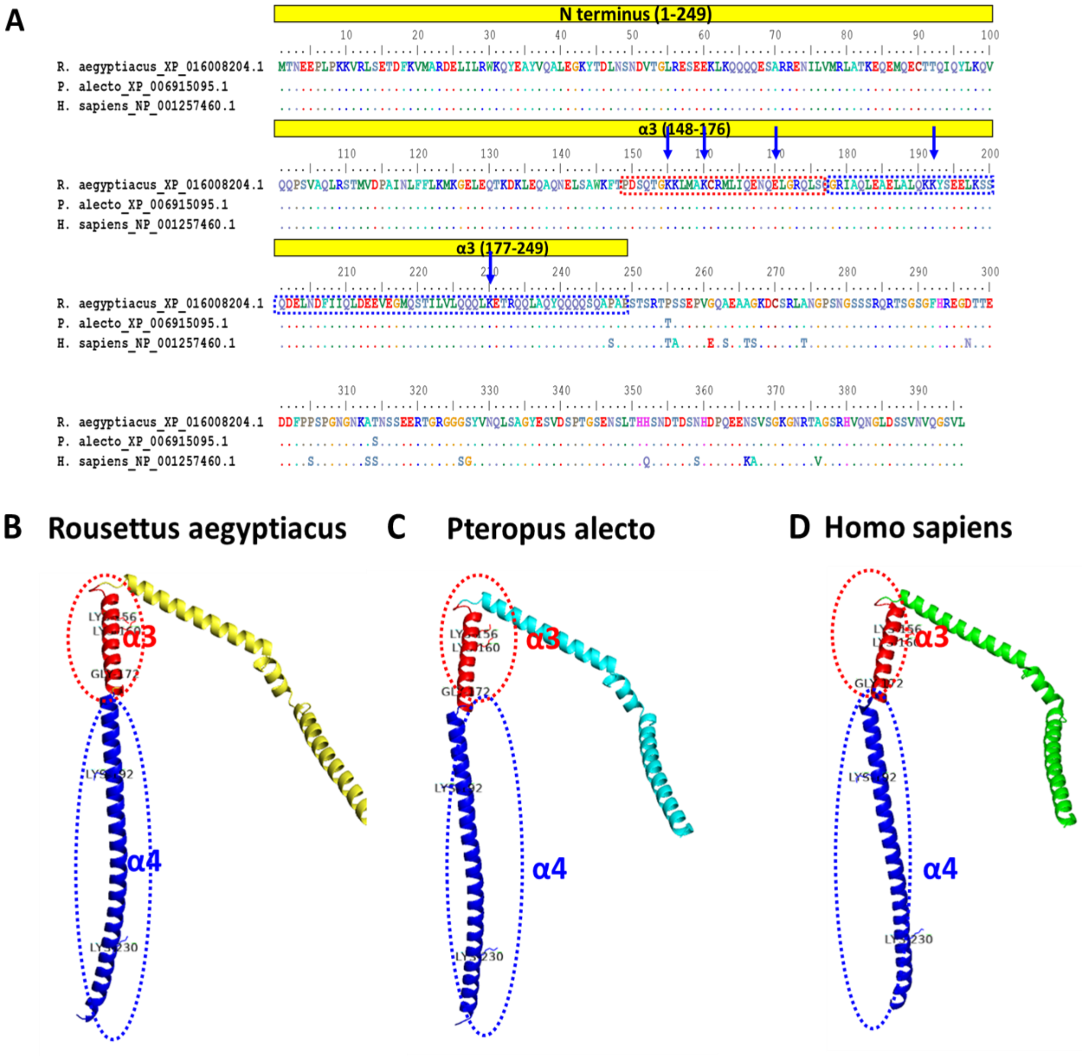

Figure 3.12. Amino acid alignment and protein structural analysis of R. aegyptiacus, P. alecto and H. sapiens WTAP. (A) WTAP amino acid sequence alignment among R. aegyptiacus, P. alecto and H. sapiens. A solid yellow rectangle highlights the corresponding sequences of the N-terminal of the WTAP. Red and blue dashed rectangles illustrate the sequences of the α3 and α4, respectively. Three-dimensional structure comparison of the WTAP N terminus among (B) R. aegyptiacus, (C) P. alecto, and (D) H. sapiens. The α3 and α4 are highlighted in red and blue dashed circles, respectively. PDB ID from which the N terminus of the WTAP was adapted is 7VF5. Figure adapted from [313] with modification applied to the imported figure.

FTO is an m6A eraser that mediates oxidative demethylation of the RNA via two functional domains, the NTD (residues 32–326) and the CTD (327–498). The NTD carries the protein catalytic motif (jelly roll motif), and the iron-binding coordinates, His 231, Asp 233 and His 307 and the Trp 230. While the CTD contributes to NTD stability. The nucleic acid selectivity of the FTO is facilitated via the L1 loop (residues 213–224), which binds to the jelly roll motifs via the iron binding residues [243].

Despite the numerous amino acid variations (insertion, deletion, substitutions) detected across *R. aegyptiacus*, *P. alecto* and *H. sapiens* FTOs, those which form the L1 loop and mediate the metal binding remained conserved across the species (**Figure 3.13A**). It is worth noting that the detected amino acid variants differed between *H. sapiens* and the two bat species, as well as between the two bat species themselves. Similarly, the structure comparison of the FTO revealed a distinctive configuration of the protein in each of the mammalian species; however, the protein integrity at the L1 loop region remained undisrupted (**Figure 3.13B–D**).

Crystal structure analysis of the ALKBH5 has shown the iron coordinates, His 204, Asp 206 and His 266, in the vicinity of the Alk domain (residues 74–294), forming the conserved H*X*(D/E) *XnH* motif. ALKBH5 nucleic acid selectivity and recognition are mediated via three regions in the protein referred to as Flip1, 2 and 3. Flip 1 (residues 117–129) and Flip 2 (residues 136–165) are primarily responsible for the nucleotide recognition, while Flip 3 maintains the selectivity of the protein against unmethylated double-stranded nucleic acids. Notably, the Flip 3 formed as a result of a disulfide bond between residues Cys 230 and Cys 267 [245]

Amino acid sequence alignment of the Alk domain was maintained, except for one, all residues in *R. aegyptiacus*, *P. alecto* and *H. sapiens* (**Figure 3.14A**). Additionally, structural integrity analysis of the domain across the three species has revealed conservation of the Flip1 and Flip2 regions; however, notable structural divergence was observed between the human and two bats within the region encompassing the metal-binding residues and the distinctive disulfide bond (**Figure 3.14B–G**).

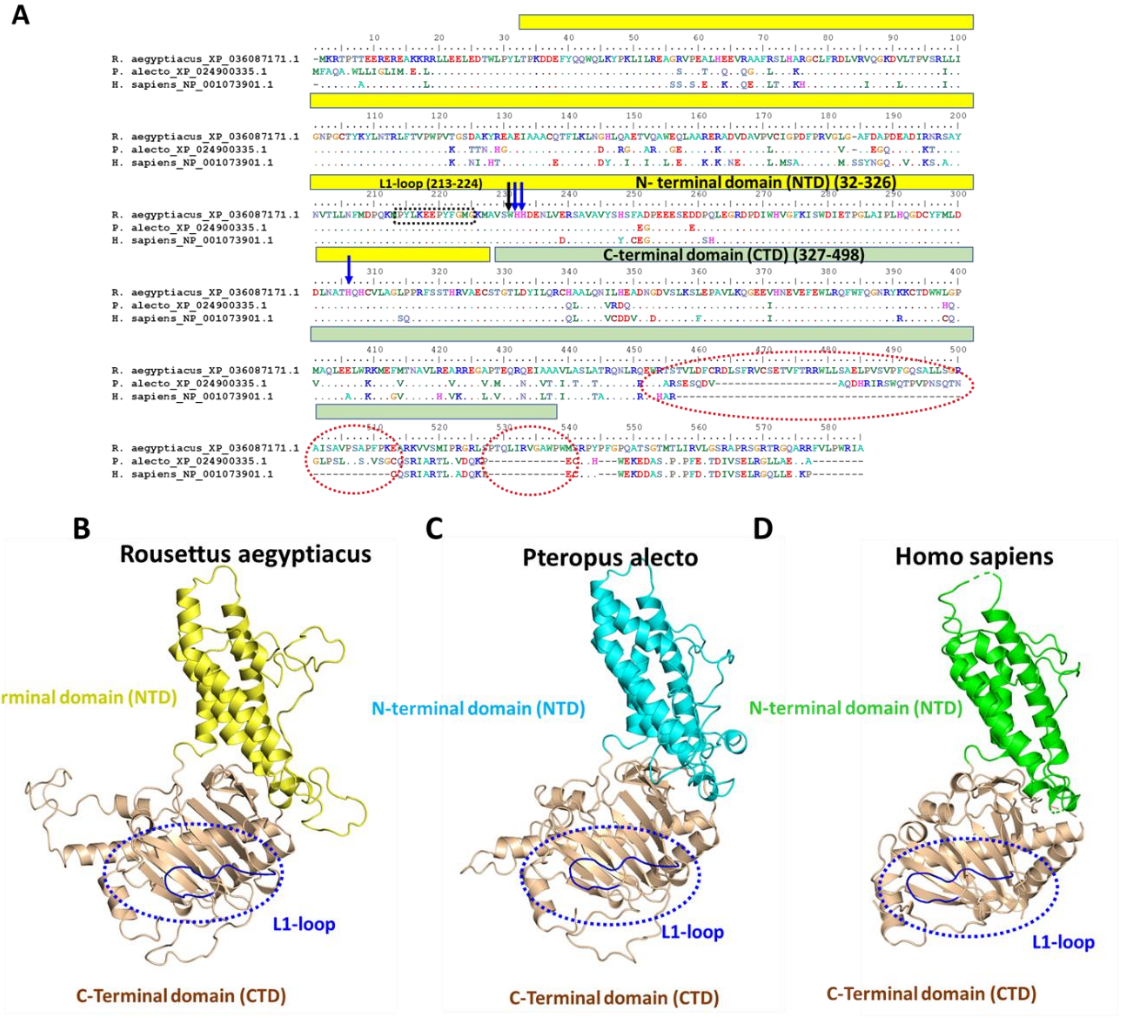

Figure 3.13. Amino acid alignment and protein structural analysis of R. aegyptiacus, P. alecto and H. sapiens FTO. (A) FTO amino acid sequence alignment among R. aegyptiacus, P. alecto and H. sapiens. Solid yellow and green rectangles highlight the corresponding sequences of the FTO NTD and CTD. A black dash rectangle highlights the L1 Loop residues. Blue and black arrows indicate the metal binding coordinates His 231, Asp 233 and His 307 and the conserved Trp 230. Red dashed circles highlighted the deletions in the CTD across the three species. Three-dimensional structure comparison of FTO among (B) R. aegyptiacus, (C) P. alecto, and (D) H. sapiens. Blue dashed circles are present around the L1-loop of the proteins. PDB ID of FTO NTD and CTD is 3LFM. Figure adapted from [313] with modification applied to the imported figure.

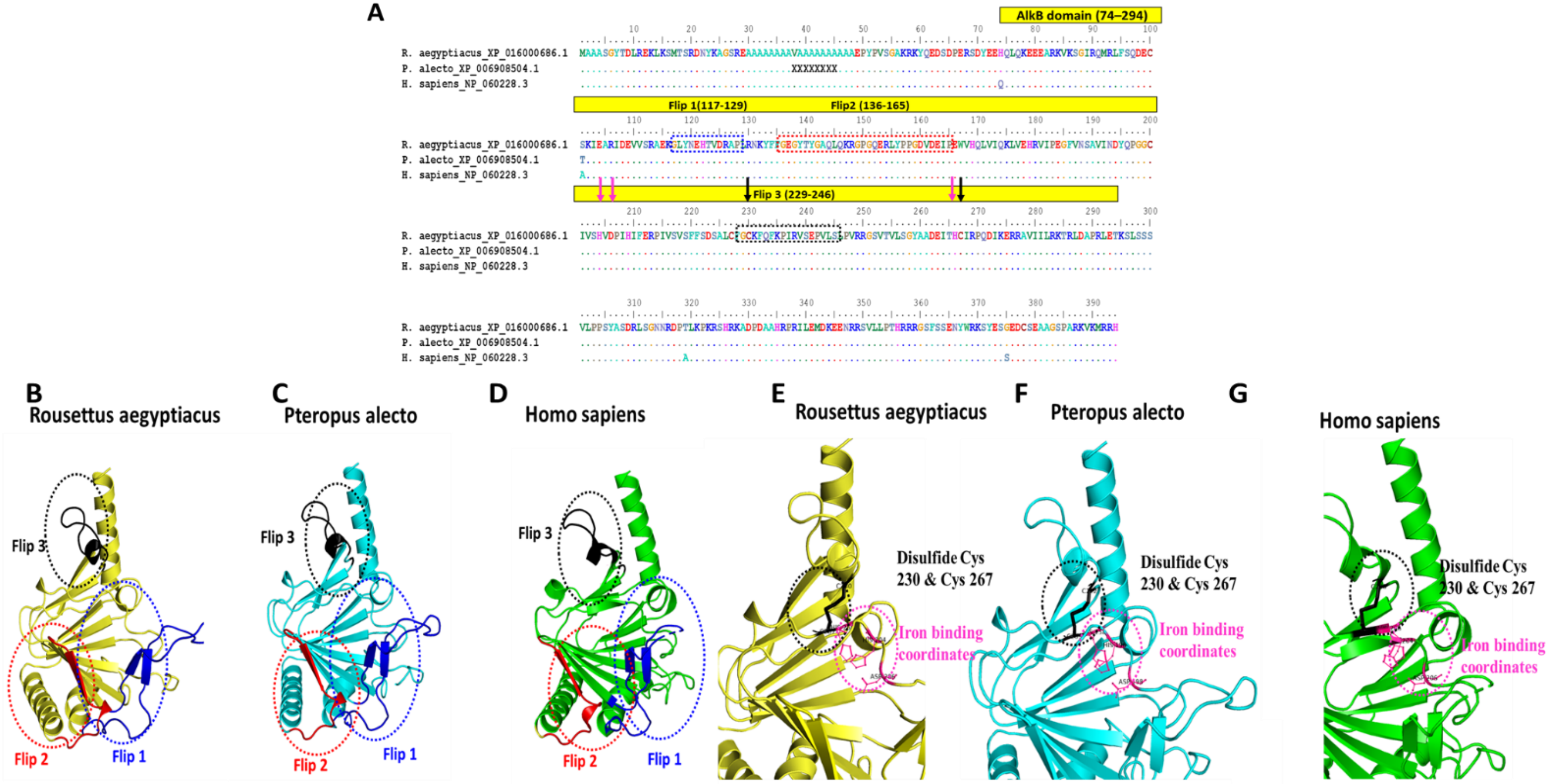

Figure 3.14. Amino acid alignment and protein structural analysis of R. aegyptiacus, P. alecto and H. sapiens ALKBH5. (A) ALKBH5 amino acid sequence alignment among R. aegyptiacus, P. alecto and H. sapiens. A solid yellow rectangle highlights the corresponding sequences of the AlkB domain. Blue, red, and black dashed rectangles highlight residues of Flips 1, 2, and 3, respectively. Magenta arrows indicate the metal binding coordinates, His 204, Asp 206, and His 266. Black arrows indicate the cysteines 230 and 267, which form the Flip 3 disulfide bond. Three-dimensional structure comparison of ALKBH5 among (B) R. aegyptiacus, (C) P. alecto, and (D) H. sapiens. Blue, red, and black dashed circles are used to highlight regions of Flip 1, 2 and 3, respectively. Zoom in on areas of metal binding residues and Flips 3 among (E) R. aegyptiacus, (F) P. alecto and (G) H. sapiens. Black and Magenta dashed circles illustrate the changes in the structures of the areas. PDB ID of ALKBH5 is 4NJN. Figure adapted from [313] with modification applied to the imported figure.

m6A readers are a group of five proteins that recognise the m6A modification via the YTH domain, thereby facilitating further RNA processing and metabolism. In the YTHF readers (YTHDF1, 2, and 3), the domain corresponds to residues 361–559, 380–579, and 403–571, respectively; while in YTHDC readers (YTHDC1 and 2), the domain is located at residues 345–509 and 1277–1430, respectively [256–259].

Alignment analysis of the bat-human readers demonstrated a broad spectrum of mutations distributed across the YTH domains of the five core reader proteins (**Figure 3.15–3.17**). Among these, YTHDF1 exhibited the highest mutation rate (**Figure 3.15A**). Notably, the majority of mutations were conserved between *R. aegyptiacus* and *P. alecto;* however, a long insertion, unique to *R. aegyptiacus,* was detected toward the end of the YTHDF2 domain. This insertion was absent in the corresponding orthologue of *P. alecto* (**Figure 3.15B**). In fact, the YTHDF2 domain of *P. alecto* exhibited a similar level of conservation to that of *H. sapiens*.

An important characteristic of the YTH domain family is the presence of an aromatic cage that pins the methylated adenine. This cage is made from hydrophobic residues that facilitate π–π stacking interactions with the modified base. Trp 411, Trp 465, and Trp 470 make up the cage in YTHDF1, whereas Tyr 418, Trp 432, Trp 486, and Trp 491 are included in YTHDF2. Trp 492, Trp 438 and Trp 497 are the pocket residues for YTHDF3, while Trp 377, Trp 428, and Leu 439 are included in YTHDC1. Similarly, Trp 1310, Trp 1360, and Leu 1365 form the cage in YTHDC2 [257,260,261]. Those coordinates showed conservation in the bat-human alignment; however, an exception was observed at position 439 in the YTHDC1 protein of *P. alecto*, where leucine was substituted with glutamine (Leu439Gln) (**Figure 3.17A**). Indeed, this mutation disrupted the typical π–π stacking interaction of the aromatic cage in *P. alecto*, compared to the corresponding structures in *R. aegyptiacus* and *H. sapiens*. The substitution in the black flying fox resulted in the formation of an atypical hydrogen bond between the $–NH_2$ group of the mutated glutamine and the N7 of the methylated adenine (**Figure 3.17B–D**).

Studies revealed that the YTH domain is conserved among the m6A readers. For example, the YTH of YTHDF1 RNA binding pocket comprises the C-terminal regions of β1, α1, and β2, the N-terminal region of α2, and the loop connecting β4 and β5

[256]. Alignment of *R. aegyptiacus***,** *P. alecto and H. sapiens* readers' domain has revealed that the β5 strand is composed of an equal number of amino acid residues in all three species. In contrast, the interloop region connecting β4 and β5 exhibited variable length among the species (**Figure 3.18A**); however, in the 3D structural comparison, the superimposed β5 sheets appeared shorter in both bats compared to the human, whereas the β4 and β5 interconnecting loops were found to be longer in bats than in humans (**Figure 3.18B–D)**.

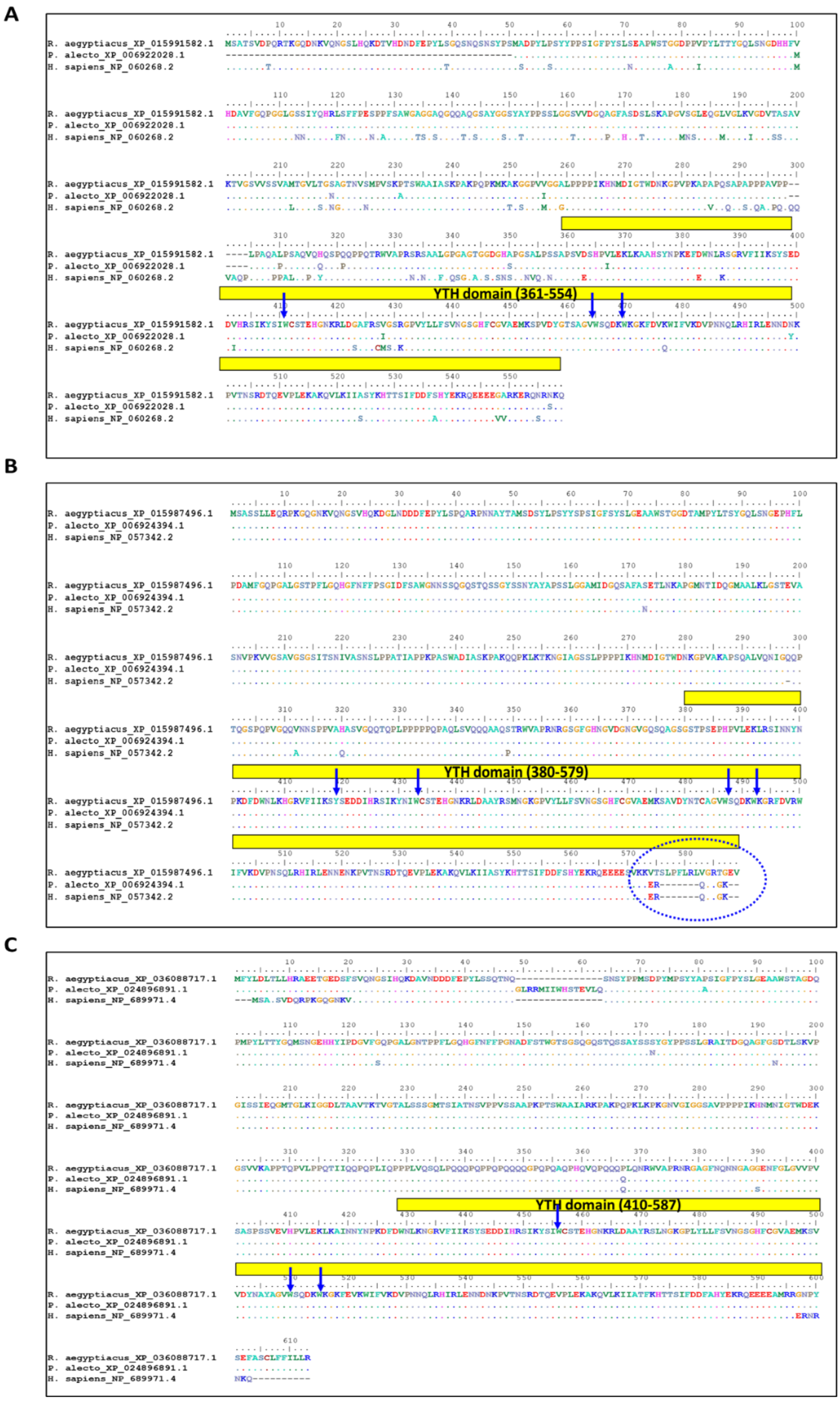

Figure 3.15. Multiple sequence alignment of YTHDF readers among R. aegyptiacus, P. alecto and H. sapiens. (A) Amino acid sequence alignment of YTHDF1. (B) Amino acid sequence alignment of YTHDF2. (C) Amino acid sequence alignment of YTHDF3. Solid yellow rectangles are used to illustrate the corresponding YTH domain of each protein. Blue arrows are used to mark the corresponding residues forming the aromatic cage of each protein. Blue dashed circle is used to highlight the structural variation of the YTHDF2 domain among R. aegyptiacus, P. alecto and H. sapiens. Figure adapted from [313] with modification applied to the imported figure.

Figure 3.16. Multiple sequence alignment of YTHDC2 reader among R. aegyptiacus, P. alecto and H. sapiens. The YTH domain is illustrated with a yellow rectangle. The conserved aromatic cage residues are marked with blue arrows. Figure adapted from [313] with modification applied to the imported figure.

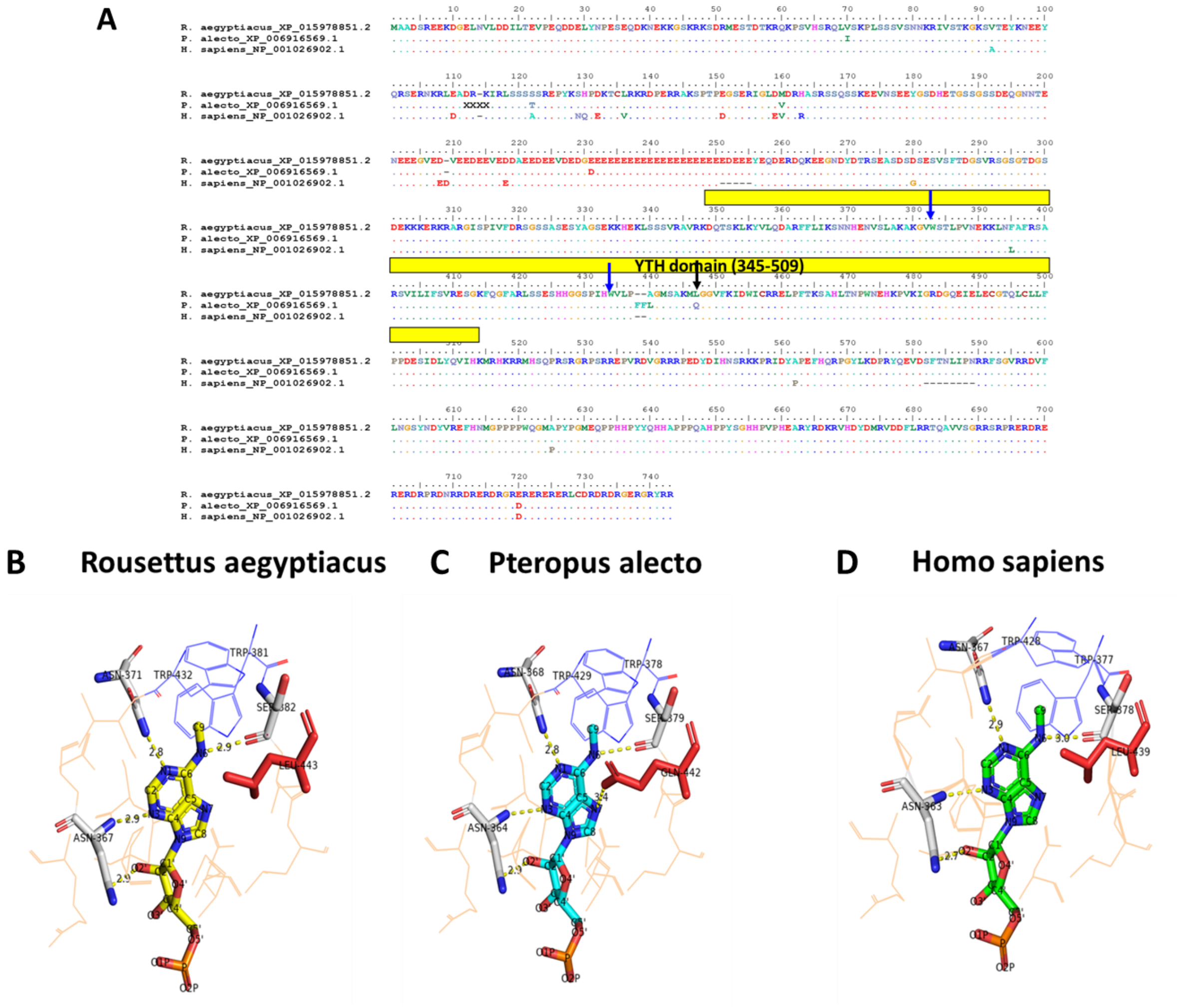

Figure 3.17. Amino acid sequence alignment and m6A interaction of YTHDC1 among R. aegyptiacus, P. alecto and H. sapiens. (A) Alignment of R. aegyptiacus, P. alecto and H. sapiens YTHDC1 proteins. A solid yellow rectangle highlights the YTH domain. Blue arrows indicate the conserved aromatic residues Trp 377 and Trp 428. A black arrow indicates the Leu439Gln substitution. Overall structural comparison of the m6A interaction area of YTHDC1 among (B) R. aegyptiacus, (C) P. alecto, and (D) H. sapiens. The hydrogen bond formed due to the Leu439Gln replacement in P. alecto is marked in a black dashed circle. PDB ID of YTHDC1 is 4R3I. Figure adapted from [313] with modification applied to the imported figure.

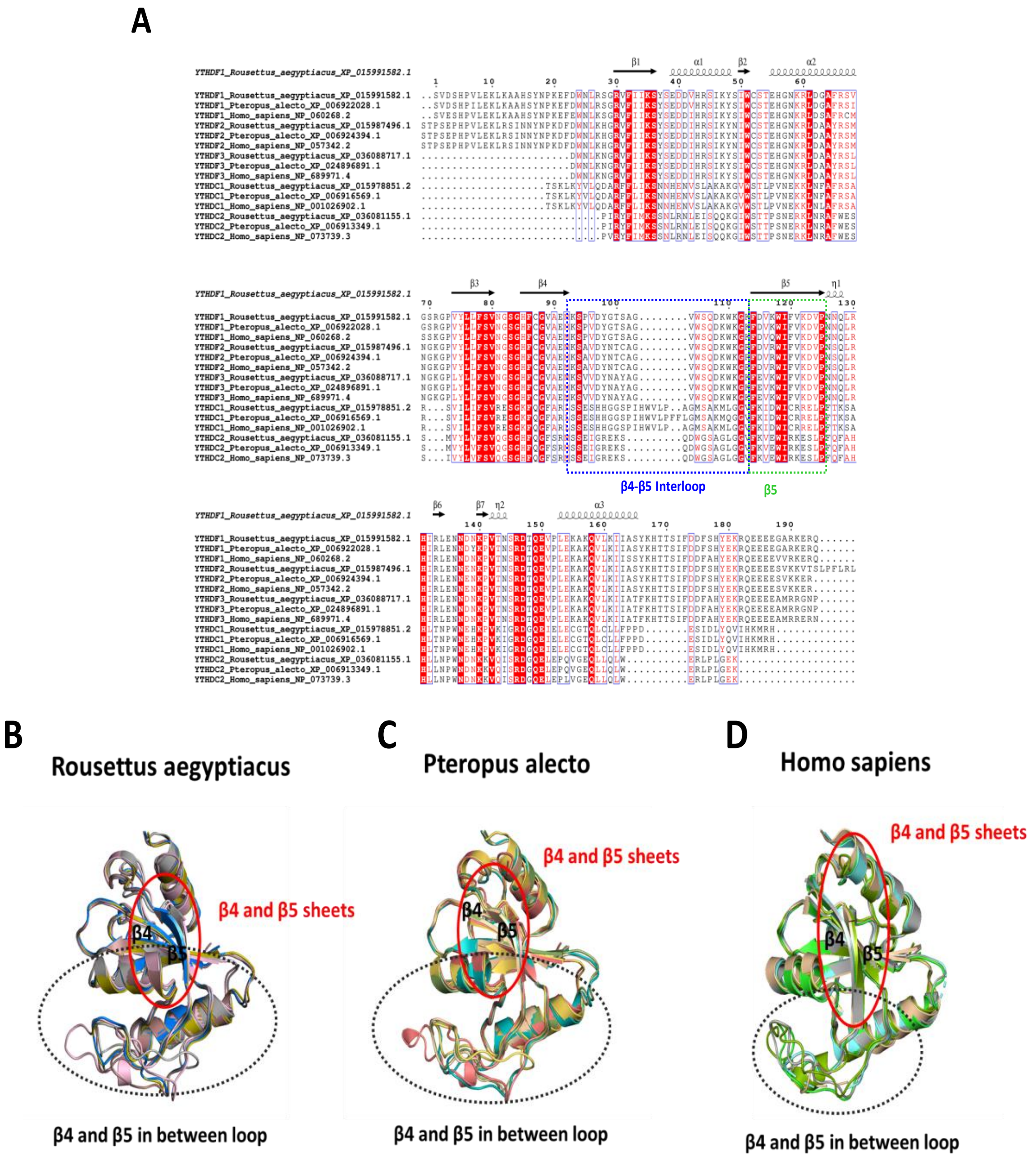

Figure 3.18. Alignment and superimposition of m6A readers' YTH domain among R. aegyptiacus, P. alecto and H. sapiens. (A) YTH domains alignment combined with the corresponding secondary structures. Superimposition of YTH domain's tertiary structure among (B) R. aegyptiacus, (C) P. alecto and (D) H. sapiens. Black dashed, and solid red circles are used to highlight β4-β5 interloop and β4-β5 sheets, respectively. PDB IDs of the domain are 4RCI, 4WQN, 5ZOT, 4R3I and 6K6U, in YTHDF1, YTHDF2, YTHDF3, YTHDC1 and YTHDC2 respectively. Figure adapted from [313] with modification applied to the imported figure.

3.4. Discussion

Among the epi-transcriptomic modifications, m6A is the most widely studied across a wide variety of mammalian and non-mammalian hosts due to its crucial role in virus and host cell RNA regulation [219,298,299]. The m6A machinery comprises a set of cellular proteins categorised into writers (METTL3, METTL14, and WTAP), erasers (FTO and ALKBH5), and readers (YTHDF1-3, YTHDC1-2), which add, remove, and recognise methylated RNA, respectively [322]. The m6A epi-transcriptomic machinery is well-characterised in human and non-mammalian hosts [298,299,304]; however, such information is lacking for Chiroptera (bats). Therefore, this research gap was addressed in the present study by combining computational methods to characterise m6A in *R. aegyptiacus* and *P. alecto* relative to that in *H. sapiens*.

The amino acid identity analysis revealed high sequence similarity between the m6A proteins of *R. aegyptiacus* and *P. alecto*, demonstrating high sequence conservation between the two bats and mammalian m6A orthologues, with METTL3 and YTHDF2 being the most conserved in the bat-mammalian and bat-human comparisons. In contrast, FTO displayed the lowest identity in both comparisons, reflecting the species-specific amino acid divergence of the FTO among bats, in addition to the broader bat-mammalian differentiation. Nevertheless, the high identity percentage in the m6A machinery of *R. aegyptiacus*, *P. alecto* and *H. sapiens* could point to functional conservation of the proteins among the three mammalian species.

Over the last few years, comparative genomics and genetic synteny have enabled research to uncover gene function by examining the conserved DNA elements across species [323,324]. Thus, to further elucidate the functions of m6A genes in *R. aegyptiacus* and *P. alecto*, genomic alignment and synteny analyses were conducted in comparison with their human orthologues. Comparative genomic analysis revealed that m6A genes are distributed across multiple autosomal chromosomes in *H. sapiens*, where METT14 and YTHDC1 were located on the fourth chromosome. However, this comparison could not be applied to the bat's genome, as the genetic information is present on unplaced scaffolds in NCBI. Results from the gene synteny analysis demonstrated that multiple genes within the m6A loci are conserved across *R. aegyptiacus*, *P. alecto*, and *H. sapiens*, supporting the functional conservation of the m6A machinery across the three species. The genome of *H. sapiens* is well annotated to the chromosomal level, while that of the *R. aegyptiacus* and *P. alecto* is scaffold-based [325–327]. Recently, the bat1K genome initiative aims at sequencing and annotating the Chiropteran genomes to the chromosomal level [328]. However, till this project ends, these findings provide intuitive insight into the m6A functionality and characterisation in *R. aegyptiacus* and *P. alecto*.

To date, information regarding the structure of m6A machinery in bats is lacking; therefore. To establish a structural comparison of *R. aegyptiacus* and *P. alecto* m6A proteins with their *H. sapiens* counterpart, amino acid alignment and 3D protein structure comparison were employed to predict the structural features and functional domains of the m6A-related proteins across the three species. PDB was used to retrieve the relevant protein of the human, while SWISS-MODEL was used to predict the m6A set of the two bats. The selection of the SWISS-MODEL in this study was due to its feasibility, accuracy, and integration of multiple quality control and template optimisation features. Moreover, it takes into account the degree of similarity and evolutionary distance when choosing a template, in addition to supporting a benchmark for the detection of protein-ligand interactions [290,291,329].

The METTL3-METTL14-WTAP complex is responsible for the addition of the methyl group on the adenosine base of the RNA with the aid of the SAM molecule [330]. Protein alignment comparison of the complex among *R. aegyptiacus*, *P. alecto*, and *H. sapiens* revealed sequence similarity in the functional regions and core domains, which are involved in the m6A methylation reaction. This similarity was also seen across the 3D structural comparison, which together suggests conserved catalytic reaction and function of the writers among the three mammals.

FTO and ALKBH5 are demethylases that utilise a high-valent iron-oxo complex (Fe (IV)-oxo) to remove the m6A from RNA [331]. The identification of the target nucleic acid to be demethylated is achieved by the L1 loop and Flips 1-3 regions of the two proteins, respectively [243,245]. The FTO bat-human alignment demonstrated the highest mutational rate among the ten proteins, with substitutions, insertions and deletions seen across the amino acids of the CTD and NTD. This is expected since the FTO was the least conserved protein. However, the L1 loop and iron-binding coordinates were conserved among *R. aegyptiacus*, *P. alecto*, and *H. sapiens*. Similarly, the configuration of the L1 loop was maintained across the three species despite the observed overall structural dissimilarity. This suggests that these residues are critical for the protein's m6A functional integrity and further confirms the preservation of protein m6A function despite substantial amino acid and structure changes. In contrast, ALKBH5 demonstrated in its catalytic domain only one mutational difference between the bats and humans, but the structural prediction was disrupted at the metal-binding residues and disulfide region. Validation by crystallography must be warranted to investigate this misconfiguration and determine whether it would affect the protein's m6A selectivity in such a case.

The m6A readers are a large group of proteins, among them, the YTH family are the most important. In humans, there are five well-characterised YTH readers with distinct three or four hydrophobic residues caging the methylated adenine [256,332]. The alignment of the m6A readers bats and humans displayed multiple amino acid variants in the YTH domain across the five proteins, with substitutions, insertions, and deletions observed. Although this did not affect the aromatic cage residues in humans and the Egyptian fruit bat, it affected the binding pocket of the black flying fox YTHDC1, where Lue439Gln substitution was observed.

At the structural level, the YTHDC1-m6A binding of *H. sapiens* and *R. aegyptiacus* involved interaction of Ser 378, Ser 371, Asn 367, and Asn 363, and Asn 382 with the sixth, first, and third nitrogen atoms, as well as C2′-ribosyl hydroxyl oxygen of the methylated nucleotide, respectively. Notably, the Asn 363 and Asn 382 bind to both N3 and C2′-ribosyl hydroxyl oxygen of m6A. However, replacement of Leu439Gln in *P. alecto* has created an additional hydrogen bond between the NH2 group of the mutated Gln and the N7 nitrogen of the methylated adenine. Leucine is a hydrophobic residue, while glutamine is a hydrophilic amino acid [333,334]. Therefore, the Leu439Gln substitution likely alters the classic hydrophobic interaction of the m6A-binding pocket of *P. alecto* YTHDC1, influencing RNA recognition. Further studies are required to examine this effect on the biological function of the protein.

Structural studies regarding the m6A readers demonstrated conserved RNA binding pocket architecture of the YTH domain that consists of C-terminal regions of β1, α1 and β2, the N-terminal part of α2, as well as the interface loop between β4 and β5 [256]. Tertiary structural analysis of the bats' YTH domains revealed, when superimposed, shorter β5 sheets and longer in between β4-β5 loops when compared to those of the human. Although the domains' alignment was comparable among the three species, this highlights the need to establish crystal structure studies of the m6A machinery in *R. aegyptiacus* and *P. alecto* to verify whether the differences in YTH domain RNA binding pocket between humans and the two bats are present in vivo, similar to the prediction, and, if so, how that length difference would affect RNA binding. In conclusion, these findings highlighted the similarity of the m6A regulators in *R. aegyptiacus*, *P. alecto* and *H. sapiens* while also emphasising the need for crystallographic and functional validation to elucidate the architecture and role of m6A not only in *R. aegyptiacus* but also in *P. alecto* relative to those in humans.

Chapter 4. The m6A Machinery as a Potential Antiviral Regulator of CedPV in Bat and Human Cells

4.1. Introduction

m6A is a highly prevalent modification that modulates virus replication in either a positive or negative direction [214,300]. Recent research has identified three mechanisms implicated in the m6A-virus interaction, including regulation of the viral genome, modulation of the cellular transcriptome following viral infection, and modification of innate immunity [335]. Typically, these mechanisms are governed by the m6A machinery [336]

METTL3 is the core writer, which contributes to viral-host interactions by introducing m6A methylation on cellular and viral RNAs or by modulating the antiviral immune defence [337]. Generally, METTL3 promotes viral replication by adding m6A to the viral RNA, thereby enabling immune evasion, although its specific role depends on the viral context. For example, METTL3-mediated m6A on SARS-CoV-2 and EV-71 genomes reduces RIG-I sensing, dampens type I IFN responses, and stabilises the viral RNA [275,280], and its re-localisation promotes the viral replication in VSV and Ebola [277,338]. METTL3 acts as an antiviral regulator by participating directly in immune [282,283], highlighting METTL3's dual role depending on the virus.

CedPV is a less pathogenic henipavirus that was isolated in 2009 from a *Pteropus* spp colony roosting at Cedar Grove, Australia [14]. Although Cedar shares features with the NiV and HeV, such as genomic length and general structure, it lacks the P gene RNA editing that encodes IFN-antagonist V/W proteins, rendering it susceptible to host immunity. Additionally, no human cases have been documented to be infected with CedPV, in contrast to NiV and HeV [339]. Nevertheless, CedPV can infect human cells and can represent an excellent proxy to study the pathogenesis and antiviral targets against the pathogenic henipaviruses using the rCedPV-GFP virus that was rescued in CL2 [44,340].

To this end, studying the m6A can be applied to rCedPV-GFP in different hosts, including humans and bats, to understand the functional similarity between different host systems. Moreover, it could be used to assess whether CedPV could be used as a model for targeted m6A therapy against NiV and HeV in human cells, and whether structural conservation of the m6A machinery among bat species contributes to their shared susceptibility to CedPV and other related henipaviruses. *R. aegyptiacus* is a frugivorous bat with a wide geographical distribution in Africa, where it is associated with the isolation of diverse henipa-related viruses [181,312]. Additionally, the Egyptian fruit bats are phylogenetically and genetically close to the black flying foxes [341,342], which supports transmission and isolation of the CedPV [14] as well as transmission of NiV and HeV [310,311].

In this study, it was hypothesised that m6A influences CedPV replication in either a proviral or antiviral manner and could be further targeted as a potential antiviral strategy against pathogenic henipaviruses in *H. sapiens*, using CedPV as a model. Furthermore, it was assumed that the previously identified in silico similarity and identity between the m6A machinery of *R. aegyptiacus* and *H. sapiens* contribute to comparable intracellular regulation of CedPV in the two species. Therefore, this chapter aimed to test these hypotheses in human and *R. aegyptiacus* bat cells.

4.2. Specific Objectives

4.2.1. Propagation and quantification of rCedPV-GFP using VeroE6.

4.2.2. Adaptation and passaging of rCedPV-GFP in *R. aegyptiacus* cell lines.

4.2.3. Screening the antiviral and proviral roles of the hm6A machinery in infected rCedPV-GFP A549 cells.

4.2.4. Designing a bicistronic pB cassette for the expression of RE-METTL3 and mScarlet.

4.2.5. Cloning of putative domains of RE-METTL3 using the designed vector

4.2.6. Establishment of stable R06E cell lines expressing the putative domains

4.2.7. Assessing the role of METTL3 and its associated domains in the replication of rCedPV-GFP in R06E

4.2.8. Determining the effect of rCedPV-GFP on the subcellular localisation of the RE-METTL3 and the domains using confocal microscopy

4.3. Results

4.3.1. Propagation of rCedPV-GFP in VeroE6 Cells

Prior to assessing the replication of rCedPV-GFP in human and *R. aegyptiacus* cells, the virus was first propagated in VeroE6 cells. The cells were inoculated with 100 µL of virus stock for 2 h and observed daily for virus growth and development of CPE (formation of giant multinucleated cells, or syncytia). Viral GFP and syncytia were detected in VeroE6 at 24 hpi and progressively increased over 48 and 72 hpi. When the maximum GFP and syncytia were reached at 72 hpi, the virus was harvested, clarified and further titrated using the standard 10-fold serial dilution (**Figure 4.1**).

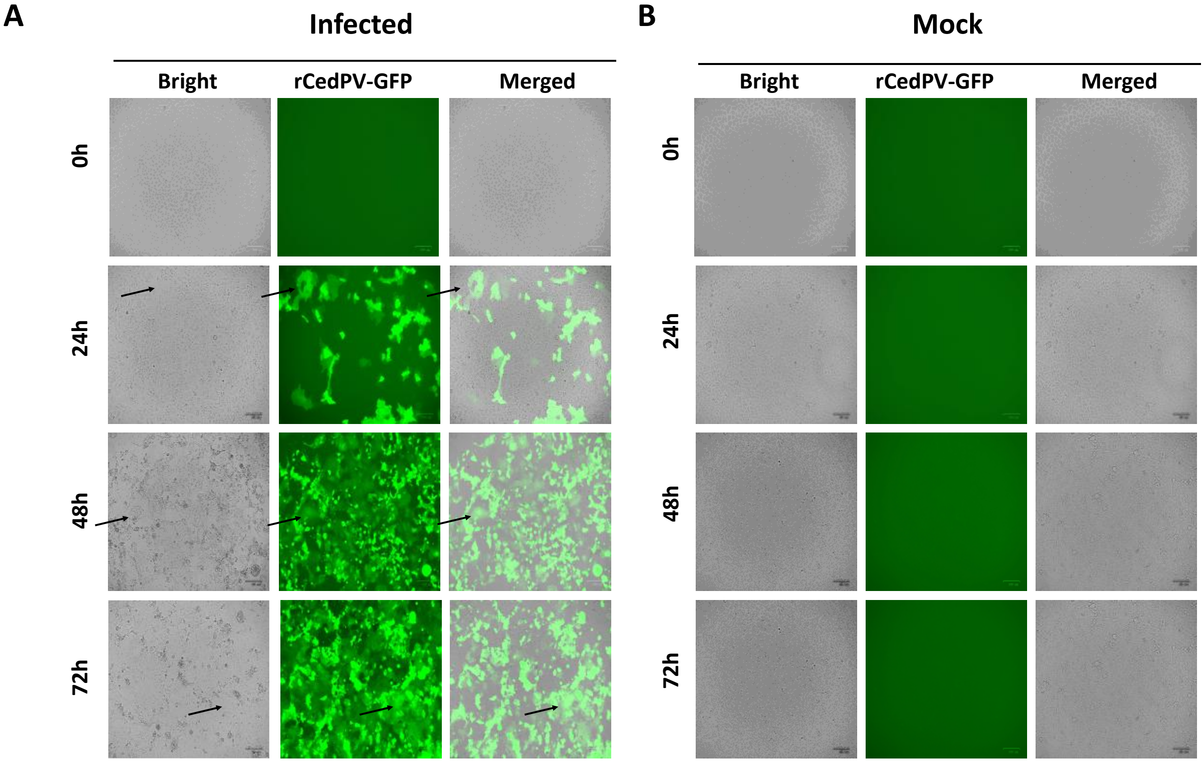

Figure 4.1. rCedPV-GFP propagation in VeroE6 cells. (A) Viral GFP and syncytia were detected at 24 hpi and progressively increased over the 72 h infection period. rCedPV-GFP syncytia are marked with black arrows. (B) Mock-infected cells served as a negative control. Scale bar = 100 µm

4.3.2. Adaptation Confers Efficient Replication of rCedPV-GFP in Bat Cells

Following viral propagation in VeroE6, *R. aegyptiacus* bat cells (R05T and R06E) were inoculated in a 6-well plate with 0.5 MOI of rCedPV-GFP. Surprisingly, neither of the *R. aegyptiacus* cells supported efficient viral replication. At 24 hpi, both cell lines exhibited a weak viral-GFP signal in several infected cells. However, over time, from 24 to 72 hpi, the infection signal progressively decreased rather than increased, while the cell death increased. Originally, the CedPV was isolated from the urine of *P. alecto*, and the virus produced strong CPE in *P. alecto* brain (PaBr) and kidney (PaKi) cells [14,343]. However, previously, infection and replication in the *R. aegypticus* bat cells have not been successful.

Compared to R06E, R05T is easier to maintain and can tolerate excessive handling under repeated passaging or intensive subculturing. However, R05T is harder to transfect and is a relatively slower grower when compared with R06E. Therefore, R05T was employed for the rCedPV-GFP adaptation in *R. aegypticus* bat cells, while R06E was used for the subsequent experiments throughout the whole thesis.

For rCedPV-GFP adaptation, several approaches were employed. Initially, the virus was passaged in R05T cells using the entire viral harvest collected at 24 h post-infection, corresponding to the time point of maximal viral GFP expression. However, this approach did not result in detectable GFP expression upon the second passage in R05T cells.

Next, the virus was adapted using alternative passaging between the bat cells and BHK-21, given that BHK-21 supports replication of both NiV and CedPV to high titres [356]. For this purpose, the virus was propagated in BHK-21 cells, harvested at 72 hpi, and inoculated into R05T cells. In contrast to VeroE6-derived rCedPV-GFP, virus propagated in BHK-21 cells resulted in an abortive infection in R05T cells, with only minimal GFP-positive dots observed at 24 h post-infection (**Figure 4.2A** and **B)**. This occurred despite robust viral replication and pronounced syncytium formation in BHK-21 cells prior to inoculation into bat cells (**Figure 4.2C**).

Accordingly, rCedPV-GFP, which was derived from VeroE6 cells, was selected for processing the adaptation in bat cells rather than the one derived from BHK-21. For this purpose, rCedPV-GFP-derived VeroE6 was inoculated and harvested alternately between the VeroE6 and R05T at 120 and 24 hpi, respectively, using the entire rCedPV-GFP harvest from bat cells at each passage. This process was repeated until the infection was successfully established in the bat cells (i.e., six passages) (**Figure 4.3**). Ultimately, this method of alternative passaging conferred productive infection and successful adaptation of rCedPV-GFP in both R06E and R05T even when passaging the virus in one cell line or from one cell line to another.

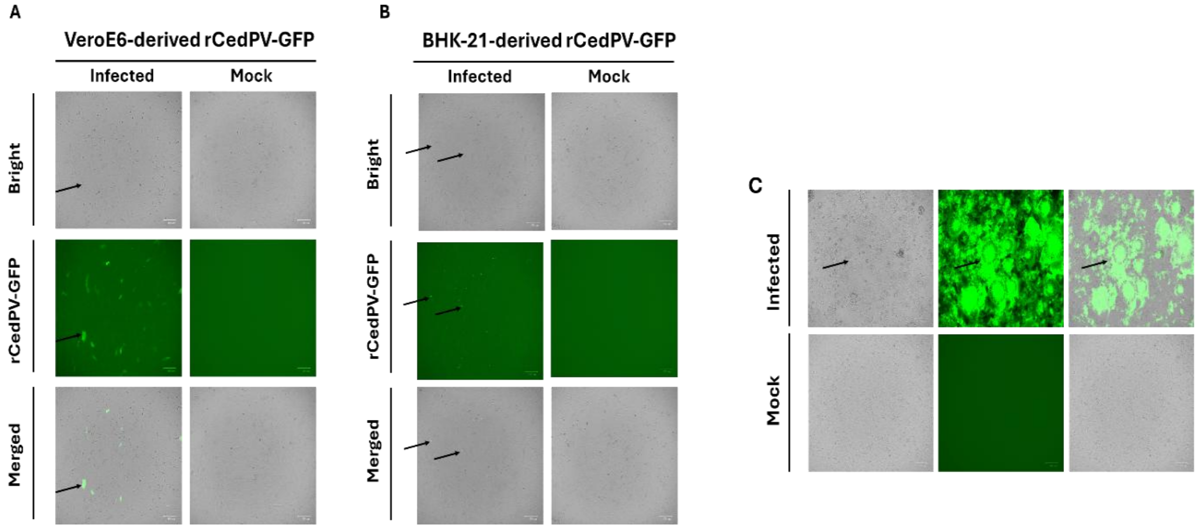

Figure 4.2. Comparison of rCedPV-GFP adaptation in R05T cells using viruses from VeroE6 and BHK-21 cells. (A) R05T cells infected with rCedPV-GFP derived from VeroE6 showed weak but successful replication, as indicated by scattered green, fluorescent cells at 24 hpi. (B) R05T cells infected with rCedPV-GFP from BHK-21 showed abortive infection, as indicated by GFP dots. (C) rCedPV-GFP replication in BHK-21 cells for R05T inoculation exhibited strong CPE and syncytia at 72 hpi prior to harvest. rCedPV-GFP syncytia are marked with black arrows across panels. Scale bar = 100 µm

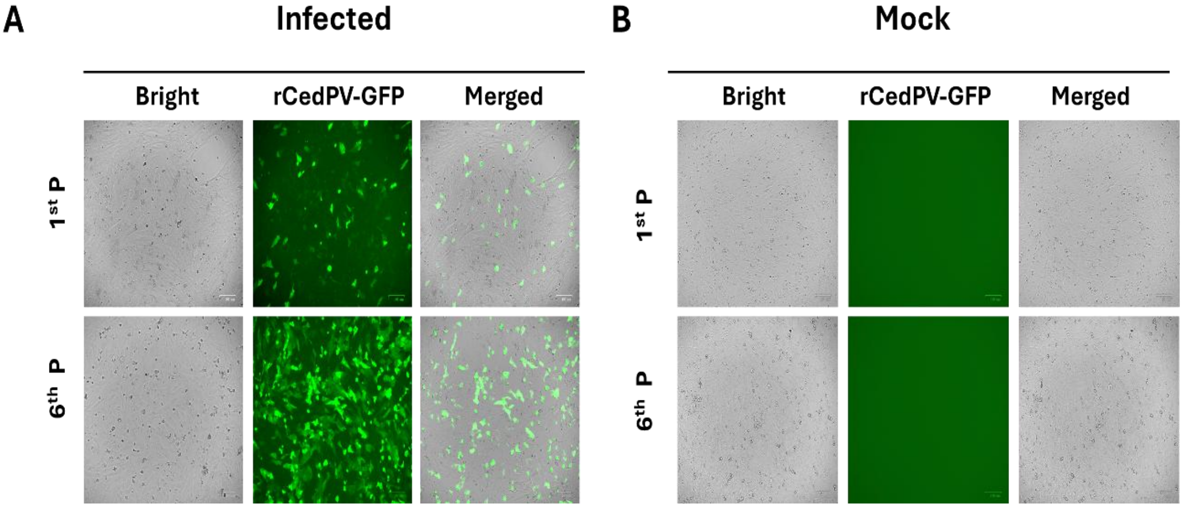

Figure 4.3. rCedPV-GFP adaptation in R05T using VeroE6-derived virus. R05T was infected with the virus harvested from VeroE6. At 24 hpi, the virus was harvested and inoculated into Vero6E cells, then reinoculated into R05T. Inoculation and harvesting of the virus were alternated between VeroE6 and RO5T until the virus was adapted. (A) 1st and 6th passages of rCedPV-GFP adaptation in R05T. (B) Mock-infected R05T cells served as a negative infection control. Scale bar = 100 µm.

4.3.3. Overexpression of the Human m6A Machinery Inhibits Replication of rCedPV-GFP in A549 Cells

In order to investigate the role of m6A in replication of rCedPV-GFP in human and bat cells, and to select the m6A protein for overexpression study in *R. aegyptiacus* R06E cells, the ten hm6A machineries were screened against the rCedPV-GFP using A549 cells. For that purpose, A549 cells were plated in a 24-well plate, and each well was transiently transfected with plasmids encoding the ten human m6A proteins. pCAGGs-Empty and pCAGGs-GFP vectors were included in the study as infection and transfection controls, respectively. At 24 h post-transfection, cells were infected with the rCedPV-GFP at an MOI of 4 (the best MOI revealed strong antiviral effect based on evaluating different MOIs to assess the antiviral effects of m6A) and examined microscopically for the anti-/proviral effects of the machinery at 24 hpi. Additionally, supernatants from the overexpressed wells were collected for the virus quantification in VeroE6.

Out of the three writer proteins, hMETTL3 overexpression demonstrated the most potent antiviral effect against rCedPV-GFP, where the virus had shown limited replication, weak GFP signals and fewer plaques. The antiviral effect of the hWTAP was moderate and weaker than that of hMETTL3. Virus multiplication and spread were comparable to those of the pCAGGs-Empty when hMETTL14 was transfected (**Figure 4.4**). Overexpression of hFTO failed to show either proviral or antiviral effects against rCedPV-GFP replication in any of the replicates. In contrast, the hALKBH5 demethylases resulted in robust inhibition of rCedPV-GFP in A549 (**Figure 4.5**). Remarkably, all five human readers effectively inhibited the rCedPV-GFP when overexpressed, with YTHDC2 showing the most potent inhibition (**Figure 4.6**). Of note, the antiviral effect of YTHDC2 was the most potent among the m6A machinery against the rCedPV-GFP.

Collectively, these results highlight the antiviral role of the m6A machinery against CedPV in human cells A549. Although based on the high similarity between hMETTL3 and RE-METTL3 observed in in silico analyses, and considering METTL3's central role in m6A methylation, regulation of innate immunity, and control of multiple viruses [219,236,281,282], METTL3 was chosen for further investigation to define its specific function against CedPV in R06E bat cells.

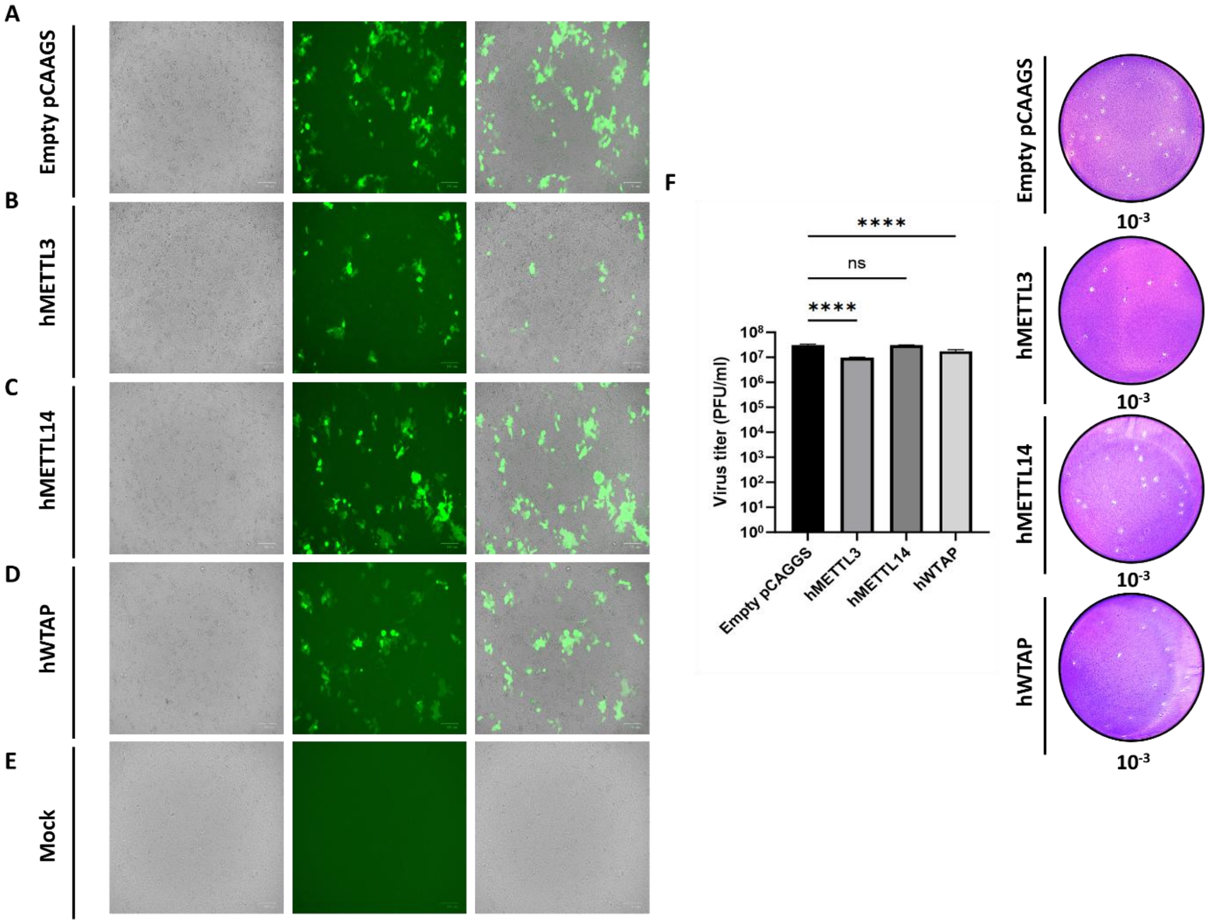

Figure 4.4. Overexpression of hMETTL3 inhibits the rCedPV-GFP replication in A549 cells. (A-D) Microscopic examination of A549 cells transfected with hm6A writes and infected with rCedPV-GFP showed strongly reduced viral replication in hMETTL3 overexpressed cells compared to cells transfected with the empty PCAAGs vector. Overexpression of hWTAP resulted in a moderate reduction in viral replication, whereas hMETTL14 overexpression had no significant effect. (E) Mock-infected cells served as a negative infection control. Scale bar = 100 µm. (F) Statistical analysis of the quantification of rCedPV-GFP from the supernatants of transfected A549 cells showed a significant decrease in rCedPV-GFP production in hMETTL3-overexpressing cells compared to PCAAGs, hWTAP, and hMETTL14 groups. Data are presented as mean ± SD from three replicate wells. Statistical analysis was performed using One-way ANOVA with Dunnett's multiple comparisons.

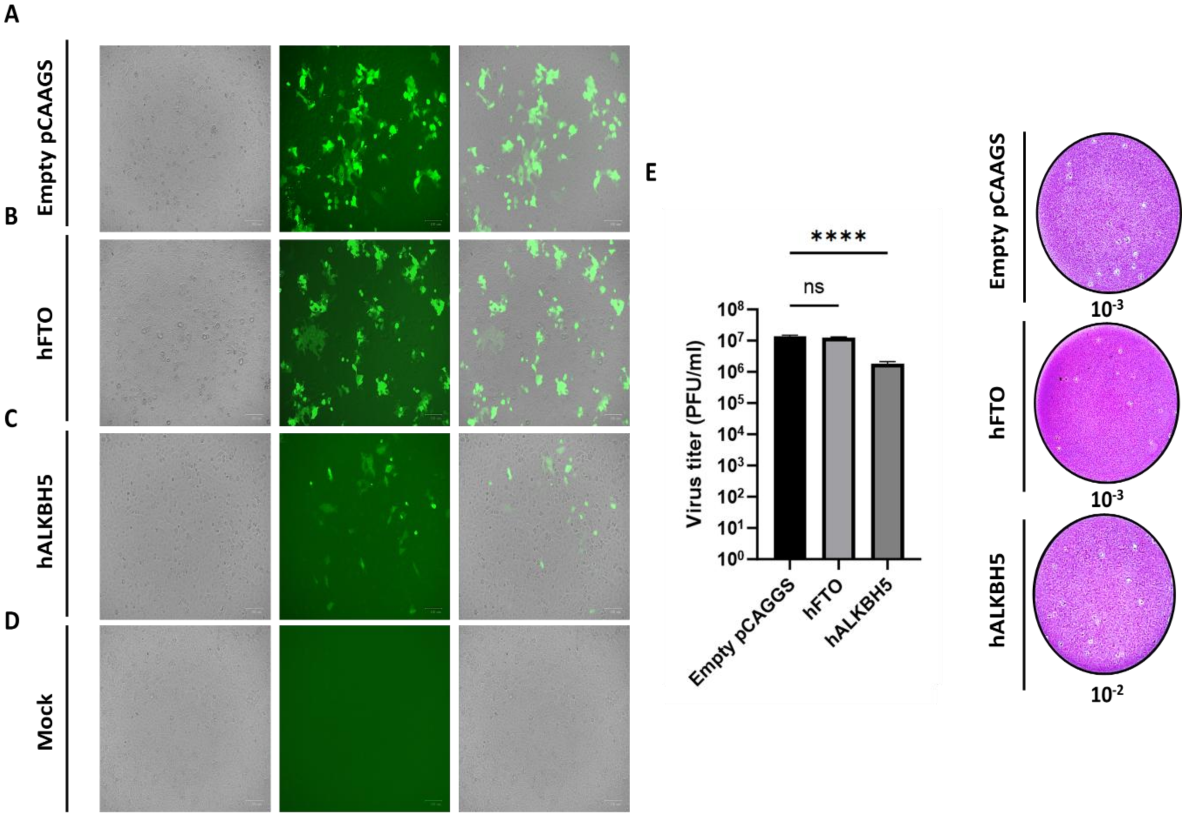

Figure 4.5. Overexpression of hALKBH5 inhibits the rCedPV-GFP replication in A549 cells. (A-C) Microscopic examination of A549 cells transfected with hm6A demethylase and infected with rCedPV-GFP showed reduced viral replication in hALKBH5 overexpressed cells compared to cells transfected with the empty PCAAGs vector. Overexpression of hFTO was inert to the rCedPV-GFP replication. (D) Mock-infected cells served as a negative infection control. Scale bar = 100 µm. (E) Statistical analysis of the quantification of rCedPV-GFP from the supernatants of transfected A549 cells showed a significant decrease in rCedPV-GFP production in hALKBH5-overexpressing cells compared to PCAAGs and hFTO groups. Data are presented as mean ± SD from three replicate wells. Statistical analysis was performed using One-way ANOVA with Dunnett's multiple comparisons.

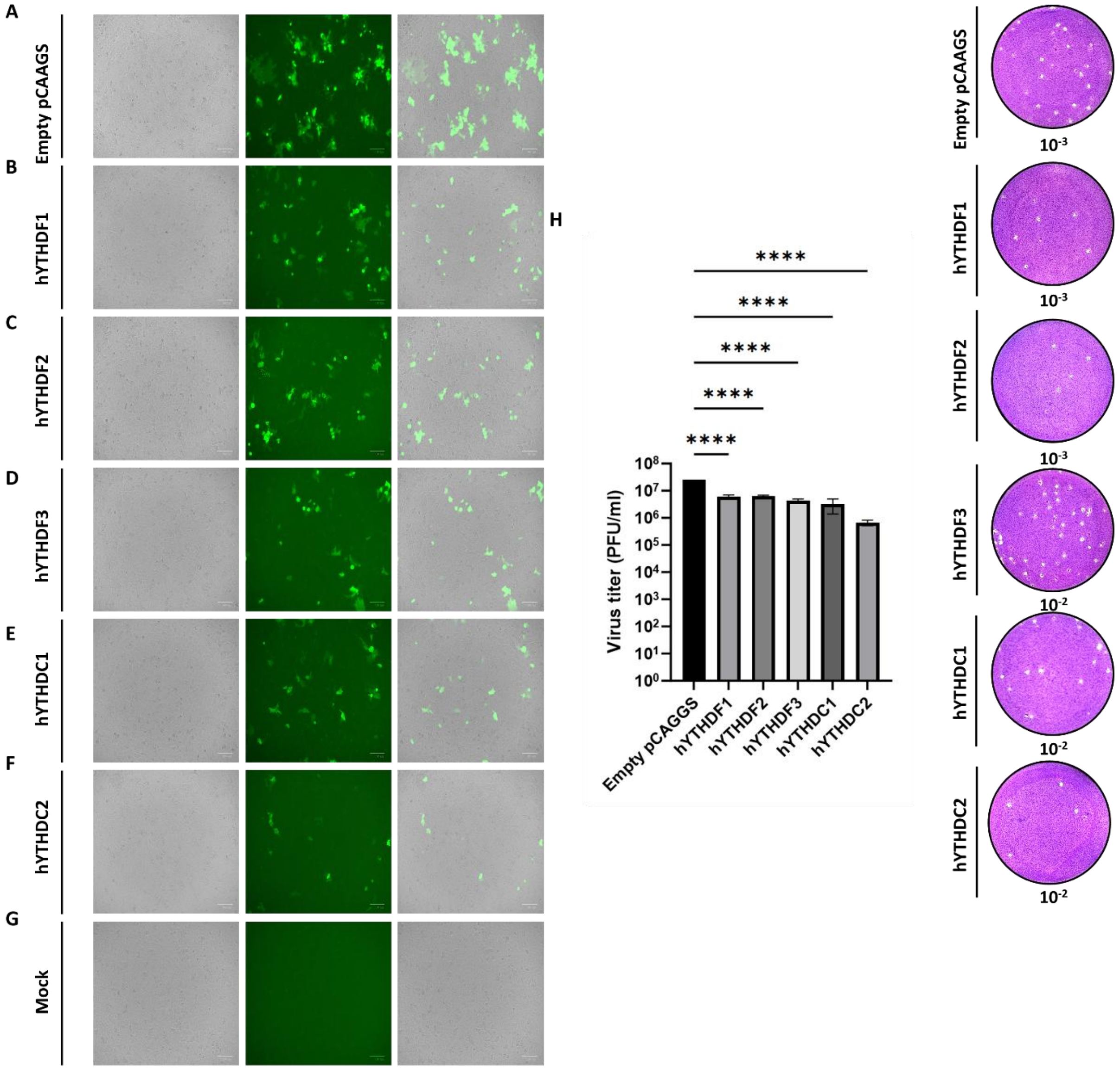

Figure 4.6. Overexpression of hm6A readers inhibits the rCedPV-GFP replication in A549 cells. (A-F) Microscopic examination of A549 cells transfected with hm6A readers and infected with rCedPV-GFP showed reduced viral replication in overexpressed cells compared to cells transfected with the empty PCAAGs vector, with hYTHDC2 showing the lowest viral GFP signals. (G) Mock-infected cells served as a negative infection control. Scale bar = 100 µm. (H) Statistical analysis of the quantification of rCedPV-GFP from the supernatants of transfected A549 cells showed a significant decrease in rCedPV-GFP production in readers-overexpressing cells compared to PCAAGs. hYTHDC2 is the strongest antiviral protein. Data are presented as mean ± SD from three replicate wells. Statistical analysis was performed using One-way ANOVA with Dunnett's multiple comparisons.

4.3.4. Design of *Rousettus aegyptiacus* METTL3 Bicistronic Piggy-Bac Plasmid Cassette

Plasmids expressing the RE-METTL3 are not commercially available, and compared to other mammalian cells, the transfection efficiency of bat cells is extremely low. These obstacles limited the use of transient transfection in R06E cells. Moreover, fusing a fluorescent protein to the RE-METTL3 can disrupt the protein's folding and interactions. Additionally, the presence of GFP in the recombinant CedPV genome added further complications to the m6A-viral study by limiting the fluorescence protein options. Thus, to overcome these limitations, the ORF of *RE-METTL3* was synthesised and cloned into the pB-CAG-EGFP vector backbone to generate a RE-METTL3 vector for the stable integration of the protein in the R06E cell line. Additionally, a V5 tag was added to the N-terminus of the protein to enable tracking in the downstream applications.

To evaluate the transfection in R06E and to allocate the transfected cells in the cell line establishment, mScarlet was added to the plasmid cassette. An additional Kozak sequence was added upstream to the mScarlet to enhance the protein expression. TGA stop codons were added at the end of the two ORFs, and the two proteins were linked by IRES2 instead of the WT IRES to improve the downstream translation of the mScarlet. Therefore, in the designed cassette, RE-METTL3, mScarelt were co-expressed under the IRES2, whereas the expression of puromycin in the pB-CAG-EGFP remained under the effect of WT IRES integrated in the vector backbone. The schematic diagram of the synthesised cassette in the pB plasmid, as well as the detailed sequence of the designed cassette, is illustrated in (**Figure 4.7** and **Figure 4.8**).

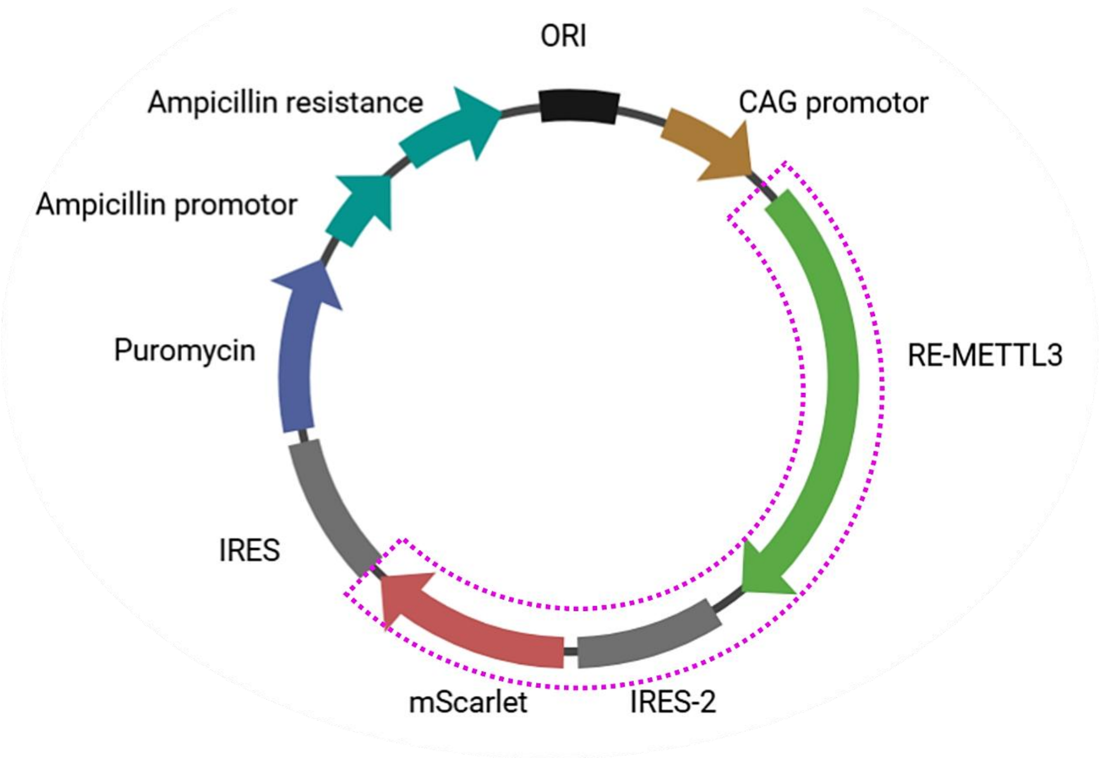

Figure 4.7. A schematic diagram of RE-METTL3-WT-V5-N-mScarlet-pB. RE-METTL3 ORF was synthesised and cloned into the pB-CAG-EGFP vector backbone. mScarlet was added to the cassette for the tracking of the transfection and cell line establishment. IRES2 was used to co-express RE-METTL3 and mScarlet under the control of the CAG promoter. A dashed violet crescent is used to highlight the designed bicistronic cassette. Figure made by BioRender.

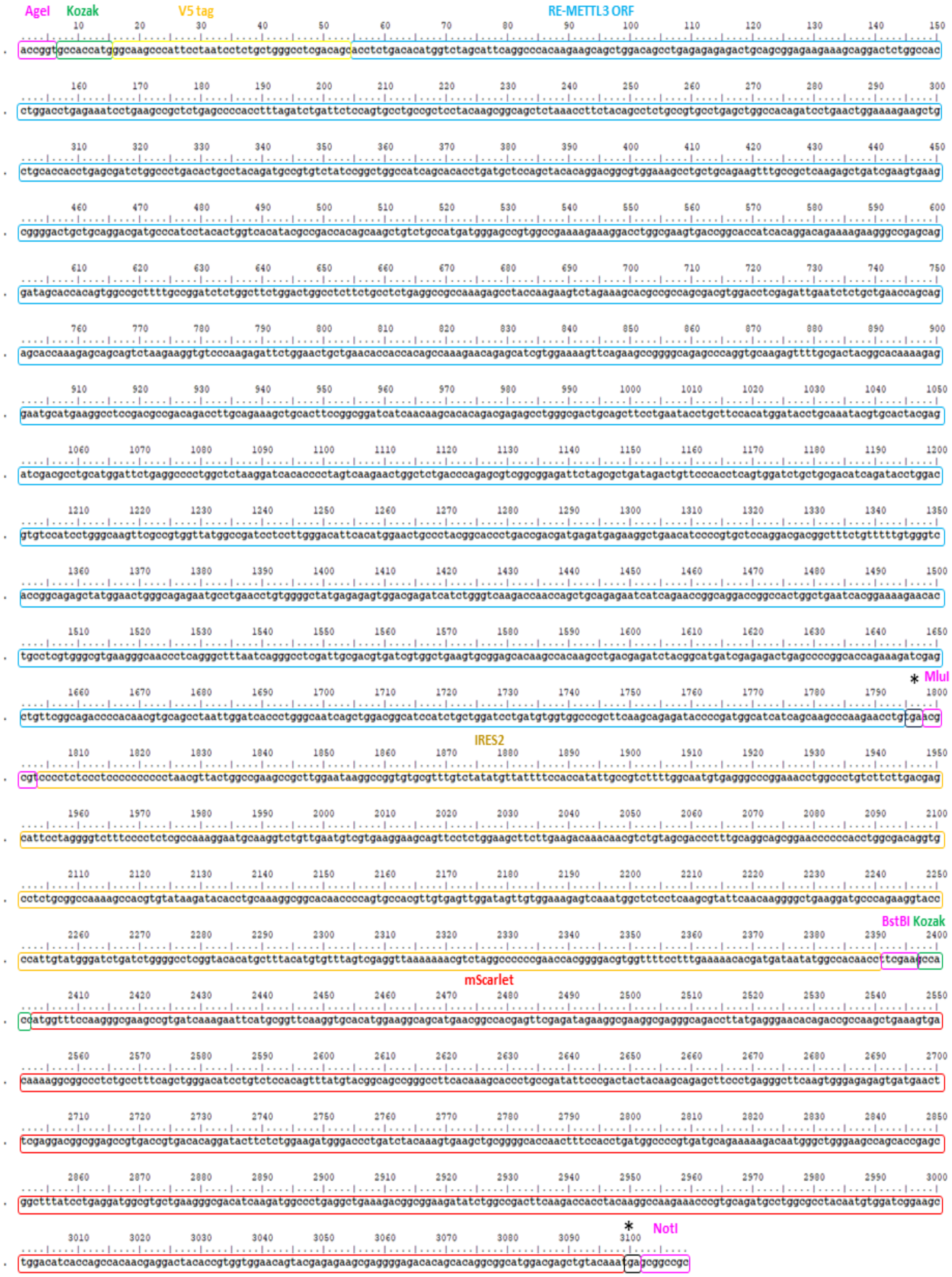

Figure 4.8. RE-METTL3-mScarlet bicistronic cassette map sequence. ORF of RE-METTL3 is highlighted in a sky-blue rectangle. The IRES2 sequence is highlighted in a yellow rectangle. mScarlet ORF is highlighted in a red rectangle. Stop codon sequences are marked with asterisks and highlighted with black rectangles. Restriction enzyme sites and Kozak sequences are highlighted in violet and green rectangles, respectively.

Following cassette synthesis, the cloned vector was transfected into the A549 cells to test the RE-METTL3 and mScarlet protein expression. A549 was cultured on cover slips in a 24-well plate and transfected with the plasmid. A non-transfected well was included in parallel as a control. At 24 h post-transfection, cells were subjected to immunofluorescence imaging for the expression of mScarlet and RE-METTL3 using an anti-V5 tag antibody. As expected, mScarlet protein was expressed successfully with intense red fluorescence, whereas the METTL3 protein was expressed and tagged successfully in A549 (**Figure 4.9**).

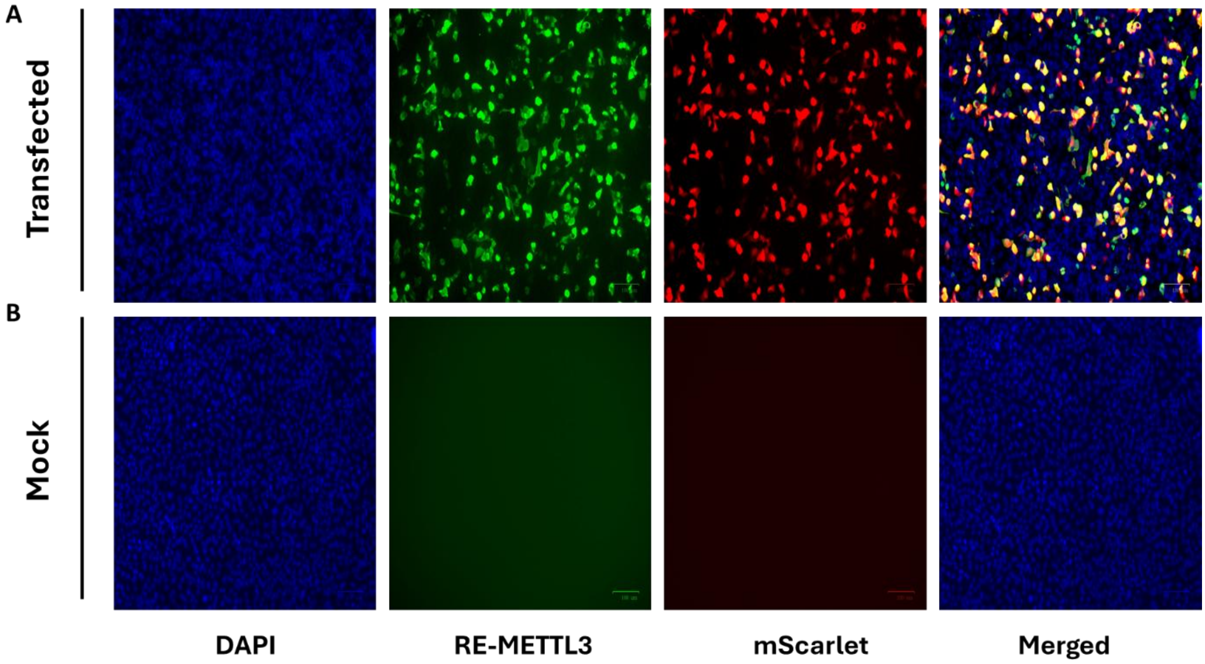

Figure 4.9. Immunofluorescence imaging of RE-METTL3-WT-V5-N-mScarlet-pB plasmid transfection in A549. Cells were transfected with the plasmid and subjected to immunofluorescence imaging at 24 h post-transfection for protein expression. (A) transfected A549 with RE-METTL3-WT-V5-N-mScarlet-pB plasmid. The nuclei were stained with DAPI stain (blue). RE-METTL3 was visualised by detection of the V5 tag using Anti-V5 tag antibody [SV5-Pk1] (green). Expression of mScarlet is visualised successfully (red). (B) Mock-transfected cell showed only the DAPI field. Scale bar = 100 µm.

4.3.5. Cloning of RE-METTL3 Domains Vector Constructs

Data from the in-silico and bioinformatic analyses revealed that RE-METTL3 domains have identical amino acid sequences and a similar position to those of hMETTL3. To gain insight into its structural and functional role in rCedPV-GFP replication in R06E, RE-METTL3 protein domains (ZFD1, ZFD2, and MTD) were determined using the in-silico analysis and cloned either individually or in combination into the RE-METTL3-WT-V5-N-mScarlet-pB plasmid.

The domains were amplified using targeted primers that included the V5 tag, AgeI and MluI restriction sites. An additional PCR reaction was performed to amplify the mScarlet to be used as a control in the experiments. All PCR products were purified from the gel and subjected to restriction digestion along with the original vector RE-METTL3-WT-V5-N-mScarlet-pB plasmid. Inserts were subsequently ligated to the cut vector and transformed successfully into DH5α cells. Bacterial colonies were selected, and plasmids were positively confirmed using the colony PCR and Sanger sequencing (**Figure 4.10** and **Figure 4.11**).

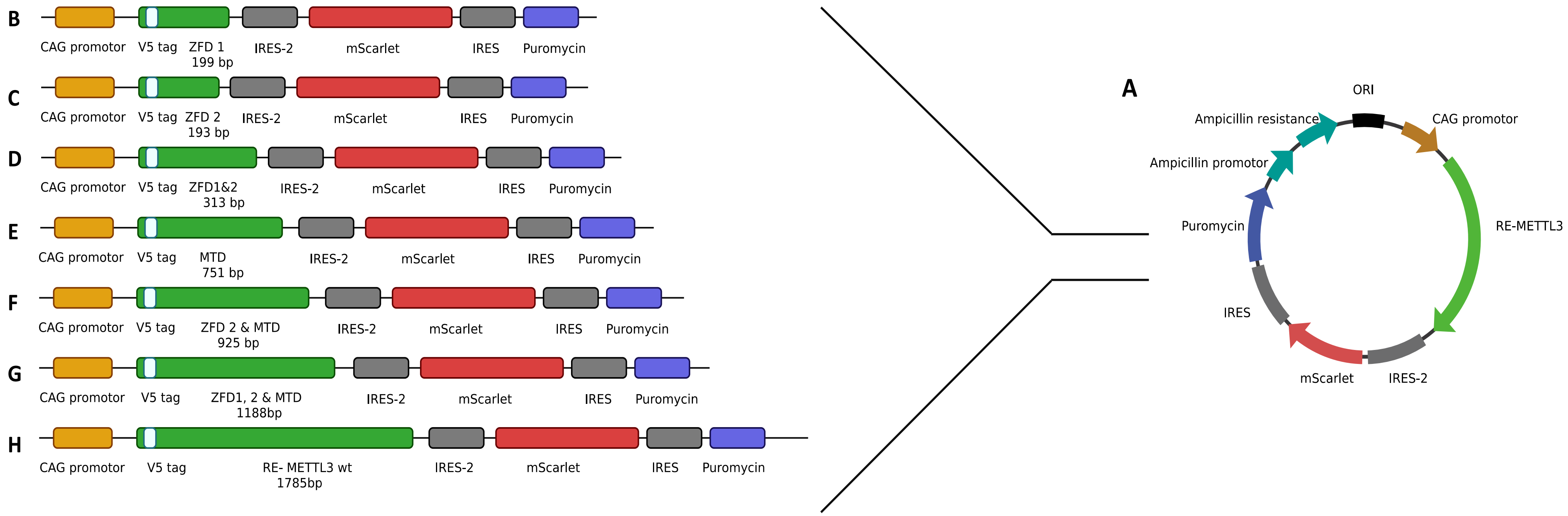

Figure 4.10. A schematic map of RE-METTL3 vectors. (A) A schematic diagram of the RE-METTL3-WT-V5-N-mScarlet-pB vector. (B) RE-METTL3-ZFD1- V5-N -mScarlet-pB. (C) RE-METTL3-ZFD2-V5-N-mScarlet-pB. (D) RE-METTL3-ZFD1 & 2-V5-N-mScarlet-pB. (E) RE-METTL3-MTD-V5-N-mScarlet-pB. (F) RE-METTL3-ZFD2 & MTD-V5-N-mScarlet-pB. (G) RE-METTL3-ZFD1, 2 & MTD-V5-N-mScarlet-pB. (H) RE-METTL3-WT-V5-N-mScarlet-pB. Figure made by BioRender

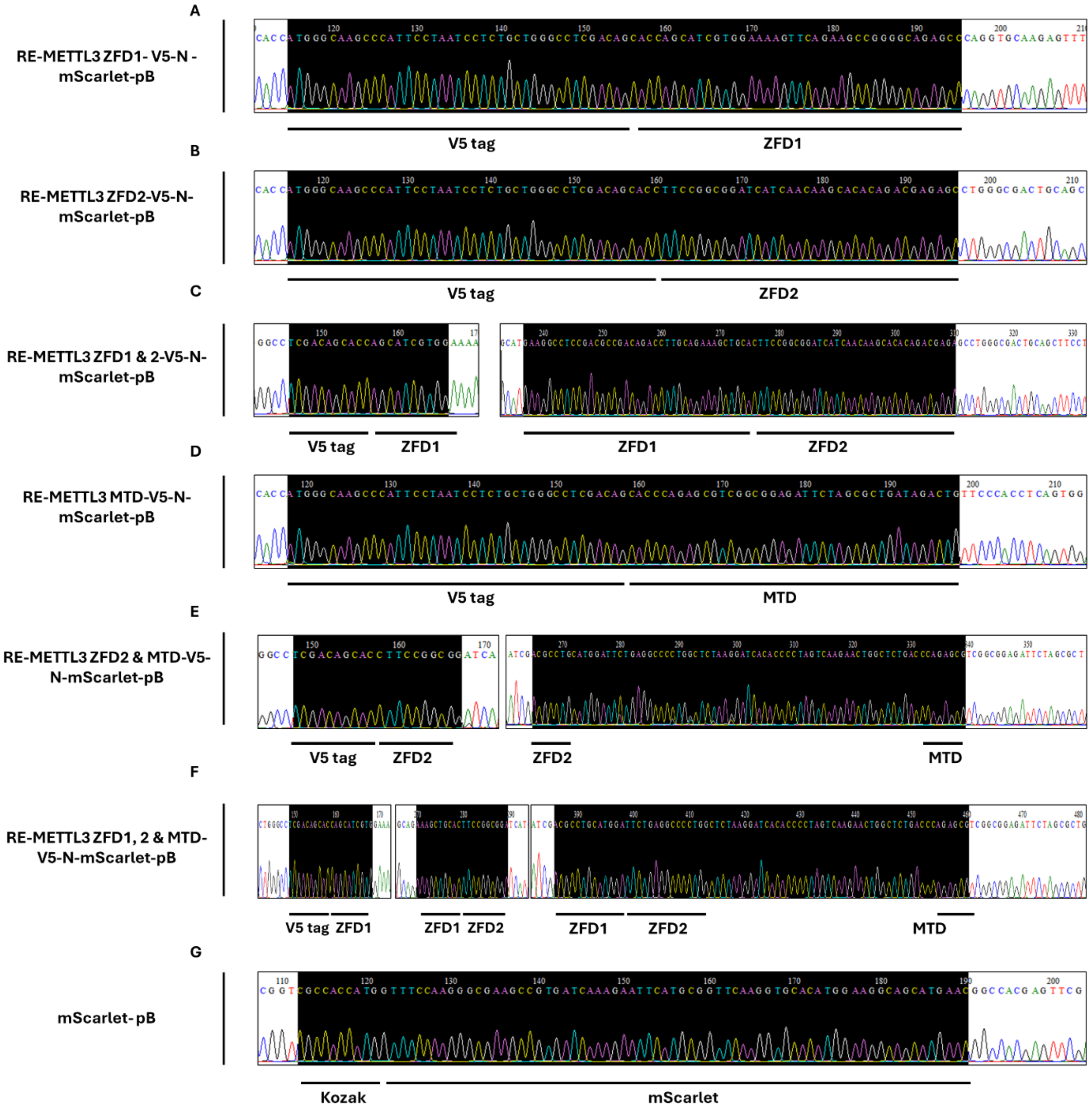

Figure 4.11. Sanger sequencing results of the cloned RE-METTL3 domains and mScarlet constructs. (A) RE-METTL3-ZFD1- V5-N -mScarlet-pB. (B) RE-METTL3-ZFD2-V5-N-mScarlet-pB. (C) RE-METTL3-ZFD1 & 2-V5-N-mScarlet-pB. (D) RE-METTL3-MTD-V5-N-mScarlet-pB. (E) RE-METTL3-ZFD2 & MTD-V5-N-mScarlet-pB. (F) RE-METTL3-ZFD1, 2 & MTD-V5-N-mScarlet-pB. (G) mScarlet-pB.

4.3.6. Generation and Validation of R06E Cell Lines Stably Expressing RE-METTL3 Constructs

Following cloning of the METTL3 and mScarlet vectors, R06E cells were plated and co-transfected with Hybase-CAG and the cloned vectors. Cells were examined under the microscope at 24 h post-transfection and subsequently selected using puromycin. All cell lines were successfully expanded and transferred to T25 for further cultivation (**Figure 4.12**).

The established cell lines were validated by WB using the anti-V5 tag antibody. R06E WT was included in the analysis for the comparison, and α-tubulin was loaded in the assay as a loading control. Expression of full-length RE-METTL3 was seen at ~ 66kDa, while expression of ZFD1, 2 and MTD were seen at ~ 38 kDa. In contrast, ZFD2&MTD were detected at ~ 33 kDa, and MTD was noticed at ~ 25 kDa. As anticipated, α-tubulin was detected at ~ 47 kDa in all cell lines (**Figure 4.13A).**

Owing to the low molecular weight of the ZFDs (~ 4 to 9 kDa), none of the ZFD cell line constructs (R06E-METTL3-ZFD1-mScarlet, R06E-METTL3-ZFD2-mScarlet, and R06E-METTL3-ZFD1 & 2-mScarlet) were detected in the WB analysis. Alternatively, PCR was performed to detect the integrated genes in the established cell lines using RE-METTL3-ZFD1- V5-N -mScarlet-pB, RE-METTL3-ZFD2- V5-N -mScarlet-pB and RE-METTL3-ZFD1&2- V5-N -mScarlet-pB plasmids as positive controls. As expected, ZFDs were successfully integrated into the genome of the cells; ZFD1 (R06E-METTL3-ZFD1-mScarlet) was detected at 199 bp, ZFD2 (R06E-METTL3-ZFD1-mScarlet) was observed at 191 bp, and the combined domains (R06E-METTL3-ZFD1 & 2 -mScarlet) were observed at 313 bp (**Figure 4.13B−D**).

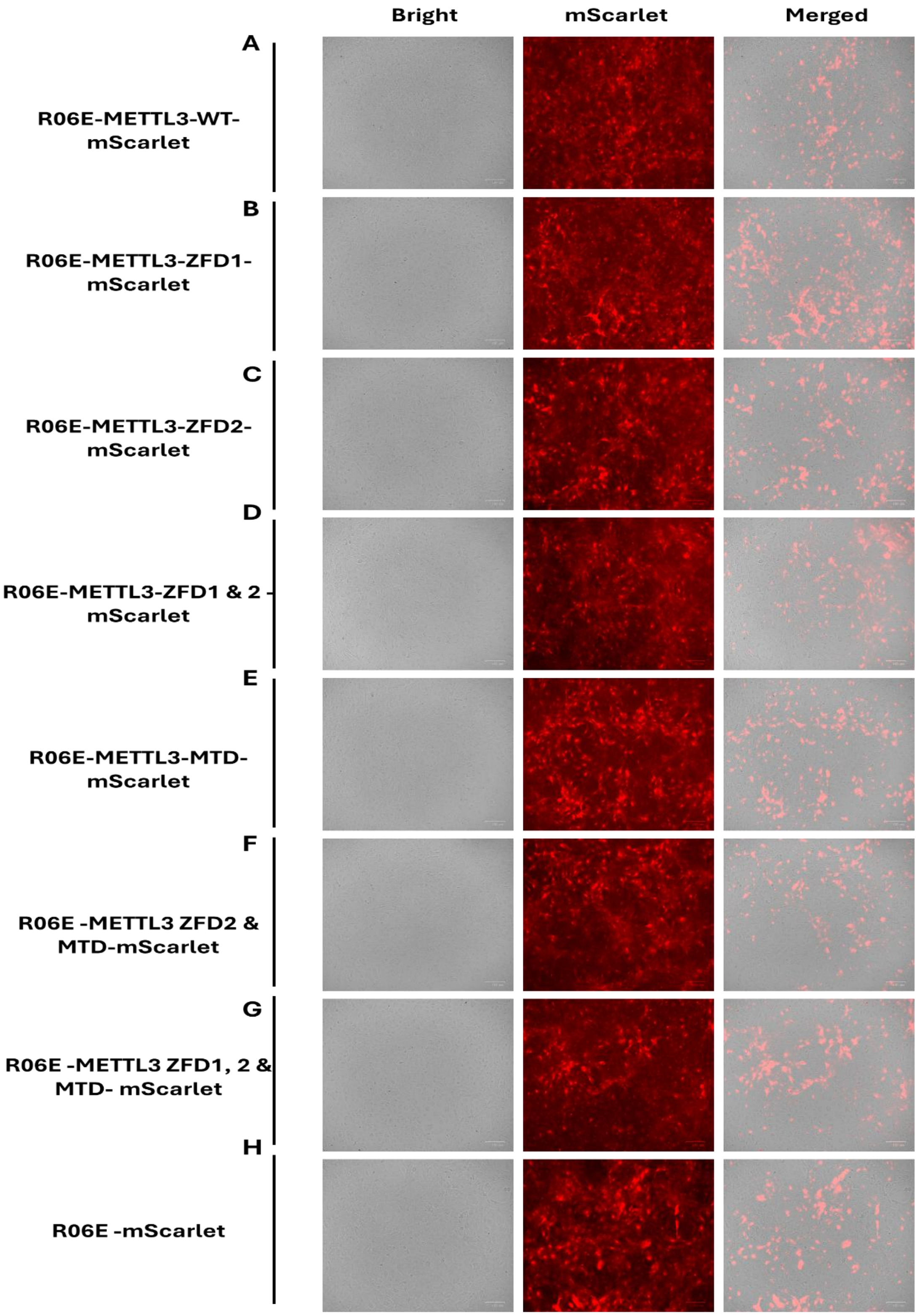

Figure 4.12. RE-METTL3 established R06E cell lines. (A) R06E-METTL3-WT-mScarlet. (B) R06E-METTL3-ZFD1-mScarlet. (C) R06E-METTL3-ZFD2-mScarlet. (D) R06E-METTL3-ZFD1 & 2 -mScarlet. (E) R06E-METTL3-MTD-mScarlet. (F) R06E -METTL3-ZFD 2 & MTD- mScarlet. (G) R06E -METTL3-ZFD1, 2 & MTD-mScarlet. (H) R06E -mScarlet. Scale bar = 100 µm.

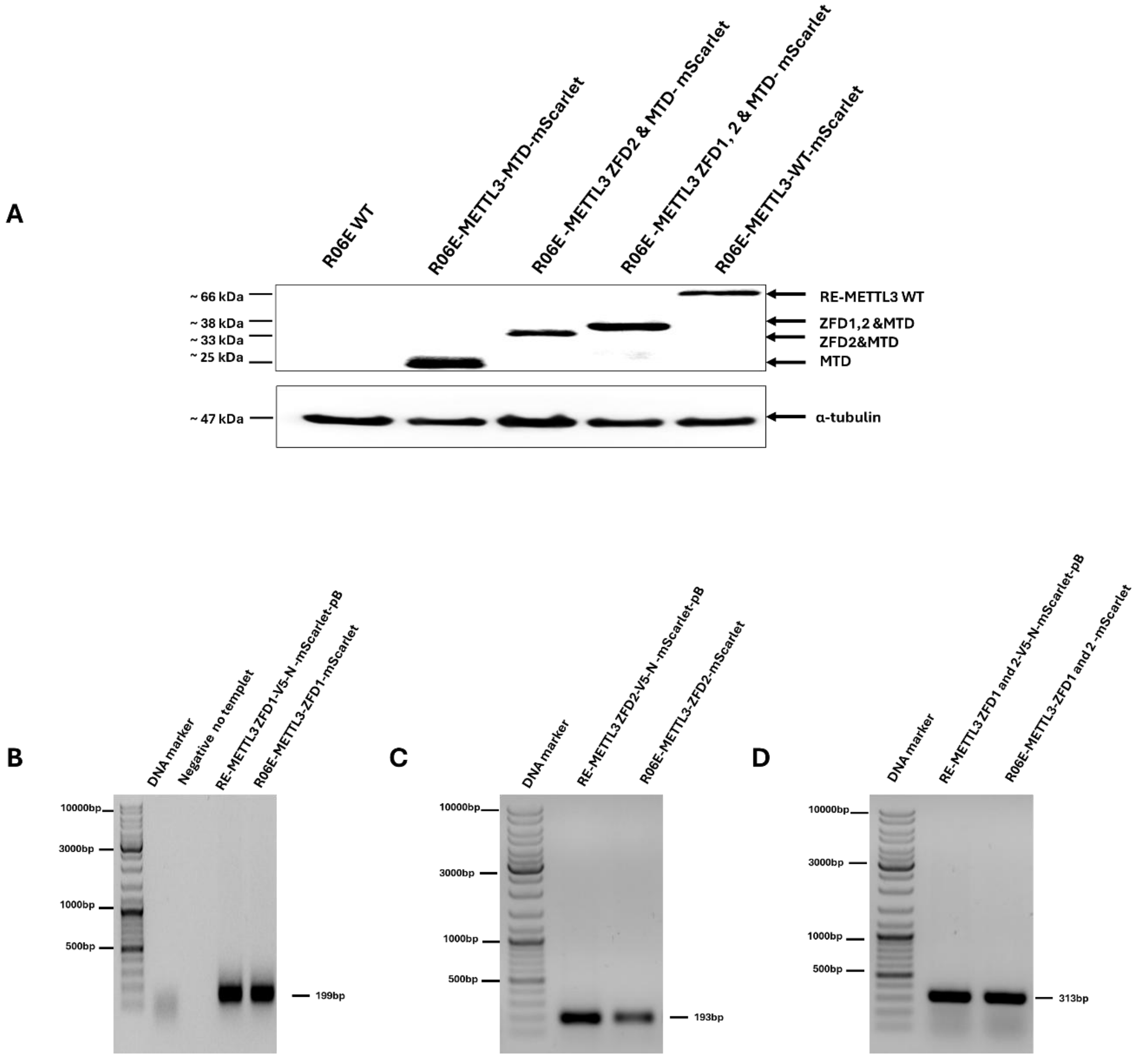

Figure 4.13. Validation of RE-METTL3 stable R06E cell lines. (A) WB analysis of established METTL3 R06E cell lines. R06E-METTL3-MTD-mScarlet, R06E-METTL3-ZFD 2 & MTD- mScarlet, R06E-METTL3-ZFD1, 2 & MTD- mScarlet, and R06E-METTL3-WT-mScarlet showed target bands at ~ 25, 33, 38, and 66 kDa, respectively. R06E WT did not demonstrate detection of any bands. The loading control, α-tubulin, was detected at ~ 47 kDa in all cell lines. (B-D) Agarose gel electrophoresis of METTL3-associated ZFDs R06E cell lines. R06E-METTL3-ZFD1-mScarlet, R06E-METTL3-ZFD2-mScarlet, and R06E-METTL3-ZFD1 & 2 -mScarlet showed the target bands at 199, 193, 313 bp, respectively.

4.3.7. Determination of Adapted rCedPV-GFP MOI in R06E Cells.

To establish an infection system for rCedPV-GFP in R06E, three MOI doses of the adapted virus (0.2, 1, and 2) have been inoculated into the R06E in 6-well plates, which in principle correspond to low, moderate, and high doses, respectively. Infection was assessed in the cells at 24 hpi.

At 0.2 MOI, approximately 30-50% of the cell population was expressing the viral GFP. However, this level might not be sufficient for the overexpression of METTL3 or investigating the viral pathogen-host interaction in the cells in subsequent experiments. In contrast to MOI 2, which demonstrated strong CPE and excessive cell death that would overwhelm the cellular machinery, leading to lower viral GFP, MOI 1 showed infection in the majority of cells with no major detrimental effect on the cells. Thus, MOI 1 was further selected for the subsequent experiments (**Figure 4.14**).

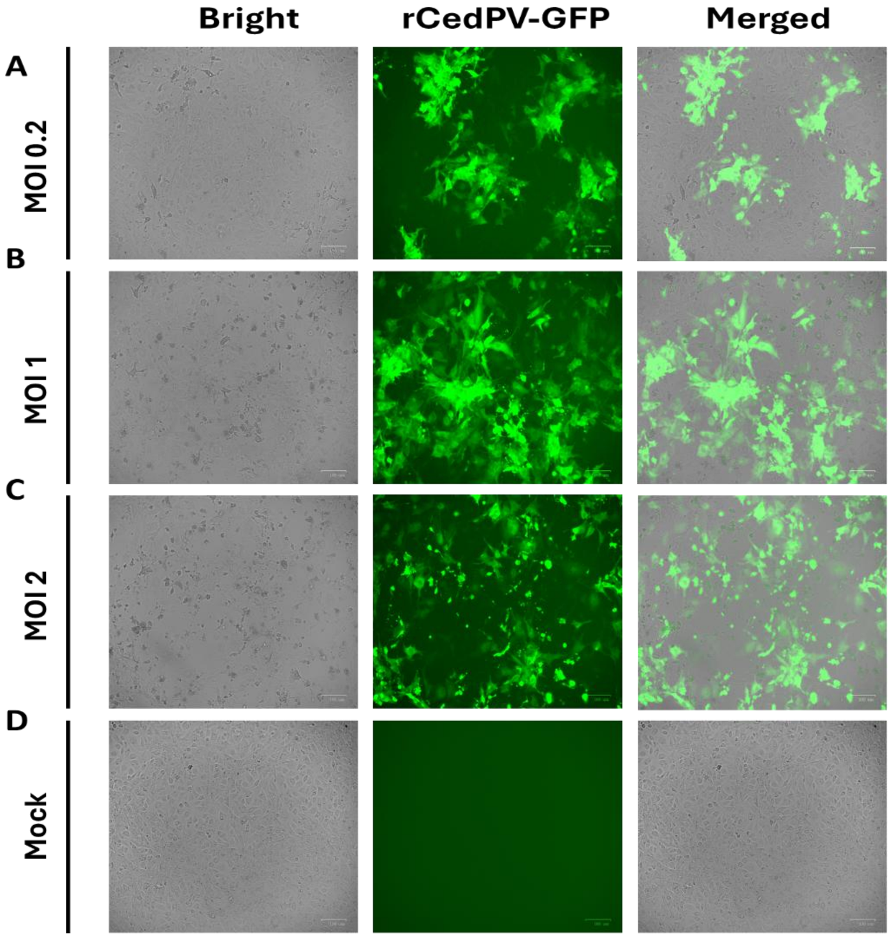

Figure 4.14. rCedPV-GFP MOI determination in R06E. (A) MOI 0.2 showed infection in 30-50% of the cells. (B) MOI 1 showed infection in the majority of cells with no detrimental effect on cells. (C) MOI 2 demonstrated strong CPE and excessive cell cytotoxicity. (D) Mock-infected cells served as a negative infection control. Scale bar = 100 µm.

4.3.8. RE-METTL3 and its Domains Reduce Replication of rCedPV-GFP Virus in R06E Cells

To investigate the role of RE-METTL3 in CedPV, R06E overexpressing METTL3 cell lines were plated in a 24-well plate and infected with rCedPV-GFP at an MOI of 1 for 24 h. Similarly, cells overexpressing the mScarlet (R06E-mScarlet) were plated as an infection control. Cells were checked under the microscope, and the supernatants were collected for viral titration. Compared to the R06E-mScarlet cells, R06E-METTL3-WT-mScarlet overexpressed cells demonstrated a significant reduction in the intracellular viral GFP signal as well as titration. Moreover, typical CedPV syncytia were detected in the mScarlet control cells more than in the METTL3 overexpressed cells, which showed either absence or minute syncytia (**Figure 4.15A−H**).

MTD is the main functional domain of the METTL3 writer, and ZFD are the RNA recognition domains of the protein [236]. Therefore, to determine which domain is responsible for the antiviral activity, METTL3-related domains from R06E cell lines were included in the analysis. Overexpression of all METTL3 domains resulted in antiviral outcomes comparable to those of METTL3-WT under the microscope. Similarly, when the virus was titrated, comparable antiviral activity was observed with the full-length protein and its domains, resulting in a significant reduction with 1 log lower virus titre than the mScarlet control (**Figure 4.15I**).

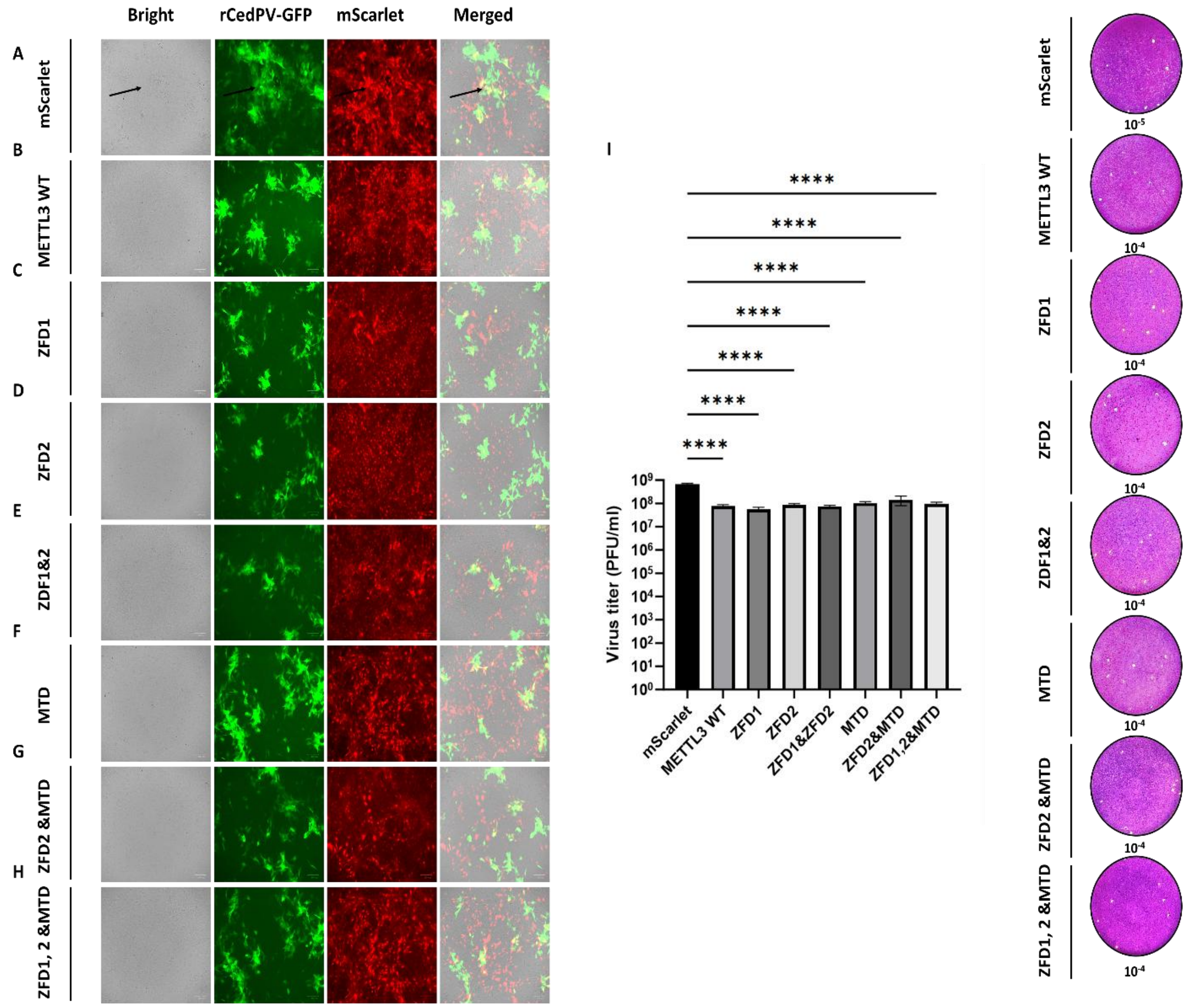

Figure 4.15. RE-METTL3 and its associated domains confer reduced replication of rCedPV-GFP virus in R06E cells. Overexpressed METTL3 R06E cell lines were infected with the rCedPV-GFP at an MOI of 1. At 24 hpi, cells were checked microscopically, and the supernatants were collected and titrated. (A-H) R06E-mScarlet showed high rCedPV-GFP viral replication compared to RE-METTL3-associated R06E cell lines. rCedPV-GFP syncerium in mScarlet control is highlighted in black arrows. Scale bar = 100 µm. (I) Statistical analysis of titrated rCedPV-GFP derived from the RE-METTL3 established R06E cell lines illustrated a significant reduction of the virus quantity in the METTL3 overexpressed cell lines in comparison to R06E-mScarlet. Data are presented as mean ± SD from three replicate wells. Statistical analysis was performed using One-way ANOVA with Dunnett's multiple comparisons.

4.3.9. RE-METTL3 Translocated to the Cytoplasm in the R06E upon rCedPV-GFP Virus Infection

The NLS of hMETTL3 is located at the N-terminus, upstream of the protein domains [235]. Thus, based on in-silico findings, the corrsponding domains of RE-METTL3 were cloned without including the NLS. Nevertheless, the retention of the domains' antiviral activity in the absence of the NLS has led us to think whether rCedPV-GFP re-localised the protein. Thus, to investigate this question, RE-METTL3-overexpressed R06E cell lines were seeded on glass coverslips for immunofluorescence examination with and without rCedPV-GFP. Infection was performed at 1 MOI for 24 h, and the cells were fixed. The overexpressed full-length protein and its domains were visualised using the V5 anti-tag antibody.

Microscopically, under normal conditions, RE-METTL3 was predominantly expressed in the nucleus, similar to hMETTL3 [235]. This nuclear localisation occurred despite the presence of Ala210Thr substitution in the core NLS of the METTL3 in *H. sapiens* and *R. aegyptiacus* (**Figure 4.16**). Although, as expected, upon stimulation with the rCedPV-GFP virus, the METTL3 protein was re-localised to the cytoplasm (**Figure 4.17B**). In contrast, all RE-METTL3 domains were expressed in the cytoplasm in both infected and mock cells (**Figure 4.17C− H**). Although a weak nuclear localisation was observed in both conditions.

In contrast to the WB, combined ZFDs (~ 9 kDa) could be detected with the fluorescence microscope using the V5 tag antibody, although the individual ZFDs (~ 4 and 5 kDa) remained indistinguishable from the background (**Figure 4.17C−E**).

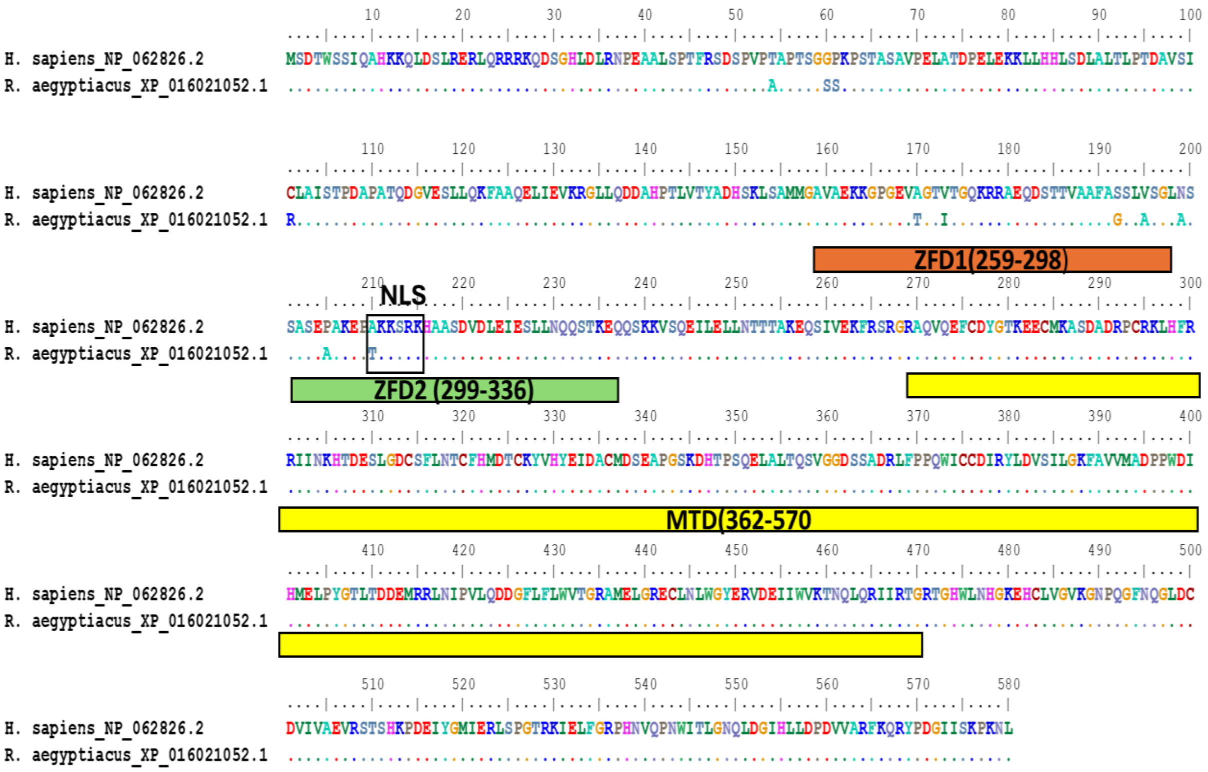

Figure 4.16. RE-METTL3 alignment between H. sapiens and R. aegyptiacus, showing the position and mutation of the NLS of the protein. Ala210Thr mutation of the protein NLS. NLS is highlighted in a black box.

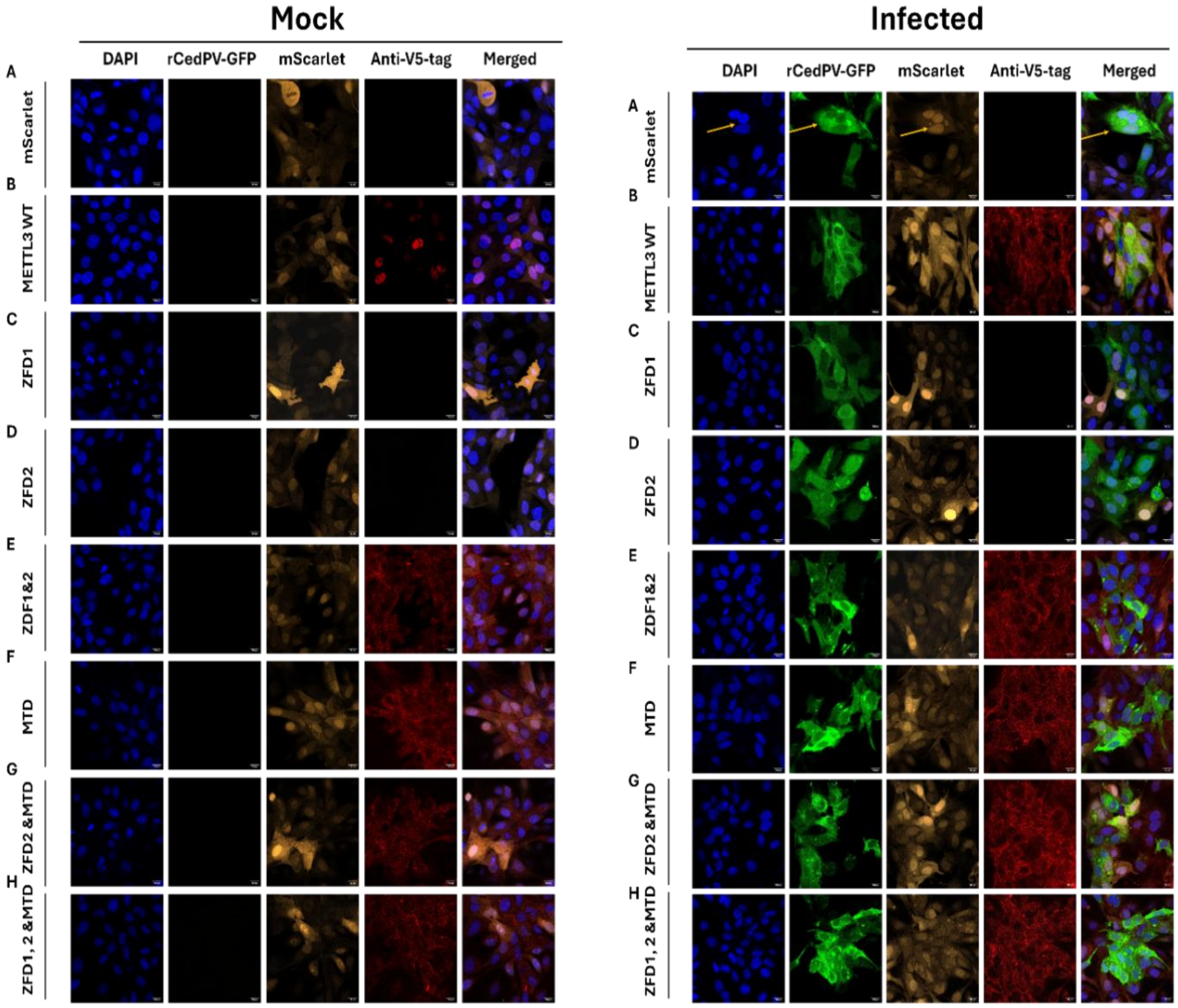

Figure 4.17. Cellular localisation of RE-METTL3 and the associated domain in the R06E with and without rCedPV-GFP stimulation, as demonstrated by the immunofluorescence imaging. The full-length RE-METTL3 showed nuclear localisation in mock cells, whereas the protein was translocated to the cytoplasm upon rCdPV-GFP infection. The related domains remained in the cytoplasm regardless of the presence or absence of the infection. (A) Mock-infected and infected R06E -mScarlet. (B) Mock-infected and infected R06E-METTL3-WT-mScarlet. (C) Mock-infected and infected R06E-METTL3-ZFD1-mScarlet. (D) Mock-infected and infected R06E-METTL3-ZFD2-mScarlet. (E) Mock-infected and infected R06E-METTL3-ZFD1 & 2 -mScarlet. (F) Mock-infected and infected R06E-METTL3-MTD-mScarlet. (G) Mock-infected and infected R06E -METTL3- ZFD 2 & MTD-mScarlet. (H) Mock-infected and infected R06E -METTL3 -ZFD1, 2 & MTD- mScarlet. DAPI (blue). rCedPV-GFP (green). METTL3 protein and related domains (red). mScalert (orange). rCedPV-GFP syncytia in mScarlet control are highlighted with an orange arrow. Scale bar = 100 µm.

4.4. Discussion

m6A is an RNA epi-transcriptomic modification that regulates many viruses across several host cell lines [276,344,345]. Therefore, it can act as a potential therapeutic target [346,347]. However, its role in viral replication remains largely unknown in bats and CedPV. Throughout this study, the role of m6A was investigated in the replication of CedPV, using rCedPV-GFP, in A549 and R06E cell lines. *R. aegyptiacus* brain (R05T) and liver cells (R06E) were infected with rCedPV-GFP; nevertheless, neither of the cell lines resulted in successful replication unless virus adaptation was employed. This was quite surprising, particularly for the brain cells, since rCedPV-GFP was able to replicate in the brain cell line of *P.alecto* (PaBr) [343], and *R. aegyptiacus and P. alecto* are closely related [313,342]. *P. alecto* is proposed to be a reservoir of CedPV; however, during the initial isolation of the virus, only kidney cells of *P. alecto* (PaKi) supported the viral replication, whereas other cell lines from the same species did not [14].

During the conduct of this research, Mohl, Diederich et al showed non-productive CedPV infection in *R. aegyptiacus* bats upon intranasal inoculation [348]. This finding might be consistent with the in vitro results in this study, which indicated that both *R. aegyptiacus* cell lines were not supportive of rCedPV-GFP replication. However, while drafting the thesis, Lenhard et al were able to establish an immortalised *R. aegyptiacus* cell line and employed it for a successful CedPV infection [349]. It remains unclear if Lenhard et al applied any viral adaptation method prior to the infection, although they used a nose-epithelium-derived *R. aegyptiacus* cell line (RaNep) to establish the infection, which contrasts with this study, which utilised *R. aegyptiacus* liver and brain tissue cell lines (R06E and R05T), respectively.

Previous computational analysis in the study suggested comparable m6A in *R. aegyptiacus* and *P. alecto*. However, the results from the infection experiments indicate profound differences in CedPV replication outcomes between the two bats and their related cell lines, suggesting that while the m6A regulatory system is structurally conserved and potentially functionally comparable between *R. aegyptiacus* and *P. alecto*, it does not play a substantial role in CedPV replication and restriction specificity among the two bats or tropism within their cell lines. Instead, other host and cell line-specific constraints likely exist. It is worth mentioning that *R. aegyptiacus* could not replicate NiV efficiently upon experimental inoculation, and several novel henipaviruses related to CedPV have been isolated from *R. aegyptiacus* in Africa [181,312]. Thus, molecular barriers influence the implication of this species as a potential reservoir for henipavirus members worth further investigation.

The adaptation of rCedPV-GFP in the *R. aegyptiacus* cells failed to achieve efficient replication of the virus in the first passage, and the CedPV-GFP signal was lost during subsequent passaging. The presence of efficient virus replication and an adequate titre of released infectious virus from the host cell are minimal requirements for virus adaptation, while using a proper, highly permissive host cell line is critical for obtaining an adapted virus, as such a cell line allows the adapted virus to spread within it rather than be lost during subsequent passages [350]. That might be an explanation of why rCedPV-GFP adaptation failed using passaging in *R. aegyptiacus* cells.

BHK-21 and VeroE6 are type I IFN-deficient cell lines [351,352] which support CedPV replication to high titre [340,353]. However, only VeroE6 yielded a virus capable of producing infection in *R. aegyptiacus* bat cells, whereas rCedPV-GFP generated from BHK-21 failed to produce, except for GFP dots, in R05T cells, implying unsuccessful replication despite the strong virus syncytia observed in the BHK-21 prior to the bat cell inoculation. Virus replication within a host is a complex process governed by a wide array of host intrinsic factors, which drive changes in the intruding virus, shaping its ability to propagate in the subsequent host [354,355].

In a recent study assessing the selection bias of different cell lines in the virus propagation and further downstream analysis, Vero cells were the most enriched cell line in proviral genes, followed by BHK-21 [356], which allows higher viral progeny production with a higher mutation rate than BHK-21. Additionally, while both VeroE6 and BHK-21 are deficient in type I IFN, only VeroE6 is obliterated in this response due to a genetic defect in the locus producing this response, while production of the type I IFN is minimally secreted in BHK-21 [357–359], a factor that could restrict the production of rCedPV-GFP mutant variants, impacting the replication in *R. aegyptiacus* cell lines. Taken together, it is likely that VeroE6 mutants were able to initiate replication in *R. aegyptiacus* cells, but failed to sustain the replication following 24h, probably due to the strong innate immune response that was elicited (as indicated by the progressive cell death) and overcame these few mutant viruses.

By harvesting the mutants at 24 hpi, when peaking and before they were lost, and applying alternative passaging between VeroE6 and bat cells, the viruses were expanded during each cycle in the permissive VeroE6 cells while becoming progressively better adapted to replication in the bat cell environment. Indeed, a similar result was obtained in CHIKV, where the virus increased fitness following alternating passaging between *Aedes albopictus* (C6/36) cells and BHK-21 and between the C6/36 and HeLa [360].

m6A is a major regulatory modification during virus replication, and it can be a targeted therapy against viruses [231,361,362], yet it has not been investigated in CedPV. Screening of hm6A machinery in A549 cells for a potential antiviral/proviral role in rCedPV-GFP revealed that overexpression of hMETTL3, but not hMETT14, had the strongest inhibitory effect on replication of rCedPV-GFP in A549 cells, while hWTAP had a moderate impact. METTL3 is the core catalytic subunit of the m6A methyltransferase complex, which exerts the methylation reaction on the target RNA [238]. Whereas METTL14 primarily functions as an RNA-binding protein that stabilises the METTL3-RNA interaction and lacks catalytic activity. On the other hand, WTAP recruits the METTL3-METTL14 dimer complex to initiate the catalytic reaction [233,238].

Research studies across different viruses highlight the role of METTL3 as an antiviral protein affecting viral transcripts and protein abundance either by directly affecting the m6A on the virus or influencing the immune response [269,282,283,363]. Additionally, an adequate level of METTL3 prevents the degradation of METTL14 and upregulates the WTAP protein level [364,365]. In the HCV, WTAP was translocated to the cytoplasm in infected cells, facilitating the interaction of the METTL3-METTL14 complex with the virus RNA [366], and it was hypothesised to relocate the heterodimer complex to methylate the *IRF3* and interferon alpha and beta receptor subunit 1 (*IFNAR1*) transcripts [367].

Although it remains to be clarified the details beyond these results, one can conclude that, while the METTL3-METTL14 complex works synergistically, METTL3 is the core antiviral protein of the human m6A writer complex against rCedPV-GFP, and overexpression of METTL4 alone will not result in any significant difference from what was present in the cells since the excess METTL14 will be degraded as the METTL3 has not been co-overexpressed (i.e. the basic level of METTL3 in the cells will not stabilise the overexpressed METTL14). In contrast, overexpressed WTAP increases recruitment of the m6A methyltransferase complex to target RNAs, where METTL3 can function as an antiviral. Notably, METTL3 functions independently of METTL14 and WTAP, increasing cellular translation [368]. Although such activity is not typical, in such a case, the possibility that the overexpression of METTL3 enhances translation of immune genes independently of METTL14 and WTAP cannot be excluded. However, this assumption raises an important question that needs to be addressed regarding the mechanism underlying the antiviral activity of WTAP independent of its partner METTL3, and whether WTAP itself functions as an independent antiviral factor.

Increasing the expression of hALKBH5 in A549 reduced rCedPV-GFP replication, whereas overexpression of hFTO was inert. Explanation of this finding might be due to the substrate specificity and the role of each protein as a modulator of the cellular innate response. ALKBH5 is selective toward m6A, while FTO has a broader substrate range, including m6A, m1A and m6Am; the latter appears to be its primary target [369,370]. FTO regulates energy and fat metabolism [371], whereas ALKBH5 is strongly associated with innate and antiviral response. The antiviral effect of ALKBH5 is due to removing viral/ host RNA m6A marks, influencing RNA nuclear export, stability, biogenesis and expression of viral or innate genes [372–374].

Overexpression of the five human readers was antiviral against rCedPV-GFP, with hYTHDC2 showing the most robust effect. Previous investigations have shown that cellular RNA translation is enhanced by YTHDF1, while the decay is provoked by YTHDF2, and YTHDF3 binds both proteins, mediating their processes. YTHDC1 is responsible for the alternative splicing and nuclear export, whereas YTHDC2 promotes the translation while decreasing the transcripts' abundance [336]; in other words, m6A readers directly recognise m6A and play a direct role in RNA processing, thus, they could be anticipated to have the greatest effect against the virus compared with the writers or erasers. Although it is interesting that hYTHDC2 was the most potent antiviral reader in rCedPV-GFP. In fact, the antiviral activity provoked by the hYTHDC2 was the most robust among all ten m6A machinery. This could point to a particular role played by YTHDC2 during the rCedPV-GFP infection in the cells. It is important to notice that YTHDC2 is an RNA helicase protein that binds non-m6A-bearing RNAs through its other RNA-binding domains, and in vivo studies suggested that mutations in its m6A binding pocket are not essential to maintain the functional integrity of the protein [375]. Thus, the particular role of YTHDC2 in CedPV needs further illustration.

The findings in this study illustrated that m6A machinery can be targeted for CedPV inhibition in human cells; however, it is important to interpret these results with caution regarding other pathogenic henipaviruses. Throughout the preparation of this thesis, Luo et al [220] demonstrated antiviral and inert roles of ALKBH5 and FTO, respectively, when overexpressed against NiV in Vero cells, consistent with this research work, while also providing a proviral role of METTL3 under the same conditions, which is contradictory to this research outcome of its inhibitory effect. As stated earlier, m6A is a potent virus regulator, either directly acting on the virus or indirectly using the innate immunity.

While CedPV is an excellent model for testing antiviral drugs against NiV and HeV due to its low biohazard risk compared with NiV and HeV, and results from this study indicated indeed similarity between the role of m6A in NiV and CedPV, it is important to note that they remain different viruses with particular immune responses, and CedPV has limited immune evasion capacity compared to NiV and HeV [14]. In this study, A549 was employed, which is immunocompetent, whereas Luo et al utilised Vero cells that are IFN-deficient [220], which might further affect the magnitude of the m6A-mediated antiviral response obtained in this study. Thus, intensive research on CedPV is warranted in diverse in vivo and in vitro models, in parallel with NiV and HeV or their proteins, wherever feasible, to determine if CedPV could be used as a model for targeted m6A therapy in humans against NiV and HeV.

Owing to the importance of METTL3 in methylation reaction, viral and immune regulation [237,282,283,307,376], combined with the in vitro and computational analysis demonstrating its inhibitory effect against rCedPV-GFP, and its high similarity to the human counterpart, METTL3 was selected to explore its role further against rCedPV-GFP in *R. aegyptiacus* R06E cells. The RE-METTL3 study in bat cells was complicated by several limitations, including low transfection efficacy of R06E, the possibility of protein misfolding upon fusing to a fluorescent protein, and incorporation of GFP into the CedPV genome, which limited the choice of selection of reporter protein.

To overcome these limitations, a bicistronic pB vector cassette that expresses V5-tagged RE-METTL3 and mScarlet fluorescent protein was designed under a single CAG promoter using IRES2 and two Kozak sequences at the beginning of each gene. Bicistronic cassette expression under the effect of one promoter ensures the expression of both genes, using IRES or 2A, with minimal transcriptional interference, which can occur when different promoters are applied [377,378]. Although one putative limitation of this strategy is the lower expression level of the second gene compared to the first when employing IRES, and inefficient protein cleavage with 2A sequences [378–380], the former offers additional advantages over the latter, including complete separation of the proteins and operating the translation under viral infections that shut down the cap-dependent translation [379]. Therefore, IRES2, which is an improved version of WT IRES, was employed, with the addition of the Kozak sequence at the beginning of the gene to enhance the translation of the mScarlet [381,382]. The expression trial of this cassette in A549 cells, prior to the bat cells, demonstrated comparable levels of RE-METTL3 and mScarlet, indicating the utility of this construct across different cell culture models.

In order to study the structural and functional role of RE-METTL3, the functional domains, ZFD1, 2, and MTD, were cloned either individually or combined into the RE-METTL3-WT-V5-N-mScarlet-pB vector and established stable R06E cell lines expressing these domains using the pB transposition. The transposition involves cutting a DNA sequence (insert) from the donor pB vector at its flanked inverted terminal repeats (ITR) and integrating this sequence into a TTAA-rich region of the host genome via the transposase enzyme, which is typically expressed from a separate vector co-transfected with the pB construct. The engineered cell can then be selected and expanded using a selectable marker (puromycin) that was added to the pB cassette downstream to the DNA insert [383]. This system enables efficient, feasible and flawless integration into the host genome, even in hard-to-transfected cells like the bat cells, while minimising the cellular stress and immune responses typically associated with conventional viral integration methods [384–386].

The cell lines were generated successfully and verified successfully using the WB, although target bands could not be seen in cells expressing ZFD, which might be due to the low molecular weight of the domains ZFDs (~ 4 and 9 kDa), to be detected using the standard WB procedures, as alternative the integration of the ZFDs cassette within the cell lines' genomes was detected using the conventional PCR.

Infection with rCedPV-GFP in the R06E cell line yielded inhibition of viral replication when the full-length METTL3 protein or its domains were overexpressed. This is consistent with the antiviral effect observed for hMETTL3 in A549 cells and with the in-silico analysis, which suggests a similar core function between *H. sapiens* and *R. aegyptiacus* METTL3 in line with the bioinformatics analysis.

Despite the Ala210Thr mutation observed in the core NLS between the human and Egyptian fruit bat, RE-METTL3 was found microscopically to localise predominantly in the nucleus of R06E cells, similar to its human counterpart [235], whereas its domains were restricted mainly to the cytoplasm, as expected due to the absence of the NLS. The weak nuclear localisation of the domains suggests the passive diffusion of the domains due to their small size into the nucleus rather than the presence of an intrinsic NLS [387]. Together, these findings either suggest that the NLS of the RE-METTL3 is located in the N-terminus, and the conservation of the alanine residue is not essential for maintaining nuclear localisation in *R. aegyptiacus* or imply that RE-METTL3 possesses additional NLSs within its N-terminus.

In infected rCedPV-GFP cells, RE-METTL3 was translocated from the nucleus to the cytoplasm. Typically, during viral infection, viruses redirect METTL3 to the cytoplasm, where viral replication occurs, to reprogram host and viral m6A methylation, through binding directly with the protein, and overexpression of the METTL3 results in suppressing the antiviral immunity and enhancing the virus replication; this strategy is universal across many viruses including paramyxoviruses [277,280,388], CedPV is a paramyxovirus, and replication of these viruses occurs in the cytoplasm [13,26]. To the best of our knowledge, CedPV is the first virus reported to be inhibited by overexpression of METTL3.

During nuclear-cytoplasmic shuttling of the M protein of bovine parainfluenza virus type 3 (BPIV3), the viral protein redirects METTL3 from the nucleus to the cytoplasm, where it methylates the viral N protein. This enhances N protein stability while leaving host IFN-β transcripts in the nucleus less methylated. Together, these effects inhibit the antiviral immune response and promote viral replication. This strategy is also observed in other paramyxoviruses, including Nipah, Sendai, and measles [388]. Since CedPV cannot evade the IFN-β responses, in contrast to other paramyxoviruses, it is likely that overexpression of METTL3 in R06E cells led to saturation of the rCedPV-GFP M, leaving excess METTL3 in the nucleus. This residual nuclear METTL3 can methylate IFN-β transcripts, thereby enhancing the antiviral immune response.

It is worth noting that paramyxovirus M-METTL3 binding is mediated by the MTD domain of the protein. Thus, overexpression of MTD alone may bind all available rCedPV-GFP M protein, producing a similar effect to overexpression of the full-length protein. It is worth mentioning that paramyxovirus M-METTL3 binding is mediated by the MTD of the protein [388]. Hence, it is also likely that when MTD was overexpressed, it bonded to all rCedPV-GFP M, leading to a similar effect as the overexpressed full-length protein. In contrast, ZFDs bind to methylated RNA [236]. Thus, their antiviral effect might be due to blocking the viral RNA from engaging in replication.

As mentioned, CedPV has limited immune evasion capacity compared to NiV and HeV. The results of this study indicate that although the mechanism of METTL3 recruitment is conserved across paramyxoviruses, the outcome of METTL3 overexpression differs in CedPV. This limits the use of CedPV as a model for targeted m6A-based therapies against pathogenic henipaviruses. Nevertheless, these findings could be exploited to design drugs that target the M region responsible for METTL3 binding or to develop molecules that mimic the MTD domain. Additionally, given that the CedPV redirects METTL3 to the cytoplasm, further clarification is needed to determine whether other m6A writers, WTAP and METTL14, are translocated as well to the cytoplasm with METTL3 to methylate the viral transcripts.

Overall, this study provides insight into the m6A-CedPV paradigm in both bat and human cell models and lays a cornerstone for upcoming research whereby host epi-transcriptomic regulation constitutes a critical layer of future antiviral interventions against henipaviruses.

Chapter 5. ACE2 as a Key Determinant Unlocks Replication of BtCoV HKU5-SE in *Rousettus aegyptiacus* Cells

5.1. Introduction

Bats are discrete flying mammals with more than 1,400 species, accounting for approximately 20% of mammalian species [152]. Their remarkable ecology, life longevity, and roosting behaviours have facilitated the maintenance of diverse viral communities, positioning bats as important reservoirs for many zoonotic viruses [155,165,166].

Over decades, BtCoVs have gained attention from the scientific community due to their potential for spillover transmission to humans, either directly or indirectly via an intermediate host [104,389]. Such examples include SARS-CoV, MERS-CoV, and SARS-CoV-2. These viruses triggered pandemics, economic crises, and caused tremendous loss of millions of human lives in the past few years [390–392].

The capacity of coronaviruses to cross species barriers depends on multiple factors. While TMPRSS2 and CTSL are important determinants for coronavirus entry [393,394]. Receptor usage is among the factors that constrain the host tropism and interspecies transmission of coronaviruses by mediating direct interaction with host cell receptors [395,396]. Several types of receptors have been identified for coronavirus species, including APN, DDP4, and ACE2 [166]. Among these, ACE2 serves as a well-studied entry receptor utilised by several coronaviruses, including SARS-CoV, SARSCoV-2, and various bat-derived beta coronaviruses [395,397–399]. In this context, expressing the ACE2 of different bat orthologs in the HEK 293T cell line, which lacks expression of the receptor, resulted in varying degrees of SARS-CoV and SARS-CoV-2 entry, reflecting different degrees of susceptibility of coronaviruses among the Chiroptera [397].

Recently, the discovery of the bat HKU5 coronavirus lineage 2 (HKU5-CoV-2) has raised concerns about its spillover potential due to its similarity to MERS-CoV and its interaction with hACE2 as a functional receptor for entry into human cells [59,105]. This finding points to the potential adaptability of the receptor usage of the virus, which may enhance the zoonotic potential of certain BtCoVs. Meanwhile, the risk posed by HKU5-CoV lineage 1(HKU5-CoV-1), which cannot engage with humans but with the *Pipistrellus abramus* (*P. abramus*) bat ACE2, cannot be entirely dismissed, given the continuous evolution and adaptation of coronaviruses in different hosts and the identification of numerous SARS-like coronaviruses in bats [154,400–402] which makes it difficult to determine which bat species is likely to be a reservoir of such a virus.

Recently, the susceptibility and shedding of SARS-CoV-2 by *R. aegyptiacus* have highlighted the urgency of understanding factors associated with the potential for this species [403,404]. Till this end, it was assumed that ACE2 could be one of these factors. Understanding the role of ACE2 in *R. aegyptiacus* is crucial for assessing the likelihood of cross-species transmission and identifying host factors that either facilitate or hinder SARS-like coronavirus replication in such species.

This study aimed to determine whether the ACE2 receptor of *R. aegyptiacus* acts as a barrier to the emergence of SARS-like HKU5 lineage 1, using the HKU5-SE virus and R06E cells.

5.2. Specific Objectives

- **6.2.1.** Propagation, titration, and establishment of a TaqMan assay for quantification of BtCoV HKU5-SE.
- **6.2.2.** Testing susceptibility of R06E WT to BtCoV HKU5-SE virus and determination of the molecular barriers to the efficient viral replication.
- **6.2.3.** Cloning and tagging of hACE2 and RE-ACE2 in the pB CAG-EGFP vector.
- **6.2.4.** Establishment of stably expressing hACE2 and RE-ACE2 BHK-21, A549, and R06E cell lines using the cloned pB vectors and verification of these cell lines using WB.
- **6.2.5.** Investigating the role of both hACE2 and RE-ACE2 receptors in the replication of BtCoV HKU5-SE in the R06E cells using viral quantification, growth and replication kinetics as well as immunofluorescence analysis.
- **6.2.6.** Understanding the role of TMPRSS2 and CTSL in the entry of BtCoV HKU5-SE in R06E cells.
- **6.2.7.** qPCR quantification of *hACE2*, *RE-ACE2*, *TMPRSS2* and *CTSL* in humanised R06E cells upon peak BtCoV HKU5-SE infection.
- **6.2.8.** Heat map analysis of the top ten differentially expressed genes and RE-ACE2 isoform switching in the humanised R06E at the peak BtCoV HKU5-SE infection.

5.3. Results

5.3.1. Propagation of BtCoV HKU5-SE in VeroE6 Cells

For the propagation of BtCoV HKU5-SE, VeroE6 cells were seeded and inoculated with 100 µL of the virus stock for 2 h; infected cells were monitored daily for viral infectivity and the development of CPE. At 24 hpi, VeroE6 cells exhibited cell rounding and syncytia, which progressed to cell lysis, death, and detachment at 48 hpi. At 72 hpi, almost all cells were lysed and sloughed off the flask surface (**Figure 5.1**). The supernatant was collected at that point, the virus was clarified, titrated, and stored at -80 ºC for further use.

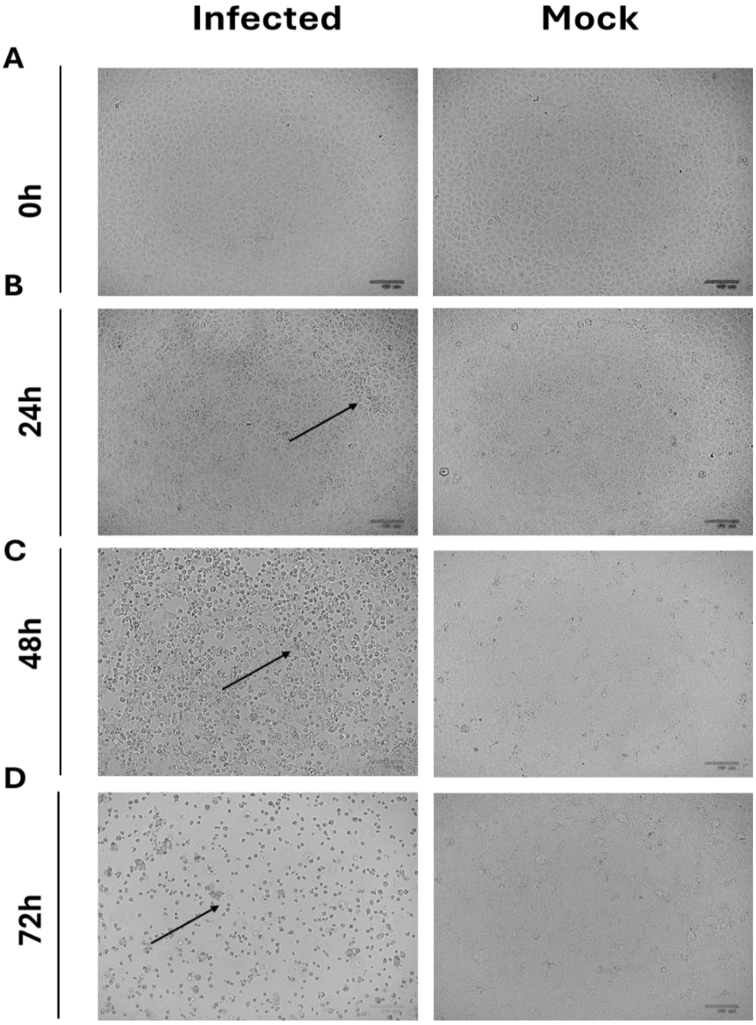

Figure 5.1. BtCoV HKU5-SE propagation in VeroE6. Cells were inoculated with 100 µL of the virus stock, and the viral CPE was observed for 72 h till the virus was harvested. (A) Viral infection at 0 h showed no CPE. (B) Viral Infection at 24 h showed cell rounding and syncytia. (C) Viral infection at 48 h showed cell lysis, death, and detachment. (D) Viral infection at 72 h showed increased cell lysis, death, and detachment. Mock-infected cells, which served as a negative control of infection, are shown in parallel. Scale bar = 100 µm.

5.3.2. TaqMan RT-qPCR Assay for the Quantitative Detection of BtCoV HKU5-SE Showed Specificity and Sensitivity to the Viral N Gene

In order to study the entry barriers against the BtCoV HKU5-SE infection in different cell lines, it was essential to determine the quantity of the virus accurately. For the TaqMan assay development, a region spanning 100 to 236 bp of the N gene of the parental HKU5 virus was selected to design the primer. The TaqMan probe was designed proximal to the forward primer. To evaluate the specificity of the designed primers-probe set, BtCoV HKU5-SE and SARS-CoV-2 were successfully propagated in VeroE6 cells and subjected to RNA extraction. The isolated RNAs were used as templates in triplicate in the TaqMan RT-qPCR assays employing the designed primers and probe. The assay yielded successful positive amplification of the N gene of the BtCoV HKU5-SE across the three replicates, while no amplification of the SARS-CoV-2 Omicron (B.1.1.529) N gene was observed, confirming the specificity of the established TaqMan RT-qPCR assay for BtCoV HKU5-SE (**Figure 5.2**).

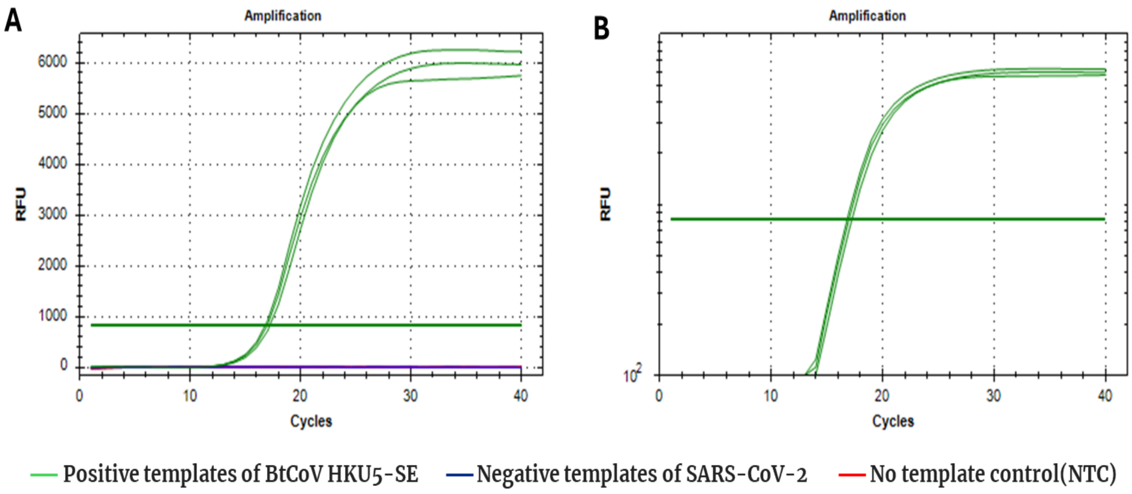

Figure 5.2.TaqMan amplification assay of BtCoV HKU5-SE showing amplification of the BtCoV HKU5-SE N gene compared to SARS-CoV-2. (A) Linear amplification curve (B) The logarithmic amplification curve. TaqMan RT-qPCR assay was performed in triplicate.

Next, the IVT was conducted to generate RNA templates required to determine the standard curve for copy number determination. Viral RNA previously extracted from VeroE6 was subjected to reverse transcription to produce cDNA, which was then amplified in conventional RT-qPCR using the same primer set used in TaqMan BtCoV HKU5-SE with the T7 promoter appended upstream of the forward primer. The PCR amplicon containing the T7 promoter was run on the agarose gel electrophoresis and yielded a band at 157 bp successfully. The amplicon was purified and used as a template for the IVT reaction (**Figure 5.3A**). The pGEM® Express Positive Control Template was used simultaneously to validate the reaction.

On agarose gel, the pGEM® Express Positive Control Template showed two transcribed RNA bands as expected (**Figure 5.3B**), which indicated the successful transcription of the BtCoV HKU5-SE N gene. The IVT reaction products were then treated with DNase I to remove residual DNA and run on an agarose gel. Treated and untreated pGEM® Express Positive Control Template samples were run on an agarose gel for comparison. While the non-treated pGEM® Express Control could be visualised on the gel, the DNase I-treated one could not be detected (**Figure 5.3C**). Similarly, the agarose gel of the N gene DNase I product was empty, with no bands detected (data not shown). Taken together, this indicates the efficient removal of the residual template DNA.

Measuring the two DNase I treatment reaction products (i.e., IVT RNA of the virus and the pGEM® plasmid) by the nanodrop has shown a reading for the BtCoV HKU5-SE RNA, not the pGEM® plasmid, indicating the presence of only viral RNA for the downstream qPCR. These findings collectively confirm the successful IVT of the BtCoV HKU5-SE N gene.

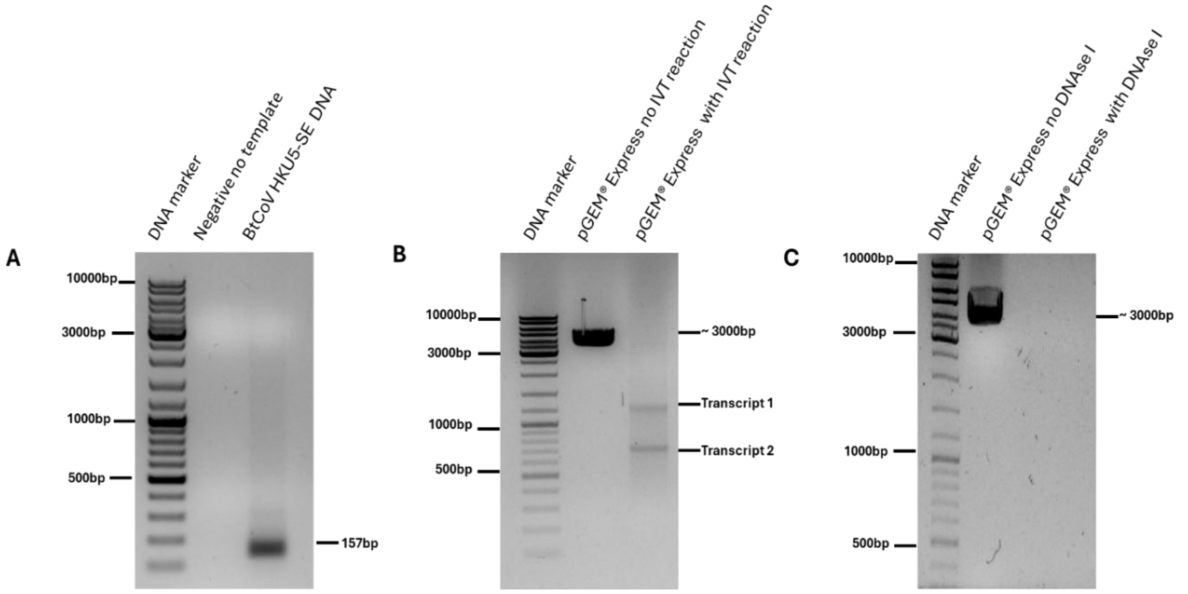

Figure 5.3. cDNA synthesis and IVT of BtCoV HKU5-SE gel analysis. (A) RT-PCR of the virus showed amplification of the viral N gene with the T7 promoter. (B) IVT reaction of pGEM® Express Control showed two transcripts. (C) DNAse I treatment of pGEM® Express Control showed the absence of the plasmid DNA band following the DNAse I treatment.

The resulting transcribed viral RNA was then serially diluted ten-fold using NFW to generate concentrations ranging from approximately 3.4 × 10^{10} to 3.4 RNA copies, which were equal to 2.5 ng RNA and 0.25 attogram (ag), respectively. The dilution standards were analysed in the assay in duplicates. Additionally, no RT and negative template control reactions were run in parallel for confirmation of the absence of contamination.

From the first to the ninth dilution, the intra-assay variability ranged from 0.03 to 0.49 cycles (i.e., from Cq 8.89 to 36.71). However, that difference between the replicates increased in the next dilution onward, where the 10th dilution showed a 1.68 Cq value difference, and the 11th dilution had only one replica that was able to pass the threshold limit (**Table 5.1** and **Figure 5.4)**.

Data from the standards were fitted to a straight line on the plot; however, the data of the 10th dilution showed deviation of the duplicates from the straight line of the plot, and at the 11th dilution, only one replica was plotted, while the other was outside the linear range of the curve.

To assess the performance of the standards, Y intercept, slope, and PCR efficiency (E) were calculated based upon the replicates which fitted the curve (i.e. till the 10th dilution standards). The curve showed a slope value of -3.3266, which was equal to 99.8% PCR efficiency. Moreover, the intercept was 44.406 (**Figure 5.5B**). Thus, the LOD for BtCoV HKU5-SE was determined as approximately 342 RNA copies/reaction (i.e. Cq value 36.71).

Table 5.1. Cq values of Bt CoV HKU5-SE standards

Dilution	RNA copies/reaction	Cq value	Cq difference
11	3.428	N/A	N/A
		38.96	
10	34.28	38.62	1.68
		36.94	
9	342.8	36.71	0.29
		36.42	
8	3428	32.91	0.45
		33.36	
7	34280	29.73	0.23
		29.96	
6	342800	26.32	0.15
		26.17	
5	3428000	23.22	0.45
		22.77	
4	34280000	19.35	0.12
		19.47	
3	342800000	15.99	0.18
		15.81	
2	3428000000	12.49	0.02
		12.47	
1	34280000000	8.99	0.10
		8.89	

N/A, not applicable (did not pass the threshold limit)

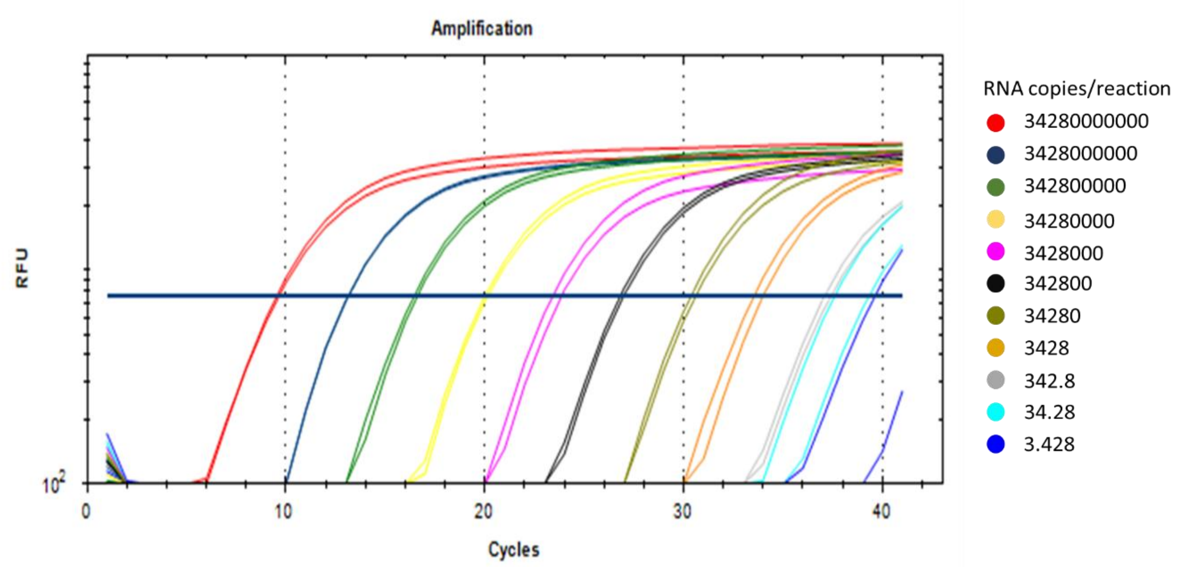

Figure 5.4. Amplification plot of BtCoV HKU5-SE standards in duplicates. All dilution standards were detected above the threshold, except for the final, most dilute standard, RNA copy number ~ 3.4. Different colours indicate the dilution standards. Copies per reaction are illustrated in the figure.

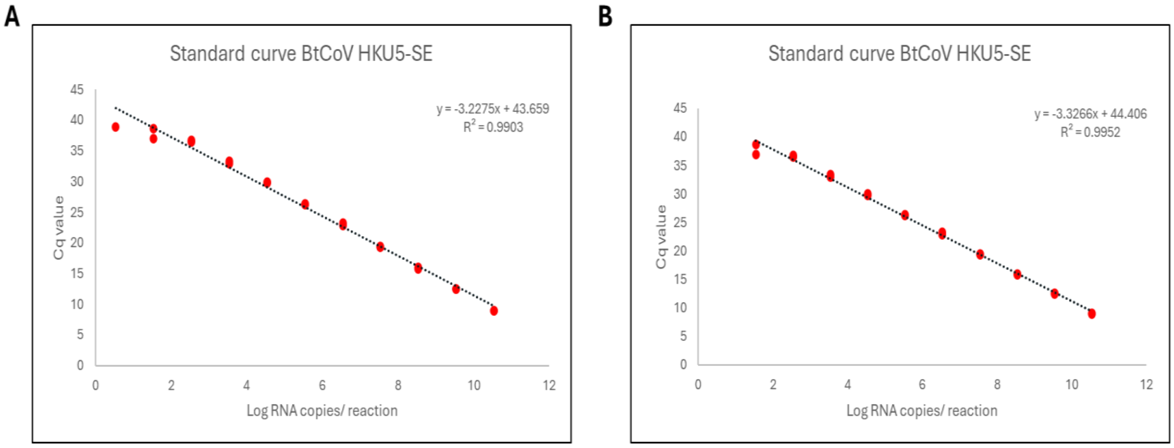

Figure 5.5. Standard curve of BtCoV HKU5-SE. Data from the viral dilution standards duplicates were fitted with a linear regression, except for the two lowest-concentration dilutions. (A) Standard curve with all standards data. (B) Standard curve generated using data from the 1st to the 10th dilution only. Y intercept, slope, and PCR efficiency (E) are shown for each curve, respectively.

5.3.3. Resistance of R06E WT Bat Cells to BtCoV HKU5-SE Infection.

In order to initially assess the BtCoV HKU5-SE replication in *R. aegypticus* cells, R06E WT cells were seeded in a 12-well plate and infected with the virus at an MOI of 1. VeroE6 was used in parallel as a known positive control for the infection. At 24 hpi, supernatants were collected from both cell lines, and the infected monolayers were examined microscopically for the development of any signs of virus-induced CPE.

As expected, VeroE6 displayed the characteristics of CPE of the coronavirus, including cell syncytia and rounding. In contrast, R06E WT showed no observed signs of viral infection or morphological change at the same time point (**Figure 5.6A**). Moreover, clear and distinct BtCoV HKU5-SE plaques were produced from the VeroE6 supernatant, while no plaques were observed from the R06E-derived supernatant (**Figure 5.6B**). These results suggested abortive infection of the BtCoV HKU5-SE in the R06E WT.

Different assumptions that could explain this observation, including, (i), inability of virus to attach or enter the cells (lack of expression of the key entry determinants including ACE2 receptor, TMPRSS2, CTSL), (ii) failure of viral replication, (iii) transcription or (iv) egress due to defect of the cellular machinery that supports these processes and (v) finally elimination of the virus by the R06E due to an immune response. Indeed, bats have a unique immune response that can counteract many infections [405]. To test these hypotheses, first, the ability of the R06E WT to express *ACE2* under normal physiological conditions was assessed by RT-qPCR. The R06E was indeed expressing *ACE2* under normal physiological conditions, albeit at a relatively low level (Cq value ~ 27), approximately half that of the housekeeping gene *EEF1A1* (Cq value ~14) ((**Figure 5.7A** and **B**). Subsequently, the input amount of the BtCoV HKU5-SE virus in R06E WT and VeroE6 was compared at 0 hpi. R06E WT showed lower uptake of the virus than VeroE6, where the viral amount entered the R06E WT was beyond the detection limit of the TaqMan qPCR assay (**Figure 5.7C).**

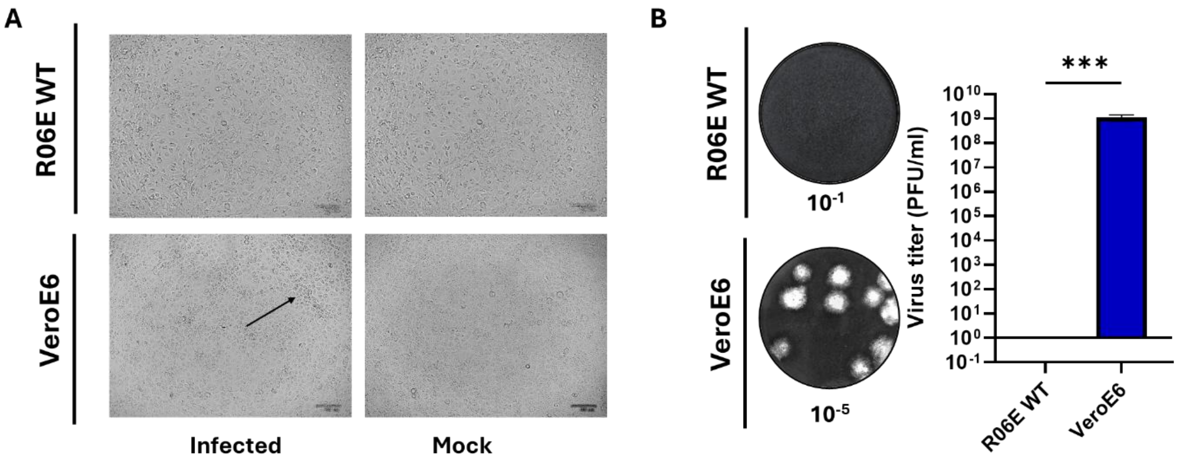

Figure 5.6. BtCoV HKU5-SE infection in R06E MO 1 at 24 hpi. (A) R06E WT demonstrated no signs of viral infection, whereas VeroE6 showed cell rounding and syncytia. Mock-infected cells served as a negative infection control. Scale bar = 100 µm. (B) Plaque assay titration of BtCoV HKU5-SE showed the absence of virus replication and plaque formation in R06E WT compared to VeroE6, which displayed clear plaque formation. Data are presented as mean ± SD of four independent experiments. The statistical analysis was performed using a two-tailed, unpaired t-test.

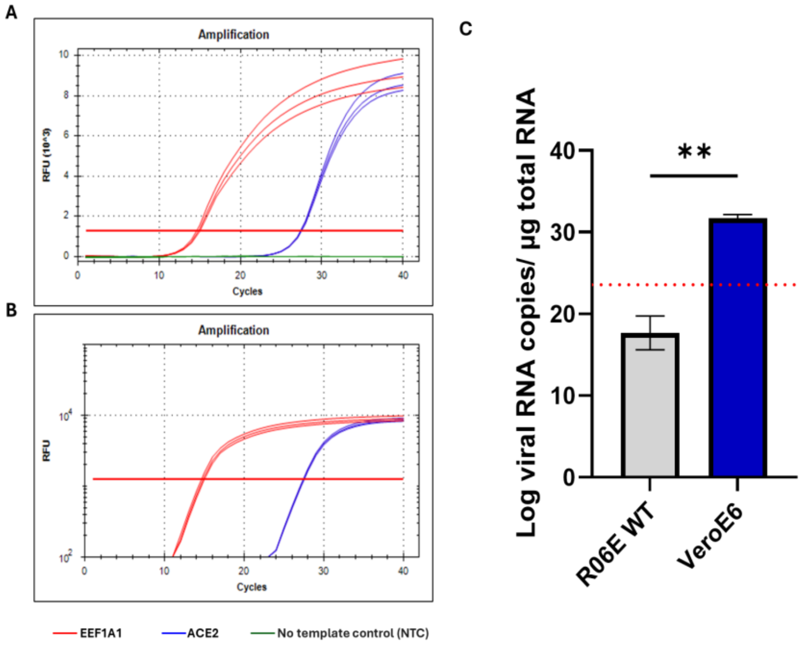

Figure 5.7. Low expression of RE-ACE2 contributes to low entry of BtCoV HKU5-SE in R06E (A) Linear amplification plot and (B) logarithmic amplification plot of dye-based quantitative RT-qPCR showing relatively lower expression levels of R06E ACE2 compared to the reference gene EEF1A1. The exponential amplification of R06E ACE2 occurred approximately at cycle 27, and EEFA1A at cycle 14. (C) TaqMan quantification of cell-associated BtCoV HKU5-SE viral RNA in R06E and VeroE6 at 0 hpi of 1 MOI of the virus. R06E WT exhibited lower viral input uptake with RNA levels remaining below the assay's LOD, in contrast to VeroE6. The dye-based RT-qPCR data represented three technical replicates. Data from the TaqMan are presented as mean ± SD of four independent experiments. The statistical analysis was performed using a two-tailed, unpaired t-test. LOD of the RT-qPCR assay is shown in dashed red.

In silico and receptor-based studies have demonstrated that the ACE2 receptor of *R. aegyptiacus* had low binding affinity to the SARS-CoV-2 spike, allowing less virus entry and replication [150,406]. Although no analogous studies related to SARS-CoV have been undertaken in *R. aegyptiacus,* a similar situation in the SARS ectodomain (SE)-engineered virus was hypothesised, given the high amino acid similarity between SARS-CoV and SARS-CoV-2 spikes [62]. This could explain the reduced virus entry that was observed early in the RT-qPCR. However, that explanation alone won't be adequate if other cellular barriers exist, such as protease deficiency, immunity or viral replication machinery defects that would all eventually lead to the resulting abortive infection.

To investigate these barriers, the BtCoV HKU5-SE infection was boosted with an exogenous trypsin TPCK; however, R06E displayed significant cytotoxicity to the TPCK at concentrations as low as 0.25 and 0.5 µg/mL, in contrast to the more resistant VeroE6 cells, limiting the utility of this approach. Alternatively, the virus infection was increased to 5 MOI, CPE was inspected, and supernatants were collected from both cell types.

Compared to the VeroE6, which showed increased CPE at 5 MOI, at 24 hpi, R06E showed very few scattered cells detaching from the monolayer (**Figure 5.8A**). In parallel, R06E showed small numbers of plaques restricted to the first viral dilution compared to the VeroE6 (**Figure 5.8B**). Due to these inconclusive signs, the MOI of BtCoV HKU5-SE was increased to 15. At 24 hpi, R06E exhibited a higher rate of cell detachment and plaque formation, although few (**Figure 5.9**), confirming the compatibility of R06E machinery to BtCoV HKU5-SE replication and egress.

Given the minimal CPE and plaque formation of R06E at the higher MOI dose, 15 suggested that ACE2 is the primary barrier to BtCoV HKU5-SE replication in R06E cells, rather than limitations in cellular proteolytic processing or innate immune responses.

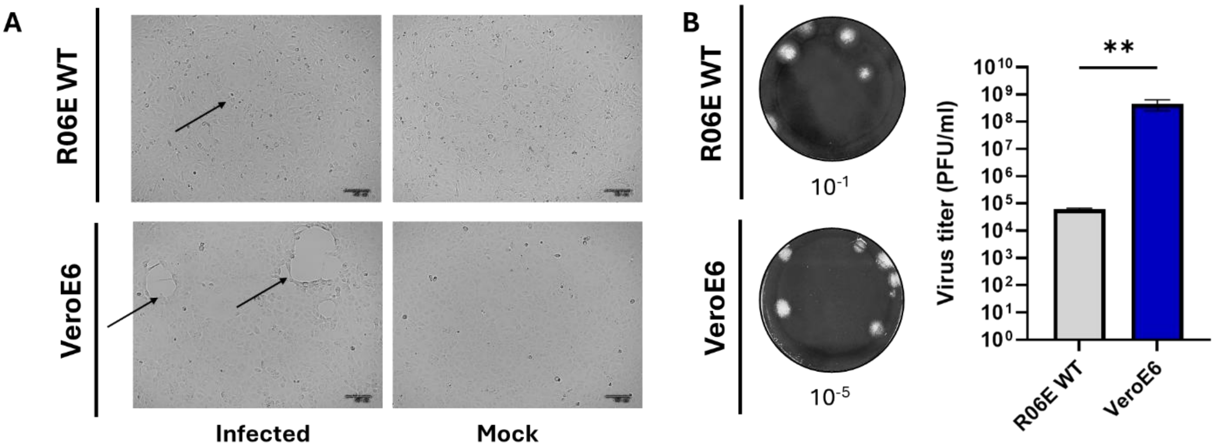

Figure 5.8. BtCoV HKU5-SE infection in R06E MO 5 at 24 hpi. (A). Infected R06E WT demonstrated spares and dispersed cell detachment in contrast to VeroE6, which showed extensive cell lysis and sloughing. Mock-infected served as a negative infection control. Scale bar = 100 µm. (B). Plaque assay titration of BtCoV HKU5-SE at MOI 5 showed fewer plaques in R06E WT than in VeroE6. Data are presented as mean ± SD of four independent experiments. The statistical analysis was performed using a two-tailed, unpaired t-test.

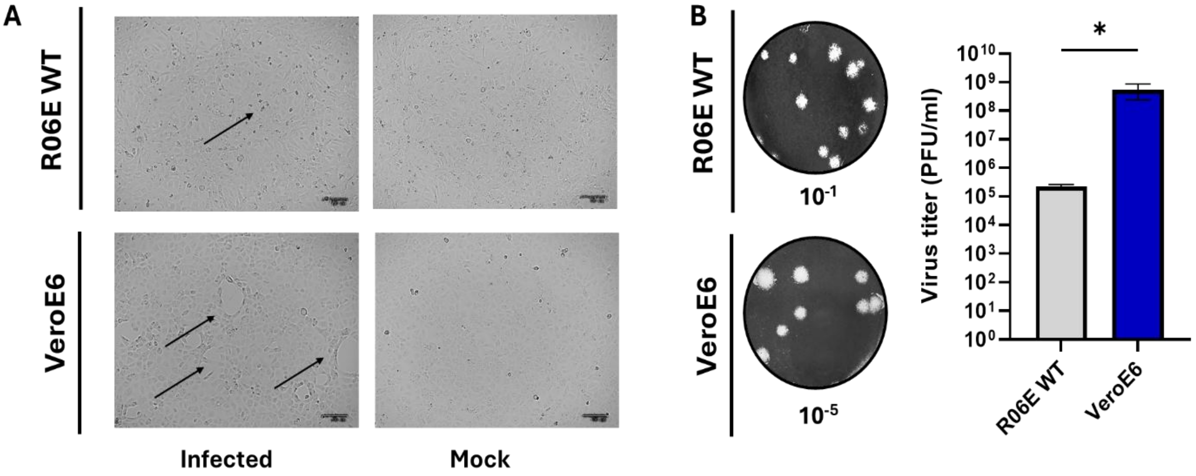

Figure 5.9.BtCoV HKU5-SE infection in R06E MO 15 at 24 hpi. (A) Infected R06E WT showed increased detachment and sloughing, while VeroE6 demonstrated marked cell lysis and detachment over the monolayer. Mock-infected cells were included as a negative infection control. Scale bar = 100 µm. (B) BtCoV HKU5-SE plaque assay titration showed a higher number of plaques and virus replication in R06E WT at 15 MOI, whereas viral replication levels in VeroE6 cells remained unchanged compared to lower MOIs. Data are presented as mean ± SD of four independent experiments. The statistical analysis was performed using a two-tailed, unpaired t-test.

5.3.4. Establishment of hACE2 and RE-ACE2 Stable Cell Lines Receptors Via PiggyBac Transposition

Previous observation demonstrated that BtCoV HKU5-SE failed to replicate efficiently in the R06E WT cell line due to the receptor barrier. Therefore, to investigate whether the expression level or the species-specific nature of the Egyptian rousette ACE2 was the barrier to the replication of BtCoV HKU5-SE, the bat receptor (RE-ACE2) was ectopically expressed, along with its human counterpart (hACE2), the functional receptor for the SARS-CoV [407], in R06E and BHK-21. The latter lacks the endogenous ACE2 expression [408].

The pB transposon system was utilised to integrate the hACE2 and RE-ACE2 receptors into the genome of the cells. Cloning of the hACE2-EGFP-Flag-C-pB was successfully performed through PCR amplification of the hACE2-EGFP gene from the pcDNA3.1-ACE2-GFP vector using primers tagged with the AgeI and NotI restriction sites. While cloning of RE-ACE2-Flag-mScarlet pB vectors involved amplification of the receptor from the RE-ACE2-EGFP-pB using primers tagged with the AgeI and MluI restriction sites.

To enable detection of the receptors in downstream applications, the flag tag was included in the hACE2 reverse primer, since the tagging of the hACE2 receptor is typically performed at the C-terminus of the receptor [409,410]. However, such information regarding the RE-ACE2 is lacking; thus, the flag tag was included either in the N- or C-terminus of the receptor. Digestion and ligation of the hACE2-EGFP and RE-ACE2 inserts to the pB-CAG-EGFP vector and RE-CAG-mScarlet-pB were executed using the corresponding restriction enzymes and T4 ligase, respectively, and the cloned constructs were successfully transformed. All generated constructs were positively confirmed by colony PCR and Sanger sequencing (**Figure 5.10).**

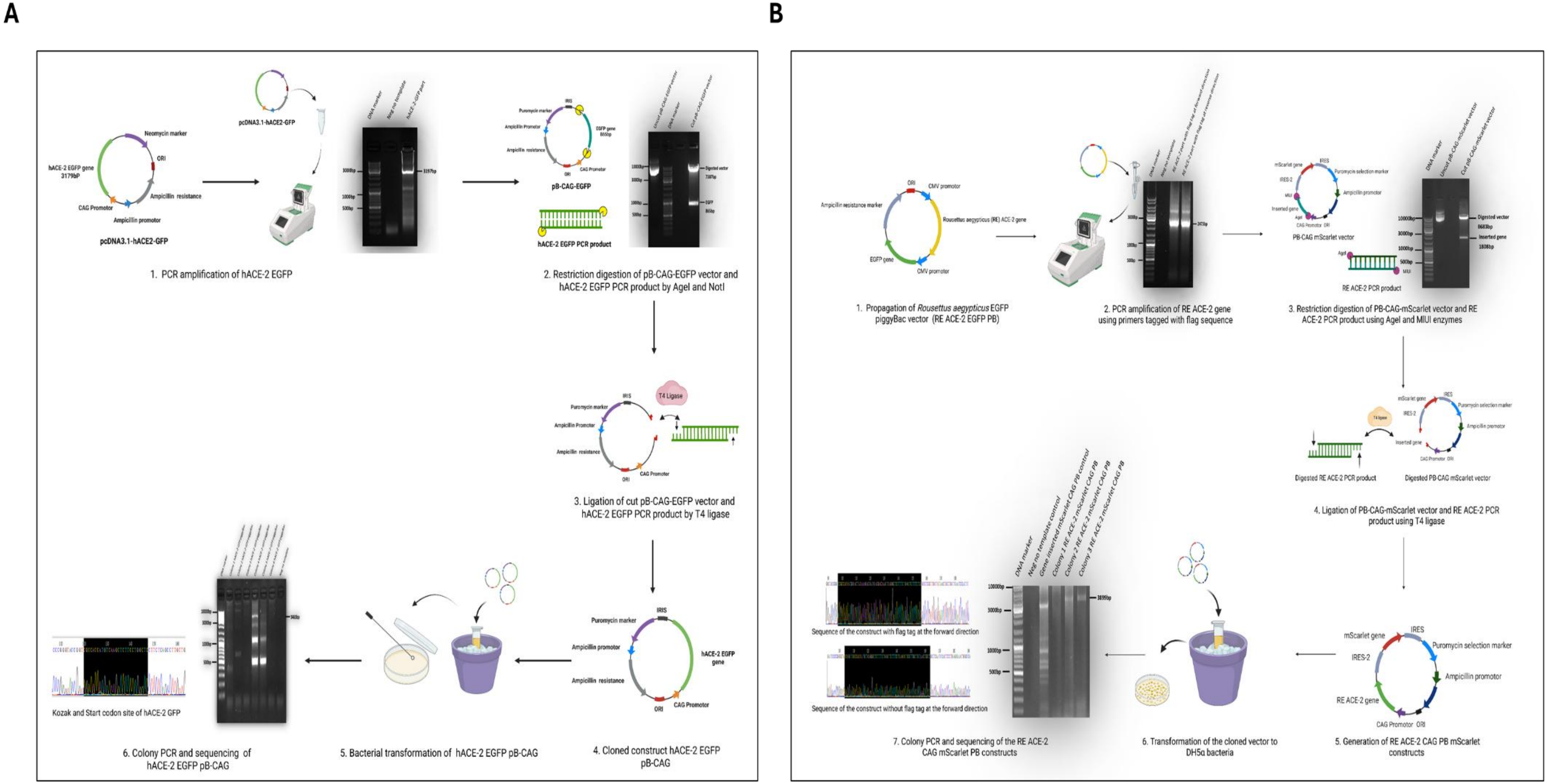

Figure 5.10. Schematic diagrams for the cloning results for hACE2-EGFP-Flag-C-pB and RE-ACE2-Flag-mScarlet pBs. (A) Cloning and generation of hACE2-EGFP-Flag-C-pB vector. (B) Cloning and generation of RE-ACE2-Flag-mScarlet pBs. Receptors were successfully amplified from the corresponding vectors, digested and ligated to the pB vector backbone using T4 ligase enzyme. Transformation of the ligated vectors was performed, and constructs were confirmed by colony PCR and visualised on agarose gel. The plasmid constructs were subsequently confirmed by Sanger sequencing.

To establish the hACE2 and RE-ACE2 cell lines, the cloned vectors (hACE2-EGFP-Flag-C-pB, RE-ACE2-Flag-N-mScarlet pB, and RE-ACE2-Flag-N-mScarlet pB) were co-transfected with the helper plasmid Hybase-CAG into BHK-21 and R06E WT cell lines. At 24 h post-transfection, cells were examined under a fluorescence microscope to assess transfection efficiency.

The transfection rate in BHK-21 cells ranged from 50–60%, whereas in R06E cells, it was markedly lower, at approximately 15% or less **(Figure 5.11A** and **B** and **Figure 5.12)**. Transfected cells expressing the two receptors were subjected to puromycin selection. The selection was maintained till the complete elimination of non-transfected cells was observed. During the selection, a minor fraction of transfected cells underwent cell death, which was expected and did not affect the antibiotic selection of the RE-ACE2 in BHK21/R06E. However, during the selection of hACE2-expressing cells, the puromycin treatment in R06E was terminated prematurely on the fourth day to prevent a significant loss of the few transgenic cells, and FACS was performed to enrich the population with transfected cells.

FACS was performed by gating for EGFP-positive cells (>99%) to ensure successful enrichment of hACE2-EGFP–expressing R06E cells. The enriched cells were subsequently expanded in a T25 for 2 weeks to allow full recovery and stabilisation. Post-sorting analysis has demonstrated successful enrichment and an increase in the proportion of fluorescent cells compared to pre-sort levels (**Figure 5.11C and D**).

Expansion of all cells was performed following the discontinuation of the antibiotic, using the normal growth medium containing 10% FBS; however, during the expansion of RE-ACE2 cell lines, the cells expressing the flag tag at the N-terminus of the RE-ACE2 receptor were expanding slightly less than those transfected with RE-ACE2-Flag-C-mScarlet pB. Therefore, the cell line clones expressing the flag tag at the receptor's C-terminus were selected to proceed with the subsequent experiments (referred to as R06E/BHK-21 RE-ACE2-mScarlet) rather than those having the flag tag at the N-terminus of the receptor (**Figure 5.12**).

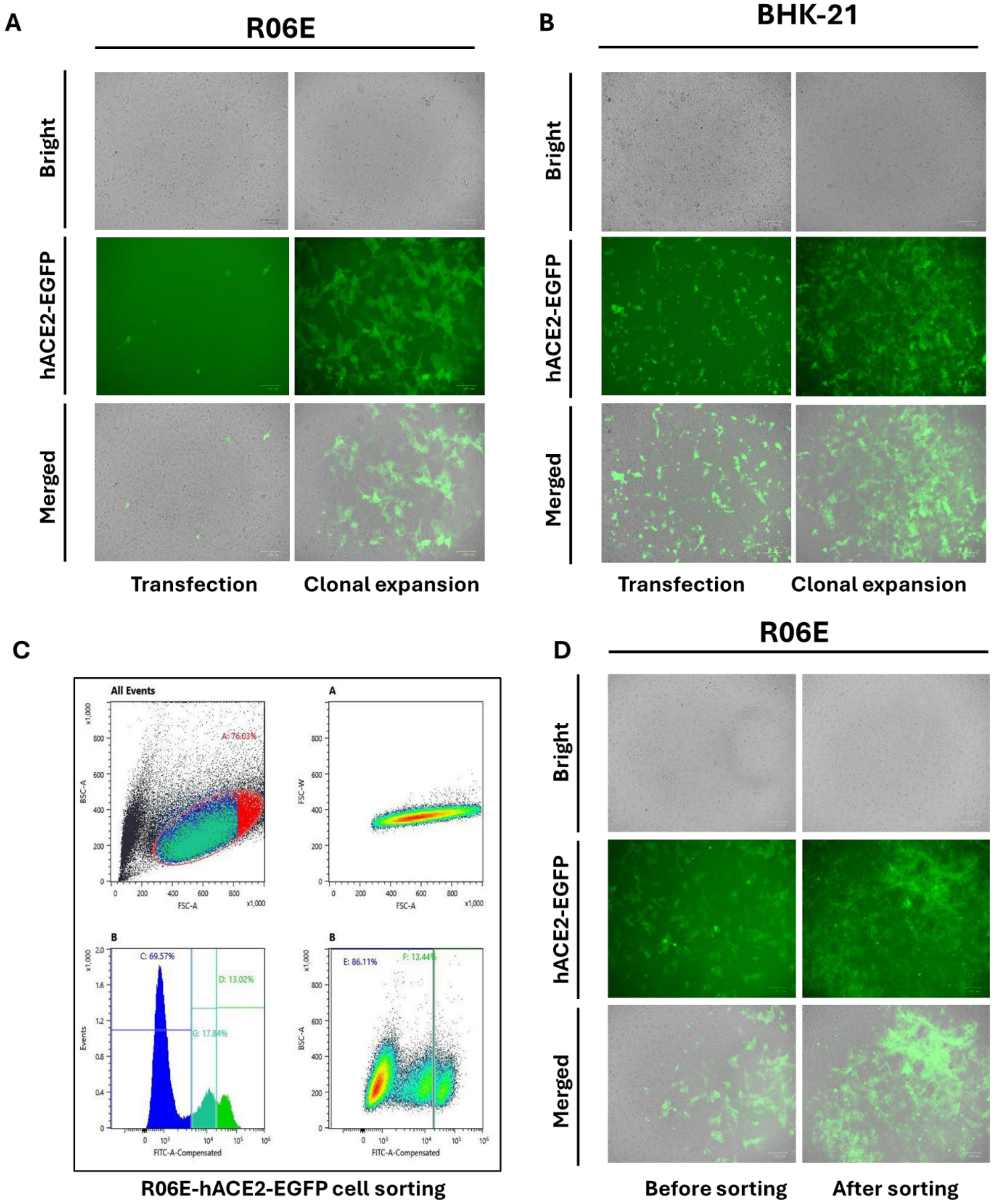

Figure 5.11.Establishment of R06E and BHK-21-hACE2-EGFP cell lines. (A) Transfection and expansion of R06E-hACE2-EGFP cell line. (B) Transfection and clonal expansion of BHK-21-hACE2-EGFP cell line. (C) FACS of the R06E-hACE2-EGFP. (D) Post-sorting analysis of R06E-hACE2-EGFP. Scale bar = 100 μm.

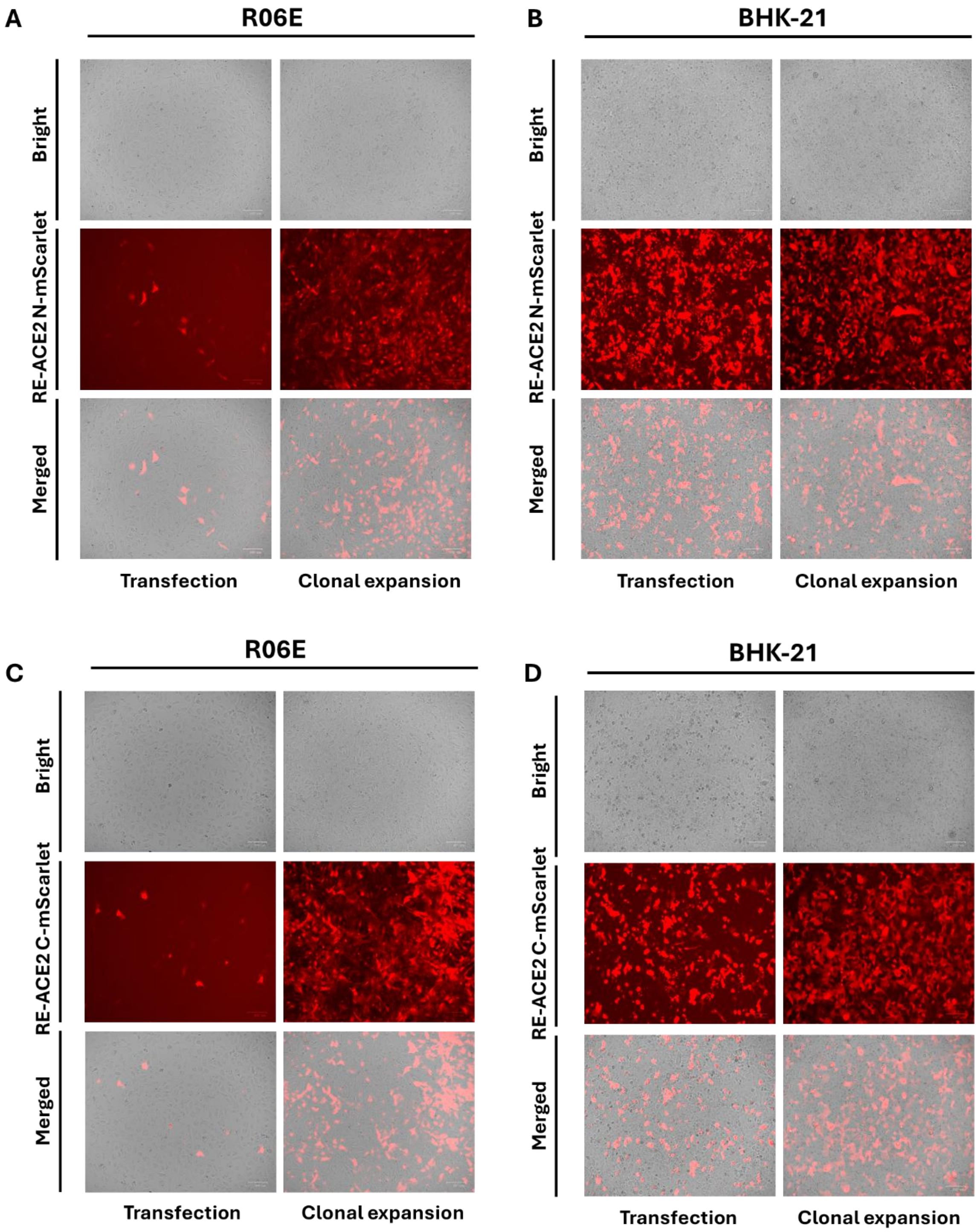

Figure 5.12. Establishment of R06E and BHK-21 RE-ACE2- mScarlet cell lines. (A) Transfection and expansion of the R06E-RE-ACE2-N-mScarlet cell line. (B) Transfection and expansion of the BHK-21-RE-ACE2-N-mScarlet cell line. (C) Transfection and expansion of the R06E-RE-ACE2-C-mScarlet cell line. (D) Transfection and expansion of the BHK-21-RE-ACE2-N-mScarlet cell line. Scale bar = 100 µm.

To confirm the validation and expression of the hACE2-EGFP and the RE-ACE2 in the established cell lines R06E and BHK-21, a WB was performed employing the flag tag present at the C-terminus of each of the receptors. R06E and BHK-21 WT were included in the analysis for the comparison as negative controls, and α-tubulin was loaded in the assay as a loading control. Analysis of the WB has detected the α-tubulin band in all cell lines, at ~ 47 kDa. Moreover, RE-ACE2 bands were detected in the established cell lines at ~ 93 kDa, while the hACE2-EGFP bands were detected at ~ 120 kDa, which corresponds to the expected size of the receptors in all established cell lines. WT cells did not show any detectable bands, as expected **(Figure 5.13)**.

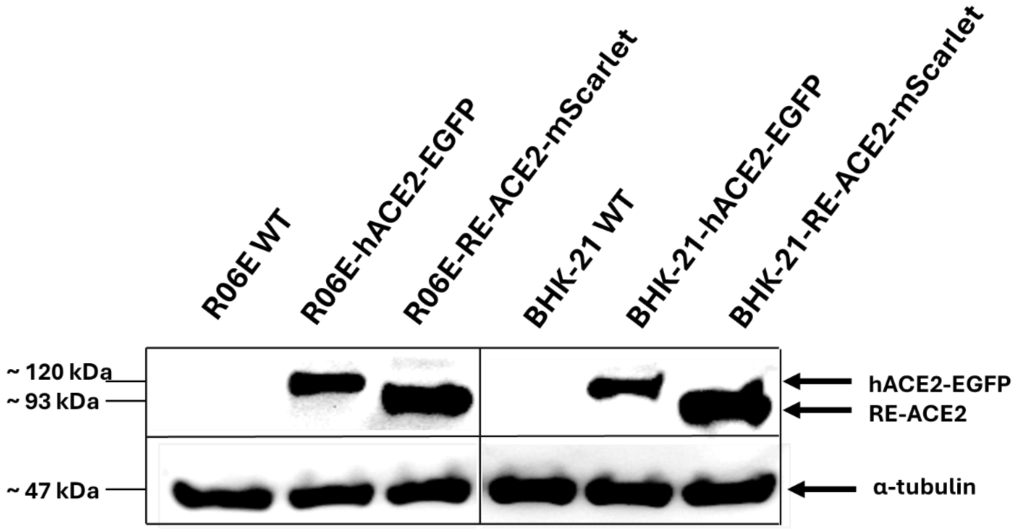

Figure 5.13. WB analysis of established RE-ACE2 and hACE2 R06E and BHK-21 cell line. RE-ACE2 and hACE2 bands were detected at ~ 93 kDa and 120 kDa, respectively. No corresponding bands were observed in WT cells. Band of α-tubulin was detected in all cell lines at ~ 47 kDa.

5.3.5. Determination of BtCoV HKU5-SE MOI Dose in the Engineered R06E-hACE2-EGFP Cell Line

To date, there are no studies that show the effect of hACE2 expression and efficiency of infection using BtCoV HKU5-SE in R06E cells. Therefore, to establish an infection system and determine the appropriate MOI level for the BtCoV HKU5-SE entry study, R06E-hACE2-EGFP was infected with three different MOIs of the virus, 0.2, 1 and 2, which correspond theoretically to low, moderate and high levels of infection, respectively.

The infection and development of CPE were subsequently observed for the next three days. At 0.2 MOI, no observable CPEs were detected during the first 48 hpi, although signs of viral infection, including cell rounding, detachment, lysis and death, were identified on the engineered cells 72 hpi (**Figure 5.14A**). On the other hand, cells displayed the CPEs at an MOI of 1 as early as 24 hpi, and the level of infection increased over the next two days, where the majority of cells showed distinct cytopathic changes by 48 hpi. At 72 hpi, many cells were dead due to excessive virus replication, yet few remained viable (**Figure 5.14B**). MOI of 2 exhibited robust CPE at 24 hpi onward, with all cells noted to undergo extensive necrosis, and death was extensive at 72 hpi, indicating that the cells died entirely somewhere between 48 and 72 hpi (**Figure 5.14C**).

Thus, based upon these observations, an MOI of 1 was selected to be used in the subsequent experiments as it allows robust and progressive viral infection while avoiding the excessive cytotoxicity and necrosis observed at higher viral loads.

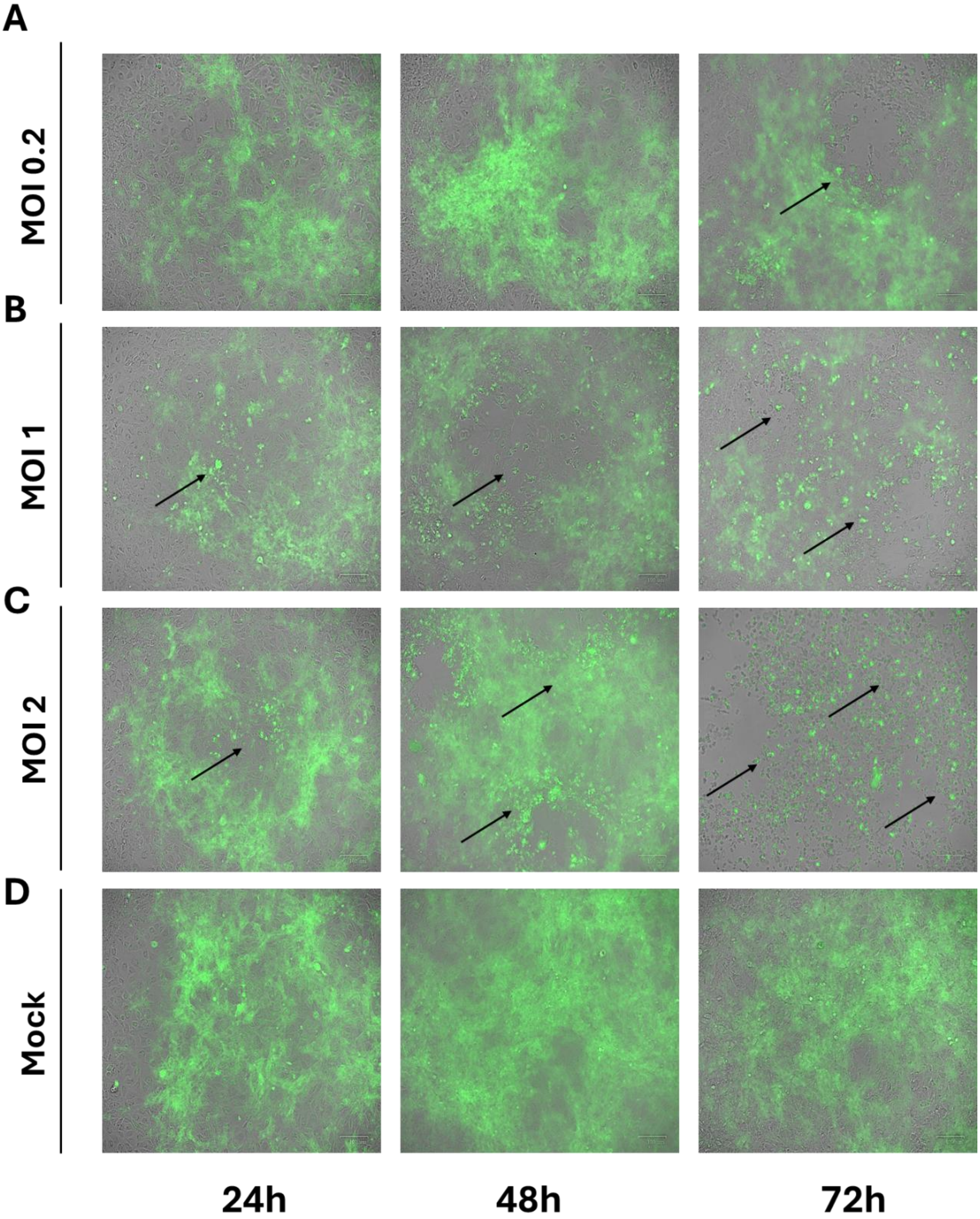

Figure 5.14. BtCoV HKU5-SE viral infection in R06E-hACE2-EGFP at varying MOIs across a 72 h time course. (A) BtCoV HKU5-SE MOI 0.2 showed no CPE at 24 and 48 hpi but showed CPE signs at 72 hpi. (B) MOI 1 showed clear, progressive and distinct viral infection over the 72 hpi. (C) MOI 2 showed robust infection at 24 and 48 hpi and extensive cell death at 72 hpi. (D) Mock-infected cells served as a negative infection control. Scale bar = 100 µm.

5.3.6. RE-ACE2 Receptor Allows Less BtCoV HKU5-SE Entry Relative to hACE2 Receptor in BHK-21 Cells

To gain a preliminary understanding of whether the species-specific capacity of RE-ACE2 affects the replication of BtCoV HKU5-SE, the receptor, along with its human counterpart were ectopically expressed in BHK-21, which lacked the endogenous ACE2 expression [408]. Cells were infected with the BtCoV HKU5-SE at an MOI of 0.5, monitored for the development of viral CPE and subjected to supernatant collection at 24 hpi. VeroE6 and BHK-21 WT were included in parallel as positive and negative controls, respectively.

As expected, no CPE or plaques were developed in BHK-21 WT. VeroE6 did not exhibit distinct pathological changes at MOI 0.5, but they established efficient virus replication and plaque formation at the same infection dose. On the other hand, BHK-21 overexpressed with the Egyptian fruit bat ACE2 (BHK-21-RE-ACE2-mScarlet) demonstrated fewer and weaker CPE compared to its human counterpart (BHK-21-hACE2-EGFP), which developed stronger and higher numbers of CPE under the same conditions (**Figure 5.15A**).

Plaque assay titration of BHK-21-RE-ACE2-mScarlet and BHK-21-hACE2-EGFP revealed lower virus titre in the BHK-21-RE-ACE2-mScarlet compared to BHK-21-hACE2-EGFP. Nevertheless, the difference in virus titre between the two cell lines was modest, with no more than one viral dilution log difference, where RE-ACE2 overexpressing cells produced less virus than their hACE2 counterpart (**Figure 5.15B**).

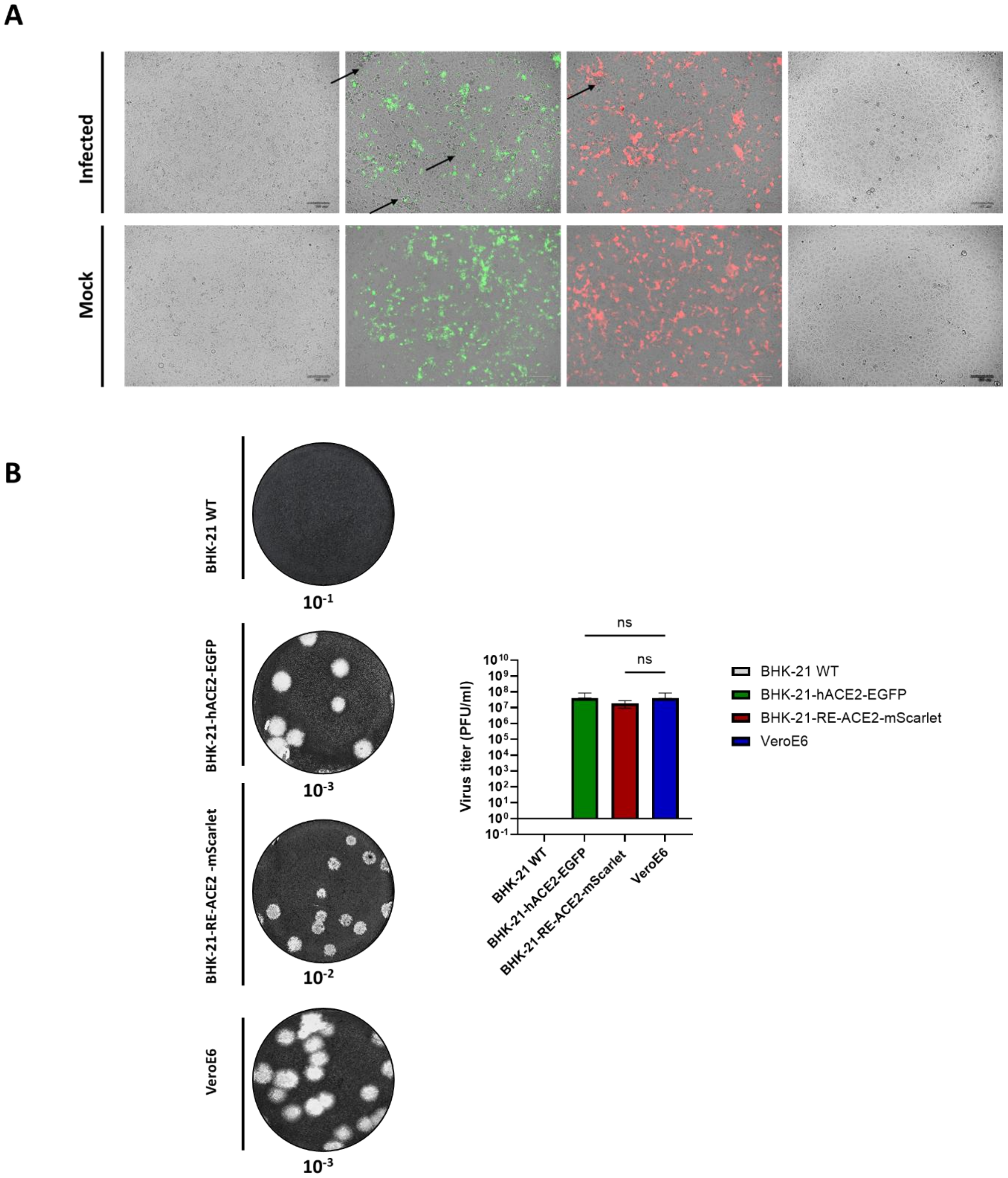

Figure 5.15. BtCoV HKU5-SE infection MOI 0.5 in ectopically expressed BHK-21 ACE2 cells at 24 hpi. (A) CPE of ectopically expressed ACE2 BHK-21 cells. BHK-21-hACE2-EGFP cells exhibited stronger and more extensive cell rounding and detachment compared to BHK-21-RE-ACE2-mScarlet cells, which showed less and weaker CPE. No detectable CPE was detected in VeroE6 or BHK-21 WT. Mock-infected cells served as a negative infection control. Viral CPEs are shown in arrows. Scale bar = 100 µm. (B) Plaque assay titration of supernatants collected from infected BtCoV HKU5-SE cells. BHK-21-hACE2-EGFP showed higher but modest plaque numbers and viral titre compared to BHK-21-RE-ACE2-mScarlet. VeroE6 showed robust plaque formation and virus titre at 0.5 MOI. No signs of plaque formation or BtCoV HKU5-SE were detected in BHK-21 WT. Data are presented as mean ± SD of three independent experiments. The statistical analysis was performed using Dunnett's multiple-comparison test on a one-way ANOVA.

5.3.7. hACE2 Expression Permits Efficient BtCoV HKU5-SE Replication in R06E Rather than the RE-ACE2 Overexpression

To determine whether lower expression of RE-ACE2 in the R06E cells was the key barrier rather than the hACE2, R06E was engineered to overexpress both RE-ACE2 and the hACE2 receptor using the pB system. Receptors-overexpressing cells were co-infected with R06E WT and VeroE6 (positive control) at an MOI of 1 with BtCoV HKU5-SE. The infection was monitored in the cells over 72 h, and viral titres were quantified to evaluate growth kinetics.

As expected, VeroE6 demonstrated cell rounding and syncytia at 24 hpi, whereas R06E WT did not show any CPE at the same time point. The overexpressed ACE2 receptor R06E cells (R06E-RE-ACE2-mScarlet and R06E-hACE2-EGFP) showed noticeable CPE at 24 hpi, characterised by cell lysis and sloughing. However, the CPE in R06E-hACE2-EGFP was stronger and more abundant than the one in R06E-REACE2-mScarlet, consistent with data from BHK-21 cells.

At 48 hpi, the CPE intensified in the three cell lines, VeroE6, R06E-hACE2-EGFP and R06E-RE-ACE2-mScarlet, where more cell lysis and sloughing were observed. However, the level of infection in R06E-RE-ACE2-mScarlet was still less abundant than R06E-hACE2-EGFP. R06E WT did not express any obvious signs of infection at that time point.

At 72 hpi, R06E-hACE2-EGFP and VeroE6 exhibited extensive necrosis, lysis and death in almost all cells. Sloughing was more prominent throughout the monolayer, leaving very few cells attached to the vessel surface, indicating that the BtCoV HKU5-SE infection reached the maximum level in R06E-hACE2-EGFP and VeroE6 approximately at 48 hpi. In contrast, the CPE in the R06E-REACE2-mScarlet continued to expand at 72 hpi, which is consistent with the lower and delayed replication dynamics. Notably, R06E WT cells started to develop CPE at 72 hpi, characterised by limited cell detachment across the field (**Figure 5.16**).

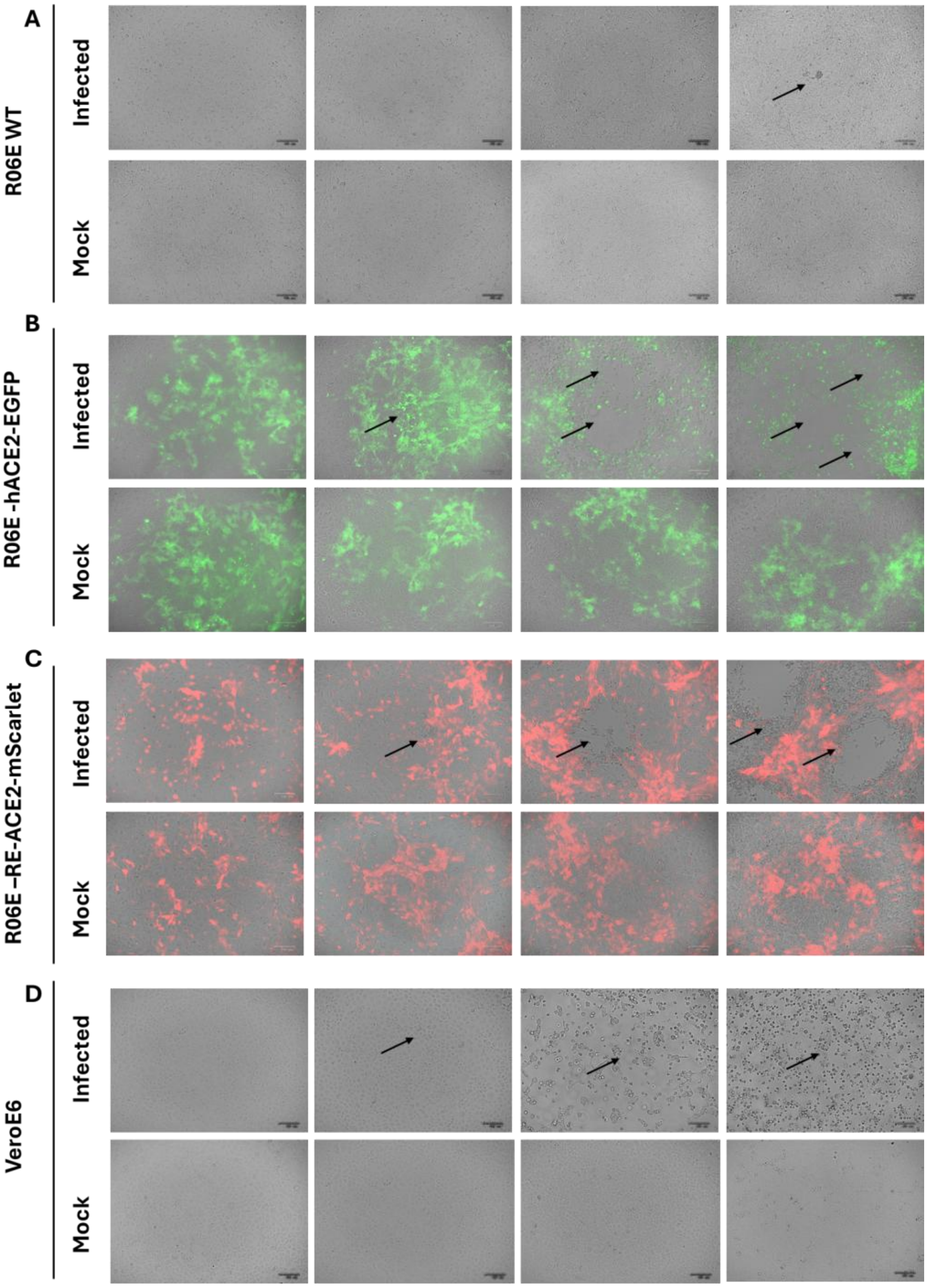

Figure 5.16. Cytopathic effects of BtCoV HKU5-SE in receptor-overexpressing and R06E WT cells. R06E WT, R06E-hACE2-EGFP, R06E-RE-ACE2-mScarlet, and VeroE6 cells were infected with BtCoV HKU5-SE at an MOI of 1 and monitored for 72 h. (A) R06E WT cells did not display any CPE till 72 hpi where minimal and scattered cell detachment was observed. (B) R06E-hACE2-EGFP exhibited CPE as early as 24 hpi, with maximum effect noticed at 48 hpi. Widespread cell death was pronounced by 72 hpi. (C) R06E-RE-ACE2-mScarlet displayed milder and less progressive CPE compared to the hACE2-expressing cells throughout the 72 h period. (D) VeroE6, which served as a positive control, displayed CPE at 24 hpi and progressed to complete lysis and death by 72 hpi. Mock-infected cells were included as a negative control. Viral CPEs are shown in black arrows. Merged GFP and Red fields are illustrated. Scale bar = 100 μm.

Growth kinetics of BtCoV HKU5-SE revealed an initial increase in virus titre in VeroE6 up to 48 hpi; however, at 72 hpi, the virus declined to a level similar to that observed at 24 hpi. In R06E WT, BtCoV HKU5-SE did not demonstrate any plaques at any time point, including 72 hpi, which exhibited mild CPE. The viral titre obtained from the R06E-hACE2-EGFP cells increased significantly over the time course, with a doubling log observed between 24 and 48 hpi. At 72 hpi, the virus had substantially declined to approximately the same titre observed at 24 hpi. Conversely, the R06E-RE-ACE2-mScarlet showed a gradual increase in viral titre over the infection period, with maximum viral egress observed at 72 hpi. Nevertheless, the BtCoV HKU5-SE release between the time points was not statistically significant.

Notably, BtCoV HKU5-SE yield from RE-ACE2-mScarlet was comparable to that obtained from the R06E-hACE2-EGFP, with one log lower at 24 hpi. However, R06E-hACE2-EGFP released double the viral quantity than its RE-ACE2-mScarlet at 48 hpi. Moreover, the humanised bat cells peaked in virus release at 48 hpi, and the titre obtained was comparable to that obtained from the IFN-deficient VeroE6 cells at the same time point. Virus release from the R06E-hACE2-EGFP declined at 72 hpi due to extensive cell death; however, it remained higher than that of RE-ACE2-mScarlet, which continued to produce virus at the same time point. These results suggest that while overexpression of RE-ACE2 significantly improved BtCoV HKU5-SE replication in R06E compared to the wild-type cells, it was still less effective than hACE2 when expressed under identical conditions (**Figure 5.17**).

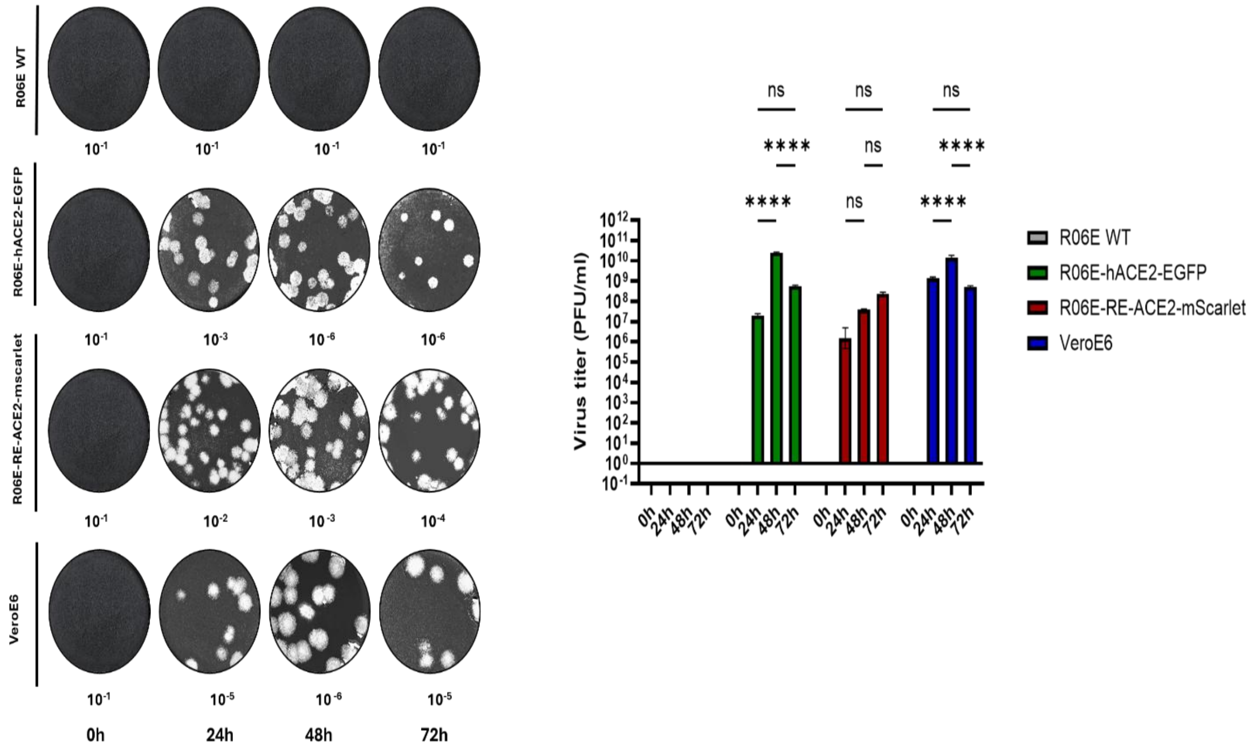

Figure 5.17. Plaque assay and growth kinetics of BtCoV HKU5-SE in WT and receptor-overexpressing R06E cells. R06E WT, R06E-hACE2-EGFP, R06E-RE-ACE2-mScarlet, and VeroE6 cells were infected with BtCoV HKU5-SE at an MOI of 1, and the supernatants were collected at 24, 48 and 72 hpi. R06E WT did not display any plaques at any of the time points. VeroE6 and R06E-hACE2-EGFP showed visible plaques across the infection time, with maximum plaques visible at 48 hpi. R06E-REACE2-mScarlet showed gradual progressive plaques over the 72 h infection period. Data are presented as mean ± SD of three independent experiments. The statistical analysis was performed using Dunnett's multiple-comparison test on a two-way ANOVA.

5.3.8. BtCoV HKU5-SE Drives Syncytia Formation and ACE2 Re-Localisation in Bat Cells Regardless of the Species Receptor.

To gain insight into BtCoV HKU5-SE receptor interaction in bat cells, R06E WT, hACE2-EGFP, and RE-ACE2-mScarlet were seeded on coverslips in 24-well plates. Cells were infected with BtCoV HKU5-SE at an MOI of 1. VeroE6 cells were used as a positive control for infection. At 24 hpi, cells were fixed, permeabilised and blocked for immunofluorescence analysis. There is no commercially available antibody specific for the HKU5 nucleocapsid protein; thus, the SARS-CoV-SE, which was inserted into the recombinant virus, was used as a proxy for viral antigen detection. In addition to the SARS spike antibody, the anti-flag primary antibody was used to visualise the RE-ACE2 receptor in the overexpressed bat cell lines.

Immunofluorescence analysis of the infected cells revealed detection of the SE antigen in the cytoplasm of the four examined cell lines. In particular, the antigen was frequently concentrated around the perinuclear region and diffusely throughout the cytoplasm. However, the intensity of the SE signal varied considerably among the cell lines; VeroE6 demonstrated the strongest SE signal, followed by R06E-hACE2-EGFP and R06E-RE-ACE2-mScarlet, respectively. In contrast, R06E WT showed a weak SE signal marginally detected above the background levels, consistent with the abortive infection previously observed at 24 hpi.

Viral syncytia, characterised by the coalescence of infected cells and presence of multiple nuclei within a shared cytoplasmic compartment, were observed in the VeroE6 as well as the hACE2-EGFP and RE-ACE2-mScarlet R06E. R06E WT did not develop any signs of syncytia, likely due to the lowest infection level observed.

In general, higher cell lysis and death were observed in the hACE2-expressed R06E than its counterpart RE-ACE2, coinciding with the higher viral replication rate of the humanised cells. In mock cells, both hACE2 and RE-ACE2 were found to localise to the plasma membrane as well as the cytoplasm; however, upon infection with BtCoV HKU5-SE, both receptors were largely reduced on the cell surface and co-localised with SE antigen in the cytoplasm.

Notably, the ectopic expression of human or bat ACE2 exhibited morphological changes in response to the viral infection, including dispersal, fragmentation, and formation of cytoplasmic puncta, with more present in the hACE2 than RE-ACE2 (**Figure 5.18**). Collectively, these findings highlight the ACE2 receptor as a target for HKU5-SE-induced trafficking and degradation, irrespective of its species origin.

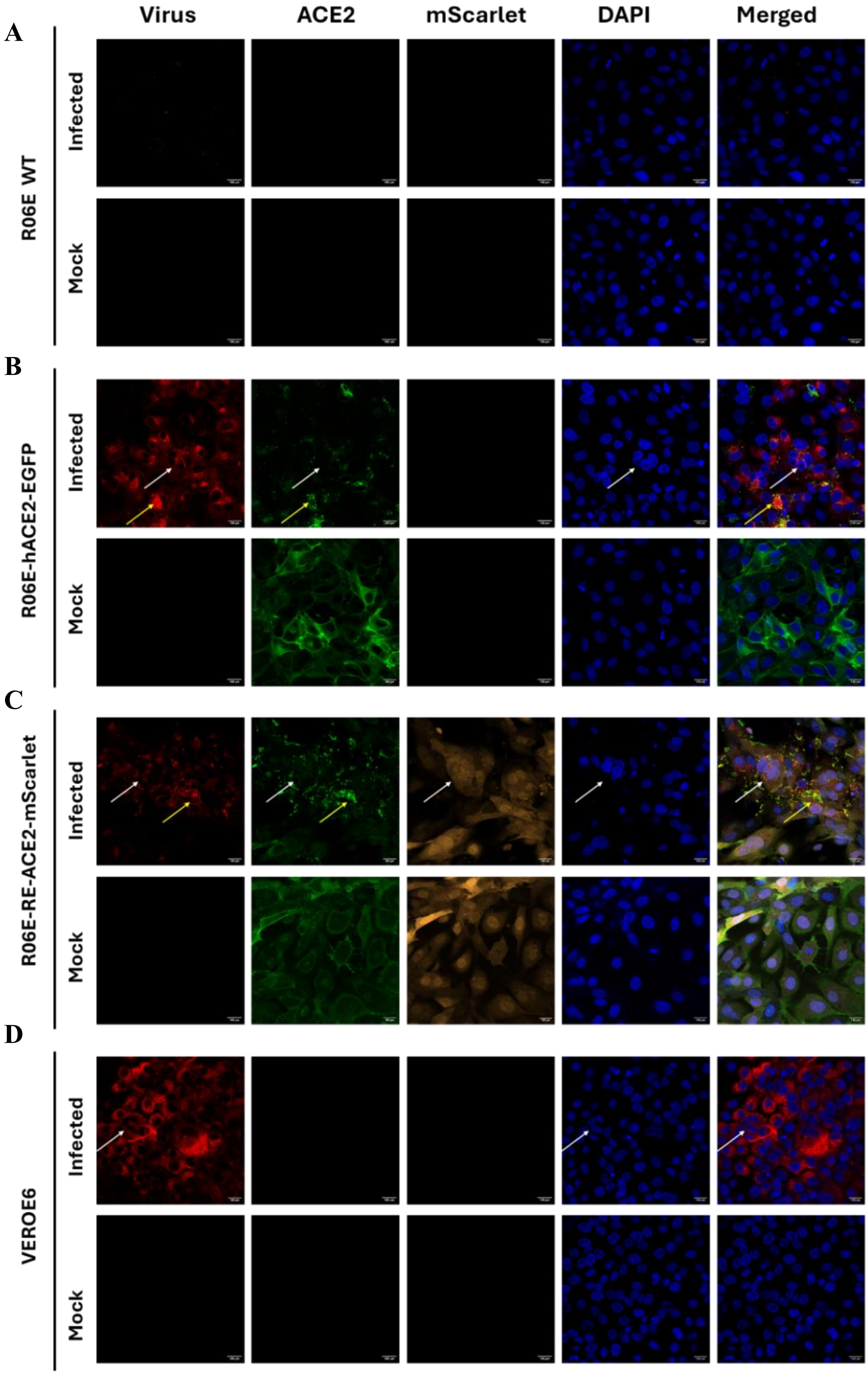

Figure 5.18. Immunofluorescence analysis of BtCoV HKU5-SE infection in bat cells. R06E WT, R06E-hACE2-EGFP, R06E-RE-ACE2-mScarlet, and VeroE6 were infected with BtCoV HKU5-SE at an MOI of 1 for 24 h and analysed under the microscope for SARS spike ectodomain (SE) antigen detection, CPE, and ACE2 localisation. (A) R06E WT showed minimal SE antigen detection with no detectable CPE or viral syncytia. (B) R06E-hACE2-EGFP demonstrated cytoplasmic localisation of the SE viral antigen, syncytia, cell lysis, and death, accompanied by marked fragmentation of hACE2. (C) R06E-RE-ACE2-mScarlet showed less signal SE antigen and RE-ACE fragmentation, whereas syncytia and CPE were evident. (D) VeroE6 cells showed a strong SE antigen signal and viral syncytia. Cell syncytia and ACE2-SE antigen co-localisation are shown in white and yellow arrows, respectively. Scale bar = 100 µm.

5.3.9. Replication Kinetics of BtCoV HKU5-SE Shows Minimal Viral Replication in Wild-Type Bat Cells Compared to its Humanised Counterparts.

Next, to further investigate the replication dynamics of BtCoV HKU5-SE in WT versus hACE2-expressing R06E cells, R06E WT and hACE2-EGFP were infected with BtCoV HKU5-SE at an MOI of 1 and assessed the virus replication using RT-qPCR at time points over 72 hpi.

At 0 hpi, the amount of the virus entered the WT cells did not exceed the limit of detection of the qPCR; that level slightly increased at 24 hpi and remained constant at 48 hpi; nevertheless, the viral RNA yields did not exceed the detection limit of the assay until 72 hpi, suggesting minimal replication and a low level of viral RNA production. In contrast, R06E-hACE2-EGFP-cells showed detectable viral RNA as early as 0 hpi, with replication steadily increasing over 24 h, peaking at 48 hpi, then plateauing by 72 hpi (**Figure 5.19**). These results confirm that R06E WT cells are not efficient producers of BtCoV HKU5-SE and underscore hACE2 as a critical determinant of entry and replication for BtCoV HKU5-SE and possibly other SARS spike-like viruses in the R06E cell line.

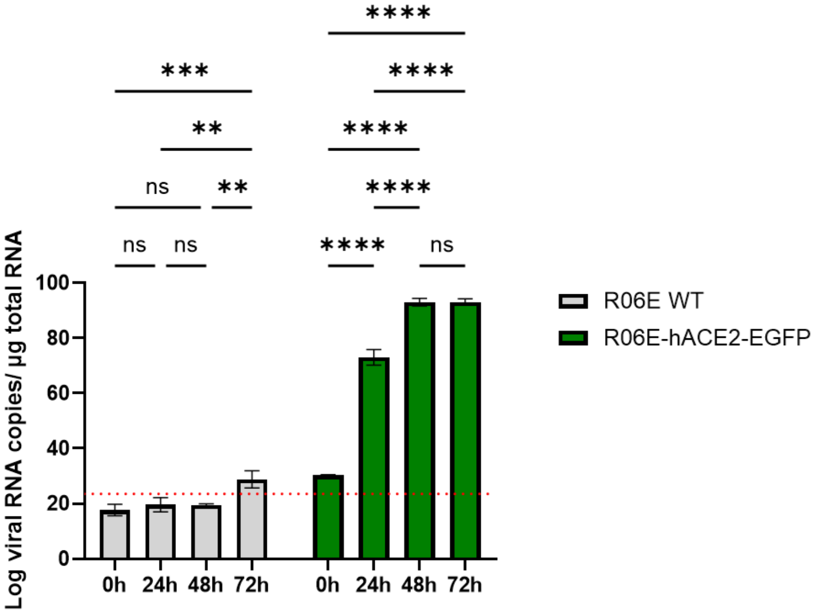

Figure 5.19. Replication kinetics of BtCoV HKU5-SE in bat cells. R06E WT and hACE2-EGFP were infected with 1 MOI of BtCoV HKU5-SE, and cell-associated viral RNA was quantified over 72 h of the infection using RT-qPCR. Infection in R06E WT remained below the assay LOD throughout the time course until 72 hpi. In contrast, the viral RNA in R06E-hACE2-EGFP was detectable as early as 0 hpi, peaked at 48 hpi and plateaued by 72 hpi. Data are presented as mean ± SD of three independent experiments. The statistical analysis was performed using Dunnett's multiple-comparison test on a two-way ANOVA. LOD of the RT-qPCR assay is shown in dashed red.

5.3.10. BtCoV HKU5-SE is Internalised in Bat Cells Using TMPRSS2 and Cathepsin L With More Dependence on TMPRSS2

To determine if BtCoV HKU5-SE uses TMPRSS2 and CTSL for entry in R06E, Camostat mesylate and EST were used to inhibit TMPRSS2 and CTSL, respectively. To achieve this, A549-hACE2-TMPRSS2 and A549-hACE2-EGFP cells were used as positive controls. The latter was established employing the same methodology used for generating the hACE2-EGFP R06E and BHK-21 cell lines, and the receptor integration was confirmed using WB analysis (**Figure 5.20**).

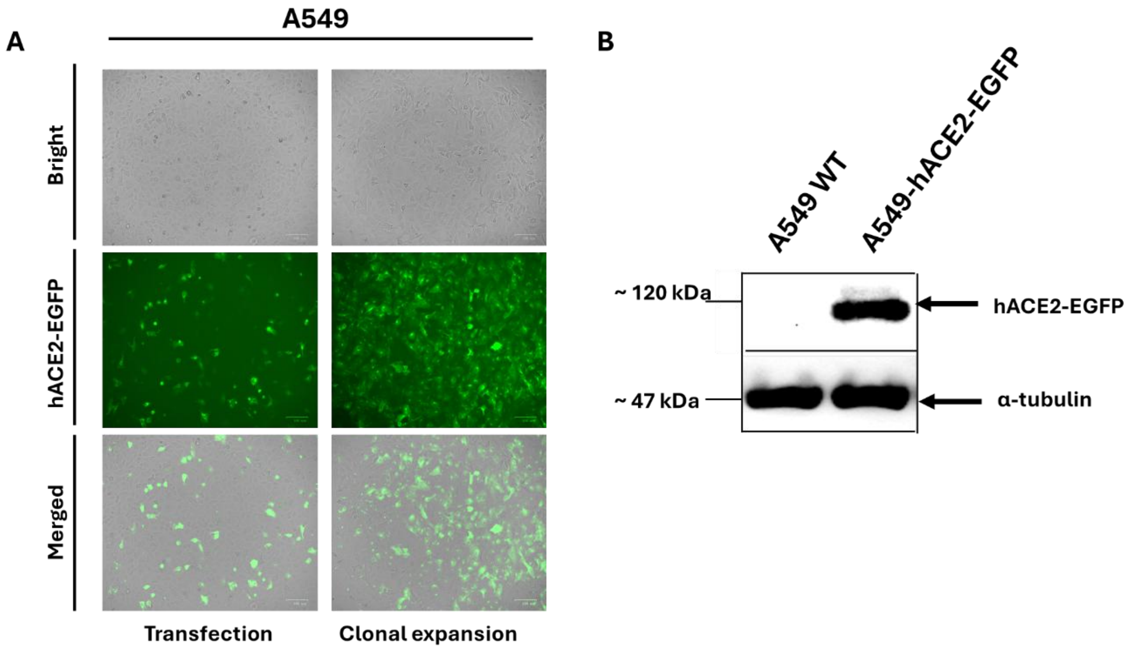

Figure 5.20. Establishment of A549-hACE2-EGFP cell line. (A) Transfection and clonal expansion of A549-hACE2-EGFP cell line. Scale bar = 100 µm. (B) WB analysis of the established cell line demonstrated detection of the hACE2-EGFP band at ~ 120 kDa and α-tubulin at ~ 47 kDa.

To determine the appropriate amount of DMSO for the compounds' reconstitution, the PrestoBlue™ cell viability reagent was used to assess the tolerability of DMSO across the tested cell lines. For this purpose, R06E-hACE2-EGFP, A549-hACE2-TMPRSS2, and A549-hACE2-EGFP cells were seeded in 96-well cell plates and treated with various concentrations of DMSO (8%, 4%, 2%, 1%, 0.5%, 0.25%, 0.125%).

At 24 h post-treatment, 10 µL PrestoBlue™ was added to the wells and incubated at 37 ºC for 1 h before reading in the plate readers. In R06E-hACE2-EGFP, DMSO at a concentration of 0.125% displayed a non-significant reduction in cell viability compared to the untreated control. However, at the subsequent concentrations (0.25%, 0.5% and 1%), cells demonstrated a gradual decrease in viability with mean values of 87%, 85 % and 81%, respectively. These levels were statistically significant, but within the generally acceptable range for a healthy cell culture [411]. In contrast, a marked decline of the R06E-hACE2-EGFP viability could be detected at 2% concentration (66%), and more pronounced cytotoxicity was evident at 4% and 8% concentrations, where the viability dropped to 35% and 1.2%, respectively (**Figure 5.21A**). These results indicated that the R06E-hACE2-EGFP could tolerate DMSO up to 1% and experience significant cytotoxicity at the higher concentrations ≥ 2%.

In the A549-hACE2-TMPRSS2. Cells treated with DMSO concentrations up to 1% maintained high viability, averaging approximately 99, with no significant reduction compared to untreated control. Toxicity gradually increased at concentrations ≥ 2%. mimicking the pattern observed in the R06E-hACE2-EGFP cell line (**Figure 5.21B).**

A549-hACE2-EGFP maintained comparable viability up to 2% DMSO with no significant reduction observed relative to the untreated control (**Figure 5.21C**). Collectively, these findings indicated that 1% DMSO was the upper safety limit in the cells when treated with Camostat mesylate and EST for 24 h. Accordingly, the stock solutions of the compounds were prepared to maintain the DMSO concentration within this limit.

A concentration of 10 µM for each compound has been widely used and reported to effectively inhibit coronavirus entry into host cells [412–414]. To ensure the safety of this dose prior to the antiviral treatments, R06E-hACE2-EGFP, A549-hACE2-TMPRSS2, and A549-hACE2-EGFP were treated with 10 µM of each compound and assessed for viability using PrestoBlue™ cell viability at 24 h post-treatment. All tested cell lines remained viable at the selected dose, with no significant difference compared to untreated controls (**Figure 5.22**).

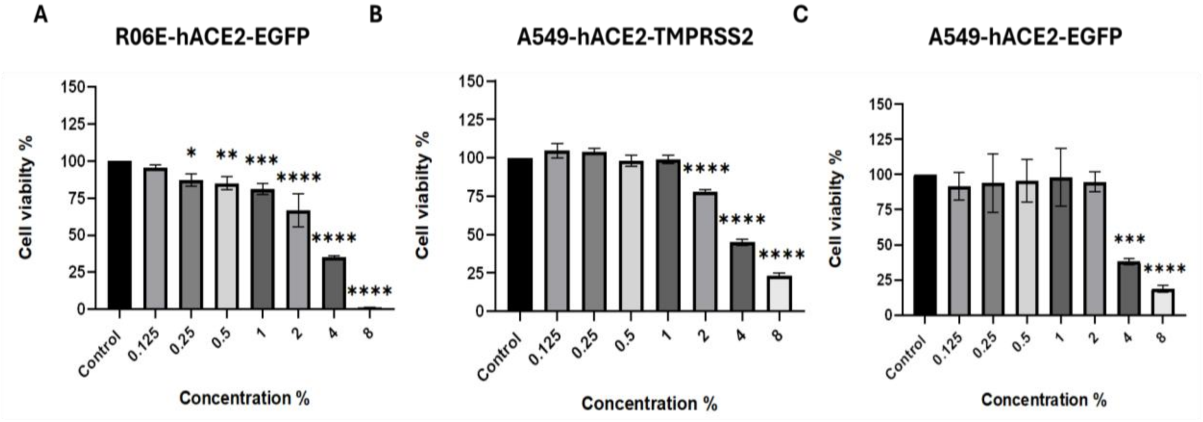

Figure 5.21. DMSO cell viability. R06E-hACE2-EGFP, A549-hACE2-TMPRSS2, and A549-hACE2-EGFP cells were treated with different concentrations of DMSO for 24 h and assessed for viability using PrestoBlue™ cell viability reagent. (A) R06E-hACE2-EGFP tolerated up to 1% DMSO, with viability declining at higher concentrations. (B) A549-hACE2-TMPRSS2 showed comparable viability up to1% DMSO with reduction observed at higher concentrations. (C) A549-hACE2-EGFP demonstrated tolerance to DMSO up to 2%. Data are presented as mean ± SD from three replicate wells. Statistical analysis was performed using Dunnett's multiple comparison test on ordinary one-way ANOVA.

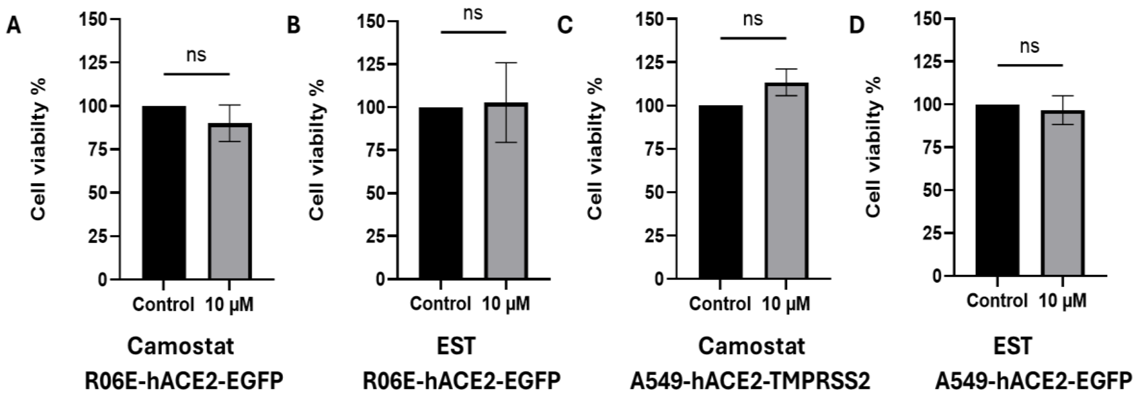

Camostat
R06E-hACE2-EGFP

EST
R06E-hACE2-EGFP

Camostat
A549-hACE2-TMPRSS2

EST
A549-hACE2-EGFP

Figure 5.22. Camostat mesylate and EST PrestoBlue™ cell viability test exhibiting no significant reduction in viability at 10 µM of each compound compared with the untreated control (A) R06E-hACE2-EGFP cells treated with Camostat mesylate. (B) R06E-hACE2-EGFP cells treated with EST. (C) A549-hACE2-TMPRSS2 treated with Camostat mesylate. (D) A549-hACE2-EGFP cells treated with Camostat mesylate. Data are presented as mean ± SD of three independent experiments. The statistical analysis was performed using a two-tailed, unpaired t-test.

Next, to address whether BtCoV HKU5-SE employs the host proteases TMPRSS2 and CTSL for entry into the bat cells, R06E-hACE2-EGFP was pre-treated with 10 µM Camostat mesylate, EST, either individually or in combination, 2 h before the viral infection. A549-hACE2-TMPRSS2 was used as a positive control for Camostat mesylate inhibition, while A549-hACE2-EGFP was used for the EST. Additionally, non-inhibitory-treated R06E-hACE2-EGFP (vehicle control) was used to assess the viral infection upon the dual treatment of both compounds. Viral infection was carried out at 1 MOI for 2 h in the presence of the respective compounds. Subsequently, the infected media were replaced with fresh ones supplied with the compounds as described. At 24 hpi, total RNA was extracted, and intracellular viral RNA levels were quantified.

Both Camostat mesylate and EST significantly inhibited the BtCoV HKU5-SE entry in R06E-hACE2-EGFP; however, a substantial effect was noted more in Camostat mesylate, not EST treatment (i.e. 18% in Camostat mesylate versus 9% EST less replication than the untreated control).

Viral infection in A549-hACE2-TMPRSS2 was comparable in both treated and untreated cells, in contrast to the A549-hACE2-EGFP, which showed a notable reduction upon the EST treatment (**Figure 5.23A** and **B**).

Dual treatment of Camostat mesylate and EST in R06E-hACE2-EGFP resulted in a significant reduction of viral RNA compared to the untreated control (~20% less); however, the reduction was slightly lower than that observed with Camostat mesylate treatment alone (**Figure 5.23C).**

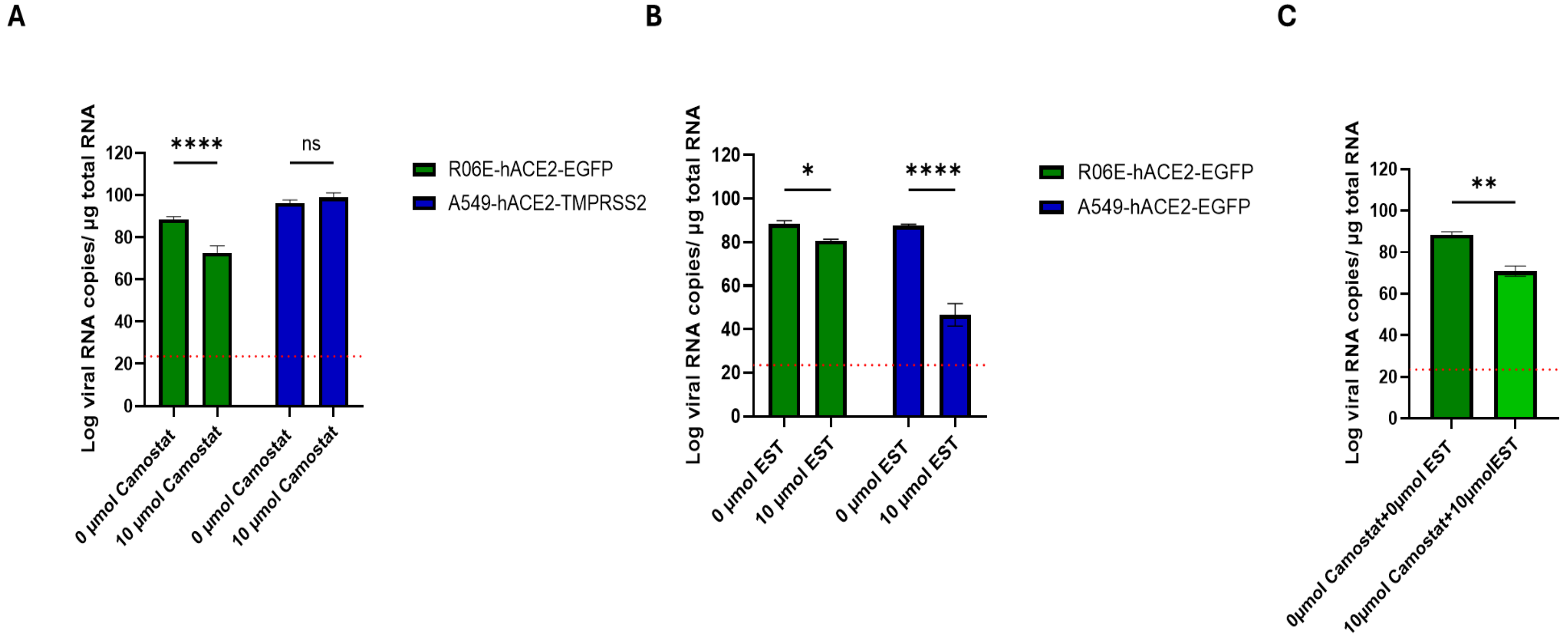

Figure 5.23. Inhibition of BtCoV HKU5-SE entry by protease inhibitors in R06E-hACE2-EGFP. R06E-hACE2-EGFP, A549-hACE2-TMPRSS2, and A549-hACE2-EGFP were pre-treated with 10 μM Camostat mesylate, EST, either individually or in combination with both compounds and infected with BtCoV HKU5-SE at 1 MOI. At 24 hpi, the intracellular viral RNA was quantified by RT-qPCR. (A) Camostat markedly reduced viral RNA in R06E-hACE2-EGFP but not in A549-hACE2-TMPRSS2. (B) EST treatment resulted in mild but significant viral reduction in R06E-hACE2-EGFP, in contrast to the more pronounced A549-hACE2-EGFP. (C) Dual Camostat mesylate and EST treatment in R06E-hACE2-EGFP reduced viral RNA, though slightly less than Camostat mesylate. Data are represented as mean ± SD from three independent experiments (n = 3). Statistical analysis was performed in the experiment using two-way ANOVA with Fisher's LSD test for individual inhibitor treatments, and an unpaired two-tailed Welch's t-test for the dual treatment comparison.

5.3.11. BtCoV HKU5-SE Induces Specific Upregulation of Viral Entry Genes *ACE2* and *TMPRSS2* in Bat Cells

Previous growth kinetics results demonstrated that the immunocompetent humanised R06E reached the same level of virus replication as the immunocompromised VeroE6. This led to the question of whether BtCoV HKU5-SE infection in bat cells modulates the expression levels of host viral entry factors, which in turn led to this finding. Thus, to investigate this question, R06E-hACE2-EGFP cells were infected with BtCoV HKU5-SE at 1 MOI and subjected to total RNA extraction at 48 hpi, corresponding to the peak of infection.

Gene expression levels of endogenous *RE-ACE2* and ectopic *hACE2*, as well as *TMPRSS2* and *CTSL,* were assessed in infected and mock cells using SYBR Green-based RT-qPCR, and relative expression was analysed using the ΔΔCt method. *RE-ACE2* expression was significantly upregulated in infected cells compared with mock-infected controls, whereas hACE2 showed a mild, non-significant increase under the same conditions. Moreover, a pronounced increase in *TMPRSS2* transcript levels was observed in infected cells, whereas *CTSL* expression remained largely unchanged (**Figure 5.24**). These results indicate that BtCoV HKU5-SE alters the regulation of its entry determinants.

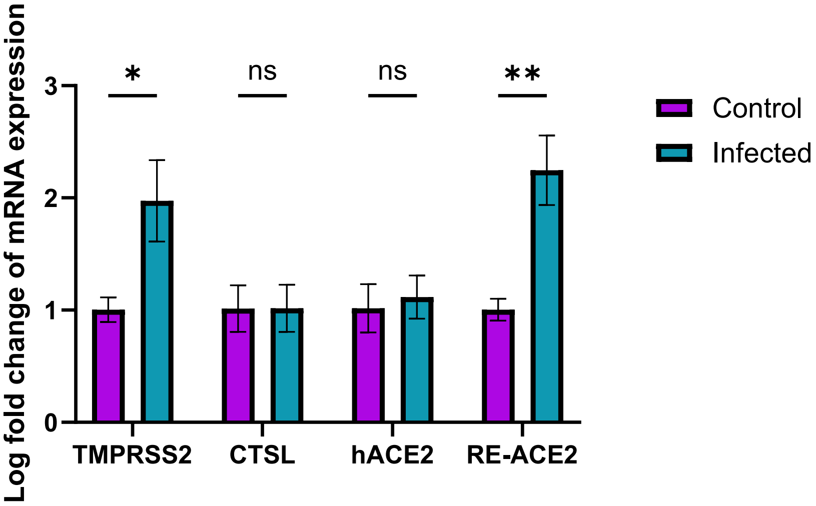

Figure 5.24. BtCoV HKU5-SE induces gene expression changes in host entry factors in bat cells. R06E-hACE2-EGFP was infected with 1 MOI of the virus and subjected to total RNA extraction at 48 hpi. Dye-based qPCR analysis revealed a significant increase in mRNA of endogenous RE-ACE2 and TMPRSS2 in infected cells, while hACE2 exhibited a modest, non-significant increase. CTSL levels remained unchanged during the infection. Statistical analysis was performed using an unpaired multiple t-test with Welch's correction, with no correction adjusted for multiple comparisons. Bars represent mean ± SD from three independent experiments.

5.3.12. *RE-ACE2* is among the Top Ten Upregulated Genes Induced by BtCoV HKU5-SE in Humanised R06E, without Isoform Switching

Previous studies indicated that *ACE2* is co-expressed with ISGs in human cells, and a truncated version of the gene is induced in IFN [415,416]. To explore whether *RE-ACE2* exhibits the same behaviour in bat cells, an RNA-seq was performed on R06E-hACE2-EGFP at 48 hpi, the peak infection time. The gene expression and isoform switching of *RE-ACE2* were analysed between infected and mock cells.

Data from the Differential gene expression analysis demonstrated that *RE-ACE2* was among the top upregulated genes in BtCoV HKU5-SE*,* along with ISGs, including interferon-induced protein with tetratricopeptide repeats 1 (*IFIT1*)*,* interferon alpha-inducible protein 6 (*IFI6*)*,* Interferon-induced protein with tetratricopeptide repeats 3 (*IFIT3*)*,* 2'-5'-oligoadenylate synthetase *1* (*OAS1*), and others (**Figure 5.25** and **Table 5.2**). Whereas the receptor did not exhibit any isoform switching except for the full-length transcript upon virus induction.

Notably, in the heatmap, the antiviral radical S-adenosyl methionine domain-containing 2 (*RSAD2*) and gene loci encoding IFIT1 products were among the top ten upregulated genes, suggesting that antiviral defence against HKU5-SE in *R. aegyptiacus* cells [417,418]. Additionally, ubiquitin-specific peptidase 18 (*USP18*), a known negative regulator of type I IFN [419], was also among the top ten upregulated genes, which might indicate an immune evasion mechanism by which BtCoV HKU5-SE may overcome the innate response in the Egyptian rousette R06E cells.

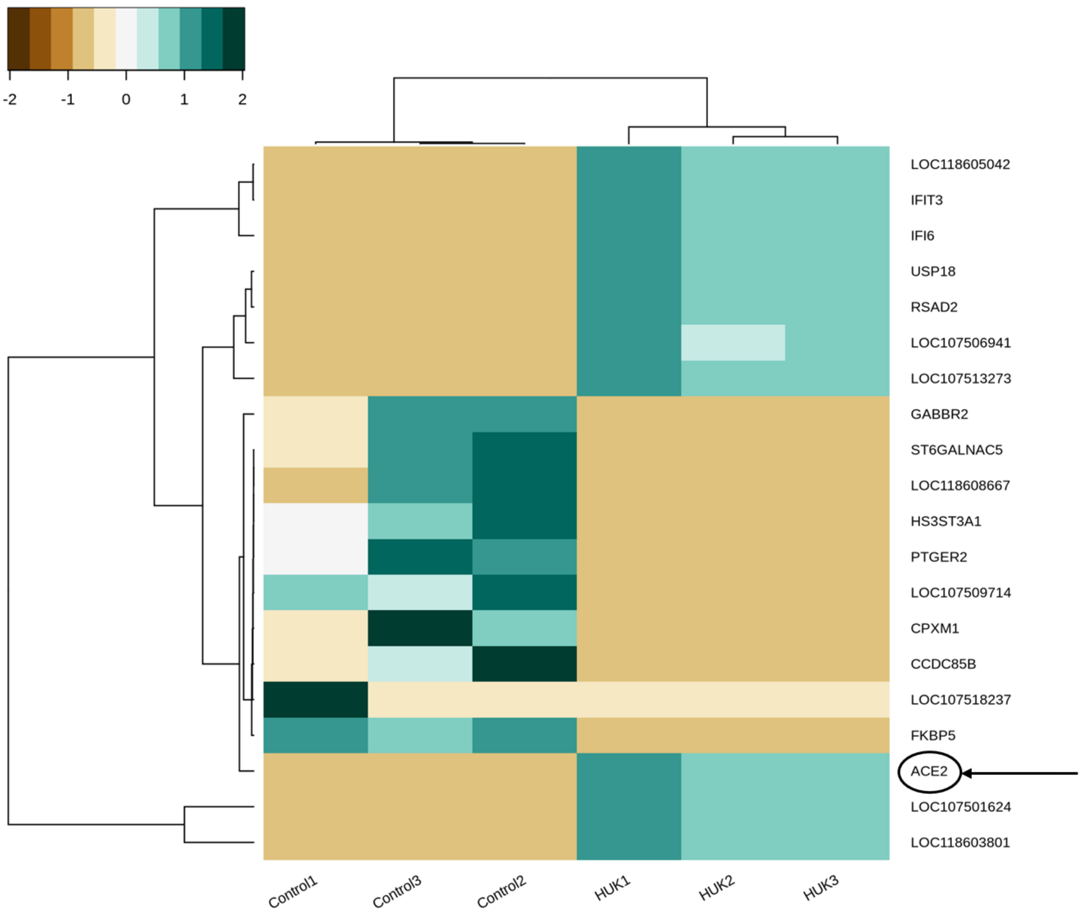

Figure 5.25. Heatmap clustering of the top ten differentially expressed genes in R06E-hACE2-EGP cells at 48 h following BtCoV HKU5-SE infection. RE-ACE2 is indicated by a black circle and arrow.

Table 5.2. Top ten significantly upregulated differentially expressed genes induced by BtCoV HKU5-SE in R06E-hACE2-EGFP cells at peak infection

Gene ID	**Transcript type**	**Encoding protein**
LOC118605042	ncRNA	N/A
IFIT3	mRNA	IFIT3
IFI6	mRNA	IFI6
USP18	mRNA	USP18
RSAD2	mRNA	Viperin
LOC107506941	mRNA	IFITM3 like
LOC107513273	mRNA	OAS1
LOC107501624	mRNA	IFIT1
LOC118603801	mRNA	IFIT1-like

N/A, not applicable; IFITM3, interferon-induced transmembrane protein 3.

Discussion

In this chapter, the molecular entry determinants of BtCoV HKU5-SE in R06E cells were investigated. Propagation of BtCoV HKU5-SE was established successfully in VeroE6 cells. This cell line is well-established for research on a wide range of coronaviruses [420–424], although it did not support the growth of the parental HKU5 lineage 1 unless the ACE2 of *P. abramus*, the natural host of HKU5, was expressed [140].

In this study, BtCoV HKU5-SE utilised the ACE2 from the parental VeroE6 to replicate; it displayed distinct phenotypic changes in VeroE6 (cell rounding and syncytia) as early as 24 hpi with progressive enhancement at 48 and 72 hpi. This efficient replication is consistent with the inclusion of the HKU5 chimeric construct with the SARS-CoV SE that is known to mediate high-affinity binding to VeroE6 ACE2 [423,425]. These findings confirm the high permissiveness of VeroE6 cells for any coronavirus with SARS-like spike and validate their use as a benchmark system for propagation and titration of BtCoV HKU5-SE virus while highlighting species-specific utilisation of ACE2 by different coronavirus spikes.

For quantification of the BtCoV HKU5-SE in cell cultures, a TaqMan RT-qPCR assay was developed to target the N gene of the virus, due to its abundant expression during virus replication, and its highly conserved sequence across coronavirus species [426–430]. Results from the TaqMan assay demonstrated sensitivity up to approximately 342 RNA copies/ reaction, although due to the limitation of SARS-CoV in our lab and given the high nucleotide identity between the N gene of SARS-CoV and SARS-CoV-2 [70], the SARS-CoV-2 N gene was used to test the specificity of the developed assay. The designed primer and probe set demonstrated specific detection of the HKU5 N gene, with no amplification in SARS-CoV-2. Additionally, the established standard curve showed a slope value of 3.3266, which was equal to 99.8% PCR amplification efficiency; these values were nearly close to the ideal values for RT-qPCR, which is -3.32, which is equal to 100% PCR efficiency [431]. The analytical performances of the developed assay confirm its establishment as a robust tool for monitoring BtCoV HKU5-SE dynamics in different cell lines.

Inoculation of BtCoV HKU5-SE in R06E WT did not result in CPE or plaque formation at an MOI of 1 at 24 hpi. This was explained by the presence of one or more barriers which could interfere with virus entry, replication and egress. At an MOI of 5, the BtCoV HKU5-SE induced minimal cell detachment and produced few plaques in R06E WT cells, which increased substantially at an MOI of 15. These results indicate that the R06E cellular machinery can support BtCoV HKU5-SE replication in a dose-dependent manner while pinpointing the ACE2 entry barrier as a determinant factor for BtCoV HKU5-SE replication in R06E. This was further supported by qPCR results, which demonstrated a low expression level of endogenous *ACE2* and undetectable input of BtCoV HKU5-SE following R06E inoculation. It has been well established that hACE2 functions as the primary entry receptor for SARS-CoV infection [432].

To investigate whether the expression level or the species-specific nature of Egyptian rousette ACE2 was the barrier to the replication of BtCoV HKU5-SE in R06E cells, the RE-ACE2, along with hACE2, were ectopically expressed in R06E as well as BHK-21, since they lack the ACE2 expression [408]. To accomplish this, hACE2 and RE-ACE2 were tagged and cloned into the pB-CAG-EGFP and RE-METTL3-WT-CAG-mScarlet-pB vectors, respectively, which use transposition to integrate the receptors into the host cell genomes. The results using the pB system demonstrated the successful and efficient integration of the hACE2 and RE-ACE2 receptors in BHK-21 cells, as well as in the hard-transfected R06E cells. This was confirmed by WB analysis, which detected the target receptor bands in both cell lines.

Infection of BtCoV HKU5-SE in BHK-21 WT did not yield any CPE or plaques, in accordance with studies showing that these cells are not natively infected with SARS-bearing spike viruses [408]. However, upon expression of the ACE2 receptor, the cells displayed a stark difference, with CPE and plaque formation in both RE-ACE2 and hACE2 integrations. RE-ACE2-overexpressing BHK-21 cells demonstrated less virus replication and entry than their human counterpart, which exhibited more cell rounding, detachment and higher virus release; however, the difference between the two cell lines was negligible in the plaque assay, with a 1-log difference. This small variance was difficult to interpret, whether it was attributed to the inconsistent level of ACE2s expression between the two cell lines due to integration, the limited 24 h duration of the experiment, which was insufficient to reveal the difference between the two receptors or simply because a minimal permissibility difference exists between RE-ACE2 and hACE2. Nevertheless, the results implied a difference in specificity between the two receptors, with RE-ACE2 allowing less BtCoV HKU5-SE entry than its human counterpart.

Growth kinetics of BtCoV HKU5-SE in R06E WT did not demonstrate productive CPE or plaque formation at any time point of the course, including at 72 hpi, where only minimal CPE was observed. This indicates non-productive infection of R06E WT with a viral titre that is too low to be detected in the plaque assay using the standard 10-fold virus dilution.

Viral CPE in RE-ACE2-overexpressing R06E was fewer and less intense than its analogue expressing the hACE2 receptor across all time points; however, BtCoV HKU5-SE growth kinetics exhibited distinct patterns between the two cell lines. In RE-ACE2-mScarlet cells, the virus increased gradually and modestly over the time course, whereas in R06E-hACE2-EGFP cells, the viral titre rose sharply from 24 hpi, peaked at 48 hpi, and then declined by 72 hpi.

At 24 hpi, BtCoV HKU5-SE released from the humanised bat cells was 1-log higher than that egressed from RE-ACE2 overexpressing cells, consistent with results obtained in BHK-21. However, it could not be particularly concluded if this log difference between the two experiments was consistent due to the ACE2 expression level between the two types of cells, but it might point to a minimal difference in entry between the two receptors in non-productive virus infection at 24 hpi due to a lower number of cells being infected. This was evident at 48 hpi, when HKU5-SE infection in R06E-hACE2-EGFP peaked, leading to egression twice the amount obtained from R06E-RE-ACE2-mScarlet, then declined at 72 hpi when most of the cells underwent death, implying the effect of delayed and inefficient virus replication cycles on receptor usage, which impacts the outcome of virus entry, propagation and egress dynamics.

Notably, overexpression of RE-ACE2 significantly enhanced the BtCoV HKU5-SE replication in R06E compared to WT cells, yet did not achieve the same level as observed in the hACE2 receptor, suggesting dramatic variation between the two receptors in viral entry, which reflected the growth kinetics of BtCoV HKU5-SE in R06E. In this regard, results of this study align with Yan et al [397], who reported less SARS-CoV entry in HEK 293T stably expressing RE-ACE2 than those expressing hACE2 and are partially consistent with Briggs et al [406], who demonstrated lower replication of SARS-CoV-2 strains (Wuhan, Delta and Lambda) in DF1 upon expression of different bat ACE2 receptor including RE-ACE2 in comparison to the human receptor. Intriguingly, the same study reported reduced Delta and Lambda viral titre from the cells with bats' ACE2 compared to the Wuhan strain, highlighting the adaptability of Delta and Lambda to the human receptor, while underlining the evolutionary events that could drive the BtCoV HKU5-SE or possibly any SARS-like virus adaptation using the ACE2 receptor, which underscores ACE2 as a major determinant for cross-species transmission.

Microscopically, the SE antigen demonstrated the strongest signal in VeroE6 cells, consistent with their immunocompromised nature, which allows the virus to spread efficiently. In ACE2 receptor-overexpressing R06E, the SE antigen signal was more intense in humanised cells than in RE-ACE2-expressing cells, which again aligns with the previous finding that hACE2 permits more HKU5-SE entry and replication than RE-ACE2. Cell syncytium forms when the coronavirus S protein escapes from its intracellular compartments during viral replication, moves to the surface of the infected cell, interacts with ACE2 on neighbouring non-infected cells, and thereby facilitates viral transmission between cells [433].

Viral syncytia were detected in VeroE6, hACE2- and RE-ACE2-overexpressing R06E but not in WT cells. This is due to insufficient ACE2 levels in the latter, which compromised initial viral entry and reduced SE antigen production, resulting in less antigen escape and limited fusion formation. In such instances, it is proposed that BtCoV HKU5-SE spreads in WT cells via the cell-free transmission method, which confers inefficient viral spread between cells, compared to cell-to-cell transmission [434], and thereby renders these cells refractory to infection. These results are in line with other studies, which found that ACE2 expression levels are crucial for the development of coronavirus syncytia regardless of species origin [435].

Under normal conditions, hACE2 and RE-ACE2 are expressed within the cytoplasm and distributed on the cell surface, although upon BtCoV HKU5-SE infection, both receptors were largely disappeared from the plasma membrane and clustered with the SE antigen in the cytoplasm, which proposes receptor internalisation and recycling to the cell surface in response to BtCoV HKU5-SE infection, consistent with other SARS-like coronavirus studies [436,437].

Signs of ACE2 lysosomal degradation, including fragmentation, dispersal, and punctuation, were seen across hACE2 and RE-ACE2, although hACE2 exhibited slightly more degradation than RE-ACE2. Since fragmentation of ACE2 is generally associated with receptor binding and internalisation [438], it is likely that RE-ACE2 has a low binding affinity with the SARS-CoV-1 spike. However, other possibilities cannot be excluded, including unique post-translational modifications, cellular machinery responses and structural features that influence one receptor over the other in trafficking and decay. Further validation by immunoprecipitation and additional studies is needed to clarify this observation.

Viral replication kinetics is a cumulative process which combines both receptor-mediated and post-entry host restrictions within the cells, while the growth kinetics quantifies the amount of infectious virus produced over time, primarily reflecting receptor-mediated entry efficiency as well as infectious virus production. Previous findings from the growth kinetics and immunofluorescence demonstrated maximum replication of BtCoV HKU5-SE in R06E upon the expression of the hACE2 receptor; however, the same results were not conclusive regarding the WT cells, which represent the parental tissue of the animal. Therefore, to address this question, the replication dynamics of BtCoV HKU5-SE in WT versus hACE2-expressing R06E cells were investigated further. These cell lines together represent a model for virus replication in parental tissue versus a condition of optimal receptor expression and maximal permissiveness; therefore, RE-ACE2 overexpressed cells were not included in this experiment, as they would not provide additional information beyond that previously obtained in the growth kinetics. Additionally, VeroE6 was excluded, despite being valuable for the growth kinetics, as in the specific aim of replication kinetics to investigate BtCoV HKU5-SE dynamics in WT and hACE2-expressing R06E cells to directly assess receptor-mediated and species-specific restrictions within relevant host backgrounds, thus VeroE6 would not add much to this relevance.

The replication dynamics demonstrated a significant variance in BtCoV HKU5-SE replication between the parental and humanised bat cells. The viral titre in the humanised cells increased sharply from 24 hpi, peaked at 48 hpi, and then plateaued by 72 hpi, with viral input detectable as early as 0 hpi. In contrast, R06E WT showed a negligible viral titre throughout the time course, which did not cross the assay's detection limit except at 72 hpi. This phenotype, while highlighting hACE2 as a key barrier for BtCoV HKU5-SE replication in R06E WT and potentially spillover transmission, also underscores the low expression level of RE-ACE2 as a gatekeeper, modulating the susceptibility of the parental *R. aegyptiacus* cells to BtCoV HKU5-SE and possibly other SARS-like viruses.

In addition to the ACE2, entry of coronaviruses is facilitated by host proteases, particularly TMPRSS2 and CTSL [394,439]. Use of Camostat mesylate and EST compounds is an important strategy for disrupting viral entry, as these compounds selectively inhibit TMPRSS2 and CTSL, respectively [434,440,441]. However, since these compounds are soluble in DMSO, which can affect cell viability [442,443]. The PrestoBlue™ cell viability test was established to ensure that the tested concentration of these compounds would not result in a DMSO level that impairs cell viability during treatment. The test indicated 1% DMSO is the upper tolerance level by all tested cells, consistent with other studies [444,445]. Additionally, using a 10 µM concentration of Camostat mesylate and EST did not affect the viability of the cells, thereby strengthening the reliability of the subsequent protease inhibitor entry assays.

qPCR viral quantification following the protease inhibitors, Camostat mesylate, was detected to have more pronounced inhibition of BtCoV HKU5-SE entry in bat cells than EST. This suggests that TMPRSS2 is the predominant entry pathway that has been utilised by BtCoV HKU5-SE in *R. aegyptiacus* cells. HKU5-SE is a recombinant virus with SARS-CoV-1 SE; thus, the findings from this experiment are consistent with SARS-CoV studies that illustrate TMPRSS2 inhibition suppresses the virus replication more than CTSL [446].

Under normal conditions, A549 cells are refractory to SARS-like viruses due to the lack of ACE2 and TMPRSS2 expression, although they retain endogenous CTSL activity [447,448]. Gene modification approaches can overexpress ACE2 and TMPRSS2 and thereby render the cells susceptible to infection [449]. In the protease inhibitors study, the commercially available A549-hACE2-TMPRSS2 was employed, whereas A549-hACE2-EGFP was developed using the in-house hACE2-EGFP-pB vector. Upon inhibition of TMPRSS2 in A549-hACE2-TMPRSS2, the cells exhibited comparable BtCoV HKU5-SE replication to the untreated control. This view suggests that the overexpression of TMPRSS2 in these cells can override the inhibition imposed by the Camostat mesylate concentration used in the study. In contrast, A549-hACE2-EGFP cells, which rely on the endogenous CTSL, showed reduced infection with EST. This highlights how protease expression levels can determine the apparent efficacy of entry inhibitors.

Notably, inhibition of TMPRSS2 or CTSL alone resulted in a reduction of virus replication by approximately 18% and 9%, respectively, compared to the untreated control, while the dual inhibition reduced the virus by approximately 20%. This was quite surprising as the suppression of both TMPRSS2 and CTSL typically leads to a strong inhibition of coronavirus that depend on these enzymes for entry [450,451] This could be explained by the low concentration of both compounds used, which resulted in partial blockage of the enzymes, which allowed residual viral entry, the high MOI dose applied, which compensates for the blockage or perhaps the existence of possible compensatory alternative protease pathways in bat cells.

Relative expression of key entry factors of BtCoV HKU5-SE in R06E-hACE2-EGFP at 48 hpi peak infection revealed significant upregulation of *RE-ACE2* and *TMPRSS2*, with a modest increase of *hACE2*, whereas *CTSL* did not exhibit any change. This is particularly interesting as only the *RE-ACE2* and *TMPRSS2* were upregulated, rather than other factors. In SARS-CoV-2, studies demonstrated that during infection, the *ACE2* mRNA expression level either decreased or remained unchanged [452,453]. Although transcriptomic profiles from healthy and diseased patients with SARS-CoV-2 detected co-expression of the receptor with the INF and ISGs components, proposing that the ACE2 regulates the innate immunity signalling [454], likewise, the mRNA expression level of *TMPRSS2* tends to be reduced or remains largely unaltered in SARS-CoV-2 infection [455,456]. Nonetheless, high *ACE2* and *TMPRSS2* are associated with IFN and inflammatory response during respiratory viral infections [457]. Accordingly, the significant upregulation of *TMPRSS2* observed in humanised R06E cells is likely related to the inflammatory response induced by BtCoV HKU5-SE infection. Meanwhile, the increased expression of endogenous *RE-ACE2* appears to be strongly associated with the innate antiviral response. Indeed, this anticipation is further supported by the fact that the mRNA expression level of *hACE2* was not significantly upregulated in the qPCR, like that of the endogenous *RE-ACE2* receptor and the differential gene expression heatmap analysis, which demonstrated *RE-ACE2* among the top ten upregulated genes co-expressed with the ISGs.

One interesting finding in this study is the absence of any other *RE-ACE2* isoforms except the full-length receptor as detected by the isoform switching analysis. This implies that the canonical full-length receptor that is responsible for viral entry is the one which co-expresses with the IFNs response in *R. aegyptiacus* R06E. Although variable human cells demonstrated induction of full-length and a truncated version of *ACE2*, delta *ACE2* (*dACE2*) upon IFN and specific respiratory viruses' stimulation [433], only *dACE2* is the true ISG induced by IFNs. This version does not participate in the coronavirus entry [415,458,459]. This could point out that the *RE-ACE2* upregulation in *R. aegyptiacus* bat cells is virus/ or coronavirus-specific, although further studies are required to elucidate this point. Additionally, more research is needed to indicate whether IFNs induce *RE-ACE2* expression in *R. aegyptiacus* bats or vice versa.

In this study, the endogenous *RE-ACE2* mRNA level was increased while the receptor underwent degradation and fragmentation in response to the virus using immunofluorescence. In this context, ACE2 degradation is strongly associated with increasing the cytokine storm in COVID-19 patients [460]. Thus, it could be concluded that the increased susceptibility of the humanised bat cells to BtCoV HKU5-SE virus at 48 hpi likely results from several converging mechanisms. First, the degraded ACE2 receptor in the virus-infected cells created a pro-inflammatory microenvironment that injured and activated *ACE2* and *TMPRSS2* in neighbouring non-infected cells, thereby increasing their permissiveness to infection. Second, the increase in *TMPRSS2* transcripts in infected cells led to increased protease activity, enhancing virus entry within the same cells or into adjacent non-infected cells upon TMPRSS2 release from lysed infected cells. Third, the high mRNA expression of *RE-ACE2* in infected cells generated ACE2 proteins that exceeded those degraded upon virus-receptor internalisation, allowing multiple cycles of virus entry and infection within the same cell and, accordingly, generating a high virus titre and syncytia, which increased virus spread to neighbouring cells. Together, these mechanisms explain why the peak viral infection of the immunocompetent R06E-hACE2-EGFP cells at 48 hpi resembled that of the immunocompromised VeroE6 cells seen in the BtCoV HKU5-SE growth kinetics.

Overall, these results demonstrated an interplay between the BtCoV HKU5-SE and *R. aegyptiacus* bat cells in which ACE2 serves as the main factor which governs the infection rate and cell permissiveness, and further suggests ACE2 as a critical key shaping the competence of *R. aegyptiacus*, spillover and cross-species transmission of BtCoV HKU5-SE or other SARS-like virus to other mammalian hosts.

Chapter 6. General Discussion

R. aegyptiacus (Egyptian fruit bat or Egyptian rousette) is a *Pteropodidae* bat with a wide geographical distribution across Africa and the Middle East, which resides in close association with human habitats [461]. It constitutes a significant reservoir for Marburg filovirus, experimentally infected with SARS-CoV-2 [404,462], and proposed as a reservoir for the Sosuga paramyxovirus [309]. CedPV is a non-pathogenic henipavirus isolated from the urine of Australian flying foxes, which is phylogenetically related to the HeV and NiV, allowing for the study of their pathogenesis and antiviral testing [13]. The m6A is one of the epi-transcriptomic modifications that controls viral replication and innate response, shaping the virus-host interaction [231]. The m6A machinery consists of cellular proteins categorised as writers, erasers, and readers. Writers, including METTL3, METTL14, and WTAP, catalyse the addition of methyl groups to RNA; erasers, FTO and ALKBH5, remove these modifications; and readers, including YTHDF1-3 and YTHDC1-2, recognise and bind methylated RNA [322].

The m6A epi-transcriptomic machinery is well-characterised in human and non-mammalian hosts as well as several other viruses [298,299,304]; however, such information is lacking for Chiroptera (bats) and bat-borne viruses. Therefore, this research gap was addressed in the present study by combining computational and experimental laboratory methods to characterise the role of m6A in the replication of bat CedPV in both human and *R. aegyptiacus* bat cells.

Initially, a comprehensive in-silico and bioinformatics analysis of the m6A machinery in *R. aegyptiacus, P. alecto,* and the well-characterised *H. sapiens* was performed. During the conduct of this research, no information was available about the role of *R. aegyptiacus* in CedPV. Therefore, *P. alecto* was included in the comparison due to its phylogenetic and genetic relatedness to *R. aegyptiacus* and its established relevance in the isolation of CedPV [14,313,341,342].

Amino acid identity of the m6A machinery of *R. aegyptiacus, P. alecto* and *H. sapiens* showed a high degree of conservation among the three species. Although FTO divergence was the highest seen among other m6A regulators in the *R. aegyptiacus* and *P. alecto*, bat-mammalian and bat-human comparisons. In contrast, METTL3 and YTHDF2 had the lowest divergence in both bat-mammalian and bat-human comparisons. Notably, the identity matrix comparison of the Egyptian rousette and black flying fox was close to that of mammals and humans, underscoring possibly conserved catalytic and recognition functions across mammals.

Comparative genomic analysis across *R. aegyptiacus*, *P. alecto*, and *H. sapiens* genomes was not definitive due to the scaffold nature of the bats' genomes; however, the genetic synteny comparison revealed conservation of neighbouring genes of the m6A machinery among the three species, suggesting possible conserved functional and regulatory linkages that may underpin m6A machinery function in bats in comparison to those of humans.

Protein sequence alignment and 3D structural analysis showed that the core functional domains of m6A writers were conserved among *R. aegyptiacus*, *P. alecto*, and *H. sapiens*. For example, METTL3's methyltransferase, gate loops, and ZFD amino acid and tertiary structures were completely conserved. Likewise, the functional regions of METTL14 and WTAP were highly similar across the three species, emphasising the conservation of the methylation reaction and the core functionality of the m6A writer group among *R. aegyptiacus*, *P. alecto*, and *H. sapiens.* In contrast, m6A erasers and readers showed modest variability in the bat-human comparison.

Alignment and structural analyses of the FTO demethylase demonstrated variations across the entire protein between the two bat species and between bats and humans. Nevertheless, the amino acid sequence and structural configuration of the L1 loop and metal-ion–binding sites, which are responsible for FTO nucleic acid selectivity and catalytic activity, respectively [243], were maintained across the three species, suggesting species-specific features of FTO and the preservation of function amid divergence. In contrast, one mutation in the ALKBH5 catalytic domain was observed between bats and humans, yet the protein's structural configuration was disrupted at metal-binding residues and disulfide regions, which function in m6A demethylation and nucleic acid selectivity, respectively [245]. Further crystallographic studies of the protein are warranted to validate this prediction.

Readers exhibited noticeable mutations in their YTH domains across *R. aegyptiacus*, *P. alecto*, and *H. sapiens*, although this did not influence the characteristic aromatic cage of any of the proteins in *R. aegyptiacus* and *H. sapiens*; it impacted that of

YTHDC1 in *P. alecto,* where Leu439 was replaced with Glu. This substitution added an extra hydrogen bond in the m6A-binding pocket, which likely disrupts the classic hydrophobic interaction in the m6A-binding pocket of *P. alecto* YTHDC1, influencing RNA recognition.

In the YTH domain alignment *R. aegyptiacus*, *P. alecto*, and *H. sapiens*, the β5 strand contained an equal number of amino acid residues in all three species, while the interloop region connecting β4 and β5 exhibited variable length: although, at the 3D structural comparison, the imposition of the bats' YTH domains revealed, when superimposed, shorter β5 sheets and longer in between β4-β5 loops when compared to those of the human. The RNA-binding pocket of the YTH domain is located within this region [256]. Thus, whether the same difference in the YTH domain structure between bats and humans is present in vivo and whether it affects RNA binding in *R. aegyptiacus* and *P. alecto* must be clarified by crystallography.

The in-silico findings demonstrated putative conservation of the m6A machinery function between *R. aegyptiacus* and *H. sapiens*, while highlighting the relatedness between the associated modification groups in *R. aegyptiacus* and *P. alecto.* Viral-immune system interactions are a major determinant of host range [463,464]; accordingly, high protein sequence similarity among species that control this response could contribute to their shared susceptibility to viruses.

As mentioned, m6A regulates the host-pathogen innate interactome and can be targeted against different viruses [231,361,362]. Thus, *R. aegyptiacus* is expected to have a comparable intracellular regulation of henipavirus replication, similar to that of *P. alecto*, assuming other factors determining infection between the two species are equivalent. Additionally, the m6A machinery of *R. aegyptiacus* is anticipated to behave similarly, particularly in the writer group, during CedPV replication, as its *H. sapiens* counterparts do. Indeed, in silico and bioinformatics are powerful analytical tools for predicting putative protein function; however, they must be accompanied by experimental verification before drawing any conclusion.

To answer these questions, rCedPV-GFP was propagated in VeroE6 and inoculated into R05T and R06E cells. Surprisingly, neither cell line supported efficient viral replication. That was particularly surprising, particularly for the brain cells, since

CedPV can propagate using the *P. alecto* brain PaBr cell line, the natural reservoir of the virus [14,343], and both *P. alecto* and *R. aegyptiacus* are closely related [313,342]. m6A regulates the viral replication and controls many biological functions in the cell [219,231,322], and in the bioinformatic analysis, m6A between *P. alecto* and *R. aegyptiacus* was highly similar. Although rCedPV-GFP did not replicate efficiently in *R. aegyptiacus* cell lines. Moreover, it cannot replicate in all cell lines of *P. alecto,* the natural host, as well. Indicating that while m6A is structurally conserved, it does not play a critical role in susceptibility of cell lines to CedPV; instead, other cellular factors exist.

rCedPV-GFP was adapted by alternating passages between bat cells and BHK-21 and VeroE6 cells. The trials demonstrated that only VeroE6 cells supported viral adaptation, suggesting cell-line-specific factors that drove CedPV progeny evolution, thus replication in *R. aegyptiacus* bat cells, which is further expanded, selected and stabilised by the application of alternative passaging between the two cell lines.

Overexpression of the hm6A writer METTL3 potently decreased the replication of CedPV in A549, whereas WTAP had a moderate effect on the virus. METTL14, on the other hand, did not increase or decrease the virus replication. Suggesting that METTL3 is the main enzyme that exerts antiviral activity against rCedPV-GFP, while METTL14 and WTAP are accessory proteins since they lack any catalytic function [233,238]. That is support that METTL14 acts as a binding RNA scaffold for METTL3 to exert its methylation reaction and is not homeostatically stabilised in the absence of METTL3 [235,237,365], whereas WTAP is important for recruiting the METTL3-METTL14 to the nuclear speckles where the m6A methylation occurs [233].

Overexpression of ALKBH5 inhibited viral replication in A549 cells, whereas FTO had no effect. This might be explained by the m6A substrate specificity and the innate immunity-regulatory role of ALKBH5 over FTO, which preferentially modifies m6A and plays a role in fat and energy metabolism. [370,372,373].

Increasing the expression of all hm6A readers negatively regulates rCedPV-GFP replication; however, YTHDC2 showed the most significant antiviral properties, suggesting a specific role in rCedPV-GFP virus replication in the cells. Collectively, these results indicate that m6A can be targeted against CedPV in human cells A549.

While rCedPV-GFP represent an excellent model to study the antiviral targets against the NiV and HeV [44], efforts must be applied to determine its validation as a model for the m6A therapy for the pathogenic henipaviruses, taking into consideration the non-adapted virus.

To study m6A in *R. aegyptiacus*, METTL3 was selected to examine its role in rCedPV-GFP replication using the R06E cell line. ORF of *RE-METTL3* was tagged, synthesised and cloned into the pB-CAG-EGFP vector. Moreover, mScarlet was linked to the protein via IRES2 to enable transfection tracking. IRES2 is a modified version of WT IRES to increase the translation efficiency of the downstream protein [236,381]. The synthesised vector successfully expressed both proteins at high intensity when transfected into A549 cells, indicating the utility of this construct across different cell culture models. Subsequently, RE-METTL3 domains were amplified individually or in combination and cloned into the synthesised plasmid to generate a series of domain constructs for ectopic expression in R06E cells. Additionally, a mScarlet pB vector was cloned in parallel as a positive control for the rCedPV-GFP infection. All RE-METTL3-related cell lines were successfully established and validated using WB or PCR for those expressing the ZFDs, and could not be detected using WB.

Inoculation of CedPV into the R06E cell lines revealed an antiviral effect of RE-METTL3, similar to that of the human, with comparable effects between full-length RE-METTL3 and its domains. All RE-METTL3 domains were expressed in the cytoplasm in both infected and noninfected conditions. That is anticipated due to the lack of the NLS. Although the weakly observed could be due to their small size, which allowed passive diffusion to the nucleus without the requirement of NLS [387]. Under basal conditions, RE-METTL3 was expressed predominantly in the nucleus of R06E; however, upon the rCedPV-GFP infection, the protein was translocated to the cytoplasm, similar to other paramyxoviruses. Additionally, translocation of METTL3 to the cytoplasm in rCedPV-GFP raises whether METTL14 and WTAP are translocated as well to aid METTL3 in its function or whether METTL3 has an m6A-independent antiviral function against rCedPV-GFP in bat cells.

HKU5-CoV is a merbecovirus that is closely related to MERS-CoV [59]. In silico and cell culture studies on this virus have identified two lineages: lineage 1, which utilises the *Neogale vison* (*N. vison*) and *P. abramus* bat ACE2 receptors [465] and lineage 2, which can utilise the hACE2 [105]. Moreover, HKU5-like viruses have been isolated from the lungs and intestines of *N. vison* [466], suggesting the robust species jump and spillover transmission of HKU5. Being bat-borne viruses, studies on the original HKU5 have long been hindered by the inability to identify its cellular receptor, which prevented successful replication using traditional cell culture systems [467,468]. In fact, the receptor of lineage 1 and the discovery of lineage 2 HKU5 virus were revealed during the drafting of this thesis [105,465]. Therefore, to study this interesting public health virus, recombinant chimeric BtCoV HKU5-SE [469] was used to overcome the challenges of testing and studying the virus.

In this study, the molecular entry barriers to BtCoV HKU5-SE (lineage 1) replication in *R. aegyptiacus* bat cells R06E were investigated. Initially, the virus was propagated in VeroE6 cells, which displayed progressive and robust infection across the time course. This is in parallel with studies that established VeroE6 as a robust system for replication of SARS spike-like viruses [422,423].

TaqMan quantification of BtCoV HKU5-SE using the N gene demonstrated sensitivity, detecting up to approximately 342 viral RNA copies/reaction and slope values of -3.3266, which is equivalent to 99.8% amplification efficacy. Moreover, it did not yield any amplification using the SARS-CoV-2 genome, confirming the sensitivity and specificity of the developed assay for monitoring the replication kinetics of BtCoV HKU5-SE.

To assess the susceptibility of *R. aegyptiacus* bat cells (R06E) to BtCoV HKU5-SE virus, the cells were inoculated with an MOI of 1 of the virus, along with VeroE6, and monitored for infection at 24 h. In contrast to VeroE6, which was highly susceptible to the virus, R06E showed no signs of infection, neither under the microscope nor in the plaque assay, indicating minimal non-productive infection. Using qPCR and high doses of BtCoV HKU5-SE virus, the low level of expression of endogenous RE-ACE2 was concluded as the barrier to BtCoV HKU5-SE replication in R06E cells.

To determine whether the low expression level of endogenous RE-ACE2 or the species nature of the receptor was the obstacle to the infection, hACE2-EGFP and RE-ACE were amplified, tagged and cloned into the pB-CAG-EGFP vector and RE-METTL3-WT-CAG-mScarlet-pB, respectively and established R06E and BHK-21cell lines stably expressing both of the individual receptors. The findings using the pB system demonstrated successful integration of the receptors in both cell lines using the WB.

Upon infection of the BtCoV HKU5-SE, RE-ACE2 allowed less viral growth than hACE2; however, the difference between the two receptors was modest (1-log) at 24 hpi. This could be explained either by the inconsistent levels of ACE2 expression between the two cell lines, the short duration of the study (i.e., 24 hpi), or the modest difference between RE-ACE2 and hACE2. Nevertheless, this finding indicates that there is a specificity difference between the two receptors regarding BtCoV HKU5-SE entry and replication.

Growth kinetics of BtCoV HKU5-SE in R06E WT produced non-productive infection over the 72 h time course of infection, with no plaque formation and negligible CPE observed only at 72 hpi, suggesting that the release of BtCoV HKU5-SE was insufficient for detection by the standard 10-fold serial dilution plaque assay. In contrast, overexpression of RE-ACE2 enhanced the virus replication and intensity of CPE in bat cells throughout the infection period; nevertheless, the egress was gradual and not significant. On the other hand, expression of the hACE2 in R06E has led to a sharp increase in the virus replication at all time points, with the virus peaking at 48 hpi to levels comparable with those in VeroE6 cells, before declining by 72 hpi. Suggesting that while overexpression of RE-ACE2 enhanced the infection of BtCoV HKU5-SE in R06E compared to WT, it did not reach the same level as that observed in hACE2, which reflects dramatic variation between the two receptors in viral entry and subsequently in replication.

The SE antigen intensity was higher in hACE2-expressing bat cells compared to their RE-ACE2 counterparts. In contrast, virus syncytia were detected in both hACE2 and RE-ACE2 bearing cells but not in WT cells, which demonstrated negligible SE antigen. This implies that the ACE2 expression level, irrespective of species origin, is critical for the development of viral syncytia, as it reflects the production of S antigen, which is responsible for triggering the syncytia in coronavirus-infected cells [433]. Of note, hACE2 and RE-ACE receptors relocated with SE antigen in the intrinsic of the cell and largely disappeared from the cell surface, suggesting receptor recycling; although it was observed that hACE2 underwent greater degradation than RE-ACE2. That might be explained by the low binding capacity of the RE-ACE2 to the SE antigen, unique post-translational modifications, cellular machinery responses and structural features that influence one receptor over the other in trafficking and decay.

Viral quantification in WT and hACE2 R06E demonstrated a substantial increase in the humanised bat cells from 24 hpi, peaked at 48 hpi, and then plateaued by 72 hpi, with viral input detectable as early as 0 hpi. In contrast, WT cells showed undetectable virus levels across the time course, except at 72 hpi, highlighting hACE2 as a key barrier for BtCoV HKU5-SE replication in R06E WT and potentially spillover transmission, while underscoring the low expression level of RE-ACE2 as a gatekeeper receptor, modulating the susceptibility of the parental *R. aegyptiacus* cells to BtCoV HKU5-SE and possibly other SARS-like viruses.

Using Camostat mesylate and EST protease inhibitors, following the DMSO and individual compound viability test, BtCoV HKU5-SE entry was found to depend on TMPRSS2 rather than CTSL, mirroring the TMPRSS2 dependency of SARS-CoV [446] since the chimeric virus is constructed with SARS-CoV-SE-SE incorporation in HKU5 and SARS-CoV dependency on TMPRSS2 for entry. In contrast, the entry of the virus could not be inhibited in A549-hACE2-TMPRSS2, which was engineered to overexpress TMPRSS2, but was suppressed in A549-hACE2-EGFP, which expressed endogenous CTSL. This suggests that the magnitude of Camostat mesylate and EST inhibition largely depends on the level of expression of TMPRSS2 and CTSL in the cells. Notably, the dual inhibition of TMPRSS2 and CTSL resulted in slightly less entry difference than that achieved using Camostat mesylate alone. This is likely due to the low concentration of both compounds used, which allowed residual viral entry, the high MOI dose applied, which compensates for the blockage or perhaps the existence of possible compensatory alternative protease pathways in bat cells.

The relative qPCR expression level of the key entry component for BtCoV HKU5-SE in the peak infection of the R06E-hACE2-GFP revealed significant upregulation of

RE-ACE2 and *TMPRSS2*, with a modest increase of *hACE2*, whereas *CTSL* did not exhibit any change. This significant increase of *TMPRSS2* and *RE-ACE2* could be due to the inflammation and IFN responses produced by the bat cells in response to BtCoV HKU5-SE infection, or perhaps the increase in *TMPRSS2* is associated with the degradation of the receptor, as TMPRSS2 is also a protease that cleaves ACE2 [470,471]. Indeed, increased expression of ACE*2* and *TMPRSS2* is noted with the inflammatory and IFN responses during viral respiratory infections [457], whereas co-expression of *ACE2* is associated with the IFN response, including ISGs [454]. This was also observed in the heatmap clustering, which detected *RE-ACE2* as one of the top ten upregulated genes in response to BtCoV HKU5-SE, along with several ISGs. Collectively, these findings indicate ACE2 as a crucial key that determines infection, susceptibility, cross-species transmission, and spillover of BtCoV HKU5-SE and potentially other SARS-like viruses in *R. aegyptiacus* bat.

In conclusion, this thesis establishes m6A RNA modifications and ACE2 receptor dynamics as crucial foundational molecular barriers that restrict replication of henipavirus and SARS-like coronavirus spillover in *R. aegyptiacus*, and fundamentally reshape the understanding of viral host-range restriction in bats.

Limitations of the Study and Future Work

Although this study provides new and novel insights with regard to m6A, CedPV immune response, and ACE2 in bats, it remains to be fulfilled by the following.

For the CedPV study and bioinformatic analysis, it was anticipated that there was a core functional similarity between the human and Egyptian rousette m6A machinery. While this was proven in terms of antiviral activity against CedPV, it is necessary to elucidate this further and to establish research on other m6A regulators as well, particularly the eraser and reader groups, which indicated a lower degree of similarity than the writers.

In this study, the lowest number of passages was employed for adapting/fine-tuning the rCedPV-GFP replication in bat cells. Although this drastically minimises adverse shifts in the viral immune response and viral-host interactions, it cannot exclude the possibility entirely. Even though it is unlikely that the adaptation process drastically affected the immune interactions of rCedPV-GFP, it is necessary to compare the findings of this study with those using the original, non-adapted virus.

This study provided insights into the role of m6A in CedPV while demonstrating METTL3 as an antiviral factor in human and bat cells. However, further research on the role of YTHDC2 in CedPV should be performed, since it was suggested as a promising candidate protein.

For the BtCoV HKU5-SE study, *R. aegyptiacus* liver cells (R06E) were used, and it was detected that RE-ACE2 is a major barrier determining infectivity and potential spillover in *R. aegyptiacus*. In a study testing the susceptibility of *R. aegyptiacus* bats to SARS-CoV-2, the level of *ACE2* expression was measured across multiple organs and compared to the *EEFA1* level using the same reference gene primers employed in this study. That study indicated inconsistency in *ACE2* expression between different tissues, where most respiratory and digestive organs exhibited high expression in contrast to others, yet the bat showed minimal manifestation with regard to SARS-CoV-2, which proposes the existence of other non-ACE2 tissue-specific barriers [422]. The RE-ACE2-overexpressing R06E cells in this study showed enhanced BtCoV HKU5-SE growth kinetics, which might anticipate a similar condition in organs where receptor expression is elevated. However, these are engineered cells representing a single organ, and therefore, RE-ACE2 expression is likely much higher and would not reflect the receptor expression of any natural organ, including those where RE-ACE2 is abundant. Although it is expected that RE-ACE2 will remain a key barrier governing infectivity, host competency, and spillover in *R. aegyptiacus*, even in tissues with high receptor expression, owing to receptor properties that restrict viral entry, replication, and binding, further investigation using cell lines derived from multiple Egyptian rousette organs is required. This would enable a more robust evaluation of the tissue-specific role of RE-ACE2 in limiting viral infection. Additionally, this research should be conducted using additional cell lines representing multiple organs of the Egyptian rousette. This would allow conclusions to be drawn regarding the extent to which RE-ACE2 acts as a vital barrier in *R. aegyptiacus* or whether other tissue-dependent factors are also involved in limiting viral replication in *R. aegyptiacus* cells and will assist in understanding tissue tropism and reservoir biology of the virus in *R. aegyptiacus*. Moreover, it would be of interest to test both lineages of the parental HKU5 in parallel with the recombinant virus in *R. aegyptiacus* cells from this study to investigate the role and interaction of RE-ACE2 against this potentially pandemic virus.

Chapter 7. Supplementary Figures

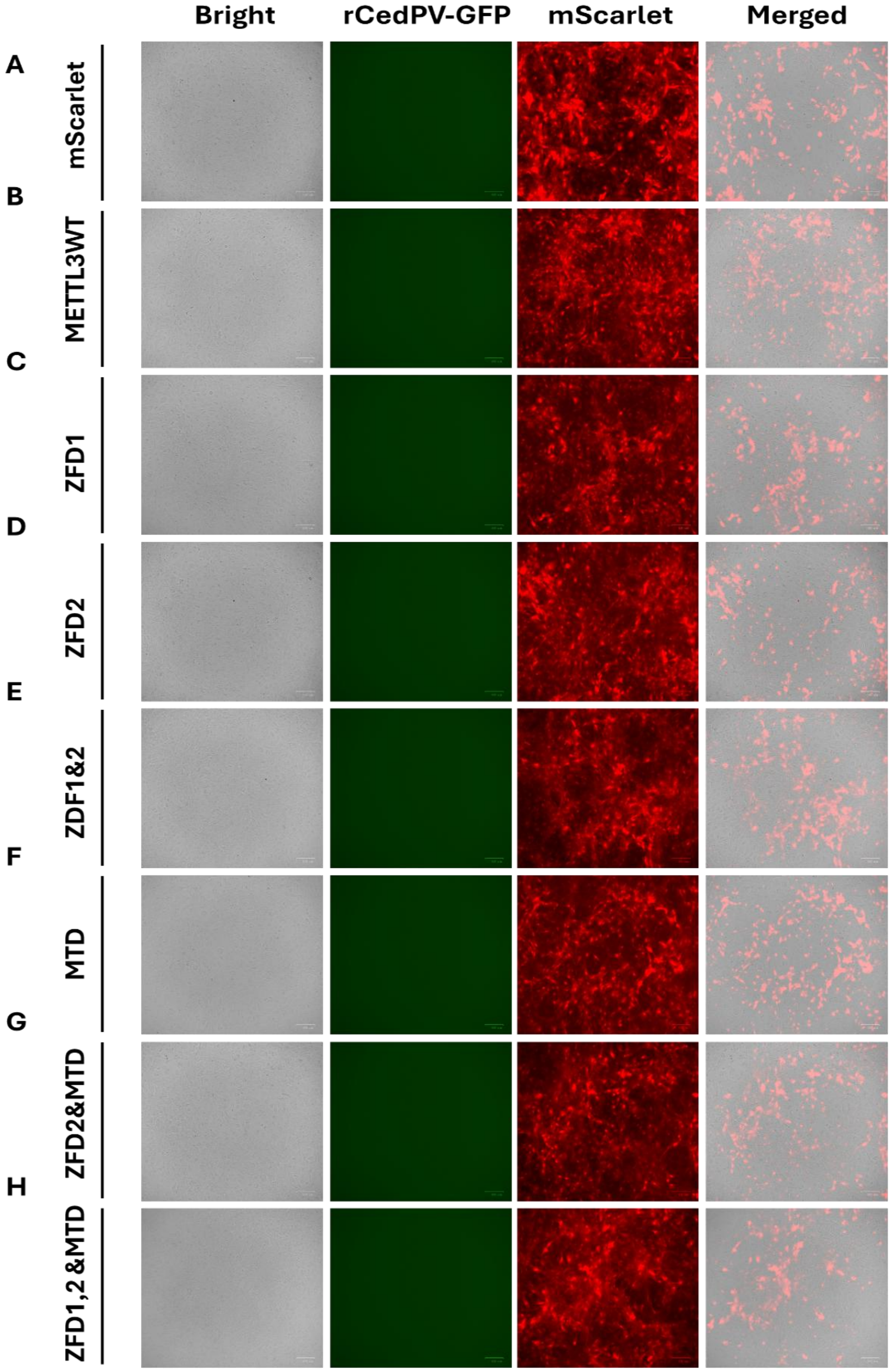

Figure 7.1. Mock-infected of RE-METTL3 and its associated domains confer reduced replication of rCedPV-GFP virus in R06E. (A) R06E -mScarlet. (B) R06E-METTL3-WT-mScarlet. (C) R06E-METTL3-ZFD1-mScarlet. (D) R06E-METTL3-ZFD2-mScarlet. (E) R06E-METTL3-ZFD1 & 2 -mScarlet. (F) R06E-METTL3-MTD-mScarlet. (G) R06E -METTL3- ZFD 2 & MTD- mScarlet. (H) R06E -METTL3 -ZFD1, 2 & MTD- mScarlet. Scale bar = 100 µm.

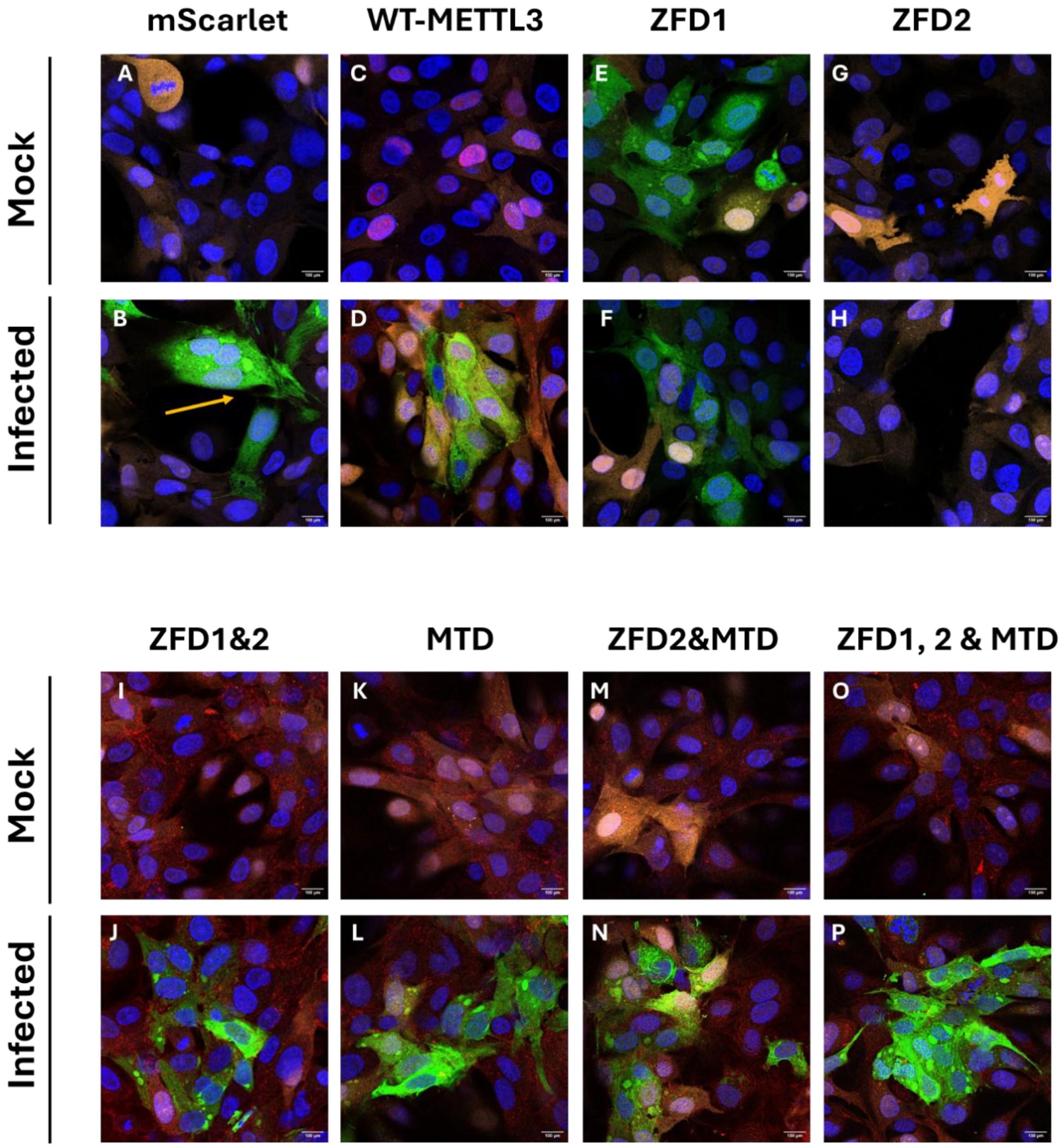

Figure 7.2. Cellular localisation of RE-METTL3 and the associated domain in the R06E with and without rCedPV-GFP stimulation, as demonstrated by the immunofluorescence imaging. The full-length RE-METTL3 showed nuclear localisation in mock cells, whereas the protein was translocated to the cytoplasm upon rCdPV-GFP infection. The related domains remained in the cytoplasm regardless of the presence or absence of the infection. (A-B) Mock-infected and infected R06E -mScarlet. (C-D) Mock-infected and infected R06E-METTL3-WT-mScarlet. (E-F) Mock-infected and infected R06E-METTL3-ZFD1-mScarlet. (G-H) Mock-infected and infected R06E-METTL3-ZFD2-mScarlet. (I-J) Mock-infected and infected R06E-METTL3-ZFD1 & 2 -mScarlet. (K-L) Mock-infected and infected R06E-METTL3-MTD-mScarlet. (M-N) Mock-infected and infected R06E -METTL3- ZFD 2 & MTD- mScarlet. (O-P) Mock-infected and infected R06E -METTL3 -ZFD1, 2 & MTD- mScarlet. DAPI (blue). rCedPV (green). METTL3 protein and related domains (red). mScalert (orange). rCedPV-GFP syncytia in mScarlet control are highlighted with an orange arrow. Scale bar = 100 µm.

Chapter 8. References

1. James MacLachlan, E.J.D. Paramyxoviridae and Pneumoviridae. *Fenner's Vet. Virol.* 2017, 327–356, doi:10.1016/B978-0-12-800946-8.00017-9.
2. Field, H.; Young, P.; Yob, J.M.; Mills, J.; Hall, L.; Mackenzie, J. The Natural History of Hendra and Nipah Viruses. *Microbes Infect.* 2001, *3*, 307–314, doi:10.1016/S1286-4579(01)01384-3.
3. O'Sullivan, J.D.; Allworth, A.M.; Paterson, D.L.; Snow, T.M.; Boots, R.; Gleeson, L.J.; Gould, A.R.; Hyatt, A.D.; Bradfield, J. Fatal Encephalitis Due to Novel Paramyxovirus Transmitted from Horses. *Lancet* 1997, *349*, 93–95, doi:10.1016/S0140-6736(96)06162-4.
4. Field, H.E.; Barratt, P.C.; Hughes, R.J.; Shield, J.; Sullivan, N.D. A Fatal Case of Hendra Virus Infection in a Horse in North Queensland: Clinical and Epidemiological Features. *Aust. Vet. J.* 2000, *78*, 279–280, doi:10.1111/J.1751-0813.2000.TB11758.X.
5. Halpin, K.; Young, P.L.; Field, H.E.; Mackenzie, J.S. Isolation of Hendra Virus from Pteropid Bats: A Natural Reservoir of Hendra Virus. *J. Gen. Virol.* 2000, *81*, 1927–1932, doi:10.1099/0022-1317-81-8-1927/CITE/REFWORKS.
6. Wang, J.; Anderson, D.E.; Halpin, K.; Hong, X.; Chen, H.; Walker, S.; Valdeter, S.; van der Heide, B.; Neave, M.J.; Bingham, J.; et al. A New Hendra Virus Genotype Found in Australian Flying Foxes. *Virol. J.* 2021, *18*, 1–13, doi:10.1186/S12985-021-01652-7/FIGURES/5.
7. Ksiazek, T.G.; Rota, P.A.; Rollin, P.E. A Review of Nipah and Hendra Viruses with an Historical Aside. *Virus Res.* 2011, *162*, 173–183, doi:10.1016/J.VIRUSRES.2011.09.026.
8. Chadha, M.S.; Comer, J.A.; Lowe, L.; Rota, P.A.; Rollin, P.E.; Bellini, W.J.; Ksiazek, T.G.; Mishra, A.C. Nipah Virus-Associated Encephalitis Outbreak, Siliguri, India - Volume 12, Number 2—February 2006 - Emerging Infectious Diseases Journal - CDC. *Emerg. Infect. Dis.* 2006, *12*, 235–240, doi:10.3201/EID1202.051247.
9. Hsu, V.P.; Hossain, M.J.; Parashar, U.D.; Ali, M.M.; Ksiazek, T.G.; Kuzmin, I.; Niezgoda, M.; Rupprecht, C.; Bresee, J.; Breiman, R.F. Nipah Virus Encephalitis Reemergence, Bangladesh. *Emerg. Infect. Dis.* 2004, *10*, 2082, doi:10.3201/EID1012.040701.
10. Luby, S.P.; Rahman, M.; Hossain, M.J.; Blum, L.S.; Husain, M.M.; Gurley, E.; Khan, R.; Ahmed, B.N.; Rahman, S.; Nahar, N.; et al. Foodborne Transmission of Nipah Virus, Bangladesh - Volume 12, Number 12—December 2006 - Emerging Infectious Diseases Journal - CDC. *Emerg. Infect. Dis.* 2006, *12*, 1888–1894, doi:10.3201/EID1212.060732.
11. Ching, P.K.G.; de Los Reyes, V.C.; Sucaldito, M.N.; Tayag, E.; Columna-Vingno, A.B.; Malbas, F.F.; Bolo, G.C.; Sejvar, J.J.; Eagles, D.; Playford, G.; et al. Outbreak of Henipavirus Infection, Philippines, 2014. *Emerg. Infect. Dis.* 2015, *21*, 328, doi:10.3201/EID2102.141433.

12. Mougari, S.; Gonzalez, C.; Reynard, O.; Horvat, B. Fruit Bats as Natural Reservoir of Highly Pathogenic Henipaviruses: Balance between Antiviral Defense and Viral ToleranceInteractions between Henipaviruses and Their Natural Host, Fruit Bats. *Curr. Opin. Virol.* 2022, *54*, doi:10.1016/j.coviro.2022.101228.

13. Sabir, A.J.; Rong, L.; Broder, C.C.; Amaya, M. Cedar Virus Biology and Its Applications as a Surrogate for Highly Pathogenic Henipaviruses. *Cell Insight* 2024, *3*, 100181, doi:10.1016/J.CELLIN.2024.100181.

14. Marsh, G.A.; de Jong, C.; Barr, J.A.; Tachedjian, M.; Smith, C.; Middleton, D.; Yu, M.; Todd, S.; Foord, A.J.; Haring, V.; et al. Cedar Virus: A Novel Henipavirus Isolated from Australian Bats. *PLoS Pathog.* 2012, *8*, doi:10.1371/JOURNAL.PPAT.1002836.

15. Wu, Z.; Yang, L.; Yang, F.; Ren, X.; Jiang, J.; Dong, J.; Sun, L.; Zhu, Y.; Zhou, H.; Jin, Q. Novel Henipa-like Virus, Mojiang Paramyxovirus, in Rats, China, 2012. *Emerg. Infect. Dis.* 2014, *20*, 1064, doi:10.3201/EID2006.131022.

16. Zhang, X.-A.; Li, H.; Jiang, F.-C.; Zhu, F.; Zhang, Y.-F.; Chen, J.-J.; Tan, C.-W.; Anderson, D.E.; Fan, H.; Dong, L.-Y.; et al. A Zoonotic Henipavirus in Febrile Patients in China. *N. Engl. J. Med.* 2022, *387*, 470–472, doi:10.1056/NEJMC2202705.

17. International Committee on Taxonomy of Viruses Current ICTV Taxonomy Release | ICTV Available online: https://ictv.global/taxonomy (accessed on 1 May 2026).

18. Cox, R.M.; Plemper, R.K. Structure and Organization of Paramyxovirus Particles. *Curr. Opin. Virol.* 2017, *24*, 105–114, doi:10.1016/J.COVIRO.2017.05.004.

19. Kolakofsky, D.; Roux, L.; Garcin, D.; Ruigrok, R.W.H. Paramyxovirus MRNA Editing, the “rule of Six” and Error Catastrophe: A Hypothesis. *J. Gen. Virol.* 2005, *86*, 1869–1877, doi:10.1099/VIR.0.80986-0.

20. Bloyet, L.-M.M.; Blackledge, M. The Nucleocapsid of Paramyxoviruses: Structure and Function of an Encapsidated Template. *Viruses* 2021, *13*, 2465, doi:10.3390/V13122465.

21. Noton, S.L.; Fearns, R. INITIATION AND REGULATION OF PARAMYXOVIRUS TRANSCRIPTION AND REPLICATION. *Virology* 2015, *0*, 545, doi:10.1016/J.VIROL.2015.01.014.

22. Samuel, A.S.; Kumar, S.; Madhuri, S.; Collins, P.L.; Samal, S.K. Complete Sequence of the Genome of Avian Paramyxovirus Type 9 and Comparison with Other Paramyxoviruses. *Virus Res.* 2009, *142*, 10–18, doi:10.1016/J.VIRUSRES.2008.12.016.

23. Morrison, T.G. Structure and Function of a Paramyxovirus Fusion Protein. *Biochim. Biophys. Acta - Biomembr.* 2003, *1614*, 73–84, doi:10.1016/S0005-

2736(03)00164-0.

24. Abdella, R.; Aggarwal, M.; Okura, T.; Lamb, R.A.; He, Y. Structure of a Paramyxovirus Polymerase Complex Reveals a Unique Methyltransferase-CTD Conformation. *Proc. Natl. Acad. Sci. U. S. A.* 2020, *117*, 4931–4941, doi:10.1073/PNAS.1919837117.

25. Alayyoubi, M.; Leser, G.P.; Kors, C.A.; Lamb, R.A.; Dutch, R.E.; Randall, R.E.; Rey, F.A. Structure of the Paramyxovirus Parainfluenza Virus 5 Nucleoprotein–RNA Complex. *Proc. Natl. Acad. Sci.* 2015, *112*, E1792–E1799, doi:10.1073/PNAS.1503941112.

26. El Najjar, F.; Schmitt, A.P.; Dutch, R.E. Paramyxovirus Glycoprotein Incorporation, Assembly and Budding: A Three Way Dance for Infectious Particle Production. *Viruses* 2014, *6*, 3019–3054, doi:10.3390/v6083019.

27. Takimoto, T.; Portner, A. Molecular Mechanism of Paramyxovirus Budding. *Virus Res.* 2004, *106*, 133–145, doi:10.1016/J.VIRUSRES.2004.08.010.

28. Durbin, A.P.; McAuliffe, J.M.; Collins, P.L.; Murphy, B.R. Mutations in the C, D, and V Open Reading Frames of Human Parainfluenza Virus Type 3 Attenuate Replication in Rodents and Primates. *Virology* 1999, *261*, 319–330, doi:10.1006/VIRO.1999.9878.

29. Shaw, M.L.; Cardenas, W.B.; Zamarin, D.; Palese, P.; Basler, C.F. Nuclear Localization of the Nipah Virus W Protein Allows for Inhibition of Both Virus- and Toll-like Receptor 3-Triggered Signaling Pathways. *J. Virol.* 2005, *79*, 6078–6088, doi:10.1128/JVI.79.10.6078-6088.2005.

30. Kitagawa, Y.; Yamaguchi, M.; Zhou, M.; Komatsu, T.; Nishio, M.; Sugiyama, T.; Takeuchi, K.; Itoh, M.; Gotoh, B. A Tryptophan-Rich Motif in the Human Parainfluenza Virus Type 2 V Protein Is Critical for the Blockade of Toll-like Receptor 7 (TLR7)- and TLR9-Dependent Signaling. *J. Virol.* 2011, *85*, 4606–4611, doi:10.1128/JVI.02012-10.

31. Yamaguchi, M.; Kitagawa, Y.; Zhou, M.; Itoh, M.; Gotoh, B. An Anti-Interferon Activity Shared by Paramyxovirus C Proteins: Inhibition of Toll-like Receptor 7/9-Dependent Alpha Interferon Induction. *FEBS Lett.* 2014, *588*, 28–34, doi:10.1016/J.FEBSLET.2013.11.015.

32. Siering, O.; Cattaneo, R.; Pfaller, C.K. C Proteins: Controllers of Orderly Paramyxovirus Replication and of the Innate Immune Response. *Viruses* 2022, *14*, 137, doi:10.3390/V14010137.

33. Laing, E.D.; Navaratnarajah, C.K.; da Silva, S.C.; Petzing, S.R.; Xu, Y.; Sterling, S.L.; Marsh, G.A.; Wang, L.F.; Amaya, M.; Nikolov, D.B.; et al. Structural and Functional Analyses Reveal Promiscuous and Species Specific Use of Ephrin Receptors by Cedar Virus. *Proc. Natl. Acad. Sci. U. S. A.* 2019, *116*, 20707–20715, doi:10.1073/PNAS.1911773116.

34. Douglas, J.; Drummond, A.J.; Kingston, R.L. Evolutionary History of

Cotranscriptional Editing in the Paramyxoviral Phosphoprotein Gene. *Virus Evol.* 2021, *7*, doi:10.1093/VE/VEAB028.

35. Hanley, L.L.; McGivern, D.R.; Teng, M.N.; Djang, R.; Collins, P.L.; Fearns, R. Roles of the Respiratory Syncytial Virus Trailer Region: Effects of Mutations on Genome Production and Stress Granule Formation. *Virology* 2010, *406*, 241, doi:10.1016/J.VIROL.2010.07.006.

36. Gazal, S.; Sharma, N.; Gazal, S.; Tikoo, M.; Shikha, D.; Badroo, G.A.; Rashid, M.; Lee, S.J. Nipah and Hendra Viruses: Deadly Zoonotic Paramyxoviruses with the Potential to Cause the Next Pandemic. *Pathog. 2022, Vol. 11, Page 1419* 2022, *11*, 1419, doi:10.3390/PATHOGENS11121419.

37. Yuen, K.Y.; Fraser, N.S.; Henning, J.; Halpin, K.; Gibson, J.S.; Betzien, L.; Stewart, A.J. Hendra Virus: Epidemiology Dynamics in Relation to Climate Change, Diagnostic Tests and Control Measures. *One Heal.* 2021, *12*, 100207, doi:10.1016/J.ONEHLT.2020.100207.

38. Alam, A.M. Nipah Virus, an Emerging Zoonotic Disease Causing Fatal Encephalitis. *Clin. Med. (Northfield. Il).* 2022, *22*, 348, doi:10.7861/CLINMED.2022-0166.

39. Marsh, G.A.; Wang, L.F. Hendra and Nipah Viruses: Why Are They so Deadly? *Curr. Opin. Virol.* 2012, *2*, 242–247, doi:10.1016/j.coviro.2012.03.006.

40. Nayak, S. Unveiling Emerging Threats: Langya and Mojiang- A Dance with Unfamiliar Foes. *Infect. Dis. Immun.* 2025, *5*, 206–218, doi:10.1097/ID9.0000000000000155.

41. Gurley, E.S.; Plowright, R.K. A Roadmap of Primary Pandemic Prevention Through Spillover Investigation. *Emerg. Infect. Dis.* 2025, *31*, 1501, doi:10.3201/EID3108.250442.

42. Mohapatra, P.; Nazli Khatib, M.; Shabil, M.; Rajput, P.; Sharma, N.; Satapathy, P.; Bhopte, K.; Jena, D.; Sah, S.; Bushi, G. Addressing the Nipah Virus Threat: A Call for Global Vigilance and Coordinated Action. *Clin. Infect. Pract.* 2024, *24*, 100390.

43. World Health Organization Nipah Virus Available online: https://www.who.int/news-room/fact-sheets/detail/nipah-virus (accessed on 20 September 2025).

44. Laing, E.D.; Amaya, M.; Navaratnarajah, C.K.; Feng, Y.R.; Cattaneo, R.; Wang, L.F.; Broder, C.C. Rescue and Characterization of Recombinant Cedar Virus, a Non-Pathogenic Henipavirus Species. *Virol. J.* 2018, *15*, 56, doi:10.1186/S12985-018-0964-0.

45. Souilmi, Y.; Lauterbur, M.E.; Tobler, R.; Huber, C.D.; Johar, A.S.; Moradi, S.V.; Johnston, W.A.; Krogan, N.J.; Alexandrov, K.; Enard, D. An Ancient Viral Epidemic Involving Host Coronavirus Interacting Genes More than 20,000 Years Ago in East Asia. *Curr. Biol.* 2021, *31*, 3504-3514.e9,

doi:10.1016/j.cub.2021.05.067.

46. Kahn, J.S.; McIntosh, K. History and Recent Advances in Coronavirus Discovery. *Pediatr. Infect. Dis. J.* 2005, *24*, doi:10.1097/01.inf.0000188166.17324.60.

47. Peiris, J.S.M.; Lai, S.T.; Poon, L.L.M.; Guan, Y.; Yam, L.Y.C.; Lim, W.; Nicholls, J.; Yee, W.K.S.; Yan, W.W.; Cheung, M.T.; et al. Coronavirus as a Possible Cause of Severe Acute Respiratory Syndrome. *Lancet* 2003, *361*, 1319–1325, doi:10.1016/S0140-6736(03)13077-2.

48. Cherry, J.D.; Krogstad, P. SARS: The First Pandemic of the 21st Century. *Pediatr. Res.* 2004, *56*, 1, doi:10.1203/01.PDR.0000129184.87042.FC.

49. Lau, S.K.P.; Woo, P.C.Y.; Li, K.S.M.; Huang, Y.; Tsoi, H.W.; Wong, B.H.L.; Wong, S.S.Y.; Leung, S.Y.; Chan, K.H.; Yuen, K.Y. Severe Acute Respiratory Syndrome Coronavirus-like Virus in Chinese Horseshoe Bats. *Proc. Natl. Acad. Sci. U. S. A.* 2005, *102*, 14040, doi:10.1073/PNAS.0506735102.

50. Cui, J.; Li, F.; Shi, Z.L. Origin and Evolution of Pathogenic Coronaviruses. *Nat. Rev. Microbiol.* 2019, *17*, 181–192, doi:10.1038/S41579-018-0118-9.

51. Ye, Z.W.; Yuan, S.; Yuen, K.S.; Fung, S.Y.; Chan, C.P.; Jin, D.Y. Zoonotic Origins of Human Coronaviruses. *Int. J. Biol. Sci.* 2020, *16*, 1686, doi:10.7150/IJBS.45472.

52. Zaki, A.M.; van Boheemen, S.; Bestebroer, T.M.; Osterhaus, A.D.M.E.; Fouchier, R.A.M. Isolation of a Novel Coronavirus from a Man with Pneumonia in Saudi Arabia. *N. Engl. J. Med.* 2012, *367*, 1814–1820, doi:10.1056/NEJMOA1211721.

53. Müller, M.A.; Corman, V.M.; Jores, J.; Meyer, B.; Younan, M.; Liljander, A.; Bosch, B.J.; Lattwein, E.; Hilali, M.; Musa, B.E.; et al. MERS Coronavirus Neutralizing Antibodies in Camels, Eastern Africa, 1983–1997. *Emerg. Infect. Dis.* 2014, *20*, 2093, doi:10.3201/EID2012.141026.

54. European Centre for Disease Prevention and Control MERS-CoV Worldwide Overview Available online: https://www.ecdc.europa.eu/en/middle-east-respiratory-syndrome-coronavirus-mers-cov-situation-update (accessed on 11 September 2025).

55. World Heath Organization COVID-19 Deaths | WHO COVID-19 Dashboard Available online: https://data.who.int/dashboards/covid19/deaths (accessed on 27 April 2026).

56. Holmes, E.C.; Goldstein, S.A.; Rasmussen, A.L.; Robertson, D.L.; Crits-Christoph, A.; Wertheim, J.O.; Anthony, S.J.; Barclay, W.S.; Boni, M.F.; Doherty, P.C.; et al. The Origins of SARS-CoV-2: A Critical Review. *Cell* 2021, *184*, 4848–4856, doi:10.1016/J.CELL.2021.08.017.

57. Mo, Y.; Lim, L.S.; Ng, S.K. A Systematic Review on Current Approaches in Bat Virus Discovered between 2018 and 2022. *J. Virol. Methods* 2024, *329*,

115005, doi:10.1016/J.JVIROMET.2024.115005.

58. Banerjee, A.; Kulcsar, K.; Misra, V.; Frieman, M.; Mossman, K. Bats and Coronaviruses. *Viruses* 2019, *11*, 41, doi:10.3390/V11010041.

59. Ludovici, G.M.; Tassi, P.A.; Iannotti, A.; Russo, C.; Quaranta, R.; Manenti, G.; Malizia, A. Emerging Zoonotic Threats: HKU5-CoV-2 and the CBRNE Approach to Pandemic Prevention. *Infect. Dis. Immun.* 2025, doi:10.1097/ID9.0000000000000171.

60. Zhou, Z.; Qiu, Y.; Ge, X. The Taxonomy, Host Range and Pathogenicity of Coronaviruses and Other Viruses in the Nidovirales Order. *Anim. Dis.* 2021, *1*, 1–28, doi:10.1186/S44149-021-00005-9/FIGURES/5.

61. Chen, B.; Tian, E.K.; He, B.; Tian, L.; Han, R.; Wang, S.; Xiang, Q.; Zhang, S.; El Arnaout, T.; Cheng, W. Overview of Lethal Human Coronaviruses. *Signal Transduct. Target. Ther. 2020 51* 2020, *5*, 89-, doi:10.1038/s41392-020-0190-2.

62. Kumar, S.; Nyodu, R.; Maurya, V.K.; Saxena, S.K. Morphology, Genome Organization, Replication, and Pathogenesis of Severe Acute Respiratory Syndrome Coronavirus 2 (SARS-CoV-2). *Coronavirus Dis. 2019* 2020, 23, doi:10.1007/978-981-15-4814-7_3.

63. Grudlewska-Buda, K.; Wiktorczyk-Kapischke, N.; Wałecka-Zacharska, E.; Kwiecińska-Piróg, J.; Buszko, K.; Leis, K.; Juszczuk, K.; Gospodarek-Komkowska, E.; Skowron, K. Sars-Cov-2—Morphology, Transmission and Diagnosis during Pandemic, Review with Element of Meta-Analysis. *J. Clin. Med.* 2021, *10*, 1962, doi:10.3390/JCM10091962/S1.

64. Fehr, A.R.; Perlman, S. Coronaviruses: An Overview of Their Replication and Pathogenesis. *Coronaviruses* 2015, *1282*, 1, doi:10.1007/978-1-4939-2438-7_1.

65. Lang, Y.; Li, W.; Li, Z.; Koerhuis, D.; Van Den Burg, A.C.S.; Rozemuller, E.; Bosch, B.J.; Van Kuppeveld, F.J.M.; Boons, G.J.; Huizinga, E.G.; et al. Coronavirus Hemagglutinin-Esterase and Spike Proteins Coevolve for Functional Balance and Optimal Virion Avidity. *Proc. Natl. Acad. Sci. U. S. A.* 2020, *117*, 25759–25770, doi:10.1073/PNAS.2006299117.

66. Mijwil, M.M.; Al-Zubaidi, E.A. Medical Image Classification for Coronavirus Disease (COVID-19) Using Convolutional Neural Networks. *Iraqi J. Sci.* 2021, *62*, 2740–2747, doi:10.24996/IJS.2021.62.8.27.

67. Centers for Disease Control and Prevention MERS-CoV Photos | CDC Archive Available online: https://archive.cdc.gov/www_cdc_gov/coronavirus/mers/photos.html (accessed on 12 September 2025).

68. Ghallab, M.A.; Barsoum, C.H.; Polak, S.; El Hassoun, O.; Ghallab, A.M. Electron Microscope Images of Human Coronaviruses Reality versus Illusion. *Bratislava Med. J.* 2021, *122*, 900–911, doi:10.4149/BLL_2021_146.

69. Kim, C.H. Anti–SARS-CoV-2 Natural Products as Potentially Therapeutic

Agents. *Front. Pharmacol.* 2021, *12*, 590509, doi:10.3389/FPHAR.2021.590509/FULL.

70. Chan, J.F.W.; Kok, K.H.; Zhu, Z.; Chu, H.; To, K.K.W.; Yuan, S.; Yuen, K.Y. Genomic Characterization of the 2019 Novel Human-Pathogenic Coronavirus Isolated from a Patient with Atypical Pneumonia after Visiting Wuhan. *Emerg. Microbes Infect.* 2020, *9*, 221–236, doi:10.1080/22221751.2020.1719902.

71. Woo, P.C.Y.; Huang, Y.; Lau, S.K.P.; Yuen, K.Y. Coronavirus Genomics and Bioinformatics Analysis. *Viruses 2010, Vol. 2, Pages 1804-1820* 2010, *2*, 1804–1820, doi:10.3390/V2081803.

72. Weiss, S.R.; Leibowitz, J.L. Coronavirus Pathogenesis. *Adv. Virus Res.* 2011, *81*, 85, doi:10.1016/B978-0-12-385885-6.00009-2.

73. Sohrab, S.S.; Alsaqaf, F.; Hassan, A.M.; Tolah, A.M.; Bajrai, L.H.; Azhar, E.I. Genomic Diversity and Recombination Analysis of the Spike Protein Gene from Selected Human Coronaviruses. *Biol. 2024, Vol. 13, Page 282* 2024, *13*, 282, doi:10.3390/BIOLOGY13040282.

74. Brant, A.C.; Tian, W.; Majerciak, V.; Yang, W.; Zheng, Z.M. SARS-CoV-2: From Its Discovery to Genome Structure, Transcription, and Replication. *Cell Biosci.* 2021, *11*, 1–17, doi:10.1186/S13578-021-00643-Z.

75. Low, Z.Y.; Zabidi, N.Z.; Yip, A.J.W.; Puniyamurti, A.; Chow, V.T.K.; Lal, S.K. SARS-CoV-2 Non-Structural Proteins and Their Roles in Host Immune Evasion. *Viruses 2022, Vol. 14, Page 1991* 2022, *14*, 1991, doi:10.3390/V14091991.

76. Jiao, Y.; Zhao, P.; Xu, L.D.; Yu, J.Q.; Cai, H.L.; Zhang, C.; Tong, C.; Yang, Y. Le; Xu, P.; Sun, Q.; et al. Enteric Coronavirus Nsp2 Is a Virulence Determinant That Recruits NBR1 for Autophagic Targeting of TBK1 to Diminish the Innate Immune Response. *Autophagy* 2024, *20*, 1762, doi:10.1080/15548627.2024.2340420.

77. Moustaqil, M.; Ollivier, E.; Chiu, H.P.; Van Tol, S.; Rudolffi-Soto, P.; Stevens, C.; Bhumkar, A.; Hunter, D.J.B.; Freiberg, A.N.; Jacques, D.; et al. SARS-CoV-2 Proteases PLpro and 3CLpro Cleave IRF3 and Critical Modulators of Inflammatory Pathways (NLRP12 and TAB1): Implications for Disease Presentation across Species. *Emerg. Microbes Infect.* 2021, *10*, 178–195, doi:10.1080/22221751.2020.1870414.

78. Zimmermann, L.; Zhao, X.; Makroczyova, J.; Wachsmuth-Melm, M.; Prasad, V.; Hensel, Z.; Bartenschlager, R.; Chlanda, P. SARS-CoV-2 Nsp3 and Nsp4 Are Minimal Constituents of a Pore Spanning Replication Organelle. *Nat. Commun.* 2023, *14*, 1–12, doi:10.1038/S41467-023-43666-5.

79. Hillen, H.S. Structure and Function of SARS-CoV-2 Polymerase. *Curr. Opin. Virol.* 2021, *48*, 82, doi:10.1016/J.COVIRO.2021.03.010.

80. Rohaim, M.A.; El Naggar, R.F.; Clayton, E.; Munir, M. Structural and

Functional Insights into Non-Structural Proteins of Coronaviruses. *Microb. Pathog.* 2021, *150*, 104641, doi:10.1016/J.MICPATH.2020.104641.

81. Malone, B.; Urakova, N.; Snijder, E.J.; Campbell, E.A. Structures and Functions of Coronavirus Replication–Transcription Complexes and Their Relevance for SARS-CoV-2 Drug Design. *Nat. Rev. Mol. Cell Biol.* 2022, *23*, 21–39, doi:10.1038/S41580-021-00432-Z.

82. Chang, L.J.; Chen, T.H. NSP16 2′-O-MTase in Coronavirus Pathogenesis: Possible Prevention and Treatments Strategies. *Viruses* 2021, *13*, 538, doi:10.3390/V13040538.

83. Kakavandi, S.; Zare, I.; VaezJalali, M.; Dadashi, M.; Azarian, M.; Akbari, A.; Ramezani Farani, M.; Zalpoor, H.; Hajikhani, B. Structural and Non-Structural Proteins in SARS-CoV-2: Potential Aspects to COVID-19 Treatment or Prevention of Progression of Related Diseases. *Cell Commun. Signal.* 2023, *21*, 110, doi:10.1186/S12964-023-01104-5.

84. Redondo, N.; Zaldívar-López, S.; Garrido, J.J.; Montoya, M. SARS-CoV-2 Accessory Proteins in Viral Pathogenesis: Knowns and Unknowns. *Front. Immunol.* 2021, *12*, 708264, doi:10.3389/FIMMU.2021.708264.

85. Liu, D.X.; Fung, T.S.; Chong, K.K.L.; Shukla, A.; Hilgenfeld, R. Accessory Proteins of SARS-CoV and Other Coronaviruses. *Antiviral Res.* 2014, *109*, 97, doi:10.1016/J.ANTIVIRAL.2014.06.013.

86. Müller, M.; Herrmann, A.; Fujita, S.; Uriu, K.; Kruth, C.; Strange, A.; Kolberg, J.E.; Schneider, M.; Ito, J.; Müller, M.A.; et al. ORF3c Is Expressed in SARS-CoV-2-infected Cells and Inhibits Innate Sensing by Targeting MAVS. *EMBO Rep.* 2023, *24*, e57137, doi:10.15252/EMBR.202357137.

87. Zhou, Y.; Zheng, R.; Liu, S.; Disoma, C.; Du, A.; Li, S.; Chen, Z.; Dong, Z.; Zhang, Y.; Li, S.; et al. Host E3 Ligase HUWE1 Attenuates the Proapoptotic Activity of the MERS-CoV Accessory Protein ORF3 by Promoting Its Ubiquitin-Dependent Degradation. *J. Biol. Chem.* 2022, *298*, 101584, doi:10.1016/J.JBC.2022.101584.

88. Comar, C.E.; Goldstein, S.A.; Li, Y.; Yount, B.; Baric, R.S.; Weiss, S.R. Antagonism of DsRNA-Induced Innate Immune Pathways by NS4a and NS4b Accessory Proteins during MERS Coronavirus Infection. *MBio* 2019, *10*, e00319-19, doi:10.1128/MBIO.00319-19.

89. Menachery, V.D.; Mitchell, H.D.; Cockrell, A.S.; Gralinski, L.E.; Yount, B.L.; Graham, R.L.; McAnarney, E.T.; Douglas, M.G.; Scobey, T.; Beall, A.; et al. MERS-CoV Accessory ORFs Play Key Role for Infection and Pathogenesis. *MBio* 2017, *8*, e00665-17, doi:10.1128/MBIO.00665-17.

90. Li, J.Y.; Zhou, Z.J.; Wang, Q.; He, Q.N.; Zhao, M.Y.; Qiu, Y.; Ge, X.Y. Innate Immunity Evasion Strategies of Highly Pathogenic Coronaviruses: SARS-CoV, MERS-CoV, and SARS-CoV-2. *Front. Microbiol.* 2021, *12*, 770656, doi:10.3389/FMICB.2021.770656.

91. García-García, T.; Fernández-Rodríguez, R.; Redondo, N.; de Lucas-Rius, A.; Zaldívar-López, S.; López-Ayllón, B.D.; Suárez-Cárdenas, J.M.; Jiménez-Marín, Á.; Montoya, M.; Garrido, J.J. Impairment of Antiviral Immune Response and Disruption of Cellular Functions by SARS-CoV-2 ORF7a and ORF7b. *iScience* 2022, *25*, 105444, doi:10.1016/J.ISCI.2022.105444.

92. Zandi, M. ORF8/ORF8a: A Difference between SARS-CoV-2 and SARS-CoV. *Eur. Respir. J.* 2022, *59*, 2102818, doi:10.1183/13993003.02818-2021.

93. Chen, C.C.; Krüger, J.; Sramala, I.; Hsu, H.J.; Henklein, P.; Chen, Y.M.A.; Fischer, W.B. ORF8a of SARS-CoV Forms an Ion Channel: Experiments and Molecular Dynamics Simulations. *Biochim. Biophys. Acta - Biomembr.* 2011, *1808*, 572–579, doi:10.1016/J.BBAMEM.2010.08.004.

94. Wong, L.-Y.R.; Ye, Z.-W.; Lui, P.-Y.; Zheng, X.; Yuan, S.; Zhu, L.; Fung, S.-Y.; Yuen, K.-S.; Siu, K.-L.; Yeung, M.-L.; et al. Middle East Respiratory Syndrome Coronavirus ORF8b Accessory Protein Suppresses Type I IFN Expression by Impeding HSP70-Dependent Activation of IRF3 Kinase IKKε. *J. Immunol.* 2020, *205*, 1564, doi:10.4049/JIMMUNOL.1901489.

95. Wu, J.; Shi, Y.; Pan, X.; Wu, S.; Hou, R.; Zhang, Y.; Zhong, T.; Tang, H.; Du, W.; Wang, L.; et al. SARS-CoV-2 ORF9b Inhibits RIG-I-MAVS Antiviral Signaling by Interrupting K63-Linked Ubiquitination of NEMO. *Cell Rep.* 2021, *34*, 108761, doi:10.1016/J.CELREP.2021.108761.

96. Andres, A.D.; Feng, Y.; Campos, A.R.; Yin, J.; Yang, C.-C.; James, B.; Murad, R.; Kim, H.; Deshpande, A.J.; Gordon, D.E.; et al. SARS-CoV-2 ORF9c Is a Membrane-Associated Protein That Suppresses Antiviral Responses in Cells. *bioRxiv* 2020, 2020.08.18.256776, doi:10.1101/2020.08.18.256776.

97. Li, X.; Hou, P.; Ma, W.; Wang, X.; Wang, H.; Yu, Z.; Chang, H.; Wang, T.; Jin, S.; Wang, X.; et al. SARS-CoV-2 ORF10 Suppresses the Antiviral Innate Immune Response by Degrading MAVS through Mitophagy. *Cell. Mol. Immunol.* 2021, *19*, 67, doi:10.1038/S41423-021-00807-4.

98. Zhang, R.; Wang, K.; Ping, X.; Yu, W.; Qian, Z.; Xiong, S.; Sun, B. The Ns12.9 Accessory Protein of Human Coronavirus OC43 Is a Viroporin Involved in Virion Morphogenesis and Pathogenesis. *J. Virol.* 2015, *89*, 11383, doi:10.1128/JVI.01986-15.

99. Gunawardene, C.D.; Pandey, I.; Chatterjee, S.; Penaflor-Tellez, Y.; Odle, A.; Messyasz, A.; Rajsbaum, R.; Sariol, A.; Wong, L.-Y.R. Characterization of Betacoronavirus HKU-1 and OC43 Internal Proteins Using a Prototypic Coronavirus. *bioRxiv* 2025, 2025.04.23.650176, doi:10.1101/2025.04.23.650176.

100. Wu, Y.; Zhao, S. Furin Cleavage Sites Naturally Occur in Coronaviruses. *Stem Cell Res.* 2021, *50*, 102115, doi:10.1016/J.SCR.2020.102115.

101. Laporte, M.; Raeymaekers, V.; van Berwaer, R.; Vandeput, J.; Marchand-Casas, I.; Thibaut, H.J.; van Looveren, D.; Martens, K.; Hoffmann, M.; Maes, P.; et al.

The SARS-CoV-2 and Other Human Coronavirus Spike Proteins Are Fine-Tuned towards Temperature and Proteases of the Human Airways. *PLoS Pathog.* 2021, *17*, doi:10.1371/JOURNAL.PPAT.1009500.

102. Zhao, M.M.; Yang, W.L.; Yang, F.Y.; Zhang, L.; Huang, W.J.; Hou, W.; Fan, C.F.; Jin, R.H.; Feng, Y.M.; Wang, Y.C.; et al. Cathepsin L Plays a Key Role in SARS-CoV-2 Infection in Humans and Humanized Mice and Is a Promising Target for New Drug Development. *Signal Transduct. Target. Ther.* 2021, *6*, 1–12, doi:10.1038/S41392-021-00558-8.

103. Xiu, S.; Dick, A.; Ju, H.; Mirzaie, S.; Abdi, F.; Cocklin, S.; Zhan, P.; Liu, X. Inhibitors of SARS-CoV-2 Entry: Current and Future Opportunities. *J. Med. Chem.* 2020, *63*, 12256, doi:10.1021/ACS.JMEDCHEM.0C00502.

104. Tang, G.; Liu, Z.; Chen, D. Human Coronaviruses: Origin, Host and Receptor. *J. Clin. Virol.* 2022, *155*, 105246, doi:10.1016/J.JCV.2022.105246.

105. Chen, J.; Zhang, W.; Li, Y.; Liu, C.; Dong, T.; Chen, H.; Wu, C.; Su, J.; Li, B.; Zhang, W.; et al. Bat-Infecting Merbecovirus HKU5-CoV Lineage 2 Can Use Human ACE2 as a Cell Entry Receptor. *Cell* 2025, *188*, 1729-1742.e16, doi:10.1016/j.cell.2025.01.042.

106. Finkel, Y.; Mizrahi, O.; Nachshon, A.; Weingarten-Gabbay, S.; Morgenstern, D.; Yahalom-Ronen, Y.; Tamir, H.; Achdout, H.; Stein, D.; Israeli, O.; et al. The Coding Capacity of SARS-CoV-2. *Nature* 2021, *589*, 125–130, doi:10.1038/S41586-020-2739-1.

107. V'kovski, P.; Kratzel, A.; Steiner, S.; Stalder, H.; Thiel, V. Coronavirus Biology and Replication: Implications for SARS-CoV-2. *Nat. Rev. Microbiol.* 2021, *19*, 155–170, doi:10.1038/S41579-020-00468-6.

108. Banerjee, A.K.; Blanco, M.R.; Bruce, E.A.; Honson, D.D.; Chen, L.M.; Chow, A.; Bhat, P.; Ollikainen, N.; Quinodoz, S.A.; Loney, C.; et al. SARS-CoV-2 Disrupts Splicing, Translation, and Protein Trafficking to Suppress Host Defenses. *Cell* 2020, *183*, 1325-1339.e21, doi:10.1016/J.CELL.2020.10.004.

109. Kung, Y.-A.; Lee, K.-M.; Chiang, H.-J.; Huang, S.-Y.; Wu, C.-J.; Shih, S.-R. Molecular Virology of SARS-CoV-2 and Related Coronaviruses. *Microbiol. Mol. Biol. Rev.* 2022, *86*, e00026-21, doi:10.1128/mmbr.00026-21.

110. Wang, B.; Svetlov, D.; Artsimovitch, I. NMPylation and De-NMPylation of SARS-CoV-2 Nsp9 by the NiRAN Domain. *Nucleic Acids Res.* 2021, *49*, 8822–8835, doi:10.1093/NAR/GKAB677.

111. Chen, J.; Malone, B.; Llewellyn, E.; Grasso, M.; Shelton, P.M.M.; Olinares, P.D.B.; Maruthi, K.; Eng, E.T.; Vatandaslar, H.; Chait, B.T.; et al. Structural Basis for Helicase-Polymerase Coupling in the SARS-CoV-2 Replication-Transcription Complex. *Cell* 2020, *182*, 1560-1573.e13, doi:10.1016/J.CELL.2020.07.033.

112. Yan, L.; Yang, Y.; Li, M.; Zhang, Y.; Zheng, L.; Ge, J.; Huang, Y.C.; Liu, Z.;

Wang, T.; Gao, S.; et al. Coupling of N7-Methyltransferase and 3′-5′ Exoribonuclease with SARS-CoV-2 Polymerase Reveals Mechanisms for Capping and Proofreading. *Cell* 2021, *184*, 3474-3485.e11, doi:10.1016/J.CELL.2021.05.033.

113. Liu, C.; Shi, W.; Becker, S.T.; Schatz, D.G.; Liu, B.; Yang, Y. Structural Basis of Mismatch Recognition by a SARS-CoV-2 Proofreading Enzyme. *Science (80-.).* 2021, *373*, 1142–1146, doi:10.1126/science.abi9310.

114. Long, S. SARS-CoV-2 Subgenomic RNAs: Characterization, Utility, and Perspectives. *Viruses* 2021, *13*, doi:10.3390/V13101923.

115. Alexandersen, S.; Chamings, A.; Bhatta, T.R. SARS-CoV-2 Genomic and Subgenomic RNAs in Diagnostic Samples Are Not an Indicator of Active Replication. *Nat. Commun.* 2020, *11*, 1–13, doi:10.1038/s41467-020-19883-7.

116. Klein, S.; Cortese, M.; Winter, S.L.; Wachsmuth-Melm, M.; Neufeldt, C.J.; Cerikan, B.; Stanifer, M.L.; Boulant, S.; Bartenschlager, R.; Chlanda, P. SARS-CoV-2 Structure and Replication Characterized by in Situ Cryo-Electron Tomography. *Nat. Commun.* 2020, *11*, 1–10, doi:10.1038/S41467-020-19619-7.

117. Knoops, K.; Kikkert, M.; Van Den Worm, S.H.E.; Zevenhoven-Dobbe, J.C.; Van Der Meer, Y.; Koster, A.J.; Mommaas, A.M.; Snijder, E.J. SARS-Coronavirus Replication Is Supported by a Reticulovesicular Network of Modified Endoplasmic Reticulum. *PLOS Biol.* 2008, *6*, doi:10.1371/JOURNAL.PBIO.0060226.

118. Sicari, D.; Chatziioannou, A.; Koutsandreas, T.; Sitia, R.; Chevet, E. Role of the Early Secretory Pathway in SARS-CoV-2 Infection. *J. Cell Biol.* 2020, *219*, e202006005, doi:10.1083/JCB.202006005.

119. Hardenbrook, N.J.; Zhang, P. A Structural View of the SARS-CoV-2 Virus and Its Assembly. *Curr. Opin. Virol.* 2022, *52*, 123–134, doi:10.1016/J.COVIRO.2021.11.011.

120. Scherer, K.M.; Mascheroni, L.; Carnell, G.W.; Wunderlich, L.C.S.; Makarchuk, S.; Brockhoff, M.; Mela, I.; Fernandez-Villegas, A.; Barysevich, M.; Stewart, H.; et al. SARS-CoV-2 Nucleocapsid Protein Adheres to Replication Organelles before Viral Assembly at the Golgi/ERGIC and Lysosome-Mediated Egress. *Sci. Adv.* 2022, *8*, doi:10.1126/SCIADV.ABL4895.

121. Ghosh, S.; Dellibovi-Ragheb, T.A.; Kerviel, A.; Pak, E.; Qiu, Q.; Fisher, M.; Takvorian, P.M.; Bleck, C.; Hsu, V.W.; Fehr, A.R.; et al. β-Coronaviruses Use Lysosomes for Egress Instead of the Biosynthetic Secretory Pathway. *Cell* 2020, *183*, 1520-1535.e14, doi:10.1016/J.CELL.2020.10.039.

122. Mulabbi, E.N.; Tweyongyere, R.; Byarugaba, D.K. The History of the Emergence and Transmission of Human Coronaviruses. *Onderstepoort J. Vet. Res.* 2021, *88*, 1872, doi:10.4102/OJVR.V88I1.1872.

123. Peiris, M.; Perlman, S. Unresolved Questions in the Zoonotic Transmission of

MERS. *Curr. Opin. Virol.* 2022, *52*, 258–264, doi:10.1016/J.COVIRO.2021.12.013.

124. De Wit, E.; Van Doremalen, N.; Falzarano, D.; Munster, V.J. SARS and MERS: Recent Insights into Emerging Coronaviruses. *Nat. Rev. Microbiol.* 2016, *14*, 523, doi:10.1038/NRMICRO.2016.81.

125. Loeffelholz, M.J.; Tang, Y.W. Laboratory Diagnosis of Emerging Human Coronavirus Infections – the State of the Art. *Emerg. Microbes Infect.* 2020, *9*, 747, doi:10.1080/22221751.2020.1745095.

126. Cabeça, T.K.; Granato, C.; Bellei, N. Epidemiological and Clinical Features of Human Coronavirus Infections among Different Subsets of Patients. *Influenza Other Respi. Viruses* 2013, *7*, 1040–1047, doi:10.1111/IRV.12101.

127. Gaunt, E.R.; Hardie, A.; Claas, E.C.J.; Simmonds, P.; Templeton, K.E. Epidemiology and Clinical Presentations of the Four Human Coronaviruses 229E, HKU1, NL63, and OC43 Detected over 3 Years Using a Novel Multiplex Real-Time PCR Method. *J. Clin. Microbiol.* 2010, *48*, 2940–2947, doi:10.1128/JCM.00636-10.

128. Baj, J.; Karakuła-Juchnowicz, H.; Teresiński, G.; Buszewicz, G.; Ciesielka, M.; Sitarz, R.; Forma, A.; Karakuła, K.; Flieger, W.; Portincasa, P.; et al. COVID-19: Specific and Non-Specific Clinical Manifestations and Symptoms: The Current State of Knowledge. *J. Clin. Med.* 2020, *9*, 1753, doi:10.3390/JCM9061753.

129. Pustake, M.; Tambolkar, I.; Giri, P.; Gandhi, C. SARS, MERS and CoVID-19. *J. Fam. Med. Prim. Care* 2022, *11*, 10–17, doi:10.4103/JFMPC.JFMPC_839_21.

130. Coronavirus Death Rate (COVID-19) - Worldometer Coronavirus Death Rate (COVID-19) - Worldometer Available online: https://www.worldometers.info/coronavirus/coronavirus-death-rate/ (accessed on 21 April 2026).

131. Riedmann, U.; Chalupka, A.; Richter, L.; Sprenger, M.; Rauch, W.; Krause, R.; Willeit, P.; Schennach, H.; Benka, B.; Werber, D.; et al. COVID-19 Case Fatality Rate and Infection Fatality Rate from 2020 to 2023: Nationwide Analysis in Austria. *J. Infect. Public Health* 2025, *18*, 102698, doi:10.1016/J.JIPH.2025.102698.

132. Liu, L.; Wang, T.; Lu, J. The Prevalence, Origin, and Prevention of Six Human Coronaviruses. *Virol. Sin.* 2016, *31*, 94, doi:10.1007/S12250-015-3687-Z.

133. Veiga, A.B.G. da; Martins, L.G.; Riediger, I.; Mazetto, A.; Debur, M. do C.; Gregianini, T.S. More than Just a Common Cold: Endemic Coronaviruses OC43, HKU1, NL63, and 229E Associated with Severe Acute Respiratory Infection and Fatality Cases among Healthy Adults. *J. Med. Virol.* 2021, *93*, 1002–1007, doi:10.1002/JMV.26362.

134. Padda, I.S.; Parmar, M. COVID (SARS-CoV-2) Vaccine. *StatPearls* 2023.

135. Güner, R.; Hasanoğlu, İ.; Aktaş, F. COVID-19: Prevention and Control Measures in Community. *Turkish J. Med. Sci.* 2020, *50*, 571, doi:10.3906/SAG-2004-146.

136. Al-Tawfiq, J.A.; Azhar, E.I.; Memish, Z.A.; Zumla, A. Middle East Respiratory Syndrome Coronavirus Available online: https://www.who.int/news-room/fact-sheets/detail/middle-east-respiratory-syndrome-coronavirus-(mers-cov) (accessed on 15 September 2025).

137. Gheblawi, M.; Wang, K.; Viveiros, A.; Nguyen, Q.; Zhong, J.C.; Turner, A.J.; Raizada, M.K.; Grant, M.B.; Oudit, G.Y. Angiotensin-Converting Enzyme 2: SARS-CoV-2 Receptor and Regulator of the Renin-Angiotensin System: Celebrating the 20th Anniversary of the Discovery of ACE2. *Circ. Res.* 2020, *126*, 1456–1474, doi:10.1161/CIRCRESAHA.120.317015.

138. Donoghue, M.; Hsieh, F.; Baronas, E.; Godbout, K.; Gosselin, M.; Stagliano, N.; Donovan, M.; Woolf, B.; Robison, K.; Jeyaseelan, R.; et al. A Novel Angiotensin-Converting Enzyme-Related Carboxypeptidase (ACE2) Converts Angiotensin I to Angiotensin 1-9. *Circ. Res.* 2000, *87*, doi:10.1161/01.RES.87.5.E1.

139. Patel, V.B.; Zhong, J.C.; Grant, M.B.; Oudit, G.Y. Role of the ACE2/Angiotensin 1-7 Axis of the Renin-Angiotensin System in Heart Failure. *Circ. Res.* 2016, *118*, 1313–1326, doi:10.1161/CIRCRESAHA.116.307708.

140. Catanzaro, N.J.; Wu, Z.; Fan, C.; Jefferson, V.; Abdelgadir, A.; Schäfer, A.; Yount, B.L.; Bjorkman, P.J.; Baric, R.; Letko, M. ACE2 from Pipistrellus Abramus Bats Is a Receptor for HKU5 Coronaviruses. *Nat. Commun.* 2025, *16*, 4932, doi:10.1038/S41467-025-60286-3.

141. Ni, W.; Yang, X.; Yang, D.D.; Bao, J.; Li, R.; Xiao, Y.; Hou, C.; Wang, H.; Liu, J.; Yang, D.D.; et al. Role of Angiotensin-Converting Enzyme 2 (ACE2) in COVID-19. *Crit. Care 2020 241* 2020, *24*, 422-, doi:10.1186/S13054-020-03120-0.

142. Li, W.; Sui, J.; Huang, I.C.; Kuhn, J.H.; Radoshitzky, S.R.; Marasco, W.A.; Choe, H.; Farzan, M. The S Proteins of Human Coronavirus NL63 and Severe Acute Respiratory Syndrome Coronavirus Bind Overlapping Regions of ACE2. *Virology* 2007, *367*, 367, doi:10.1016/J.VIROL.2007.04.035.

143. Yan, R.; Zhang, Y.; Li, Y.; Xia, L.; Guo, Y.; Zhou, Q. Structural Basis for the Recognition of SARS-CoV-2 by Full-Length Human ACE2. *Science* 2020, *367*, 1444, doi:10.1126/SCIENCE.ABB2762.

144. Devaux, C.A.; Camoin-Jau, L. An Update on Angiotensin-Converting Enzyme 2 Structure/Functions, Polymorphism, and Duplicitous Nature in the Pathophysiology of Coronavirus Disease 2019: Implications for Vascular and Coagulation Disease Associated with Severe Acute Respiratory Syndrome…. *Front. Microbiol.* 2022, *13*, 1042200, doi:10.3389/FMICB.2022.1042200.

145. Hattori, T.; Saito, T.; Okuya, K.; Takahashi, Y.; Miyamoto, H.; Kajihara, M.; Igarashi, M.; Takada, A. Human ACE2 Genetic Polymorphism Affecting SARS-CoV and SARS-CoV-2 Entry into Cells. *Microbiol. Spectr.* 2022, *10*, doi:10.1128/SPECTRUM.00870-22.

146. Hikmet, F.; Méar, L.; Edvinsson, Å.; Micke, P.; Uhlén, M.; Lindskog, C. The Protein Expression Profile of ACE2 in Human Tissues. *Mol. Syst. Biol.* 2020, *16*, 9610, doi:10.15252/MSB.20209610.

147. Beyerstedt, S.; Casaro, E.B.; Rangel, É.B. COVID-19: Angiotensin-Converting Enzyme 2 (ACE2) Expression and Tissue Susceptibility to SARS-CoV-2 Infection. *Eur. J. Clin. Microbiol. Infect. Dis.* 2021, *40*, 905, doi:10.1007/S10096-020-04138-6.

148. Hu, P.; Bauer, V.L.; Sawyer, S.L.; Diaz-Griffero, F. Human ACE2 Polymorphisms from Different Human Populations Modulate SARS-CoV-2 Infection. *Viruses* 2022, *14*, 1451, doi:10.3390/V14071451.

149. Wei, Y.; Aris, P.; Farookhi, H.; Xia, X. Predicting Mammalian Species at Risk of Being Infected by SARS-CoV-2 from an ACE2 Perspective. *Sci. Reports 2021 111* 2021, *11*, 1702-, doi:10.1038/s41598-020-80573-x.

150. Damas, J.; Hughes, G.M.; Keough, K.C.; Painter, C.A.; Persky, N.S.; Corbo, M.; Hiller, M.; Koepfli, K.P.; Pfenning, A.R.; Zhao, H.; et al. Broad Host Range of SARS-CoV-2 Predicted by Comparative and Structural Analysis of ACE2 in Vertebrates. *Proc. Natl. Acad. Sci. U. S. A.* 2020, *117*, 22311–22322, doi:10.1073/PNAS.2010146117.

151. Ma, C.; Liu, C.; Xiong, Q.; Gu, M.; Shi, L.; Wang, C.; Si, J.; Tong, F.; Liu, P.; Huang, M.; et al. Broad Host Tropism of ACE2-Using MERS-Related Coronaviruses and Determinants Restricting Viral Recognition. *Cell Discov. 2023 91* 2023, *9*, 57-, doi:10.1038/s41421-023-00566-8.

152. Dutheil, F.; Clinchamps, M.; Bouillon-Minois, J.B. Bats, Pathogens, and Species Richness. *Pathog. 2021, Vol. 10, Page 98* 2021, *10*, 98, doi:10.3390/PATHOGENS10020098.

153. Kasso, M.; Balakrishnan, M. Ecological and Economic Importance of Bats (Order Chiroptera). *Int. Sch. Res. Not.* 2013, *2013*, 187415, doi:10.1155/2013/187415.

154. Letko, M.; Seifert, S.N.; Olival, K.J.; Plowright, R.K.; Munster, V.J. Bat-Borne Virus Diversity, Spillover and Emergence. *Nat. Rev. Microbiol.* 2020, *18*, 461–471, doi:10.1038/S41579-020-0394-Z.

155. Calisher, C.H.; Childs, J.E.; Field, H.E.; Holmes, K. V.; Schountz, T. Bats: Important Reservoir Hosts of Emerging Viruses. *Clin. Microbiol. Rev.* 2006, *19*, 531–545, doi:10.1128/CMR.00017-06.

156. Hallström, B.M.; Janke, A. Mammalian Evolution May Not Be Strictly Bifurcating. *Mol. Biol. Evol.* 2010, *27*, 2804–2816,

doi:10.1093/MOLBEV/MSQ166.

157. Teeling, E.C.; Springer, M.S.; Madsen, O.; Bates, P.; O'Brien, S.J.; Murphy, W.J. A Molecular Phylogeny for Bats Illuminates Biogeography and the Fossil Record. *Science (80-.).* 2005, *307*, 580–584, doi:10.1126/SCIENCE.1105113.

158. Jones, K.E.; Bininda-Emonds, O.R.P.; Gittleman, J.L. BATS, CLOCKS, AND ROCKS: DIVERSIFICATION PATTERNS IN CHIROPTERA. *Evolution (N. Y).* 2005, *59*, 2243–2255, doi:10.1111/J.0014-3820.2005.TB00932.X.

159. Serra-Cobo, J.; López-Roig, M. Bats and Emerging Infections: An Ecological and Virological Puzzle. *Emerg. Re-emerging Viral Infect.* 2016, *972*, 35, doi:10.1007/5584_2016_131.

160. O'Shea, T.J.; Cryan, P.M.; Cunningham, A.A.; Fooks, A.R.; Hayman, D.T.S.; Luis, A.D.; Peel, A.J.; Plowright, R.K.; Wood, J.L.N. Bat Flight and Zoonotic Viruses. *Emerg. Infect. Dis.* 2014, *20*, 741, doi:10.3201/EID2005.130539.

161. Wilkinson, G.S.; South, J.M. Life History, Ecology and Longevity in Bats. *Aging Cell* 2002, *1*, 124–131, doi:10.1046/J.1474-9728.2002.00020.X.

162. Sohayati, A.R.; Hassan, L.; Sharifah, S.H.; Lazarus, K.; Zaini, C.M.; Epstein, J.H.; Shamsyul Naim, N.; Field, H.E.; Arshad, S.S.; Abdul Aziz, J.; et al. Evidence for Nipah Virus Recrudescence and Serological Patterns of Captive Pteropus Vampyrus. *Epidemiol. Infect.* 2011, *139*, 1570–1579, doi:10.1017/S0950268811000550.

163. Subudhi, S.; Rapin, N.; Bollinger, T.K.; Hill, J.E.; Donaldson, M.E.; Davy, C.M.; Warnecke, L.; Turner, J.M.; Kyle, C.J.; Willis, C.K.R.; et al. A Persistently Infecting Coronavirus in Hibernating Myotis Lucifugus, the North American Little Brown Bat. *J. Gen. Virol.* 2017, *98*, 2297–2309, doi:10.1099/JGV.0.000898.

164. Boerma, D.B.; Swartz, S.M. Roosting Ecology Drives the Evolution of Diverse Bat Landing Maneuvers. *iScience* 2024, *27*, 110381, doi:10.1016/J.ISCI.2024.110381.

165. CONSTANTINE, D.G. Rabies Transmission by Nonbite Route. *Public Health Rep.* 1962, *77*, 287, doi:10.2307/4591470.

166. Gentles, A.D.; Guth, S.; Rozins, C.; Brook, C.E. A Review of Mechanistic Models of Viral Dynamics in Bat Reservoirs for Zoonotic Disease. *Pathog. Glob. Health* 2020, *114*, 407, doi:10.1080/20477724.2020.1833161.

167. Epstein, J.H.; Anthony, S.J.; Islam, A.; Marm Kilpatrick, A.; Khan, S.A.; Balkey, M.D.; Ross, N.; Smith, I.; Zambrana-Torrelio, C.; Tao, Y.; et al. Nipah Virus Dynamics in Bats and Implications for Spillover to Humans. *Proc. Natl. Acad. Sci. U. S. A.* 2020, *117*, 29190–29201, doi:10.1073/PNAS.2000429117.

168. Sun, Y.Q.; Zhang, Y.Y.; Liu, M.C.; Chen, J.J.; Li, T.T.; Liu, Y.N.; Zhang, L.Y.; Wang, T.; Yu, L.J.; Che, T. Le; et al. Mapping the Distribution of Nipah Virus Infections: A Geospatial Modelling Analysis. *Lancet Planet. Heal.* 2024, *8*,

e463–e475, doi:10.1016/S2542-5196(24)00119-0.

169. Xie, J.; Li, Y.; Shen, X.; Goh, G.; Zhu, Y.; Cui, J.; Wang, L.F.; Shi, Z.L.; Zhou, P. Dampened STING-Dependent Interferon Activation in Bats. *Cell Host Microbe* 2018, *23*, 297, doi:10.1016/J.CHOM.2018.01.006.

170. Zhou, P.; Cowled, C.; Mansell, A.; Monaghan, P.; Green, D.; Wu, L.; Shi, Z.; Wang, L.F.; Baker, M.L. IRF7 in the Australian Black Flying Fox, Pteropus Alecto: Evidence for a Unique Expression Pattern and Functional Conservation. *PLoS One* 2014, *9*, e103875, doi:10.1371/JOURNAL.PONE.0103875.

171. Banerjee, A.; Zhang, X.; Yip, A.; Schulz, K.S.; Irving, A.T.; Bowdish, D.; Golding, B.; Wang, L.F.; Mossman, K. Positive Selection of a Serine Residue in Bat IRF3 Confers Enhanced Antiviral Protection. *iScience* 2020, *23*, 100958, doi:10.1016/J.ISCI.2020.100958.

172. Ahn, M.; Anderson, D.E.; Zhang, Q.; Tan, C.W.; Lim, B.L.; Luko, K.; Wen, M.; Chia, W.N.; Mani, S.; Wang, L.C.; et al. Dampened NLRP3-Mediated Inflammation in Bats and Implications for a Special Viral Reservoir Host. *Nat. Microbiol.* 2019, *4*, 789, doi:10.1038/S41564-019-0371-3.

173. Wagner, D.M.; Klunk, J.; Harbeck, M.; Devault, A.; Waglechner, N.; Sahl, J.W.; Enk, J.; Birdsell, D.N.; Kuch, M.; Lumibao, C.; et al. Yersinia Pestis and the Plague of Justinian 541-543 AD: A Genomic Analysis. *Lancet Infect. Dis.* 2014, *14*, 319–326, doi:10.1016/S1473-3099(13)70323-2.

174. Pawan, J.L. The Transmission of Paralytic Rabies in Trinidad by the Vampire Bat (Desmodus Rotundus Murinus Wagner, 1840). *Ann. Trop. Med. Parasitol.* 1936, *30*, 101–130, doi:10.1080/00034983.1936.11684921.

175. Brauburger, K.; Hume, A.J.; Mühlberger, E.; Olejnik, J. Forty-Five Years of Marburg Virus Research. *Viruses* 2012, *4*, 1878, doi:10.3390/V4101878.

176. Wang, L.F.; Eaton, B.T. Bats, Civets and the Emergence of SARS. *Curr. Top. Microbiol. Immunol.* 2007, *315*, 325–344, doi:10.1007/978-3-540-70962-6_13.

177. Lytras, S.; Hughes, J.; Martin, D.; Swanepoel, P.; de Klerk, A.; Lourens, R.; Kosakovsky Pond, S.L.; Xia, W.; Jiang, X.; Robertson, D.L. Exploring the Natural Origins of SARS-CoV-2 in the Light of Recombination. *Genome Biol. Evol.* 2022, *14*, doi:10.1093/GBE/EVAC018.

178. Han, H.J.; Yu, H.; Yu, X.J. Evidence for Zoonotic Origins of Middle East Respiratory Syndrome Coronavirus. *J. Gen. Virol.* 2016, *97*, 274, doi:10.1099/JGV.0.000342.

179. Verma, A.; Jain, H.; Sulaiman, S.A.; Pokhrel, P.; Goyal, A.; Dave, T. An Impending Public Health Threat: Analysis of the Recent Nipah Virus Outbreak and Future Recommendations – an Editorial. *Ann. Med. Surg.* 2023, *86*, 638, doi:10.1097/MS9.0000000000001627.

180. Taylor, J.; Thompson, K.; Annand, E.J.; Massey, P.D.; Bennett, J.; Eden, J.S.; Horsburgh, B.A.; Hodgson, E.; Wood, K.; Kerr, J.; et al. Novel Variant Hendra

Virus Genotype 2 Infection in a Horse in the Greater Newcastle Region, New South Wales, Australia. *One Heal.* 2022, *15*, 100423, doi:10.1016/J.ONEHLT.2022.100423.

181. Drexler, J.F.; Corman, V.M.; Müller, M.A.; Maganga, G.D.; Vallo, P.; Binger, T.; Gloza-Rausch, F.; Rasche, A.; Yordanov, S.; Seebens, A.; et al. Bats Host Major Mammalian Paramyxoviruses. *Nat. Commun.* 2012, *3*, 796, doi:10.1038/NCOMMS1796.

182. Madera, S.; Kistler, A.; Ranaivoson, H.C.; Ahyong, V.; Andrianiaina, A.; Andry, S.; Raharinosy, V.; Randriambolamanantsoa, T.H.; Ravelomanantsoa, N.A.F.; Tato, C.M.; et al. Discovery and Genomic Characterization of a Novel Henipavirus, Angavokely Virus, from Fruit Bats in Madagascar. *J. Virol.* 2022, *96*, e00921-22, doi:10.1128/JVI.00921-22.

183. Piot, P.; Spencer, J. From 1976 to 2018: Reflections on Early Investigations into the Ebola Virus. *Trans. R. Soc. Trop. Med. Hyg.* 2018, *112*, 527–528, doi:10.1093/TRSTMH/TRY088.

184. Olival, K.J.; Hayman, D.T.S. Filoviruses in Bats: Current Knowledge and Future Directions. *Viruses* 2014, *6*, 1759, doi:10.3390/V6041759.

185. Sundaram, M.; Gottdenker, N.L.; Stephens, P.R. Where Is the Elusive Primary Ebolavirus Reservoir and How Do We Find It? *Bioscience* 2025, doi:10.1093/BIOSCI/BIAF050.

186. Kajihara, M.; Hang'Ombe, B.M.; Changula, K.; Harima, H.; Isono, M.; Okuya, K.; Yoshida, R.; Mori-Kajihara, A.; Eto, Y.; Orba, Y.; et al. Marburgvirus in Egyptian Fruit Bats, Zambia. *Emerg. Infect. Dis.* 2019, *25*, 1577, doi:10.3201/EID2508.190268.

187. Dovih, P.; Laing, E.D.; Chen, Y.; Low, D.H.W.; Ansil, B.R.; Yang, X.; Shi, Z.; Broder, C.C.; Smith, G.J.D.; Linster, M.; et al. Filovirus-Reactive Antibodies in Humans and Bats in Northeast India Imply Zoonotic Spillover. *PLoS Negl. Trop. Dis.* 2019, *13*, e0007733, doi:10.1371/JOURNAL.PNTD.0007733.

188. Mostafa, A.; Abdelwhab, E.M.; Mettenleiter, T.C.; Pleschka, S. Zoonotic Potential of Influenza A Viruses: A Comprehensive Overview. *Viruses* 2018, *10*, 497, doi:10.3390/V10090497.

189. Richard, M.; De Graaf, M.; Herfst, S. Avian Influenza A Viruses: From Zoonosis to Pandemic. *Future Virol.* 2014, *9*, 513, doi:10.2217/FVL.14.30.

190. Tong, S.; Zhu, X.; Li, Y.; Shi, M.; Zhang, J.; Bourgeois, M.; Yang, H.; Chen, X.; Recuenco, S.; Gomez, J.; et al. New World Bats Harbor Diverse Influenza A Viruses. *PLoS Pathog.* 2013, *9*, e1003657, doi:10.1371/JOURNAL.PPAT.1003657.

191. Tong, S.; Li, Y.; Rivailler, P.; Conrardy, C.; Alvarez Castillo, D.A.; Chen, L.M.; Recuenco, S.; Ellison, J.A.; Davis, C.T.; York, I.A.; et al. A Distinct Lineage of Influenza A Virus from Bats. *Proc. Natl. Acad. Sci. U. S. A.* 2012,

109, 4269–4274, doi:10.1073/PNAS.1116200109/-/DCSUPPLEMENTAL.

192. Tu, I.-T.; Lynggaard, C.; Adams, L.; Walsh, S.K.; Chen, H.; Raveendran, S.; Turnbull, M.L.; Griffiths, M.E.; Ribeiro, R.; Peréz, J.G.; et al. Spillover of H5 Influenza Viruses to Vampire Bats at the Marine-Terrestrial Interface. *bioRxiv* 2025, 2025.11.09.686930, doi:10.1101/2025.11.09.686930.

193. Pereira Igreja, R.; Schneider, M.C.; Marques De Macedo, P.; Bhatia, B.; Sonar, S.; Khan, S.; Bhattacharya, J. Pandemic-Proofing: Intercepting Zoonotic Spillover Events. *Pathog. 2024, Vol. 13, Page 1067* 2024, *13*, 1067, doi:10.3390/PATHOGENS13121067.

194. Olivero, J.; Fa, J.E.; Real, R.; Márquez, A.L.; Farfán, M.A.; Vargas, J.M.; Gaveau, D.; Salim, M.A.; Park, D.; Suter, J.; et al. Recent Loss of Closed Forests Is Associated with Ebola Virus Disease Outbreaks. *Sci. Reports 2017 71* 2017, *7*, 14291-, doi:10.1038/s41598-017-14727-9.

195. Plowright, R.K.; Foley, P.; Field, H.E.; Dobson, A.P.; Foley, J.E.; Eby, P.; Daszak, P. Urban Habituation, Ecological Connectivity and Epidemic Dampening: The Emergence of Hendra Virus from Flying Foxes (Pteropus Spp.). *Proc. R. Soc. B Biol. Sci.* 2011, *278*, 3703–3712, doi:10.1098/RSPB.2011.0522.

196. Festa, F.; Priori, P.; Chiarello, G.; Palumbo, E.; Zamperin, G.; Cosentino, F.; Maiorano, L.; Menandro, M.L.; Scaravelli, D.; De Benedictis, P.; et al. A Multi-Disciplinary Approach to Identify Spillover Interfaces of Bat Coronaviruses to Pig Farms in Italy. *PLoS One* 2025, *20*, e0332117, doi:10.1371/JOURNAL.PONE.0332117.

197. Van de Vuurst, P.; Gohlke, J.M.; Escobar, L.E. Future Climate Change and the Distributional Shift of the Common Vampire Bat, Desmodus Rotundus. *Sci. Reports 2025 151* 2025, *15*, 5989-, doi:10.1038/s41598-025-87977-7.

198. Bell, D.; Roberton, S.; Hunter, P.R. Animal Origins of SARS Coronavirus: Possible Links with the International Trade in Small Carnivores. *Philos. Trans. R. Soc. B Biol. Sci.* 2004, *359*, 1107, doi:10.1098/RSTB.2004.1492.

199. Rui, J.; Wang, Q.; Lv, J.; Zhao, B.; Hu, Q.; Du, H.; Gong, W.; Zhao, Z.; Xu, J.; Zhu, Y.; et al. The Transmission Dynamics of Middle East Respiratory Syndrome Coronavirus. *Travel Med. Infect. Dis.* 2022, *45*, 102243, doi:10.1016/J.TMAID.2021.102243.

200. Jacobsen, K.H.; Alonso Aguirre, A.; Bailey, C.L.; Baranova, A. V.; Crooks, A.T.; Croitoru, A.; Delamater, P.L.; Gupta, J.; Kehn-Hall, K.; Narayanan, A.; et al. Lessons from the Ebola Outbreak: Action Items for Emerging Infectious Disease Preparedness and Response. *Ecohealth* 2016, *13*, 200–212, doi:10.1007/S10393-016-1100-5.

201. Leslie, H.H.; Sun, Z.; Kruk, M.E. Association between Infrastructure and Observed Quality of Care in 4 Healthcare Services: A Cross-Sectional Study of 4,300 Facilities in 8 Countries. *PLOS Med.* 2017, *14*, e1002464,

doi:10.1371/JOURNAL.PMED.1002464.

202. Muzembo, B.A.; Ntontolo, N.P.; Ngatu, N.R.; Khatiwada, J.; Suzuki, T.; Wada, K.; Kitahara, K.; Ikeda, S.; Miyoshi, S.I. Misconceptions and Rumors about Ebola Virus Disease in Sub-Saharan Africa: A Systematic Review. *Int. J. Environ. Res. Public Health* 2022, *19*, 4714, doi:10.3390/IJERPH19084714/S1.

203. Katze, M.G.; He, Y.; Gale, M. Viruses and Interferon: A Fight for Supremacy. *Nat. Rev. Immunol.* 2002, *2*, 675–687, doi:10.1038/nri888.

204. Koyama, S.; Ishii, K.J.; Coban, C.; Akira, S. Innate Immune Response to Viral Infection. *Cytokine* 2008, *43*, 336–341, doi:10.1016/J.CYTO.2008.07.009.

205. Zhang, Q.; Cao, X. Epigenetic Regulation of the Innate Immune Response to Infection. *Nat. Rev. Immunol.* 2019, *19*, 417–432, doi:10.1038/s41577-019-0151-6.

206. Kelsey, G.; Stegle, O.; Reik, W. Single-Cell Epigenomics: Recording the Past and Predicting the Future. *Science (80-.).* 2017, *358*, 69–75, doi:10.1126/science.aan6826.

207. Xie, S.; Hagen, D.; Becker, G.M.; Davenport, K.M.; Shira, K.A.; Stegemiller, M.R.; Thorne, J.W.; Khilji, S.; Konetchy, D.; Villamediana, P.; et al. Analyzing the Relationship of RNA and DNA Methylation with Gene Expression. *Genome Biol.* 2025, *26*, 140, doi:10.1186/S13059-025-03617-3.

208. Kumar, S.; Mohapatra, T. Deciphering Epitranscriptome: Modification of MRNA Bases Provides a New Perspective for Post-Transcriptional Regulation of Gene Expression. *Front. Cell Dev. Biol.* 2021, *9*, 550, doi.org/10.3389/fcell.2021.628415.

209. Kumar, S.; Chinnusamy, V.; Mohapatra, T. Epigenetics of Modified DNA Bases: 5-Methylcytosine and Beyond. *Front. Genet.* 2018, *9*, 640, doi:10.3389/fgene.2018.00640.

210. Cui, L.; Ma, R.; Cai, J.; Guo, C.; Chen, Z.; Yao, L.; Wang, Y.; Fan, R.; Wang, X.; Shi, Y. RNA Modifications: Importance in Immune Cell Biology and Related Diseases. *Signal Transduct. Target. Ther. 2022 71* 2022, *7*, 334-, doi:10.1038/s41392-022-01175-9.

211. Greenberg, M.V.C.; Bourc'his, D. The Diverse Roles of DNA Methylation in Mammalian Development and Disease. *Nat. Rev. Mol. Cell Biol.* 2019, *20*, 590–607, doi:10.1038/S41580-019-0159-6.

212. Luo, C.; Hajkova, P.; Ecker, J.R. Dynamic DNA Methylation: In the Right Place at the Right Time. *Science* 2018, *361*, 1336, doi:10.1126/SCIENCE.AAT6806.

213. Lanata, C.M.; Chung, S.A.; Criswell, L.A. DNA Methylation 101: What Is Important to Know about DNA Methylation and Its Role in SLE Risk and Disease Heterogeneity. *Lupus Sci. Med.* 2018, *5*, e000285, doi:10.1136/LUPUS-2018-000285.

214. Karandashov, I.; Kachanov, A.; Dukich, M.; Ponomareva, N.; Brezgin, S.; Lukashev, A.; Pokrovsky, V.S.; Chulanov, V.; Kostyusheva, A.; Kostyushev, D. M6A Methylation in Regulation of Antiviral Innate Immunity. *Viruses* 2024, *16*, 601, doi:10.3390/v16040601.

215. Kuss-Duerkop, S.K.; Pyeon, D.; Westrich, J.A. DNA Tumor Virus Regulation of Host DNA Methylation and Its Implications for Immune Evasion and Oncogenesis. *Viruses* 2018, *10*, 82, doi:10.3390/V10020082.

216. Zhang, D.; Guo, S.; Schrodi, S.J. Mechanisms of DNA Methylation in Virus-Host Interaction in Hepatitis B Infection: Pathogenesis and Oncogenetic Properties. *Int. J. Mol. Sci.* 2021, *22*, 9858, doi:10.3390/IJMS22189858.

217. Wang, H.; Feng, J.; Fu, Z.; Xu, T.; Liu, J.; Yang, S.; Li, Y.; Deng, J.; Zhang, Y.; Guo, M.; et al. Epitranscriptomic M5C Methylation of SARS-CoV- 2 RNA Regulates Viral Replication and the Virulence of Progeny Viruses in the New Infection. *Sci. Adv.* 2024, *10*, 9519, doi:10.1126/SCIADV.ADN9519.

218. Liu, J.; Xu, Y.P.; Li, K.; Ye, Q.; Zhou, H.Y.; Sun, H.; Li, X.; Yu, L.; Deng, Y.Q.; Li, R.T.; et al. The M6A Methylome of SARS-CoV-2 in Host Cells. *Cell Res.* 2021, *31*, 404–414, doi:10.1038/S41422-020-00465-7.

219. Baquero-Perez, B.; Geers, D.; Díez, J. From a to M6a: The Emerging Viral Epitranscriptome. *Viruses* 2021, *13*, 1049, doi:10.3390/v13061049.

220. Luo, T.; Chen, Z.; Zhang, F.; Liu, H.; Huang, F.; Zhang, X.; Feng, J.; Ding, S.; Liu, L.; Guan, W.; et al. Strain-Divergent M6A Landscapes Modulate Nipah Virus Replication and METTL3 Inhibition Attenuates Virulence. *Viruses* 2025, *17*, 831, doi:10.3390/V17060831.

221. Desrosiers, R.; Friderici, K.; Rottman, F. Identification of Methylated Nucleosides in Messenger RNA from Novikoff Hepatoma Cells. *Proc. Natl. Acad. Sci. U. S. A.* 1974, *71*, doi:10.1073/PNAS.71.10.3971.

222. Mach, J. Epigenetics and Genetics: Global Profiling in Maize Inbred Lines Examines Variation in DNA Methylation. *Plant Cell* 2013, *25*, 2769–2769, doi:10.1105/TPC.113.250812.

223. Wu, F.; Cheng, W.; Zhao, F.; Tang, M.; Diao, Y.; Xu, R. Association of N6-Methyladenosine with Viruses and Related Diseases. *Virol. J.* 2019, *16*, 1–10, doi:10.1186/S12985-019-1236-3.

224. Deng, X.; Chen, K.; Luo, G.Z.; Weng, X.; Ji, Q.; Zhou, T.; He, C. Widespread Occurrence of N6-Methyladenosine in Bacterial MRNA. *Nucleic Acids Res.* 2015, *43*, 6557–6567, doi:10.1093/nar/gkv596.

225. Schwartz, S.; Mumbach, M.R.; Jovanovic, M.; Wang, T.; Maciag, K.; Bushkin, G.G.; Mertins, P.; Ter-Ovanesyan, D.; Habib, N.; Cacchiarelli, D.; et al. Perturbation of M6A Writers Reveals Two Distinct Classes of MRNA Methylation at Internal and 5’ Sites. *Cell Rep.* 2014, *8*, 284–296, doi:10.1016/J.CELREP.2014.05.048.

226. Dominissini, D.; Moshitch-Moshkovitz, S.; Schwartz, S.; Salmon-Divon, M.; Ungar, L.; Osenberg, S.; Cesarkas, K.; Jacob-Hirsch, J.; Amariglio, N.; Kupiec, M.; et al. Topology of the Human and Mouse M6A RNA Methylomes Revealed by M6A-Seq. *Nature* 2012, *485*, 201–206, doi:10.1038/nature11112.

227. Wei, C.M.; Gershowitz, A.; Moss, B. Methylated Nucleotides Block 5′ Terminus of HeLa Cell Messenger RNA. *Cell* 1975, *4*, 379–386, doi:10.1016/0092-8674(75)90158-0.

228. Meyer, K.D.; Saletore, Y.; Zumbo, P.; Elemento, O.; Mason, C.E.; Jaffrey, S.R. Comprehensive Analysis of MRNA Methylation Reveals Enrichment in 3′ UTRs and near Stop Codons. *Cell* 2012, *149*, 1635–1646, doi:10.1016/j.cell.2012.05.003.

229. Lee, M.; Kim, B.; Kim, V.N. Emerging Roles of RNA Modification: M6A and U-Tail. *Cell* 2014, *158*, 980–987, doi:10.1016/J.CELL.2014.08.005.

230. Crooks, G.E.; Hon, G.; Chandonia, J.M.; Brenner, S.E. WebLogo: A Sequence Logo Generator. *Genome Res.* 2004, *14*, 1188–1190, doi:10.1101/GR.849004.

231. Manners, O.; Baquero-Perez, B.; Whitehouse, A. M6A: Widespread Regulatory Control in Virus Replication. *Biochim. Biophys. Acta. Gene Regul. Mech.* 2019, *1862*, 370, doi:10.1016/J.BBAGRM.2018.10.015.

232. Liu, J.; Yue, Y.; Han, D.; Wang, X.; Fu, Y.; Zhang, L.; Jia, G.; Yu, M.; Lu, Z.; Deng, X.; et al. A METTL3-METTL14 Complex Mediates Mammalian Nuclear RNA N6-Adenosine Methylation. *Nat. Chem. Biol.* 2014, *10*, 93–95, doi: 10.1038/nchembio.1432.

233. Ping, X.L.; Sun, B.F.; Wang, L.; Xiao, W.; Yang, X.; Wang, W.J.; Adhikari, S.; Shi, Y.; Lv, Y.; Chen, Y.S.; et al. Mammalian WTAP Is a Regulatory Subunit of the RNA N6-Methyladenosine Methyltransferase. *Cell Res.* 2014, *24*, 177–189, doi:10.1038/cr.2014.3.

234. Tuck, M.T. Partial Purification of a 6-Methyladenine MRNA Methyltransferase Which Modifies Internal Adenine Residues. *Biochem. J.* 1992, 233–240, doi:10.1042/BJ2880233.

235. Schöller, E.; Weichmann, F.; Treiber, T.; Ringle, S.; Treiber, N.; Flatley, A.; Feederle, R.; Bruckmann, A.; Meister, G. Interactions, Localization, and Phosphorylation of the M6A Generating METTL3-METTL14-WTAP Complex. *RNA* 2018, *24*, 499–512, doi:10.1261/rna.064063.117.

236. Huang, J.; Dong, X.; Gong, Z.; Qin, L.Y.; Yang, S.; Zhu, Y.L.; Wang, X.; Zhang, D.; Zou, T.; Yin, P.; et al. Solution Structure of the RNA Recognition Domain of METTL3-METTL14 N 6 -Methyladenosine Methyltransferase. *Protein Cell* 2019, *10*, 272–284, doi:10.1007/s13238-018-0518-7.

237. Wang, X.; Feng, J.; Xue, Y.; Guan, Z.; Zhang, D.; Liu, Z.; Gong, Z.; Wang, Q.; Huang, J.; Tang, C.; et al. Structural Basis of N6-Adenosine Methylation by the METTL3-METTL14 Complex. *Nature* 2016, *534*, 575–578,

doi:10.1038/nature18298.

238. Wang, P.; Doxtader, K.A.; Nam, Y. Structural Basis for Cooperative Function of Mettl3 and Mettl14 Methyltransferases. *Mol. Cell* 2016, *63*, 306–317, doi:10.1016/j.molcel.2016.05.041.

239. Su, S.; Li, S.; Deng, T.; Gao, M.; Yin, Y.; Wu, B.; Peng, C.; Liu, J.; Ma, J.; Zhang, K. Cryo-EM Structures of Human M6A Writer Complexes. *Cell Res.* 2022, *32*, 982–994, doi:10.1038/S41422-022-00725-8.

240. Fedeles, B.I.; Singh, V.; Delaney, J.C.; Li, D.; Essigmann, J.M. The AlkB Family of Fe(II)/α-Ketoglutarate-Dependent Dioxygenases: Repairing Nucleic Acid Alkylation Damage and Beyond. *J. Biol. Chem.* 2015, *290*, 20734–20742, doi:10.1074/jbc.R115.656462.

241. Jia, G.; Fu, Y.; Zhao, X.; Dai, Q.; Zheng, G.; Yang, Y.G.Y.; Yi, C.; Lindahl, T.; Pan, T.; Yang, Y.G.Y.; et al. N6-Methyladenosine in Nuclear RNA Is a Major Substrate of the Obesity-Associated FTO. *Nat. Chem. Biol.* 2011, *7*, 885–887, doi: 10.1038/nchembio.687.

242. Tang, C.; Klukovich, R.; Peng, H.; Wang, Z.; Yu, T.; Zhang, Y.; Zheng, H.; Klungland, A.; Yan, W. ALKBH5-Dependent M6A Demethylation Controls Splicing and Stability of Long 3'-UTR MRNAs in Male Germ Cells. *Proc. Natl. Acad. Sci. U. S. A. 115*, E325–E333, doi: 10.1073/pnas.1717794115.

243. Han, Z.; Niu, T.; Chang, J.; Lei, X.; Zhao, M.; Wang, Q.; Cheng, W.; Wang, J.; Feng, Y.; Chai, J. Crystal Structure of the FTO Protein Reveals Basis for Its Substrate Specificity. *Nature* 2010, *464*, 1205–1209, doi:10.1038/NATURE08921.

244. Zheng, G.; Dahl, J.A.; Niu, Y.; Fedorcsak, P.; Huang, C.M.; Li, C.J.; Vågbø, C.B.; Shi, Y.; Wang, W.L.; Song, S.H.; et al. ALKBH5 Is a Mammalian RNA Demethylase That Impacts RNA Metabolism and Mouse Fertility. *Mol. Cell* 2013, *49*, 18, doi:10.1016/J.MOLCEL.2012.10.015.

245. Feng, C.; Liu, Y.; Wang, G.; Deng, Z.; Zhang, Q.; Wu, W.; Tong, Y.; Cheng, C.; Chen, Z. Crystal Structures of the Human RNA Demethylase Alkbh5 Reveal Basis for Substrate Recognition. *J. Biol. Chem.* 2013, *289*, 11571–11583, doi:10.1074/jbc.M113.546168.

246. Hagel, J.M.; Facchini, P.J. Expanding the Roles for 2-Oxoglutarate-Dependent Oxygenases in Plant Metabolism. *Nat. Prod. Rep.* 2018, *35*, 721–734, doi:10.1039/C7NP00060J.

247. Zhang, Z.; Theler, D.; Kaminska, K.H.; Hiller, M.; De La Grange, P.; Pudimat, R.; Rafalska, I.; Heinrich, B.; Bujnick, J.M.; Allain, F.H.T.; et al. The YTH Domain Is a Novel RNA Binding Domain. *J. Biol. Chem.* 2010, *285*, doi: 10.1074/jbc.M110.104711.

248. Hsu, P.J.; Zhu, Y.; Ma, H.; Guo, Y.; Shi, X.; Liu, Y.; Qi, M.; Lu, Z.; Shi, H.; Wang, J.; et al. Ythdc2 Is an N6 -Methyladenosine Binding Protein That

Regulates Mammalian Spermatogenesis. *Cell Res.* 2017, *27*, 1115–1127, doi:10.1038/cr.2017.99.

249. Wang, J.; Tan, L.; Jia, B.; Yu, X.X.; Yao, R.; Ouyang, N.; Yu, X.X.; Cao, X.; Tong, J.; Chen, T.; et al. Downregulation of M6A Reader YTHDC2 Promotes the Proliferation and Migration of Malignant Lung Cells via CYLD/NF-KB Pathway. *Int. J. Biol. Sci.* 2021, *17*, 2633, doi:10.7150/IJBS.58514.

250. Wang, X.; Zhao, B.S.; Roundtree, I.A.; Lu, Z.; Han, D.; Ma, H.; Weng, X.; Chen, K.; Shi, H.; He, C. N6-Methyladenosine Modulates Messenger RNA Translation Efficiency. *Cell* 2015, *161*, 1388–1399, doi:10.1016/j.cell.2015.05.014.

251. Du, H.; Zhao, Y.; He, J.; Zhang, Y.; Xi, H.; Liu, M.; Ma, J.; Wu, L. YTHDF2 Destabilizes m 6 A-Containing RNA through Direct Recruitment of the CCR4-NOT Deadenylase Complex. *Nat. Commun.* 2016, *7*, 1–11, doi:10.1038/NCOMMS12626.

252. Shi, H.; Wang, X.; Lu, Z.; Zhao, B.S.; Ma, H.; Hsu, P.J.; Liu, C.; He, C. YTHDF3 Facilitates Translation and Decay of N 6-Methyladenosine-Modified RNA. *Cell Res.* 2017, *27*, 315–328, doi:10.1038/CR.2017.15.

253. Li, A.; Chen, Y.S.; Ping, X.L.; Yang, X.; Xiao, W.; Yang, Y.; Sun, H.Y.; Zhu, Q.; Baidya, P.; Wang, X.; et al. Cytoplasmic m 6 A Reader YTHDF3 Promotes MRNA Translation. *Cell Res.* 2017, *27*, 444–447, doi:10.1038/cr.2017.10.

254. Roundtree, I.A.; Luo, G.Z.; Zhang, Z.; Wang, X.; Zhou, T.; Cui, Y.; Sha, J.; Huang, X.; Guerrero, L.; Xie, P.; et al. YTHDC1 Mediates Nuclear Export of N6-Methyladenosine Methylated MRNAs. *Elife* 2017, *6*, e31311, doi:10.7554/ELIFE.31311.

255. Mao, Y.; Dong, L.; Liu, X.M.; Guo, J.; Ma, H.; Shen, B.; Qian, S.B. M6A in MRNA Coding Regions Promotes Translation via the RNA Helicase-Containing YTHDC2. *Nat. Commun.* 2019, *10*, 1–11, doi:10.1038/s41467-019-13317-9.

256. Xu, C.; Liu, K.; Ahmed, H.; Loppnau, P.; Schapira, M.; Min, J. Structural Basis for the Discriminative Recognition of N6-Methyladenosine RNA by the Human YT521-B Homology Domain Family of Proteins. *J. Biol. Chem.* 2015, *290*, 24902–24913, doi:10.1074/jbc.M115.680389.

257. Xu, C.; Wang, X.; Liu, K.; Roundtree, I.A.; Tempel, W.; Li, Y.; Lu, Z.; He, C.; Min, J. Structural Basis for Selective Binding of M6A RNA by the YTHDC1 YTH Domain. *Nat. Chem. Biol.* 2014, *10*, 927–929, doi:10.1038/nchembio.1654.

258. Kretschmer, J.; Rao, H.; Hackert, P.; Sloan, K.E.; Höbartner, C.; Bohnsack, M.T. The M6A Reader Protein YTHDC2 Interacts with the Small Ribosomal Subunit and the 5′-3′ Exoribonuclease XRN1. *RNA* 2018, *24*, 1339–1350, doi:10.1261/rna.064238.117.

259. Li, Y.; Bedi, R.K.; Moroz-Omori, E. V.; Caflisch, A. Structural and Dynamic Insights into Redundant Function of YTHDF Proteins. *J. Chem. Inf. Model.* 2020, *60*, 5932–5935, doi:10.1021/ACS.JCIM.0C01029.

260. Zhou, W.; Han, Z.; Wu, Z.; Gong, W.; Yang, S.; Chen, L.; Li, C. Specific Recognition between YTHDF3 and M6 A-Modified RNA: An All-Atom Molecular Dynamics Simulation Study. *Proteins* 2022, *90*, 1965–1972, doi:10.1002/PROT.26389.

261. Ma, C.; Liao, S.; Zhu, Z. Crystal Structure of Human YTHDC2 YTH Domain. *Biochem. Biophys. Res. Commun.* 2019, *518*, 678–684, doi:10.1016/j.bbrc.2019.08.107.

262. Zhu, T.; Roundtree, I.A.; Wang, P.; Wang, X.; Wang, L.; Sun, C.; Tian, Y.; Li, J.; He, C.; Xu, Y. Crystal Structure of the YTH Domain of YTHDF2 Reveals Mechanism for Recognition of N6-Methyladenosine. *Cell Res.* 2014, *24*.

263. Takeuchi, O.; Akira, S. Innate Immunity to Virus Infection. *Immunol. Rev.* 2009, *227*, 75, doi:10.1111/J.1600-065X.2008.00737.X.

264. Ren, Z.; Ding, T.; Zuo, Z.; Xu, Z.; Deng, J.; Wei, Z. Regulation of MAVS Expression and Signaling Function in the Antiviral Innate Immune Response. *Front. Immunol.* 2020, *11*, 1030, doi:10.3389/fimmu.2020.01030.

265. Li, D.; Wu, M. Pattern Recognition Receptors in Health and Diseases. *Signal Transduct. Target. Ther.* 2021, *6*, 1–24, doi:10.1038/s41392-021-00687-0.

266. Zheng, Q.; Hou, J.; Zhou, Y.; Li, Z.; Cao, X. The RNA Helicase DDX46 Inhibits Innate Immunity by Entrapping M6A-Demethylated Antiviral Transcripts in the Nucleus. *Nat. Immunol.* 2017, *18*, 1094–1103, doi: 10.1038/ni.3830.

267. Durbin, A.F.; Wang, C.; Marcotrigiano, J.; Gehrke, L. RNAs Containing Modified Nucleotides Fail To Trigger RIG-I Conformational Changes for Innate Immune Signaling. *MBio* 2016, *7*, doi: 10.1128/mBio.00833-16.

268. Gokhale, N.S.; McIntyre, A.B.R.; McFadden, M.J.; Roder, A.E.; Kennedy, E.M.; Gandara, J.A.; Hopcraft, S.E.; Quicke, K.M.; Vazquez, C.; Willer, J.; et al. N6-Methyladenosine in Flaviviridae Viral RNA Genomes Regulates Infection. *Cell Host Microbe* 2016, *20*, 654–665, doi:10.1016/j.chom.2016.09.015.

269. Lichinchi, G.; Zhao, B.S.; Wu, Y.; Lu, Z.; Qin, Y.; He, C.; Rana, T.M. Dynamics of Human and Viral RNA Methylation during Zika Virus Infection. *Cell Host Microbe* 2016, *20*, 666–673, doi:10.1016/j.chom.2016.10.002.

270. Kim, B.; Arcos, S.; Rothamel, K.; Jian, J.; Rose, K.L.; McDonald, W.H.; Bian, Y.; Reasoner, S.; Barrows, N.J.; Bradrick, S.; et al. Discovery of Widespread Host Protein Interactions with the Pre-Replicated Genome of CHIKV Using VIR-CLASP. *Mol. Cell* 2020, *78*, 624-640.e7, doi:10.1016/j.molcel.2020.04.013.

271. Burgess, H.M.; Depledge, D.P.; Thompson, L.; Srinivas, K.P.; Grande, R.C.; Vink, E.I.; Abebe, J.S.; Blackaby, W.P.; Hendrick, A.; Albertella, M.R.; et al. Targeting the M6A RNA Modification Pathway Blocks SARS-CoV-2 and HCoV-OC43 Replication. *Genes Dev.* 2021, *35*, 1005–1019, doi:10.1101/GAD.348320.121/-/DC1.

272. Malbec, L.; Celerier, M.; Bizet, M.; Calonne, E.; Hofmann-Winkler, H.; Boeckx, B.; Abdelnabi, R.; Putmans, P.; Hassabi, B.; Naesens, L.; et al. The RNA Demethylase FTO Controls M6A Marking on SARS-CoV-2 and Classifies COVID-19 Severity in Patients. *bioRxiv* 2022, 2022.06.27.497749, doi:10.1101/2022.06.27.497749.

273. Liu, S.; Zhuo, L.; Wang, J.; Zhang, Q.; Li, Q.; Li, G.; Yan, L.; Jin, T.; Pan, T.; Sui, X.; et al. METTL3 Plays Multiple Functions in Biological Processes. *Am. J. Cancer Res.* 2020, *10*, 1631.

274. Lu, M.; Zhang, Z.; Xue, M.; Zhao, B.S.; Harder, O.; Li, A.; Liang, X.; Gao, T.Z.; Xu, Y.; Zhou, J.; et al. N6-Methyladenosine Modification Enables Viral RNA to Escape Recognition by RNA Sensor RIG-I. *Nat. Microbiol.* 2020, *5*, 584, doi:10.1038/S41564-019-0653-9.

275. Li, N.; Hui, H.; Bray, B.; Gonzalez, G.M.; Zeller, M.; Anderson, K.G.; Knight, R.; Smith, D.; Wang, Y.; Carlin, A.F.; et al. METTL3 Regulates Viral M6A RNA Modification and Host Cell Innate Immune Responses during SARS-CoV-2 Infection. *Cell Rep.* 2021, *35*, 109091, doi:10.1016/J.CELREP.2021.109091.

276. Zhang, X.; Hao, H.; Ma, L.; Zhang, Y.; Hu, X.; Chen, Z.; Liu, D.; Yuan, J.; Hu, Z.; Guan, W. Methyltransferase-like 3 Modulates Severe Acute Respiratory Syndrome Coronavirus-2 RNA N6-Methyladenosine Modification and Replication. *MBio* 2021, *12*, e01067-21, doi:10.1128/MBIO.01067-21.

277. Qiu, W.; Zhang, Q.; Zhang, R.; Lu, Y.; Wang, X.; Tian, H.; Yang, Y.Y.G.Y.; Gu, Z.; Gao, Y.; Yang, X.; et al. N6-Methyladenosine RNA Modification Suppresses Antiviral Innate Sensing Pathways via Reshaping Double-Stranded RNA. *Nat. Commun.* 2021, *12*, 1–16, doi.org/10.1038/s41467-021-21904-y.

278. Qiu, X.; Tian, J.; Zhao, X.; Wang, L.; Wang, L.; Bai, Y.; Sun, A.; Zhuang, G. The Tiny Epigenetic Addition Plays Big Roles: The RNA Methylation in Both Human and Animal Herpesvirus Infection. *Transbound. Emerg. Dis.* 2025, *2025*, 8542827, doi:10.1155/TBED/8542827.

279. Yao, M.; Dong, Y.; Wang, Y.; Liu, H.; Ma, H.; Zhang, H.; Zhang, L.; Cheng, L.; Lv, X.; Xu, Z.; et al. N6-Methyladenosine Modifications Enhance Enterovirus 71 ORF Translation through METTL3 Cytoplasmic Distribution. *Biochem. Biophys. Res. Commun.* 2020, *527*, 297–304, doi:10.1016/j.bbrc.2020.04.088.

280. Hao, H.; Hao, S.; Chen, H.; Chen, Z.; Zhang, Y.; Wang, J.; Wang, H.; Zhang, B.; Qiu, J.; Deng, F.; et al. N 6-Methyladenosine Modification and METTL3

Modulate Enterovirus 71 Replication. *Nucleic Acids Res.* 2018, *47*, 362, doi:10.1093/NAR/GKY1007.

281. McFadden, M.J.; McIntyre, A.B.R.; Mourelatos, H.; Abell, N.S.; Gokhale, N.S.; Ipas, H.; Xhemalçe, B.; Mason, C.E.; Horner, S.M. Post-Transcriptional Regulation of Antiviral Gene Expression by N6-Methyladenosine. *Cell Rep.* 2021, *34*, 108798, doi:10.1016/J.CELREP.2021.108798.

282. Wang, L.; Qiu, X.; Wang, L.; Yang, X.; Li, M.; Zhao, X.; Zhu, W.; Lv, L.; Kang, Y.; Yao, L.; et al. ERK-METTL3 Axis Acts as a Novel Regulator of Antiviral Innate Immunity Combating Pseudorabies Virus Infection. *PLOS Pathog.* 2025, *21*, e1013234, doi:10.1371/JOURNAL.PPAT.1013234.

283. Chen, J.; Wei, X.; Wang, X.; Liu, T.; Zhao, Y.; Chen, L.; Luo, Y.; Du, H.; Li, Y.; Liu, T.; et al. TBK1-METTL3 Axis Facilitates Antiviral Immunity. *Cell Rep.* 2022, *38*, 110373, doi:10.1016/J.CELREP.2022.110373.

284. Sayers, E.W.; Beck, J.; Bolton, E.E.; Brister, J.R.; Chan, J.; Connor, R.; Feldgarden, M.; Fine, A.M.; Funk, K.; Hoffman, J.; et al. Database Resources of the National Center for Biotechnology Information in 2025. *Nucleic Acids Res.* 2025, *53*, D20–D29, doi:10.1093/NAR/GKAE979.

285. Muhire, B.M.; Varsani, A.; Martin, D.P. SDT: A Virus Classification Tool Based on Pairwise Sequence Alignment and Identity Calculation. *PLoS One* 2014, *9*, e108277, doi:10.1371/JOURNAL.PONE.0108277.

286. Chen, C.; Chen, H.; Zhang, Y.; Thomas, H.R.; Frank, M.H.; He, Y.; Xia, R. TBtools: An Integrative Toolkit Developed for Interactive Analyses of Big Biological Data. *Mol. Plant* 2020, *13*, 1194–1202, doi:10.1016/J.MOLP.2020.06.009.

287. Rangwala, S.H.; Kuznetsov, A.; Ananiev, V.; Asztalos, A.; Borodin, E.; Evgeniev, V.; Joukov, V.; Lotov, V.; Pannu, R.; Rudnev, D.; et al. Accessing NCBI Data Using the NCBI Sequence Viewer and Genome Data Viewer (GDV). *Genome Res.* 2021, *31*, 159–169, doi:10.1101/GR.266932.120.

288. Thomas A, H. BioEdit_a_user_friendly_biological_seque. *Oxford Univ. Press* 1990.

289. Berman, H.; Henrick, K.; Nakamura, H. Announcing the Worldwide Protein Data Bank. *Nat. Struct. Biol.* 2003, *10*, 980, doi:10.1038/NSB1203-980.

290. Biasini, M.; Bienert, S.; Waterhouse, A.; Arnold, K.; Studer, G.; Schmidt, T.; Kiefer, F.; Cassarino, T.G.; Bertoni, M.; Bordoli, L.; et al. SWISS-MODEL: Modelling Protein Tertiary and Quaternary Structure Using Evolutionary Information. *Nucleic Acids Res.* 2014, *42*, W252–W258, doi:10.1093/NAR/GKU340.

291. Waterhouse, A.; Bertoni, M.; Bienert, S.; Studer, G.; Tauriello, G.; Gumienny, R.; Heer, F.T.; De Beer, T.A.P.; Rempfer, C.; Bordoli, L.; et al. SWISS-MODEL: Homology Modelling of Protein Structures and Complexes. *Nucleic*

Acids Res. 2018, *46*, doi:10.1093/NAR/GKY427.

292. Schrödinger The PyMOL Molecular Graphics System, Version 2.5 Available online: https://pymol.org/ (accessed on 27 April 2026).

293. Robert, X.; Gouet, P. Deciphering Key Features in Protein Structures with the New ENDscript Server. *Nucleic Acids Res.* 2014, *42*, W320–W324, doi:10.1093/NAR/GKU316.

294. Kearse, M.; Moir, R.; Wilson, A.; Stones-Havas, S.; Cheung, M.; Sturrock, S.; Buxton, S.; Cooper, A.; Markowitz, S.; Duran, C.; et al. Geneious Basic: An Integrated and Extendable Desktop Software Platform for the Organization and Analysis of Sequence Data. *Bioinformatics* 2012, *28*, 1647–1649, doi:10.1093/BIOINFORMATICS/BTS199.

295. Friedrichs, V.; Balkema-Buschmann, A.; Dorhoi, A.; Pei, G. Selection and Stability Validation of Reference Gene Candidates for Transcriptional Analysis in Rousettus Aegyptiacus. *Sci. Rep.* 2021, *11*, 21662, doi:10.1038/S41598-021-01260-Z.

296. Koonin, E. V. Does the Central Dogma Still Stand? *Biol. Direct* 2012, *7*, 1–7, doi:10.1186/1745-6150-7-27.

297. Bove, G.; Del Gaudio, N.; Altucci, L. Epitranscriptomics and Epigenetics: Two Sides of the Same Coin? *Clin. Epigenetics* 2024, *16*, 1–4, doi:10.1186/S13148-024-01729-4.

298. Yue, H.; Nie, X.; Yan, Z.; Weining, S. N6-methyladenosine Regulatory Machinery in Plants: Composition, Function and Evolution. *Plant Biotechnol. J.* 2019, *17*, 1194, doi:10.1111/PBI.13149.

299. Sergiev, P. V.; Golovina, A.Y.; Osterman, I.A.; Nesterchuk, M. V.; Sergeeva, O. V.; Chugunova, A.A.; Evfratov, S.A.; Andreianova, E.S.; Pletnev, P.I.; Laptev, I.G.; et al. N6-Methylated Adenosine in RNA: From Bacteria to Humans. *J. Mol. Biol.* 2016, *428*, 2134–2145, doi:10.1016/J.JMB.2015.12.013.

300. Zhang, X.; Peng, Q.; Wang, L. N 6-Methyladenosine Modification—a Key Player in Viral Infection. *Cell. Mol. Biol. Lett.* 2023, *28*, 1–15, doi:10.1186/S11658-023-00490-5.

301. Wang, S.; Lv, W.; Li, T.; Zhang, S.; Wang, H.; Li, X.; Wang, L.; Ma, D.; Zang, Y.; Shen, J.; et al. Dynamic Regulation and Functions of MRNA M6A Modification. *Cancer Cell Int.* 2022, *22*, 1–12, doi:10.1186/S12935-022-02452-X.

302. Bhat, G.R.; Sethi, I.; Rah, B.; Kumar, R.; Afroze, D. Innovative in Silico Approaches for Characterization of Genes and Proteins. *Front. Genet.* 2022, *13*, 865182, doi:10.3389/FGENE.2022.865182.

303. Chen, J.; Gu, Z.; Lai, L.; Pei, J. In Silico Protein Function Prediction: The Rise of Machine Learning-Based Approaches. *Med. Rev.* 2023, *3*, 487, doi:10.1515/MR-2023-0038.

304. Bayoumi, M.; Rohaim, M.A.; Munir, M. Structural and Virus Regulatory Insights Into Avian N6-Methyladenosine (M6A) Machinery. *Front. Cell Dev. Biol.* 2020, *8*, 543, doi:10.3389/FCELL.2020.00543.

305. Liu, P.; Liu, H.; Zhao, J.; Yang, T.; Guo, S.; Chang, L.; Xiao, T.; Xu, A.; Liu, X.; Zhu, C.; et al. Genome-Wide Identification and Functional Analysis of MRNA M6A Writers in Soybean under Abiotic Stress. *Front. Plant Sci.* 2024, *15*, 1446591, doi:10.3389/FPLS.2024.1446591.

306. Shen, X.; Hu, B.; Xu, J.; Qin, W.; Fu, Y.; Wang, S.; Dong, Q.; Qin, L. The M6A Methylation Landscape Stratifies Hepatocellular Carcinoma into 3 Subtypes with Distinct Metabolic Characteristics. *Cancer Biol. Med.* 2020, *17*, 937–952, doi:10.20892/J.ISSN.2095-3941.2020.0402.

307. Lichinchi, G.; Gao, S.; Saletore, Y.; Gonzalez, G.M.; Bansal, V.; Wang, Y.; Mason, C.E.; Rana, T.M. Dynamics of the Human and Viral M6A RNA Methylomes during HIV-1 Infection of T Cells. *Nat. Microbiol. 2016 14* 2016, *1*, 1–9, doi:10.1038/nmicrobiol.2016.11.

308. Albariño, C.G.; Foltzer, M.; Towner, J.S.; Rowe, L.A.; Campbell, S.; Jaramillo, C.M.; Bird, B.H.; Reeder, D.A.M.; Vodzak, M.E.; Rota, P.; et al. Novel Paramyxovirus Associated with Severe Acute Febrile Disease, South Sudan and Uganda, 2012. *Emerg. Infect. Dis.* 2014, *20*, 211, doi:10.3201/EID2002.131620.

309. Amman, B.R.; Albariño, C.G.; Bird, B.H.; Nyakarahuka, L.; Sealy, T.K.; Balinandi, S.; Schuh, A.J.; Campbell, S.M.; Ströher, U.; Jones, M.E.B.; et al. A Recently Discovered Pathogenic Paramyxovirus, Sosuga Virus, Is Present in Rousettus Aegyptiacus Fruit Bats at Multiple Locations in Uganda. *J. Wildl. Dis.* 2015, *51*, 774, doi:10.7589/2015-02-044.

310. Roche, S.E.; Costard, S.; Meers, J.; Field, H.E.; Breed, A.C. Assessing the Risk of Nipah Virus Establishment in Australian Flying-Foxes. *Epidemiol. Infect.* 2014, *143*, 2213, doi:10.1017/S0950268813003336.

311. Páez, D.J.; Giles, J.; McCallum, H.; Field, H.; Jordan, D.; Peel, A.J.; Plowright, R.K. Conditions Affecting the Timing and Magnitude of Hendra Virus Shedding across Pteropodid Bat Populations in Australia. *Epidemiol. Infect.* 2017, *145*, 3143, doi:10.1017/S0950268817002138.

312. Mortlock, M.; Geldenhuys, M.; Dietrich, M.; Epstein, J.H.; Weyer, J.; Pawęska, J.T.; Markotter, W. Seasonal Shedding Patterns of Diverse Henipavirus-Related Paramyxoviruses in Egyptian Rousette Bats. *Sci. Rep.* 2021, *11*, 24262, doi:10.1038/S41598-021-03641-W.

313. Nasr, A.; Copeland, N.; Munir, M. Structural Analysis of Virus Regulatory N6-Methyladenosine (M6A) Machinery of the Black Flying Fox (Pteropus Alecto) and the Egyptian Fruit Bat (Rousettus Aegyptiacus) Shows Evolutionary Conservation Amongst Mammals. *Genes (Basel).* 2024, *15*, 1361, doi:10.3390/GENES15111361.

314. Zapata-García, J.A.; Riveros-Magaña, A.R.; Ortiz-Lazareno, P.C.; Hernández-

Flores, G.; Jave-Suárez, L.F.; Aguilar-Lemarroy, A. Comparative Genomic Hybridization and Transcriptome Sequencing Reveal Genes with Gain in Acute Lymphoblastic Leukemia: JUP Expression Emerges as a Survival-Related Gene. *Diagnostics* 2022, *12*, 2788, doi:10.3390/diagnostics12112788.

315. Jones, M.R.; Peng, P.C.; Coetzee, S.G.; Tyrer, J.; Reyes, A.L.P.; Corona, R.I.; Davis, B.; Chen, S.; Dezem, F.; Seo, J.H.; et al. Ovarian Cancer Risk Variants Are Enriched in Histotype-Specific Enhancers and Disrupt Transcription Factor Binding Sites. *Am. J. Hum. Genet.* 2020, *107*, 622–635, doi:10.1016/j.ajhg.2020.08.021.

316. Liu, H.; Gu, J.; Jin, Y.; Yuan, Q.; Ma, G.; Du, M.; Ge, Y.; Qin, C.; Lv, Q.; Fu, G.; et al. Genetic Variants in N6-Methyladenosine Are Associated with Bladder Cancer Risk in the Chinese Population. *Arch. Toxicol.* 2021, *95*, 299–309, doi:10.1007/s00204-020-02911-2.

317. Fawcett, K.A.; Barroso, I. The Genetics of Obesity: FTO Leads the Way. *Trends Genet.* 2010, *26*, 266, doi:10.1016/J.TIG.2010.02.006.

318. Chen, P.; Li, S.; Zhang, K.; Zhao, R.; Cui, J.; Zhou, W.; Liu, Y.; Zhang, L.; Cheng, Y. N6-Methyladenosine Demethylase ALKBH5 Suppresses Malignancy of Esophageal Cancer by Regulating MicroRNA Biogenesis and RAI1 Expression. *Oncogene 2021 4037* 2021, *40*, 5600–5612, doi:10.1038/s41388-021-01966-4.

319. Zhang, C.; Dang, D.; Cong, L.; Sun, H.; Cong, X. Pivotal Factors Associated with the Immunosuppressive Tumor Microenvironment and Melanoma Metastasis. *Cancer Med.* 2021, *10*, 4710–4720, doi:10.1002/cam4.3963.

320. Liu, J.; Cheng, J.; Li, L.; Li, Y.; Zhou, H.; Zhang, J.; Li, S.; Xia, H.; He, J.; Yang, Z. YTHDF1 Gene Polymorphisms and Neuroblastoma Susceptibility in Chinese Children: An Eight-Center Case-Control Study. *J. Cancer* 2021, *12*, 2465, doi:10.7150/JCA.54496.

321. Nishizaki, S.S.; Haghani, N.K.; La, G.N.; Mariano, N.A.F.; Uribe-Salazar, J.M.; Kaya, G.; Regester, M.; Andrews, D.S.; Nordahl, C.W.; Amaral, D.G.; et al. M6A-MRNA Reader YTHDF2 Identified as a Potential Risk Gene in Autism With Disproportionate Megalencephaly. *Autism Res.* 2025, *18*, 966–982, doi:10.1002/AUR.3314.

322. Jiang, X.; Liu, B.; Nie, Z.; Duan, L.; Xiong, Q.; Jin, Z.; Yang, C.; Chen, Y. The Role of M6A Modification in the Biological Functions and Diseases. *Signal Transduct. Target. Ther.* 2021, *6*, 1–16.

323. Sivashankari, S.; Shanmughavel, P. Comparative Genomics - A Perspective. *Bioinformation* 2007, *1*, 376, doi:10.6026/97320630001376.

324. Kemkemer, C.; Kohn, M.; Cooper, D.N.; Froenicke, L.; Högel, J.; Hameister, H.; Kehrer-Sawatzki, H. Gene Synteny Comparisons between Different Vertebrates Provide New Insights into Breakage and Fusion Events during Mammalian Karyotype Evolution. *BMC Evol. Biol.* 2009, *9*, doi:10.1186/1471-

2148-9-84.

325. Jebb, D.; Huang, Z.; Pippel, M.; Hughes, G.M.; Lavrichenko, K.; Devanna, P.; Winkler, S.; Jermiin, L.S.; Skirmuntt, E.C.; Katzourakis, A.; et al. Six Reference-Quality Genomes Reveal Evolution of Bat Adaptations. *Nature* 2020, *583*, 578–584, doi:10.1038/S41586-020-2486-3.

326. Zhang, G.; Cowled, C.; Shi, Z.; Huang, Z.; Bishop-Lilly, K.A.; Fang, X.; Wynne, J.W.; Xiong, Z.; Baker, M.L.; Zhao, W.; et al. Comparative Analysis of Bat Genomes Provides Insight into the Evolution of Flight and Immunity. *Science (80-.).* 2013, *339*, 456–460, doi:10.1126/science.1230835.

327. Wang, H.; Zhou, H.; Yao, X.; Wang, H.; Zhou, H.; Yao, X. Different Species of Bats: Genomics, Transcriptome, and Immune Repertoire. *Curr. Issues Mol. Biol.* 2025, *47*, 252, doi:10.3390/CIMB47040252.

328. Teeling, E.C.; Vernes, S.C.; Dávalos, L.M.; Ray, D.A.; Gilbert, M.T.P.; Myers, E. Bat Biology, Genomes, and the Bat1K Project: To Generate Chromosome-Level Genomes for All Living Bat Species. *Annu. Rev. Anim. Biosci.* 2018, *6*, 23–46, doi:10.1146/annurev-animal-022516-022811.

329. Dorn, M.; E Silva, M.B.; Buriol, L.S.; Lamb, L.C. Three-Dimensional Protein Structure Prediction: Methods and Computational Strategies. *Comput. Biol. Chem.* 2014, *53*, 251–276, doi: 10.1016/j.compbiolchem.2014.10.001.

330. Pandey, K.; Poh, H.X.; Jaffrey, S.R. Why Does the M6A Writer Complex Require so Many Proteins? *PLOS Biol.* 2025, *23*, e3003386, doi:10.1371/JOURNAL.PBIO.3003386.

331. Martinez, S.; Hausinger, R.P. Catalytic Mechanisms of Fe(II)- and 2-Oxoglutarate-Dependent Oxygenases. *J. Biol. Chem.* 2015, *290*, 20702, doi:10.1074/JBC.R115.648691.

332. Xu, Y.; Zhang, W.; Shen, F.; Yang, X.; Liu, H.; Dai, S.; Sun, X.; Huang, J.; Guo, Q. YTH Domain Proteins: A Family of M6A Readers in Cancer Progression. *Front. Oncol.* 2021, *11*, 25284–25292, doi:10.3389/FONC.2021.629560.

333. Pommié, C.; Levadoux, S.; Sabatier, R.; Lefranc, G.; Lefranc, M.P. IMGT Standardized Criteria for Statistical Analysis of Immunoglobulin V-REGION Amino Acid Properties. *J. Mol. Recognit.* 2004, *17*, 17–32, doi:10.1002/JMR.647.

334. Aftabuddin, M.; Kundu, S. Hydrophobic, Hydrophilic, and Charged Amino Acid Networks within Protein. *Biophys. J.* 2006, *93*, 225, doi:10.1529/BIOPHYSJ.106.098004.

335. Wang, W.; Jin, Y.; Xie, Z.; He, M.; Li, J.; Wang, Z.; Ma, S.; Zhang, W.; Tong, J. When Animal Viruses Meet N6-Methyladenosine (M6A) Modifications: For Better or Worse? *Vet. Res.* 2024, *55*, 171, doi:10.1186/S13567-024-01424-5.

336. Yang, Y.; Hsu, P.J.; Chen, Y.S.; Yang, Y.G. Dynamic Transcriptomic M6A

Decoration: Writers, Erasers, Readers and Functions in RNA Metabolism. *Cell Res. 2018 286* 2018, *28*, 616–624, doi:10.1038/s41422-018-0040-8.

337. Zhang, D.; Xu, T.; Gao, X.; Qu, Y.; Su, X. Methyltransferase-like 3-Mediated RNA N6-Methyladenosine Contributes to Immune Dysregulation: Diagnostic Biomarker and Therapeutic Target. *Front. Immunol.* 2025, *16*, 1523503, doi:10.3389/FIMMU.2025.1523503.

338. Wendt, L.; Pickin, M.J.; Bodmer, B.S.; Reiche, S.; Fénéant, L.; Hölper, J.E.; Fuchs, W.; Groseth, A.; Hoenen, T. N6-Methyladenosine Is Required for Efficient RNA Synthesis of Ebola Virus and Other Haemorrhagic Fever Viruses. *Emerg. Microbes Infect.* 2023, *12*, 2223732, doi:10.1080/22221751.2023.2223732.

339. Weatherman, S.; Feldmann, H.; de Wit, E. Transmission of Henipaviruses. *Curr. Opin. Virol.* 2017, *28*, 7, doi:10.1016/J.COVIRO.2017.09.004.

340. Amaya, M.; Cheng, H.; Borisevich, V.; Navaratnarajah, C.K.; Cattaneo, R.; Cooper, L.; Moore, T.W.; Gaisina, I.N.; Geisbert, T.W.; Rong, L.; et al. A Recombinant Cedar Virus Based High-Throughput Screening Assay for Henipavirus Antiviral Discovery. *Antiviral Res.* 2021, *193*, 105084, doi:10.1016/J.ANTIVIRAL.2021.105084.

341. Pavlovich, S.S.; Lovett, S.P.; Koroleva, G.; Guito, J.C.; Arnold, C.E.; Nagle, E.R.; Kulcsar, K.; Lee, A.; Thibaud-Nissen, F.; Hume, A.J.; et al. The Egyptian Rousette Genome Reveals Unexpected Features of Bat Antiviral Immunity. *Cell* 2018, *173*, 1098, doi:10.1016/J.CELL.2018.03.070.

342. Tian, S.; Zeng, J.; Jiao, H.; Zhang, D.; Zhang, L.; Lei, C.Q.; Rossiter, S.J.; Zhao, H. Comparative Analyses of Bat Genomes Identify Distinct Evolution of Immunity in Old World Fruit Bats. *Sci. Adv.* 2023, *9*, eadd0141, doi:10.1126/SCIADV.ADD0141.

343. Clayton, E.; Munir, M.; Unterholzner, L. Investigating the Innate Immune Systems of Bats and Their Roles as Zoonotic Viral Reservoirs. *PhD thesis* 2024, *Lancaster*.

344. Kim, G.W.; Siddiqui, A. The Role of N6-Methyladenosine Modification in the Life Cycle and Disease Pathogenesis of Hepatitis B and C Viruses. *Exp. Mol. Med. 2021 533* 2021, *53*, 339–345, doi:10.1038/s12276-021-00581-3.

345. Courtney, D.G.; Kennedy, E.M.; Dumm, R.E.; Bogerd, H.P.; Tsai, K.; Heaton, N.S.; Cullen, B.R. Epitranscriptomic Enhancement of Influenza A Virus Gene Expression and Replication. *Cell Host Microbe* 2017, *22*, 377, doi:10.1016/J.CHOM.2017.08.004.

346. Li, H.; Guo, Y.; Qi, W.; Liao, M. N6-Methyladenosine Modification of Viral RNA and Its Role during the Recognition Process of RIG-I-like Receptors. *Front. Immunol.* 2022, *13*, 1031200, doi:10.3389/FIMMU.2022.1031200.

347. Zannella, C.; Rinaldi, L.; Boccia, G.; Chianese, A.; Sasso, F.C.; De Caro, F.;

Franci, G.; Galdiero, M. Regulation of M6A Methylation as a New Therapeutic Option against COVID-19. *Pharmaceuticals* 2021, *14*, 1135, doi:10.3390/PH14111135/S1.

348. Mohl, B.P.; Diederich, S.; Fischer, K.; Balkema-Buschmann, A. Rousettus Aegyptiacus Fruit Bats Do Not Support Productive Replication of Cedar Virus upon Experimental Challenge. *Viruses* 2024, *16*, doi:10.3390/V16091359.

349. Lenhard, L.; Müller, M.; Diederich, S.; Loerzer, L.; Friedrichs, V.; Köllner, B.; Finke, S.; Dorhoi, A.; Pei, G. Ephrin B1 and B2 Mediate Cedar Virus Entry into Egyptian Fruit Bat Cells. *Viruses* 2025, *17*, 573, doi:10.3390/V17040573/S1.

350. Kaul, A.; Wörz, I.; Bartenschlager, R. Adaptation of the Hepatitis C Virus to Cell Culture. *Methods Mol. Biol.* 2009, *510*, 361–372, doi:10.1007/978-1-59745-394-3_27.

351. Prescott, J.; Hall, P.; Acuna-Retamar, M.; Ye, C.; Wathelet, M.G.; Ebihara, H.; Feldmann, H.; Hjelle, B. New World Hantaviruses Activate IFNλ Production in Type I IFN-Deficient Vero E6 Cells. *PLoS One* 2010, *5*, e11159, doi:10.1371/JOURNAL.PONE.0011159.

352. Stanwick, T.L.; Hallum, J. V. Role of Interferon in Six Cell Lines Persistently Infected with Rubella Virus. *Infect. Immun.* 1974, *10*, 810–815, doi:10.1128/IAI.10.4.810-815.1974.

353. Schountz, T.; Campbell, C.; Wagner, K.; Rovnak, J.; Martellaro, C.; Debuysscher, B.L.; Feldmann, H.; Prescott, J. Differential Innate Immune Responses Elicited by Nipah Virus and Cedar Virus Correlate with Disparate In Vivo Pathogenesis in Hamsters. *Viruses* 2019, *11*, 291, doi:10.3390/V11030291.

354. King, C.R.; Mehle, A. The Later Stages of Viral Infection: An Undiscovered Country of Host Dependency Factors. *PLoS Pathog.* 2020, *16*, e1008777, doi:10.1371/JOURNAL.PPAT.1008777.

355. Escudero-Pérez, B.; Lalande, A.; Mathieu, C.; Lawrence, P. Host–Pathogen Interactions Influencing Zoonotic Spillover Potential and Transmission in Humans. *Viruses* 2023, *15*, 599, doi:10.3390/V15030599.

356. Kim, J.-Y. V.; Pickering, B.S. Cell Line Bias in Virus Research: Implications for Viral Propagation and Biological Interpretation. *Front. Cell. Infect. Microbiol.* 2026, *15*, 1675100, doi:10.3389/FCIMB.2025.1675100.

357. Karki, S.; Li, M.M.H.; Schoggins, J.W.; Tian, S.; Rice, C.M.; MacDonald, M.R. Multiple Interferon Stimulated Genes Synergize with the Zinc Finger Antiviral Protein to Mediate Anti-Alphavirus Activity. *PLoS One* 2012, *7*, e37398, doi:10.1371/JOURNAL.PONE.0037398.

358. Habjan, M.; Penski, N.; Spiegel, M.; Weber, F. T7 RNA Polymerase-Dependent and -Independent Systems for CDNA-Based Rescue of Rift Valley Fever Virus. *J. Gen. Virol.* 2008, *89*, 2157–2166, doi:10.1099/VIR.0.2008/002097-0.

359. Emeny, J.M.; Morgan, M.J. Regulation of the Interferon System: Evidence That Vero Cells Have a Genetic Defect in Interferon Production. *J. Gen. Virol.* 1979, *43*, 247–252, doi:10.1099/0022-1317-43-1-247.

360. Coffey, L.L.; Vignuzzi, M. Host Alternation of Chikungunya Virus Increases Fitness While Restricting Population Diversity and Adaptability to Novel Selective Pressures. *J. Virol.* 2011, *85*, 1025–1035, doi:10.1128/JVI.01918-10.

361. Qian, W.; Zhou, J.; Duan, L.; Wang, H.; Xu, S.; Cao, Y. M6A Methylation: A Potential Key Player in Understanding and Treating COVID-2019 Infection. *Cell Death Discov.* 2023, *9*, 1–5, doi:10.1038/S41420-023-01580-1.

362. Zhai, Y.; Wang, L.; Lv, L.; Zhao, X.; Li, M.; Tian, J.; Qiu, X.; Yao, L.; Zhu, W.; Kang, Y.; et al. METTL3 Regulates PRRSV Replication by Suppressing Interferon Beta through Autophagy-Mediated IKKε Degradation. *J. Virol.* 2025, *99*, doi:10.1128/JVI.00098-25.

363. Imam, H.; Khan, M.; Gokhale, N.S.; McIntyre, A.B.R.; Kim, G.W.; Jang, J.Y.; Kim, S.J.; Mason, C.E.; Horner, S.M.; Siddiqui, A. N6-Methyladenosine Modification of Hepatitis b Virus RNA Differentially Regulates the Viral Life Cycle. *Proc. Natl. Acad. Sci. U. S. A.* 2018, *115*, 8829–8834, doi:10.1073/PNAS.1808319115.

364. Sorci, M.; Ianniello, Z.; Cruciani, S.; Larivera, S.; Ginistrelli, L.C.; Capuano, E.; Marchioni, M.; Fazi, F.; Fatica, A. METTL3 Regulates WTAP Protein Homeostasis. *Cell Death Dis. 2018 98* 2018, *9*, 796-, doi:10.1038/s41419-018-0843-z.

365. Zeng, Z.; Pan, Q.; Sun, Y.; Huang, H.; Chen, X.; Chen, T.; He, B.; Ye, H.; Zhu, S.; Pu, K.; et al. METTL3 Protects METTL14 from STUB1 -mediated Degradation to Maintain m 6 A Homeostasis . *EMBO Rep.* 2023, *24*, EMBR202255762-, doi:10.15252/EMBR.202255762.

366. Sacco, M.T.; Bland, K.M.; Horner, S.M. WTAP Targets the METTL3 m 6 A-Methyltransferase Complex to Cytoplasmic Hepatitis C Virus RNA to Regulate Infection . *J. Virol.* 2022, *96*, doi:10.1128/JVI.00997-22.

367. Ge, Y.; Ling, T.; Wang, Y.; Jia, X.; Xie, X.; Chen, R.; Chen, S.; Yuan, S.; Xu, A. Degradation of WTAP Blocks Antiviral Responses by Reducing the M6A Levels of IRF3 and IFNAR1 MRNA. *EMBO Rep.* 2021, *22*, e52101, doi:10.15252/EMBR.202052101.

368. Lin, S.; Choe, J.; Du, P.; Triboulet, R.; Gregory, R.I. The M6A Methyltransferase METTL3 Promotes Translation in Human Cancer Cells. *Mol. Cell* 2016, *62*, 335–345, doi:10.1016/J.MOLCEL.2016.03.021.

369. Nabeel-Shah, S.; Pu, S.; Burke, G.L.; Ahmed, N.; Braunschweig, U.; Farhangmehr, S.; Lee, H.; Wu, M.; Ni, Z.; Tang, H.; et al. Recruitment of the M6A/M6Am Demethylase FTO to Target RNAs by the Telomeric Zinc Finger Protein ZBTB48. *Genome Biol. 2024 251* 2024, *25*, 1–34, doi:10.1186/S13059-024-03392-7.

370. Gao, Z.; Zha, X.; Li, M.; Xia, X.; Wang, S. Insights into the M6A Demethylases FTO and ALKBH5 : Structural, Biological Function, and Inhibitor Development. *Cell Biosci. 2024 141* 2024, *14*, 1–20, doi:10.1186/S13578-024-01286-6.

371. Giri, S.; Kumar, V. FTO as an Epigenetic Regulator in Metabolic and Inflammatory Diseases. *INNOSC Theranostics Pharmacol. Sci. null, 0(0), 025140019* 2025, *0*, 025140019, doi:10.36922/ITPS025140019.

372. Yang, L.; Du, X.; Hu, Y.; Wu, Z.; Bao, W. Insight into Mechanism of ALKBH5-Mediated N6-Methyladenosine (M6A) Regulating Porcine Epidemic Diarrhea Virus Infection in IPEC-J2 Cells. *Int. J. Biol. Macromol.* 2025, *310*, 143501, doi:10.1016/J.IJBIOMAC.2025.143501.

373. Sun, H.-Y.; Gong, X.-Y.; Qu, Z.-L.; An, L.-L.; Guo, W.-H.; Luan, H.-Y.; Wu, M.-Y.; Yu, J.-C.; Dan, C.; Zhang, Y.-B. DDX54 Drives ALKBH5-Mediated Demethylation of Selected Transcripts to Suppress Interferon Antiviral Response. *J. Virol.* 2025, *99*, e00507-25, doi:10.1128/JVI.00507-25.

374. Li, W.; Zhou, J.; Gu, Y.; Chen, Y.; Huang, Y.; Yang, J.; Zhu, X.; Zhao, K.; Yan, Q.; Zhao, Z.; et al. Lactylation of RNA M6A Demethylase ALKBH5 Promotes Innate Immune Response to DNA Herpesviruses and Mpox Virus. *Proc. Natl. Acad. Sci. U. S. A.* 2024, *121*, e2409132121, doi:10.1073/PNAS.2409132121.

375. Li, L.; Krasnykov, K.; Homolka, D.; Gos, P.; Mendel, M.; Fish, R.J.; Pandey, R.R.; Pillai, R.S. The XRN1-Regulated RNA Helicase Activity of YTHDC2 Ensures Mouse Fertility Independently of M6A Recognition. *Mol. Cell* 2022, *82*, 1678-1690.e12, doi:10.1016/j.molcel.2022.02.034.

376. Tsai, K.; Courtney, D.G.; Cullen, B.R. Addition of M6A to SV40 Late MRNAs Enhances Viral Structural Gene Expression and Replication. *PLOS Pathog.* 2018, *14*, e1006919, doi:10.1371/JOURNAL.PPAT.1006919.

377. Wang, N.; Rajasekaran, N.; Hou, T.; Lisowski, L.; Mellins, E.D. Comparison of Transduction Efficiency among Various Lentiviruses Containing GFP Reporter in BM-HSC Transplantation. *Exp. Hematol.* 2013, *41*, 10.1016/j.exphem.2013.07.002, doi:10.1016/J.EXPHEM.2013.07.002.

378. Shaimardanova, A.A.; Chulpanova, D.S.; Kitaeva, K. V.; Abdrakhmanova, I.I.; Chernov, V.M.; Rutland, C.S.; Rizvanov, A.A.; Solovyeva, V. V. Production and Application of Multicistronic Constructs for Various Human Disease Therapies. *Pharmaceutics* 2019, *11*, 580, doi:10.3390/PHARMACEUTICS11110580.

379. Wang, X.; Marchisio, M.A. Synthetic Polycistronic Sequences in Eukaryotes. *Synth. Syst. Biotechnol.* 2021, *6*, 254–261, doi:10.1016/J.SYNBIO.2021.09.003.

380. Chan, H.Y.; Sivakamasundari, V.; Xing, X.; Kraus, P.; Yap, S.P.; Ng, P.; Lim, S.L.; Lufkin, T. Comparison of IRES and F2A-Based Locus-Specific Multicistronic Expression in Stable Mouse Lines. *PLoS One* 2011, *6*, e28885,

doi:10.1371/JOURNAL.PONE.0028885.

381. Bouabe, H.; Fässler, R.; Heesemann, J. Improvement of Reporter Activity by IRES-Mediated Polycistronic Reporter System. *Nucleic Acids Res.* 2008, *36*, e28, doi:10.1093/NAR/GKM1119.

382. Ferreira, J.P.; Overton, K.W.; Wang, C.L. Tuning Gene Expression with Synthetic Upstream Open Reading Frames. *Proc. Natl. Acad. Sci. U. S. A.* 2013, *110*, 11284–11289, doi:10.1073/PNAS.1305590110.

383. Cadiñanos, J.; Bradley, A. Generation of an Inducible and Optimized PiggyBac Transposon System. *Nucleic Acids Res.* 2007, *35*, e87, doi:10.1093/NAR/GKM446.

384. Macchiarulo, E.; Bassett, P.; Dudley, M. Challenges and Progress in Lentiviral Vector Bioprocessing. *Cell Gene Ther. Insights* 2018, *4*, 915–923, doi:10.18609/CGTI.2018.091.

385. Inada, E.; Saitoh, I.; Watanabe, S.; Aoki, R.; Miura, H.; Ohtsuka, M.; Murakami, T.; Sawami, T.; Yamasaki, Y.; Sato, M. PiggyBac Transposon-Mediated Gene Delivery Efficiently Generates Stable Transfectants Derived from Cultured Primary Human Deciduous Tooth Dental Pulp Cells (HDDPCs) and HDDPC-Derived IPS Cells. *Int. J. Oral Sci.* 2015, *7*, 144, doi:10.1038/IJOS.2015.18.

386. Sato, M.; Inada, E.; Saitoh, I.; Watanabe, S.; Nakamura, S. PiggyBac-Based Non-Viral In Vivo Gene Delivery Useful for Production of Genetically Modified Animals and Organs. *Pharmaceutics* 2020, *12*, 277, doi:10.3390/PHARMACEUTICS12030277.

387. Kurnaeva, M.A.; Zalevsky, A.O.; Arifulin, E.A.; Lisitsyna, O.M.; Tvorogova, A. V.; Shubina, M.Y.; Bourenkov, G.P.; Tikhomirova, M.A.; Potashnikova, D.M.; Kachalova, A.I.; et al. Molecular Coevolution of Nuclear and Nucleolar Localization Signals inside the Basic Domain of HIV-1 Tat. *J. Virol.* 2022, *96*, e01505-21, doi:10.1128/JVI.01505-21.

388. Okura, T.; Nakai, Y.; Kameya, T.; Mizukoshi, F.; Okura, H.; Kakizaki, M.; Kato, F.; Matsumoto, Y.; Nakatsu, Y.; Takeuchi, K.; et al. Paramyxovirus Matrix Protein Redirects METTL3 for Dual Regulation of Viral Replication and Immune Evasion. *PLOS Pathog.* 2025, *21*, e1013755, doi:10.1371/JOURNAL.PPAT.1013755.

389. Ruiz-Aravena, M.; McKee, C.; Gamble, A.; Lunn, T.; Morris, A.; Snedden, C.E.; Yinda, C.K.; Port, J.R.; Buchholz, D.W.; Yeo, Y.Y.; et al. Ecology, Evolution and Spillover of Coronaviruses from Bats. *Nat. Rev. Microbiol.* 2022, *20*, 299–314, doi:10.1038/S41579-021-00652-2.

390. da Costa, V.G.; Moreli, M.L.; Saivish, M.V. The Emergence of SARS, MERS and Novel SARS-2 Coronaviruses in the 21st Century. *Arch. Virol.* 2020, *165*, 1517–1526, doi:10.1007/S00705-020-04628-0.

391. Hiscott, J.; Alexandridi, M.; Muscolini, M.; Tassone, E.; Palermo, E.; Soultsioti, M.; Zevini, A. The Global Impact of the Coronavirus Pandemic. *Cytokine Growth Factor Rev.* 2020, *53*, 1–9, doi:10.1016/J.CYTOGFR.2020.05.010.

392. Joo, H.; Maskery, B.A.; Berro, A.D.; Rotz, L.D.; Lee, Y.K.; Brown, C.M. Economic Impact of the 2015 MERS Outbreak on the Republic of Korea's Tourism-Related Industries. *Heal. Secur.* 2019, *17*, 100, doi:10.1089/HS.2018.0115.

393. Bosch, B.J.; Bartelink, W.; Rottier, P.J.M. Cathepsin L Functionally Cleaves the Severe Acute Respiratory Syndrome Coronavirus Class I Fusion Protein Upstream of Rather than Adjacent to the Fusion Peptide. *J. Virol.* 2008, *82*, 8887–8890, doi:10.1128/JVI.00415-08.

394. Koyou, H.L.; Salleh, M.N.; Jelemie, C.S.; Badrin, M.J.Q.; Prastiyanto, M.E.; Ramachandran, V. TMPRSS2: A Key Host Factor in SARS-CoV-2 Infection and Potential Therapeutic Target. *Medeni. Med. J.* 2025, *40*, 101, doi:10.4274/MMJ.GALENOS.2025.40460.

395. Fujita, S.; Kosugi, Y.; Kimura, I.; Tokunaga, K.; Ito, J.; Sato, K.; Matsuno, K.; Nao, N.; Sawa, H.; Tanaka, S.; et al. Determination of the Factors Responsible for the Tropism of SARS-CoV-2-Related Bat Coronaviruses to Rhinolophus Bat ACE2. *J. Virol.* 2023, *97*, doi:10.1128/JVI.00990-23.

396. Webby, R.; Hoffmann, E.; Webster, R. Molecular Constraints to Interspecies Transmission of Viral Pathogens. *Nat. Med.* 2004, *10*, S77, doi:10.1038/NM1151.

397. Yan, H.; Jiao, H.; Liu, Q.; Zhang, Z.; Xiong, Q.; Wang, B.J.; Wang, X.; Guo, M.; Wang, L.F.; Lan, K.; et al. ACE2 Receptor Usage Reveals Variation in Susceptibility to SARS-CoV and SARS-CoV-2 Infection among Bat Species. *Nat. Ecol. Evol.* 2021, *5*, 600–608, doi:10.1038/s41559-021-01407-1.

398. Gao, S.; Zhang, L. ACE2 Partially Dictates the Host Range and Tropism of SARS-CoV-2. *Comput. Struct. Biotechnol. J.* 2020, *18*, 4040–4047, doi:10.1016/J.CSBJ.2020.11.032.

399. Xu, Z.; Lobato, A.C.; Liu, K.; Gao, G.F. ACE2-Using Coronaviruses: A Global Concern. *hLife* 2025, *3*, 615–617, doi:10.1016/J.HLIFE.2025.09.005.

400. Ng, O.W.; Tan, Y.J. Understanding Bat SARS-like Coronaviruses for the Preparation of Future Coronavirus Outbreaks — Implications for Coronavirus Vaccine Development. *Hum. Vaccin. Immunother.* 2016, *13*, 186, doi:10.1080/21645515.2016.1228500.

401. Temmam, S.; Vongphayloth, K.; Baquero, E.; Munier, S.; Bonomi, M.; Regnault, B.; Douangboubpha, B.; Karami, Y.; Chrétien, D.; Sanamxay, D.; et al. Bat Coronaviruses Related to SARS-CoV-2 and Infectious for Human Cells. *Nature* 2022, *604*, 330–336, doi:10.1038/S41586-022-04532-4.

402. Temmam, S.; Vongphayloth, K.; Baquero, E.; Munier, S.; Bonomi, M.;

Regnault, B.; Douangboubpha, B.; Karami, Y.; Chrétien, D.; Sanamxay, D.; et al. Author Correction: Bat Coronaviruses Related to SARS-CoV-2 and Infectious for Human Cells. *Nature* 2022, *607*, E19–E19, doi:10.1038/S41586-022-05048-7.

403. Schlottau, K.; Rissmann, M.; Graaf, A.; Schön, J.; Sehl, J.; Wylezich, C.; Höper, D.; Mettenleiter, T.C.; Balkema-Buschmann, A.; Harder, T.; et al. SARS-CoV-2 in Fruit Bats, Ferrets, Pigs, and Chickens: An Experimental Transmission Study. *The Lancet Microbe* 2020, *1*, e218–e225, doi:10.1016/S2666-5247(20)30089-6.

404. Mohl, B.P.; Blaurock, C.; Breithaupt, A.; Riek, A.; Speakman, J.R.; Hambly, C.; Bokelmann, M.; Pei, G.; Sadeghi, B.; Dorhoi, A.; et al. Increased Susceptibility of Rousettus Aegyptiacus Bats to Respiratory SARS-CoV-2 Challenge Despite Its Distinct Tropism for Gut Epithelia in Bats. *Viruses* 2024, *16*, 1717, doi:10.3390/V16111717.

405. Banerjee, A.; Baker, M.L.; Kulcsar, K.; Misra, V.; Plowright, R.; Mossman, K. Novel Insights Into Immune Systems of Bats. *Front. Immunol.* 2020, *11*, 507886, doi:10.3389/FIMMU.2020.00026.

406. Briggs, K.; Sweeney, R.; Blehert, D.S.; Spackman, E.; Suarez, D.L.; Kapczynski, D.R. SARS-CoV-2 Utilization of ACE2 from Different Bat Species Allows for Virus Entry and Replication in Vitro. *Virology* 2023, *586*, 122–129, doi:10.1016/j.virol.2023.07.002.

407. Li, W.; Zhang, C.; Sui, J.; Kuhn, J.H.; Moore, M.J.; Luo, S.; Wong, S.K.; Huang, I.C.; Xu, K.; Vasilieva, N.; et al. Receptor and Viral Determinants of SARS-Coronavirus Adaptation to Human ACE2. *EMBO J.* 2005, *24*, 1634–1643, doi:10.1038/SJ.EMBOJ.7600640.

408. Conceicao, C.; Thakur, N.; Human, S.; Kelly, J.T.; Logan, L.; Bialy, D.; Bhat, S.; Stevenson-Leggett, P.; Zagrajek, A.K.; Hollinghurst, P.; et al. The SARS-CoV-2 Spike Protein Has a Broad Tropism for Mammalian ACE2 Proteins. *PLoS Biol.* 2020, *18*, e3001016, doi:10.1371/JOURNAL.PBIO.3001016.

409. Shang, J.; Ye, G.; Shi, K.; Wan, Y.; Luo, C.; Aihara, H.; Geng, Q.; Auerbach, A.; Li, F. Structural Basis of Receptor Recognition by SARS-CoV-2. *Nat. 2020 5817807* 2020, *581*, 221–224, doi:10.1038/s41586-020-2179-y.

410. Qing, E.; Kicmal, T.; Kumar, B.; Hawkins, G.M.; Timm, E.; Perlman, S.; Gallagher, T. Dynamics of SARS-CoV-2 Spike Proteins in Cell Entry: Control Elements in the Amino-Terminal Domains. *MBio* 2021, *12*, e01590-21, doi:10.1128/MBIO.01590-21.

411. Segeritz, C.P.; Vallier, L. Cell Culture: Growing Cells as Model Systems In Vitro. *Basic Sci. Methods Clin. Res.* 2017, 151–172, doi:10.1016/B978-0-12-803077-6.00009-6.

412. Hoffmann, M.; Kleine-Weber, H.; Schroeder, S.; Krüger, N.; Herrler, T.; Erichsen, S.; Schiergens, T.S.; Herrler, G.; Wu, N.H.; Nitsche, A.; et al. SARS-

CoV-2 Cell Entry Depends on ACE2 and TMPRSS2 and Is Blocked by a Clinically Proven Protease Inhibitor. *Cell* 2020, *181*, 271, doi:10.1016/J.CELL.2020.02.052.

413. Yamamoto, M.; Matsuyama, S.; Li, X.; Takeda, M.; Kawaguchi, Y.; Inoue, J.I.; Matsuda, Z. Identification of Nafamostat as a Potent Inhibitor of Middle East Respiratory Syndrome Coronavirus S Protein-Mediated Membrane Fusion Using the Split-Protein-Based Cell-Cell Fusion Assay. *Antimicrob. Agents Chemother.* 2016, *60*, 6532, doi:10.1128/AAC.01043-16.

414. Kawase, M.; Shirato, K.; van der Hoek, L.; Taguchi, F.; Matsuyama, S. Simultaneous Treatment of Human Bronchial Epithelial Cells with Serine and Cysteine Protease Inhibitors Prevents Severe Acute Respiratory Syndrome Coronavirus Entry. *J. Virol.* 2012, *86*, 6537–6545, doi:10.1128/JVI.00094-12.

415. Oliveto, G.; Scagnolari, C.; Frasca, F.; Sorrentino, L.; Matera, L.; Nenna, R.; Viscido, A.; Scordio, M.; Petrarca, L.; Maria Zicari, A.; et al. The Non-Functional ACE2 Isoform, but Not the SARS-CoV-2 Receptor, Is Induced as an Interferon-Stimulated Gene, in SARS-CoV-2 Infected Adults. *Cytokine* 2022, *158*, 155997, doi:10.1016/J.CYTO.2022.155997.

416. Yoon, S.; Nam, D. Gene Dispersion Is the Key Determinant of the Read Count Bias in Differential Expression Analysis of RNA-Seq Data. *BMC Genomics* 2017, *18*, 1–11, doi:10.1186/S12864-017-3809-0.

417. Mattijssen, S.; Pruijn, G.J.M. Viperin, a Key Player in the Antiviral Response. *Microbes Infect.* 2012, *14*, 419–426, doi:10.1016/J.MICINF.2011.11.015.

418. McDougal, M.B.; Boys, I.N.; Maria, A.M. De; Nakahara, E.; Schoggins, J.W. IFIT1 Is Rapidly Evolving and Exhibits Disparate Antiviral Activities across 11 Mammalian Orders. *Elife* 2025, *13*, doi:10.7554/ELIFE.101929.2.

419. Basters, A.; Knobeloch, K.P.; Fritz, G. USP18 - a Multifunctional Component in the Interferon Response. *Biosci. Rep.* 2018, *38*, doi:10.1042/BSR20180250.

420. Pires De Souza, G.A.; Le Bideau, M.; Boschi, C.; Wurtz, N.; Colson, P.; Aherfi, S.; Devaux, C.; La Scola, B. Choosing a Cellular Model to Study SARS-CoV-2. *Front. Cell. Infect. Microbiol.* 2022, *12*, 1003608, doi:10.3389/FCIMB.2022.1003608.

421. Hirose, R.; Watanabe, N.; Bandou, R.; Yoshida, T.; Daidoji, T.; Naito, Y.; Itoh, Y.; Nakaya, T. A Cytopathic Effect-Based Tissue Culture Method for HCoV-OC43 Titration Using TMPRSS2-Expressing VeroE6 Cells. *mSphere* 2021, *6*, doi:10.1128/MSPHERE.00159-21.

422. Ogando, N.S.; Dalebout, T.J.; Zevenhoven-Dobbe, J.C.; Limpens, R.W.A.L.; van der Meer, Y.; Caly, L.; Druce, J.; de Vries, J.J.C.; Kikkert, M.; Barcena, M.; et al. SARS-Coronavirus-2 Replication in Vero E6 Cells: Replication Kinetics, Rapid Adaptation and Cytopathology. *J. Gen. Virol.* 2020, *101*, 925, doi:10.1099/JGV.0.001453.

423. Ng, M.L.; Tan, S.H.; See, E.E.; Ooi, E.E.; Ling, A.E. Proliferative Growth of SARS Coronavirus in Vero E6 Cells. *J. Gen. Virol.* 2003, *84*, 3291–3303, doi:10.1099/VIR.0.19505-0.

424. Coleman, C.M.; Frieman, M.B. Growth and Quantification of MERS-CoV Infection. *Curr. Protoc. Microbiol.* 2015, *37*, 1521, doi:10.1002/9780471729259.MC15E02S37.

425. Li, W.; Moore, M.J.; Vasllieva, N.; Sui, J.; Wong, S.K.; Berne, M.A.; Somasundaran, M.; Sullivan, J.L.; Luzuriaga, K.; Greeneugh, T.C.; et al. Angiotensin-Converting Enzyme 2 Is a Functional Receptor for the SARS Coronavirus. *Nature* 2003, *426*, 450–454, doi:10.1038/NATURE02145.

426. Liu, Y.; Liang, Q.Z.; Lu, W.; Yang, Y. Le; Chen, R.; Huang, Y.W.; Wang, B. A Comparative Analysis of Coronavirus Nucleocapsid (N) Proteins Reveals the SADS-CoV N Protein Antagonizes IFN-β Production by Inducing Ubiquitination of RIG-I. *Front. Immunol.* 2021, *12*, 688758, doi:10.3389/FIMMU.2021.688758.

427. Abbasi, H.; Tabaraei, A.; Hosseini, S.M.; Khosravi, A.; Nikoo, H.R. Real-Time PCR Ct Value in SARS-CoV-2 Detection: RdRp or N Gene? *Infection* 2022, *50*, 537–540, doi:10.1007/S15010-021-01674-X.

428. Zhu, X.; Zhou, F.; Zhou, Q.; Xu, J. Evaluating the Role of SARS-CoV-2 Target Genes Based on Two Nucleic Acid Assay Kits. *Front. Public Heal.* 2022, *10*, 982171, doi:10.3389/FPUBH.2022.982171.

429. Ellis, P.; Somogyvári, F.; Virok, D.P.; Noseda, M.; McLean, G.R. Decoding Covid-19 with the SARS-CoV-2 Genome. *Curr. Genet. Med. Reports 2021 91* 2021, *9*, 1–12, doi:10.1007/S40142-020-00197-5.

430. Song, W.; Fang, Z.; Ma, F.; Li, J.; Huang, Z.; Zhang, Y.; Li, J.; Chen, K. The Role of SARS-CoV-2 N Protein in Diagnosis and Vaccination in the Context of Emerging Variants: Present Status and Prospects. *Front. Microbiol.* 2023, *14*, 1217567, doi:10.3389/FMICB.2023.1217567.

431. Ma, H.; Bell, K.N.; Loker, R.N. QPCR and QRT-PCR Analysis: Regulatory Points to Consider When Conducting Biodistribution and Vector Shedding Studies. *Mol. Ther. Methods Clin. Dev.* 2020, *20*, 152, doi:10.1016/J.OMTM.2020.11.007.

432. Nie, Y.; Wang, P.; Shi, X.; Wang, G.; Chen, J.; Zheng, A.; Wang, W.; Wang, Z.; Qu, X.; Luo, M.; et al. Highly Infectious SARS-CoV Pseudotyped Virus Reveals the Cell Tropism and Its Correlation with Receptor Expression. *Biochem. Biophys. Res. Commun.* 2004, *321*, 994–1000, doi:10.1016/J.BBRC.2004.07.060.

433. Rajah, M.M.; Bernier, A.; Buchrieser, J.; Schwartz, O. The Mechanism and Consequences of SARS-CoV-2 Spike-Mediated Fusion and Syncytia Formation. *J. Mol. Biol.* 2021, *434*, 167280, doi:10.1016/J.JMB.2021.167280.

434. Zeng, C.; Evans, J.P.; King, T.; Zheng, Y.-M.; Oltz, E.M.; Whelan, S.P.J.; Saif, L.; Peeples, M.E.; Liu, S.-L. SARS-CoV-2 Spreads through Cell-to-Cell Transmission. *bioRxiv* 2021, 2021.06.01.446579, doi:10.1101/2021.06.01.446579.

435. Ma, H.; Zhu, Z.; Lin, H.; Wang, S.; Zhang, P.; Li, Y.; Li, L.; Wang, J.; Zhao, Y.; Han, J. Pyroptosis of Syncytia Formed by Fusion of SARS-CoV-2 Spike and ACE2-Expressing Cells. *Cell Discov. 2021 71* 2021, *7*, 1–4, doi:10.1038/s41421-021-00310-0.

436. Wang, H.; Yang, P.; Liu, K.; Guo, F.; Zhang, Y.; Zhang, G.; Jiang, C. SARS Coronavirus Entry into Host Cells through a Novel Clathrin- and Caveolae-Independent Endocytic Pathway. *Cell Res. 2008 182* 2008, *18*, 290–301, doi:10.1038/cr.2008.15.

437. Wang, S.; Guo, F.; Liu, K.; Wang, H.; Rao, S.; Yang, P.; Jiang, C. Endocytosis of the Receptor-Binding Domain of SARS-CoV Spike Protein Together with Virus Receptor ACE2. *Virus Res.* 2008, *136*, 8–15, doi:10.1016/J.VIRUSRES.2008.03.004.

438. Badawi, S.; Ali, B.R. ACE2 Nascence, Trafficking, and SARS-CoV-2 Pathogenesis: The Saga Continues. *Hum. Genomics 2021 151* 2021, *15*, 1–14, doi:10.1186/S40246-021-00304-9.

439. Huang, I.C.; Bosch, B.J.; Li, F.; Li, W.; Kyoung, H.L.; Ghiran, S.; Vasilieva, N.; Dermody, T.S.; Harrison, S.C.; Dormitzer, P.R.; et al. SARS Coronavirus, but Not Human Coronavirus NL63, Utilizes Cathepsin L to Infect ACE2-Expressing Cells. *J. Biol. Chem.* 2006, *281*, 3198–3203, doi:10.1074/JBC.M508381200.

440. Hoffmann, M.; Hofmann-Winkler, H.; Smith, J.C.; Krüger, N.; Sørensen, L.K.; Søgaard, O.S.; Hasselstrøm, J.B.; Winkler, M.; Hempel, T.; Raich, L.; et al. Camostat Mesylate Inhibits SARS-CoV-2 Activation by TMPRSS2-Related Proteases and Its Metabolite GBPA Exerts Antiviral Activity. *bioRxiv* 2020, 2020.08.05.237651, doi:10.1101/2020.08.05.237651.

441. Iwata-Yoshikawa, N.; Kakizaki, M.; Shiwa-Sudo, N.; Okura, T.; Tahara, M.; Fukushi, S.; Maeda, K.; Kawase, M.; Asanuma, H.; Tomita, Y.; et al. Essential Role of TMPRSS2 in SARS-CoV-2 Infection in Murine Airways. *Nat. Commun.* 2022, *13*, 6100, doi:10.1038/S41467-022-33911-8.

442. Dludla, P. V.; Jack, B.; Viraragavan, A.; Pheiffer, C.; Johnson, R.; Louw, J.; Muller, C.J.F. A Dose-Dependent Effect of Dimethyl Sulfoxide on Lipid Content, Cell Viability and Oxidative Stress in 3T3-L1 Adipocytes. *Toxicol. Reports* 2018, *5*, 1014–1020, doi:10.1016/J.TOXREP.2018.10.002.

443. Santos, L.M.; Shimabuko, D.Y.; Sipert, C.R. Dimethyl Sulfoxide Affects the Viability and Mineralization Activity of Apical Papilla Cells in Vitro. *Braz. Dent. J.* 2024, *35*, e24-6054, doi:10.1590/0103-644020246054.

444. Timm, M.; Saaby, L.; Moesby, L.; Hansen, E.W. Considerations Regarding Use

of Solvents in in Vitro Cell Based Assays. *Cytotechnology* 2013, *65*, 887, doi:10.1007/S10616-012-9530-6.

445. Moskot, M.; Jakóbkiewicz-Banecka, J.; Kloska, A.; Piotrowska, E.; Narajczyk, M.; Gabig-Cimińska, M. The Role of Dimethyl Sulfoxide (DMSO) in Gene Expression Modulation and Glycosaminoglycan Metabolism in Lysosomal Storage Disorders on an Example of Mucopolysaccharidosis. *Int. J. Mol. Sci.* 2019, *20*, 304, doi:10.3390/IJMS20020304.

446. Zhou, Y.; Vedantham, P.; Lu, K.; Agudelo, J.; Carrion, R.; Nunneley, J.W.; Barnard, D.; Pöhlmann, S.; McKerrow, J.H.; Renslo, A.R.; et al. Protease Inhibitors Targeting Coronavirus and Filovirus Entry. *Antiviral Res.* 2015, *116*, 76–84, doi:10.1016/J.ANTIVIRAL.2015.01.011.

447. Koch, J.; Uckeley, Z.M.; Doldan, P.; Stanifer, M.; Boulant, S.; Lozach, P. TMPRSS2 Expression Dictates the Entry Route Used by SARS-CoV-2 to Infect Host Cells. *EMBO J.* 2021, *40*, 107821, doi:10.15252/EMBJ.2021107821.

448. Yang, W.L.; Li, Q.; Sun, J.; Huat Tan, S.; Tang, Y.H.; Zhao, M.M.; Li, Y.Y.; Cao, X.; Zhao, J.C.; Yang, J.K. Potential Drug Discovery for COVID-19 Treatment Targeting Cathepsin L Using a Deep Learning-Based Strategy. *Comput. Struct. Biotechnol. J.* 2022, *20*, 2442–2454, doi:10.1016/J.CSBJ.2022.05.023.

449. Chang, C.W.; Parsi, K.M.; Somasundaran, M.; Vanderleeden, E.; Liu, P.; Cruz, J.; Cousineau, A.; Finberg, R.W.; Kurt-Jones, E.A. A Newly Engineered A549 Cell Line Expressing ACE2 and TMPRSS2 Is Highly Permissive to SARS-CoV-2, Including the Delta and Omicron Variants. *Viruses 2022, Vol. 14, Page 1369* 2022, *14*, 1369, doi:10.3390/V14071369.

450. Padmanabhan, P.; Desikan, R.; Dixit, N.M. Targeting TMPRSS2 and Cathepsin B/L Together May Be Synergistic against SARS-CoV-2 Infection. *PLoS Comput. Biol.* 2020, *16*, e1008461, doi:10.1371/JOURNAL.PCBI.1008461.

451. Hashimoto, R.; Sakamoto, A.; Deguchi, S.; Yi, R.; Sano, E.; Hotta, A.; Takahashi, K.; Yamanaka, S.; Takayama, K. Dual Inhibition of TMPRSS2 and Cathepsin Bprevents SARS-CoV-2 Infection in IPS Cells. *Mol. Ther. Nucleic Acids* 2021, *26*, 1107, doi:10.1016/J.OMTN.2021.10.016.

452. Yamaguchi, T.; Hoshizaki, M.; Minato, T.; Nirasawa, S.; Asaka, M.N.; Niiyama, M.; Imai, M.; Uda, A.; Chan, J.F.W.; Takahashi, S.; et al. ACE2-like Carboxypeptidase B38-CAP Protects from SARS-CoV-2-Induced Lung Injury. *Nat. Commun. 2021 121* 2021, *12*, 6791-, doi:10.1038/s41467-021-27097-8.

453. Lu, Y.; Zhu, Q.; Fox, D.M.; Gao, C.; Stanley, S.A.; Luo, K. SARS-CoV-2 down-Regulates ACE2 through Lysosomal Degradation. *Mol. Biol. Cell* 2022, *33*, ar147, doi:10.1091/MBC.E22-02-0045.

454. Richard, D.; Muthuirulan, P.; Aguiar, J.; Doxey, A.C.; Banerjee, A.; Mossman, K.; Hirota, J.; Capellini, T.D. Intronic Regulation of SARS-CoV-2 Receptor (ACE2) Expression Mediated by Immune Signaling and Oxidative Stress

Pathways. *iScience* 2022, *25*, 104614, doi:10.1016/J.ISCI.2022.104614.

455. Chen, V.H.E.; Tay, J.K.; Gurung, R.; Nair, S.; Tay, D.J.W.; Tan, K. Sen; Foo, R.S.Y.; Tambyah, P.A. ACE2 and TMPRSS2 Gene Expression Is Reduced Acutely in SARS-CoV-2 Patients but Returns to Normal with Recovery. *Sci. Reports 2025 151* 2025, *15*, 12828-, doi:10.1038/s41598-025-96279-x.

456. Wang, Y.; Thaler, M.; Ninaber, D.K.; Does, A.M. van der; Ogando, N.S.; Beckert, H.; Taube, C.; Salgado-Benvindo, C.; Snijder, E.J.; Bredenbeek, P.J.; et al. Impact of Human Airway Epithelial Cellular Composition on SARS-CoV-2 Infection Biology. *bioRxiv* 2021, 2021.07.21.453304, doi:10.1101/2021.07.21.453304.

457. Sajuthi, S.P.; DeFord, P.; Li, Y.; Jackson, N.D.; Montgomery, M.T.; Everman, J.L.; Rios, C.L.; Pruesse, E.; Nolin, J.D.; Plender, E.G.; et al. Type 2 and Interferon Inflammation Regulate SARS-CoV-2 Entry Factor Expression in the Airway Epithelium. *Nat. Commun. 2020 111* 2020, *11*, 5139-, doi:10.1038/s41467-020-18781-2.

458. Onabajo, O.O.; Banday, A.R.; Stanifer, M.L.; Yan, W.; Obajemu, A.; Santer, D.M.; Florez-Vargas, O.; Piontkivska, H.; Vargas, J.M.; Ring, T.J.; et al. Interferons and Viruses Induce a Novel Truncated ACE2 Isoform and Not the Full-Length SARS-CoV-2 Receptor. *Nat. Genet. 2020 5212* 2020, *52*, 1283–1293, doi:10.1038/s41588-020-00731-9.

459. Scagnolari, C.; Bitossi, C.; Viscido, A.; Frasca, F.; Oliveto, G.; Scordio, M.; Petrarca, L.; Mancino, E.; Nenna, R.; Riva, E.; et al. ACE2 Expression Is Related to the Interferon Response in Airway Epithelial Cells but Is That Functional for SARS-CoV-2 Entry? *Cytokine* 2021, *140*, 155430, doi:10.1016/J.CYTO.2021.155430.

460. Bastolla, U.; Chambers, P.; Abia, D.; Garcia-Bermejo, M.L.; Fresno, M. Is Covid-19 Severity Associated With ACE2 Degradation? *Front. Drug Discov.* 2021, *1*, 789710, doi:10.3389/FDDSV.2021.789710.

461. Wood, M.R.; de Vries, J.L.; Epstein, J.H.; Markotter, W. Variations in Small-Scale Movements of, Rousettus Aegyptiacus, a Marburg Virus Reservoir across a Seasonal Gradient. *Front. Zool.* 2023, *20*, 1–17, doi:10.1186/S12983-023-00502-2.

462. Kirejczyk, S.G.M.; Schuh, A.J.; Amman, B.R.; Guito, J.C.; Sealy, T.K.; Graziano, J.C.; Zhang, J.; Jones, M.E.B.; Brown, C.C.; Towner, J.S. Marburg and Kasokero Viruses Elicit Differential Antiviral Innate Immune Control by Their Natural Reservoir Bat, the Egyptian Rousette (Rousettus Aegyptiacus). *Antiviral Res.* 2025, *240*, 106211, doi:10.1016/J.ANTIVIRAL.2025.106211.

463. Rothenburg, S.; Brennan, G. Species-Specific Host-Virus Interactions: Implications for Viral Host Range and Virulence. *Trends Microbiol.* 2019, *28*, 46, doi:10.1016/J.TIM.2019.08.007.

464. Hood, G.; Carroll, M. Host–Pathogen Interactions of Emerging Zoonotic

Viruses: Bats, Humans and Filoviruses. *Curr. Opin. Virol.* 2024, *68–69*, 101436, doi:10.1016/J.COVIRO.2024.101436.

465. Madel Alfajaro, M.; Keeler, E.L.; Li, N.; Catanzaro, N.J.; Teng, I.T.; Zhao, Z.; Grunst, M.W.; Yount, B.; Schäfer, A.; Wang, D.; et al. HKU5 Bat Merbecoviruses Engage Bat and Mink ACE2 as Entry Receptors. *Nat. Commun.* 2025, *16*, 1–16, doi:10.1038/S41467-025-61583-7.

466. Zhao, J.; Wan, W.; Yu, K.; Lemey, P.; Pettersson, J.H.O.; Bi, Y.; Lu, M.; Li, X.; Chen, Z.; Zheng, M.; et al. Farmed Fur Animals Harbour Viruses with Zoonotic Spillover Potential. *Nature* 2024, *634*, 228, doi:10.1038/S41586-024-07901-3.

467. Yang, Y.; Du, L.; Liu, C.; Wang, L.; Ma, C.; Tang, J.; Baric, R.S.; Jiang, S.; Li, F. Receptor Usage and Cell Entry of Bat Coronavirus HKU4 Provide Insight into Bat-to-Human Transmission of MERS Coronavirus. *Proc. Natl. Acad. Sci.* 2014, *111*, 12516–12521, doi:10.1073/PNAS.1405889111.

468. Menachery, V.D.; Dinnon, K.H.; Yount, B.L.; McAnarney, E.T.; Gralinski, L.E.; Hale, A.; Graham, R.L.; Scobey, T.; Anthony, S.J.; Wang, L.; et al. Trypsin Treatment Unlocks Barrier for Zoonotic Bat Coronavirus Infection. *J. Virol.* 2020, *94*, e01774-19, doi:10.1128/JVI.01774-19.

469. Agnihothram, S.; Yount, B.L.; Donaldson, E.F.; Huynh, J.; Menachery, V.D.; Gralinski, L.E.; Graham, R.L.; Becker, M.M.; Tomar, S.; Scobey, T.D.; et al. A Mouse Model for Betacoronavirus Subgroup 2c Using a Bat Coronavirus Strain HKU5 Variant. *MBio* 2014, *5*, doi:10.1128/MBIO.00047-14.

470. Heurich, A.; Hofmann-Winkler, H.; Gierer, S.; Liepold, T.; Jahn, O.; Pöhlmann, S. TMPRSS2 and ADAM17 Cleave ACE2 Differentially and Only Proteolysis by TMPRSS2 Augments Entry Driven by the Severe Acute Respiratory Syndrome Coronavirus Spike Protein. *J. Virol.* 2014, *88*, 1293–1307, doi:10.1128/JVI.02202-13.

471. Bian, J.; Li, Z. Angiotensin-Converting Enzyme 2 (ACE2): SARS-CoV-2 Receptor and RAS Modulator. *Acta Pharm. Sin. B* 2021, *11*, 1–12, doi:10.1016/J.APSB.2020.10.006.